Oxidation of vanadium nitrides thin films : a novel method to form efficient thermochromic VO

Alexis C. García-Wong

THÈSE

Pour l'obtention du titre de

DOCTEUR de L'UNIVERSITÉ DE LORRAINE

Spécialité : Science des Matériaux

Présentée par

Alexis Carlos GARCÍA WONG

Oxidation of vanadium nitrides thin films: a novel method to form efficient thermochromic VO_2

Thèse soutenue publiquement le 15 Juin 2021 à Nancy, devant le jury composé de :

Corinne MARCEL	Rapporteur	Ingénieur, CEA Le Ripault
Fabien PAUMIER	Rapporteur	Maître de Conférences, Institut Pprime, Université de Poitiers
Corinne CHAMPEAUX	Examinateur	Professeur, IRCER, Université de Limoges
Stéphane ANDRIEU	Examinateur	Professeur, Institut Jean Lamour, Université de Lorraine
Fabien CAPON	Co-directeur de thèse	Maître de Conférences, Institut Jean Lamour, Université de Lorraine
Jean-François PIERSON	Directeur de thèse	Professeur, Institut Jean Lamour, Université de Lorraine
David PILLOUD	Invité	Ingénieur CNRS, Institut Jean Lamour, Université de Lorraine

Institut Jean Lamour, UMR 7198, ARTEM - CS 50840-54011 Nancy Cedex

Université de Lorraine – Ecole doctorale : Chimie - Mécanique - Matériaux- Physique (C2MP)

Abstract

In this thesis, we study the formation of vanadium dioxide (VO_2) from a two-step procedure. We demonstrate for the first time that high-quality thermochromic VO_2 can be obtained from the air oxidation of sputter-deposited VN and V_2N polycrystalline films. Depending on the annealing conditions (duration and temperature) VO_2 and V_2O_5 are the two principal phases formed during the oxidation process of the nitride films. The first oxide obtained is VO_2(M), which coexists with the precursor for a prolonged period at 450°C or suddenly disappeared at 525 and 550°C. For optimized durations at each temperature VO_2(M) is the predominant phase. For higher durations, the VO_2 phase is oxidized into V_2O_5. The thermochromic performance of the vanadium oxide films is strongly influenced by the oxidation duration. TEM analysis indicates that both VN and V_2N precursors follow different oxidation kinetics. Concerning the VN oxidation, there is an abrupt interface between the polycrystalline VN films and the formed VO_2. On the other hand, EELS results for the V_2N oxidation evidence a formation of a VN layer at the interface between the remaining V_2N layer and the growing VO_2 one. Besides, the influence of the V_2N thickness on the optical modulation properties of the formed VO_2(M) is studied. The oxidation of 100 nm-thick V_2N films on Si substrate yields a negative emissivity switch ($\Delta\varepsilon$). On the contrary, the annealing of 445 nm V_2N samples produces a positive value for $\Delta\varepsilon$. These findings indicate the possibility to control the sign of the optical modulation of the formed VO_2 depending on the initial thickness of the V_2N precursor. Furthermore, we investigate the oxidation of epitaxial VN thin films, which follow a different path than polycrystalline VN films, caused by the absence of grain boundaries in the epitaxial layers. This process depicts the epitaxial growth of a VO_2(B) layer on the remaining VN, as shown by TEM results. Finally, we apply a simple criterion to transpose the deposition conditions between the two sputtering machines used in the thesis based on the thermochromic performance.

Résumé

Dans cette thèse, nous étudions la formation de dioxyde de vanadium (VO_2) à partir d'un procédé en deux étapes. Nous démontrons pour la première fois que l'oxydation contrôlée de films polycristallins VN et V_2N déposés par pulvérisation cathodique conduit à la formation de VO_2 thermochromique de haute qualité. L'optimisation de la durée du recuit s'avère fondamentale pour former la phase désirée. VO_2 et V_2O_5 sont, en général, les seules phases formées lors du processus d'oxydation des films polycristallins de VN et V_2N. Le premier oxyde obtenu est VO_2(M), qui coexiste avec le précurseur azoté pendant une période prolongée à des températures comprises entre 450 et 550 °C. Les performances thermochromiques des films oxydés sont affectées lorsque l'oxydation n'est pas complète ou lorsqu'elle est totale en raison de la formation de V_2O_5 pour des temps de recuit dépassant la valeur optimale. L'analyse MET indique que les deux précurseurs suivent des cinétiques d'oxydation différentes. Concernant l'oxydation de VN, il existe une interface abrupte entre les films polycristallins de VN et le VO_2 formé. D'autre part, les résultats EELS pour l'oxydation de V_2N mettent en évidence la formation d'une couche de VN à l'interface entre la couche de V_2N restante et la couche de VO_2 en croissance. De plus, l'influence de l'épaisseur de V_2N sur le signe de la variation d'émissivité de VO_2(M) formé a été étudiée. L'oxydation de films de V_2N de 100 nm d'épaisseur déposés sur un substrat en Si donne un changement d'émissivité négatif ($\Delta\varepsilon$). Au contraire, le recuit d'échantillons de V_2N de 445 nm produit une valeur positive pour $\Delta\varepsilon$. Ces résultats indiquent pour la première fois qu'il est possible de contrôler le signe de la variation d'émissivité de VO_2 formé à partir de l'épaisseur initiale du précurseur V_2N. Par ailleurs, nous avons également étudié l'oxydation des couches minces épitaxiées de VN, qui suivent un chemin différent des films polycristallins de VN, causé par l'absence de joints de grains dans les couches épitaxiées. Ce processus conduit à la croissance épitaxiée d'une couche de VO_2(B) sur le VN restant, comme le révèlent les résultats TEM. Enfin, nous avons appliqué un critère simple pour transposer les conditions de dépôt entre les deux machines de pulvérisation utilisées durant cette thèse à partir des performances thermochromiques des films.

Acknowledgements

I believe that it is an impossible task to acknowledge everyone related to the conclusion of this thesis. For this reason, I will like to begin with my sincere gratitude to all of you I will not name in the following, but have made this journey more easy and enjoyable for me.

I would like to thank my co-supervisor Fabien Capon, for your conviction in my application when I didn't have a background in any specific area of the thesis proposal. Thanks for the trust, for letting me develop my ideas and the encouragement to work independently.

A special thanks to David Pilloud, without whom, this work would never have been done. You have been a support and guidance during these years. I appreciate every one of our "only 5 minutes" discussions. You are the kindest person I have ever met, and it has been a privilege to work with you.

I would like to express my genuine admiration and gratitude to my supervisor Jean-François Pierson. For your full implication in my work, your patience and trust over the past few years. You are an amazing supervisor, a great researcher from who I have learned a lot. I appreciate the confidence and the liberty that you gave me during this thesis. One of the things that impressed me the most is how you care about your students. I always remember a talk that we had in Garmisch when you asked me if I was happy in France; if I thought that I made the right choice leaving Brasil, because I completely changed my scientific research topic. Your sincere concern during the pandemic was crucial for continuing the work in the confinement. For all your support, thanks Jeff!

Furthermore, I honestly thank my former supervisors for introducing me to research and helping me enjoy it so much. If I ever have the opportunity to be a supervisor, I will have all of you like my guides.

Stéphanie Bruyère thank you so much for our priceless TEM sessions, for being always available to help, and also for the "pas mal" of phrases that you taught me during our sessions.

I wish to thank the members of the *CC-Microscopique*: Jaafar Ghanbaja for your permanent desire to help, Christine Gendarme for the training in SEM, Sylvie Migot and Hiba Kabbara for their TEM lamella preparation, Denis Mangin for the SIMS analysis, and Sandrine Mathieu for

the training in the SEM and EBSD images. I need to address how much I enjoy the time with Sylvie Migot and Sandrine Mathieu, their smiles, and their honest wish to help always made me want to come back to the -1 floor.

I also want to thank Pascal Boulet for the XRD formation, Arnaud Voignier for the hardness measurements, and Sébastien Hupont for the Raman and Reflectance measurements and our entertaining discussions about music.

I would like to thank all the other members of team 202: Silvère Barrat for letting me have a first experience teaching in French, Brigitte Vigolo for your encouragement and support, Alexandre Nominé for always good pieces of advice, and the funny music links. A special thanks to David Horwat for your interest in my research, ideas, and suggestions, and for allowing me to be part of a research project where I learned and enjoyed it a lot.

I also want to acknowledge members of different teams who made valuable contributions to this work: Michel Vilasi for your ideas, proposals, discussions, and interest in the nitrides oxidation; Lionel Aranda for the TGA measurements, discussions and the readiness to help; Ludovic Pasquier for the assistance with the sample transfers in the Tube and the RHEED measurements. Finally, to Stéphane Andrieu whose support was fundamental for the growth of the VN epitaxial layers, for the RHEED measurements, and staying with me after work hours (together with Ludovic), even when I was not your student.

Thanks to Thierry Czerwiec, Grégory Marcos and Thomas Gries for giving me the opportunity to continue working in the IJL and for the patience during these last months.

I am grateful to the French PIA project “Lorraine Université d’Excellence”, reference ANR-15-IDEX-04-LUE for financing this PhD scholarship. The *Davm competence center* of IJL is deeply acknowledged for giving me access to the UHV magnetron sputtering deposition facility.

For the support with the administrative process, I thank Valérie Franck, Valérie Madeline, Martine Tailleur, Amandine Reiter, Georges Billant, and the always smiling Christine Sartori.

To all the colleagues in and out of the lab who made these years so special: Joseph, Benjamin, Christophe, Daria, Christy, Jiaqi, Lucia, Adrian, Aurélien Etiemble, Aurélien Didelot, Soufiane, Thiago and Catalina. To Zil and Sofia for the “Spanish” lessons and all the

laughs. To Fahad and Osama, my immense gratitude for our discussion about football, religion, and the amazing moments in the office. A very special thanks to Nicole, for your patience and help with the French bureaucracy and translations, but most of all for your magnificent *raclette*, *tartiflette*, and *fondue*. To Agathe for your help with the French, and for the amazing Christmas with your lovely family. To Magali for all the parties together and the amazing vegan food, thanks a lot. For the *chicken tikka masala* and always making me laugh, a distinct thanks to Shantanu the "King of Mumbai". To Vitalis "son of Odysseus" thanks for your friendship and for trying to make me talk softer. To Feriel, Bassem, Zeineb, and Kenza for all the parties and marvelous moments together.

I believe that I'm a fortunate person. I have made a lot of friends, with the time some of them became my family. They are spread all over the world: Cuba, USA, Spain, Brazil, and Austria, their support, video calls, and messages make my life out of Cuba easier and happier. Besides, in these three years in France, two old friends became also family, thanks Borro and Claudia for all our wonderful moments together (there are so much more to come!).

I'm truly convinced that I'm a happy person because I grew up with a lot of love. The credit goes to my family, especially my mother. Her strong character, sacrifices to raise us, her continued concern for our well-being, for our education and happiness, together with our passionate discussions have been a central influence on the person I am, and the person I aspire to be. Thanks for all your love!

Finally, to Mariana, these years you have been my partner, my force, and one of the reasons that I want to be a better person. You became my wife and we had the privilege to have two incredible weddings. To be considered a member of your family and feel all their love is beyond description. As already said: the best moments of my days are when I go to sleep and wake up with you. Te amo Cuchi!

Résumé étendu

Les matériaux X-chromes présentent des changements réversibles de leurs propriétés optiques sous l'action d'un stimulus externe. Il existe différents types de matériaux X-chromes, les plus courants étant les matériaux électrochromes, photochromes et thermochromes, où les stimuli sont respectivement les variations du champ électrique appliqué, l'irradiation par la lumière et la température appliquée. Le marché de ces matériaux intelligents augmente au fil des ans et couvre les secteurs de l'aéronautique, des fenêtres intelligentes, de l'automobile et bien d'autres. De nombreux matériaux X-chromes ont fait l'objet de recherches au cours des dernières décennies. Parmi les matériaux électrochromes, les plus pertinents sont NiO, les oxydes Ni_xW_{1-x} et WO_3 tandis que TiO_2 et MoO_3 sont les plus étudiés pour les matériaux photochromes. Pour les matériaux thermochromes, la variation de température entraîne une modification de leurs propriétés optiques et électriques. Plusieurs matériaux présentent cette propriété comme les pérovskites de terres rares (cobaltites, nickelates, manganites) et le dioxyde de vanadium.

Parmi les matériaux thermochromes, le dioxyde de vanadium (VO_2(M)) est le composé le plus étudié. Le VO_2(M) subit une transition métal-isolant (MIT) réversible à une température d'environ 68°C. À basse température, cet oxyde présente un comportement semi-conducteur avec une transmission élevée dans la région infrarouge (IR) et une résistivité électrique élevée. Au contraire, à haute température, le VO_2(M) présente une faible transmittance dans la région IR et une faible résistivité électrique. Le changement spectaculaire de ses propriétés physiques ouvre la voie à diverses applications, telles que de nouveaux dispositifs électroniques et optiques, des capteurs solaires thermiques, des fenêtres intelligentes, des radiateurs passifs, entre autres. Néanmoins, l'élaboration de films thermochromes purs de VO_2(M) sur de grandes surfaces reste considérée comme un défi. La raison de cette défiance est la difficulté d'éviter la formation d'autres phases appartenant au système vanadium-oxygène.

Dans cette thèse, nous avons obtenu pour la première fois du VO_2(M) thermochrome à partir de l'oxydation contrôlée de films polycristallins VN et V_2N déposés par pulvérisation

cathodique. Nous avons discuté de l'importance d'optimiser la durée du recuit à chacune des températures d'oxydation étudiées pour obtenir un VO_2(M) thermochrome de haute qualité.

Au cours du processus d'oxydation à 450 °C sur substrat Si, il n'y a que deux phases appartenant au système V-O : VO_2(M) et V_2O_5 qui ont été détectées. En fonction du temps, le premier oxyde formé est VO_2(M). Plusieurs techniques (XRD, Raman, thermométrie IR et méthode des quatre pointes) nous permettent de confirmer que VO_2(M) est présent dans de nombreux échantillons oxydés entre 10 et 40 min. Par ailleurs, V_2O_5 n'est détecté qu'après l'oxydation totale du VN. La quantité de V_2O_5 présente sur les échantillons augmente avec le temps d'oxydation (après 30 min) et affecte les performances thermochromes des films oxydés. Après 50 min d'oxydation, la seule phase identifiée est V_2O_5 et aucune propriété thermochrome n'est mise en évidence. En rassemblant les résultats de XRD et Raman, ainsi que l'étude des propriétés optiques et électriques, un diagramme de phase de l'oxydation du VN a pu être tracé montrant la formation des différentes phases en fonction du temps d'oxydation à 450°C.

En ce qui concerne les films polycristallins de VN déposés sur un substrat en aluminium oxydés à différentes températures (450, 525 et 550°C), les résultats indiquent que pour tous les systèmes étudiés l'oxydation du VN se déroule selon les mêmes étapes que celles décrites précédemment. Le premier oxyde formé est VO_2(M), il coexiste avec VN pendant une longue période à 450°C ou disparaît soudainement à 525 et 550°C. De plus, V_2O_5 est détecté après l'oxydation totale du VN. Ces résultats confirment l'oxydation de l'état V^{4+} vers l'état V^{5+} avec l'augmentation du temps de recuit et correspondent aux résultats des études précédentes.

Concernant les propriétés optiques des films oxydés, le meilleur changement d'émissivité ($\Delta\varepsilon$) dans chaque système est assez similaire (entre 0.20 et 0.22), quelle que soit la température d'oxydation. En revanche, la morphologie des films est fortement dépendante de la température d'oxydation. Ainsi, le changement de la morphologie de surface des films n'influence pas leurs propriétés optiques. Cela indique que les propriétés optiques du VO_2(M) dans la gamme 7,5-13 µm sont indépendantes de la morphologie de la surface.

Les résultats de l'oxydation du VN polycristallin déposé sur les deux substrats montrent que les meilleures performances thermochromes ont été obtenues après l'oxydation presque complète ou complète du précurseur. Il a été démontré qu'une couche de précurseur restante affecte la performance thermochrome des films. Les analyses MET ont montré que l'interface entre les films polycristallins de VN et le VO_2(M) formé est abrupte.

Nous avons également déposé du VN épitaxié sur un substrat monocristallin de MgO dans un réacteur de pulvérisation à l'échelle du laboratoire. Les films épitaxiés ont été soumis à un traitement thermique après leur dépôt pour obtenir des films de VN stœchiométriques. Les résultats des analyses de microscopie XRD, RHEED, EBSD et HRTEM prouvent que les films VN croissent avec des relations épitaxiales film/substrat : VN (100) || MgO (100) et VN [010] || MgO [010]. Les films épitaxiés de VN ont été oxydés dans les mêmes conditions que pour les échantillons polycristallins, mais leur chemin d'oxydation complètement différent. Même une fine couche de VN (environ 55 nm) est très difficile à oxyder, ce qui pourrait être dû à l'absence de joints de grains dans les couches épitaxiées. Les résultats XRD et Raman montrent un mélange de phases, avec VO_2(B) comme composé prédominant. Remarquablement, l'oxydation conduit à une croissance épitaxique entre VO_2(B) et VN avec les relations suivantes : VO_2(B) (001) || VN (200) hors du plan et VO_2(B) (200) || VN (020) dans le plan, comme le montrent les résultats MET. De plus, les images MEB et les résultats AFM montrent une morphologie de surface complètement différente pour la phase VO_2(B), avec des nanorods perpendiculaires au substrat. Comme prévu, la phase VO_2(B) ne présente pas de comportement thermochrome, corroboré par les résultats de la caméra IR.

De plus, nous avons appliqué un critère pour comparer les conditions de dépôt entre les deux machines de pulvérisation utilisées dans cette thèse. Trois séries de films VN ont été déposées, la série II avec les conditions équivalentes de la chambre semi-industrielle, la série I avec une pression de travail inférieure et la série III avec une pression de travail supérieure. Tous les films ont été oxydés à 550°C pendant un maximum de 3,5 minutes. Les résultats XRD, Raman et MEB montrent que :

Les échantillons de VN oxydés de la série I (0,22 Pa) présentent une couche résiduelle de VN significative, avec la phase VO_2(M) comme oxyde prédominant.

Les films VN recuits à l'air de la série III (0.83 Pa) sont complètement oxydés, avec V_2O_5 comme seule phase présente.

Les échantillons de VN oxydés de la série II ne sont pas complètement oxydés. Cependant, il y a moins de VN que dans les films recuits à l'air de la série I. La phase principale de ces films est la phase VO_2(M).

Aucun des échantillons oxydés VN déposés à 0,22 et 0,83 Pa ne présente de propriétés thermochromes. Pour les films de la série I, c'est une conséquence de la couche résiduelle de VN trouvée dans les échantillons. Pour la série III, elle est due à la conversion complète du VN en V_2O_5. Seuls les films oxydés déposés dans des conditions analogues (série II) présentent des performances thermochromes, même avec une fine couche résiduelle de VN. Notre critère montre qu'il est possible de transposer le dépôt d'une chambre de pulvérisation à une autre (même à l'échelle industrielle).

Le dernier chapitre offre une vue d'ensemble de l'oxydation contrôlée par air des films V_2N déposés sur des substrats de Si. Dans la première section, nous comparons la structure, les propriétés mécaniques, électriques et optiques des composés VN et V_2N. Les résultats montrent que les spectres EELS peuvent être utilisés comme une « empreinte digitale » pour distinguer les deux phases. La valeur de dureté du V_2N est plus de deux fois supérieure à celle du VN. Les deux phases ont des propriétés métalliques, la résistivité étant augmentée avec la température. Néanmoins, VN ($TCR_{VN} = 3.7\ 10^{-4}\ K^{-1}$) a un coefficient de température de résistance plus élevé que V_2N ($TCR_{V_2N} = 2.0\ 10^{-4}\ K^{-1}$).

Nous étudions l'oxydation des films V_2N à deux températures (450 et 550°C). Pour la première fois, notre travail montre que le V_2N peut également être considéré comme un précurseur pour la synthèse de VO_2 thermochrome. Au cours de l'étape d'oxydation, VO_2(M) est le premier oxyde formé, il coexiste avec V_2N pendant une longue durée à 450°C ou disparaît rapidement à 550°C. Une augmentation supplémentaire de la durée d'oxydation conduit à la formation de phases V_6O_{13} ou V_2O_5 qui ne présentent pas de propriétés thermochromes. La

caractérisation EELS de films V_2N oxydés minces et épais met en évidence la formation d'une couche intermédiaire VN très mince (environ 25 nm) à l'interface V_2N-VO_2(M). Ces résultats montrent que l'oxydation de V_2N en VO_2(M) se produit en deux étapes. L'oxydation du V_2N conduit à la libération d'azote qui diffuse dans deux directions opposées : vers la surface et vers le substrat et contribue à former la couche intermédiaire de VN. Pour une durée d'oxydation élevée, VO_2(M) s'oxyde en V_2O_5, ce qui affecte considérablement la réponse thermochrome des films. Les valeurs de $\Delta\varepsilon$ des films V_2N oxydés sont similaires à celles obtenues après oxydation de VN.

Enfin, nous fournissons un premier aperçu de l'influence de l'épaisseur de V_2N sur les propriétés de modulation optique du VO_2(M) formé. Nous avons réussi à changer le signe du $\Delta\varepsilon$ pour les films oxydés en modifiant l'épaisseur initiale de V_2N. Pour les échantillons de VO_2(M) obtenus par l'oxydation d'un film de V_2N de 100 nm, le $\Delta\varepsilon$ est négatif, avec l'effet direct du substrat de Si. En revanche, pour les films VO_2(M) obtenus après le recuit à l'air d'une couche de V_2N de 445 nm, le $\Delta\varepsilon$ est positif. Cela signifie que la combinaison d'une couche épaisse de V_2N avec le substrat de Si se comporte comme un substrat hautement réflecteur IR tel que l'aluminium.

Nous estimons que les résultats de cette thèse peuvent ouvrir la voie à de futures investigations sur l'oxydation de VN et V_2N comme nouveaux précurseurs pour former du VO_2(M) thermochrome de haute qualité.

Contents

Introduction

Chromogenic materials display changes in their optical properties thanks to an external stimulus. There are different types of chromogenic materials, the most common are electrochromic, photochromic, and thermochromic, where the stimuli are the variations in the applied electrical field, irradiation by light, and in the applied temperature, respectively. The market for these smart materials is increasing over the years and covers aircraft, smart windows, automotive, and many others [1]. Numerous chromogenic materials have been the subject of research in the last decades. Among the electrochromic ones, the most relevant are NiO [2], Ni_xW_{1-x} oxides [3] and WO_3 [4], while TiO_2 and MoO_3 are the most studied for photochromic ones [5]. For the thermochromic materials, the temperature variation leads to a modification of their optical and electrical properties. Several materials present this property, such as rare earth perovskites such as cobaltites [6,7], nickelates [8], manganites [9,10] and vanadium dioxide [11].

Among the thermochromic materials, vanadium dioxide (VO_2) is the most studied compound. The VO_2 undergoes a reversible metal-insulator transition (MIT) approximately at T_{MIT} = 68°C. At low temperature, this oxide presents a semiconductor behavior with high transmittance in the infrared (IR) region and high electrical resistivity. On the contrary, at high temperature, VO_2 exhibits a low transmittance in the IR region and low electrical resistivity. The dramatic change in its physical properties offers a path to diverse applications, such as novel electronic and optical devices, thermal solar collectors, smart windows, passive radiator, among others. Nevertheless, the elaboration of pure thermochromic VO_2 films on large surfaces remains considered a challenge. The reason behind this defiance is the difficult task of avoiding other phases belonging to the vanadium-oxygen system.

This thesis aims to achieve thermochromic VO_2 films from a new process based on the controlled oxidation of sputter-deposited VN and V_2N films. The manuscript is composed of six chapters, one appendix, and a general conclusions section:

In chapter 1, we depict the principal crystallographic structures of VO_2 as a function of the temperature. A short comment on the different VO_2 polymorphs is presented. Furthermore, the physical properties, the band structures, and the transition phase mechanism are also described. Finally, possible application and synthesis methods of VO_2, with an emphasis on magnetron sputtering are discussed.

In Chapter 2, technical and fundamental aspects of the magnetron sputtering and characterization techniques used throughout this thesis are presented. Moreover, we develop a simple approach to obtain analogous samples independently of the sputtering machines used in the present work.

Chapter 3 provides the first results on the controlled oxidation of VN films deposited on Si in a semi-industrial sputtering reactor. Depending on the oxidation duration, several phases can be identified by XRD and Raman spectrometry. Four-point probe and emissivity measurements evidence an optimized oxidation duration to form thermochromic VO_2. From these results, a VN oxidation phase diagram is plotted.

In chapter 4, thermochromic VO_2 films are synthesized by air oxidation of VN samples on Al performed at three temperatures (450, 525, and 550°C) at various durations (lower than 50 min). Once again, the air-annealed duration (at each temperature) determines the formed phases in the oxidized films. We study the relationship between the maximum emissivity switch with the oxidation temperature and the surface morphology of the samples.

In chapter 5, a standard sputtering reactor is employed to deposit single crystallized VN thin films on MgO substrates. The air-annealing process of the epitaxial VN films is investigated. Furthermore, we explore the possibility to transpose the deposition conditions between the two sputtering machines employed in the thesis.

In chapter 6, continue working with the standard sputtering reactor, V_2N thin films are growth on Si substrates. The films are oxidized at two temperatures, once again, the annealing duration controls the detected phases. TEM analysis allows us to differentiate the oxidation mechanisms of VN and V_2N. Finally, we explore the effect of the initial precursor thickness on the optical modulation properties of the oxidized films.

General conclusions and perspectives to the main findings of the thesis are given.

Finally, an appendix is dedicated to preliminary results on the thermogravimetric analysis of the VN and V_2N oxidation. The preliminary results indicate a possible crucial role of water vapor on the oxidation of the films.

Chapter 1

General introduction

Abstract

In this chapter, we describe the principal characteristics of vanadium dioxide (VO_2), with particular attention to the crystallographic structure, band structure and physical properties. A brief discussion of the metal-insulator transition (MIT) and possible application is presented. The issue of obtaining a thermochromic VO_2 thin film on large surfaces is discussed. Some deposition methods are described, with a more detailed discussion on the magnetron sputtering one. The influence of the deposition parameters and oxidation conditions on the VO_2 properties are also highlighted.

Contents

1.1 Vanadium and its compounds

Vanadium is a transition metal with the symbol V and atomic number 23. Its molecular weight is 50.9 g/mol and its electronic configuration is [Ar] $3d^3$ $4s^2$. At room temperature vanadium is solid and crystallizes in the body-centered cubic (bcc) structure. It presents several oxidation states, between 0 and 5. It reacts easily with non-metallic atoms to form borides, carbides, nitrides, oxides… Details on the V-N and V-O binary systems are presented in the two following paragraphs.

1.1.1 The vanadium-nitrogen binary system

The V-N binary system contains two principal compounds: a face-centered cubic δ VN_x and a hexagonal close packed β V_2N_x have been well documented [12] (Figure 1.1).

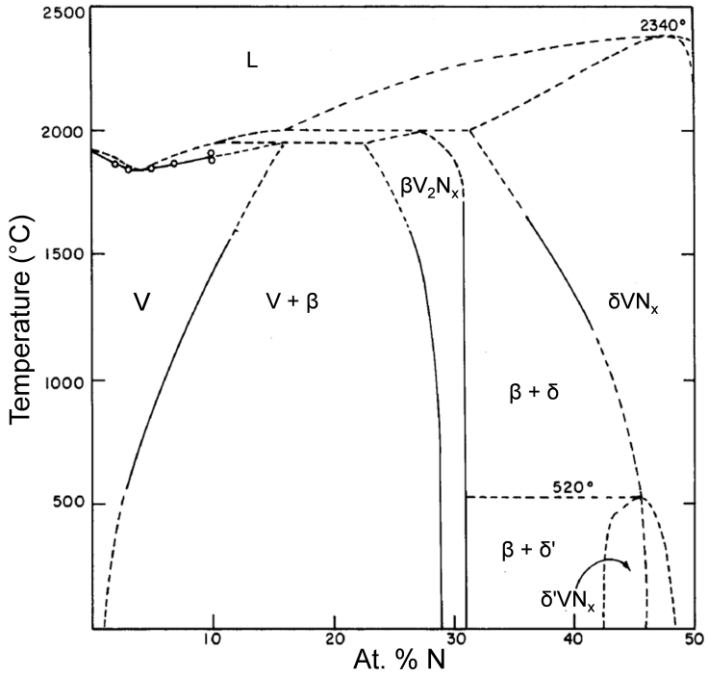

Figure 1.1 Phase diagram of the V-N system. Modified from [12].

The δ VN_x phase exhibits the NaCl-type B1 structure (space group $Fm\bar{3}m$) and occurs over a wide range of compositions (from $VN_{0.72}$ and $VN_{1.00}$) [12]. The stoichiometric VN phase has a lattice constant a_{VN} = 4.139 Å [13]. The composition variation of the δ VN_x is caused almost entirely for vacancies on the N sites [12]. VN thin films have been studied for several applications, for instance, for their self-lubricious abilities reaching low friction coefficients

when converted into vanadium oxides during high-temperature tribology tests [14,15], and as electrode materials for electrochemical supercapacitors [16,17].

The β V_2N_x metallic phase displays a hexagonal structure with space group $P\bar{3}1m$ and a narrow range of homogeneity (see Figure 1.1) [12]. According to Christiansen and Lebech, the lattice constants are a_{V2N} = 4.917 Å and c_{V2N} = 4.568 Å [18]. Throughout the present work, we use the notation VN and V_2N to denote the δ VN_x and the β V_2N_x phases. To our knowledge, there is not abundant literature on possible applications of V_2N and on the synthesis of such nitride in thin film form. Nitride materials being sensitive of oxidation, VN and V_2N will be considered in the present work as precursor to obtain thermochromic VO_2 using a controlled oxidation process.

1.1.2 The vanadium-oxygen binary system

Contrary to the V-N system, the V-O one contains a high amount of phases (Figure 1.2). Among these oxides, VO_2 and V_2O_5 are the most used compounds for optical or energy applications. The properties of these vanadium oxides are strongly dependent on their stoichiometry. V_7O_{13} exhibits metallic properties while V_2O_5 is insulating. Between these two compounds, the vanadium oxides exhibit properties that are dependent on the temperature. At low temperature, they are semiconducting or even insulating while at high temperatures they exhibit metallic-like properties. The change of the properties occurs at a temperature called T_{MIT} that refers to the metal to insulating transition. The value of T_{MIT} is strongly dependent on stoichiometry; it varies from -203 to 157°C (Table 1.1) [19,20].

Table 1.1 Transition temperatures of different oxydes of the V-O system.

Oxyde	V_8O_{15}	VO	V_5O_9	V_6O_{13}	V_2O_3	V_6O_{11}	V_4O_7	VO_2	V_3O_5
T_{MIT} (°C)	-203	-147	-138	-123	-108	-96	-23	68	157

Figure 1.2 highlights the need to control with great accuracy the stoichiometry of the vanadium oxides to obtain a single compound. For instance, for VO_2, the amount of oxygen must be approx. between 1.98 and 2.02 [21]. However, even for a single compound, a small change in the stoichiometry could affect the physical properties and transition temperature. In

1974, Griffiths *et al*. sputter-deposited VO_2 films on quartz and polished sapphire. The samples displayed a drop in the transition temperature and the resistivity ratio (between low and high temperatures) with the decrease of the oxygen amount in the films [22]. One year later, Brückner *et al*. showed two orders of magnitude of resistivity ratio changes in VO_2 monocrystalline samples with a stoichiometry difference of 0.3% [23]. More recently, in 2013, Liu *et al.* studied the dynamic behaviors of photoinduced insulator-metal phase transition in VO_2 thin films with different oxygen stoichiometry using optical pump-terahertz probe spectroscopy. They observed a correlation between photoinduced phase transition and oxygen stoichiometry. The excessive oxygen content in vanadium dioxide reduces the magnitude of phase transition [24]. Therefore, for industrial applications on large surfaces, it is even harder to control the stoichiometry.

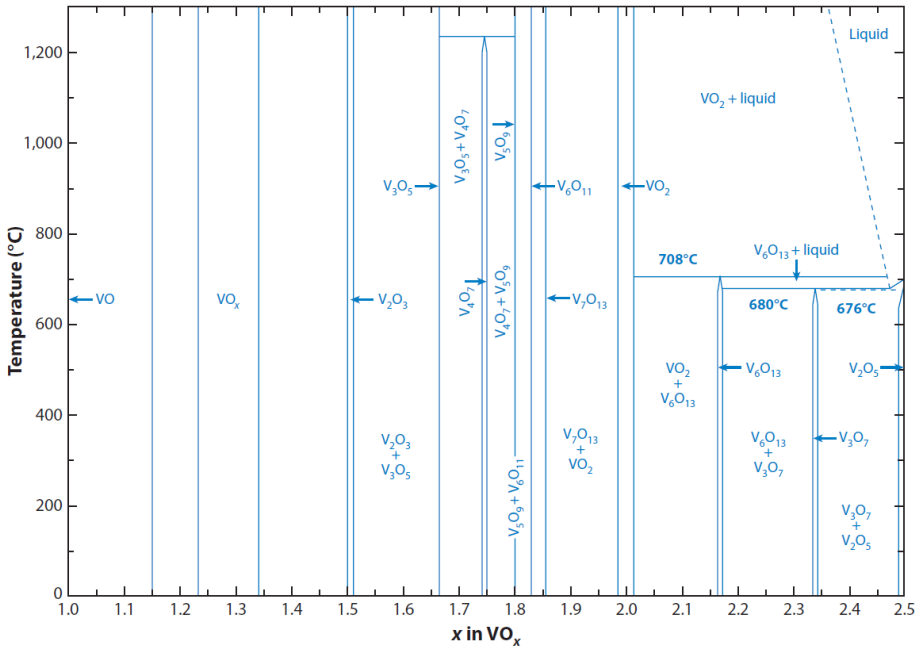

Figure 1.2 Phase diagram of the V-O system [19].

1.2 Crystallographic structures of VO_2

Among the oxides of the V-O system, VO_2 is a compound with several polymorphs, including VO_2(R) [25], VO_2(M) [26], VO_2(B) [27], VO_2(A) [28], VO_2(C) [29], VO_2(D) [30], and VO_2(P) [31]. These phases transform into each other under certain specific conditions [30–36]. Only the couple monoclinic VO_2(M) and rutile-type VO_2 (R) undergoes a fully reversible

metal-insulator transition as a function of the temperature. For this reason, they are the main phases in the scope of this thesis and also in the literature.

The VO_2 at high temperature ($T > T_{MIT}$), noted VO_2(R), presents a rutile structure (Figure 1.3) composed of a tetragonal lattice with space group $P4_2/mnm$ [37,38]. The lattice constant are $a_R = b_R = 4.5546$ Å and $c_R = 2.8514$ Å [37]. The basic structural unit is a VO_6 octahedron (vanadium atoms of oxidation state +4 are surrounded by six oxygen atoms of oxidation state -2). The VO_6 octahedra share edges along the *c*-axis direction and corners in the *a*–*b* planes (Figure 1.3). VO_2(R) is opaque to infrared radiation and exhibits a low electrical resistivity [39,40] typical of metal-like materials.

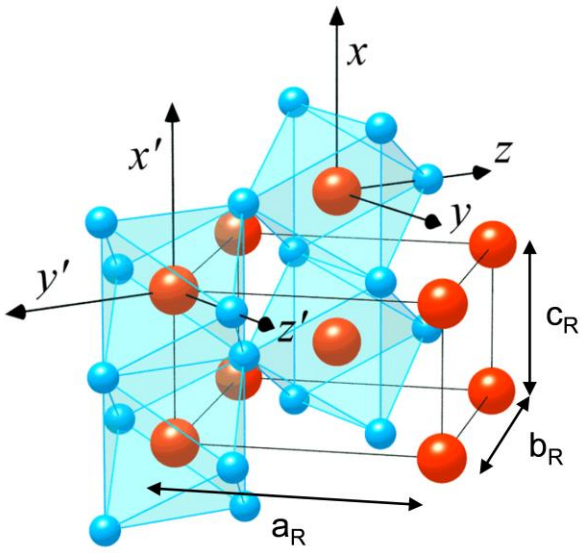

Figure 1.3 The VO_2 rutile structure. Large red and blue small spheres denote V and O atoms, respectively. The VO_6 octahedron is also shown. Modified figure from [41].

The VO_2 at temperatures lower than T_{MIT} exhibits a monoclinic structure (VO_2(M)) characterized by a monoclinic lattice with space group $P2_1/c$ [42,43] (Figure 1.4). This phase is described as a distortion resulting from the stretching along the c_R axis of two superimposed lattices of the VO_2(R), followed by a torsion. Anderson reported lattice constants $a_M = 5.743$ Å, $b_M = 4.517$ Å, $c_M = 5.375$ Å, and an angle $\beta_M = 122.6°$ [43]. There is a close connection between the rutile and monoclinic structures (compare Figure 1.3 and Figure 1.4). The relation existing between the rutile-type cell and the monoclinic unit cell of VO_2 can be approx. written as: $\vec{a}_M = 2\vec{c}_R$, $\vec{b}_M = \vec{a}_R$ and $\vec{c}_M = \vec{a}_R - \vec{c}_R$ [43]. Figure 1.4 displays the characteristic metal-metal zigzag pairing along a_M axis, with two alternate V-V distances of 2.619 and 3.164 Å.

Furthermore, there are two different vanadium-oxygen interatomic distances noted V-O_1 and V-O_2, with respective lengths of 1.77 and 2.01 Å [41]. VO_2(M) behaves as a semiconductor with high IR transmittance and high electrical resistivity [44,45].

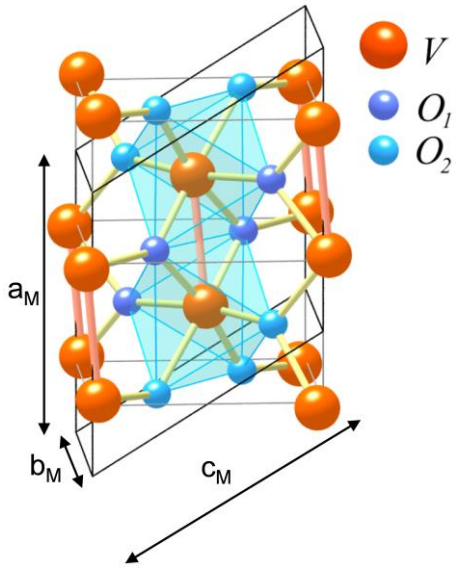

Figure 1.4 The VO_2 monoclinic structure. Modified figure from [41].

Moreover, at low temperature, a metastable modification of the M phase, noted $VO_2(M_2)$, crystallizes in a centered monoclinic lattice with space group *C2/m* [47]. This phase is usually obtained when stress is applied during film growth [48,49] or when VO_2 is doped with certain elements such as titanium [50], aluminum [51,52] or chromium [53]. However, the $VO_2(M_2)$ is not part of the scope of this thesis.

VO_2(A) and VO_2(B) are the other two most commonly studied VO_2 polymorphs. The metastable VO_2(A) undergoes an irreversible first-order phase transition at 162°C, in which the resistance can change one order of magnitude [54]. At low temperature LTP-VO_2(A) adopts the tetragonal system *P4/ncc* with $a_A = b_A = 8.440$ Å and $c_A = 7.666$ Å, while at high temperature HTP-VO_2(A) depicts the body-centered tetragonal system *I4/m* with $a_A = b_A = 8.476$ Å and $c_A = 3.824$ Å [28]. On the other hand, distinct from monoclinic VO_2(M) and VO_2(A), VO_2(B) has no MIT characteristic or drastic variations in electric and optical properties. The metastable VO_2(B) displays a monoclinic structure similar to the layered V_6O_{13} structure [55]. The parameters of the VO_2(B) cell are $a_B = 12.03$ Å, $b_B = 3.693$ Å, $c_B = 6.42$ Å, and $\beta_B = 106.6°$, and the space group is *C2/m* [55,56]. Thanks to its layered structure and outstanding

electrochemical performance, VO_2(B) is considered a promising cathode material for lithium-ion batteries [57,58].

1.3 Band structure of VO_2

To understand the VO_2 band structure, we must describe the atomic *d* levels. From molecular orbital theory, we know that the V^{4+} ion in the VO_2 is a d^1 system, which means that there is one electron in the *d* band.

In the spherical crystal field the *d* band is composed of fivefold degenerate levels. Once we consider the V^{4+} ion inside the VO_2 structure, the *d* levels are split by the crystal field (Figure 1.5 a)). The octahedral field (of the six oxygens) provides a splitting into a triply degenerate lower state of t_{2g} symmetry and a doubly degenerate upper state of e_g symmetry (Figure 1.5 a)). On the figure, each level is labeled according to the symmetry of the corresponding atomic *d* orbital, following the rectangular coordinate system in Figure 1.5 b). These levels give rise in the crystal to the partially occupied lowest *d* bands. According to a band model proposed by Goodenough [59], the $d_{x^2-y^2}$ orbital gives rise to a band which he labels $d_{\parallel}$ whereas the other two t_{2g} orbitals (d_{xz} and d_{yz}) mix with the anion *2p* orbital forming a wider π^* band [60].

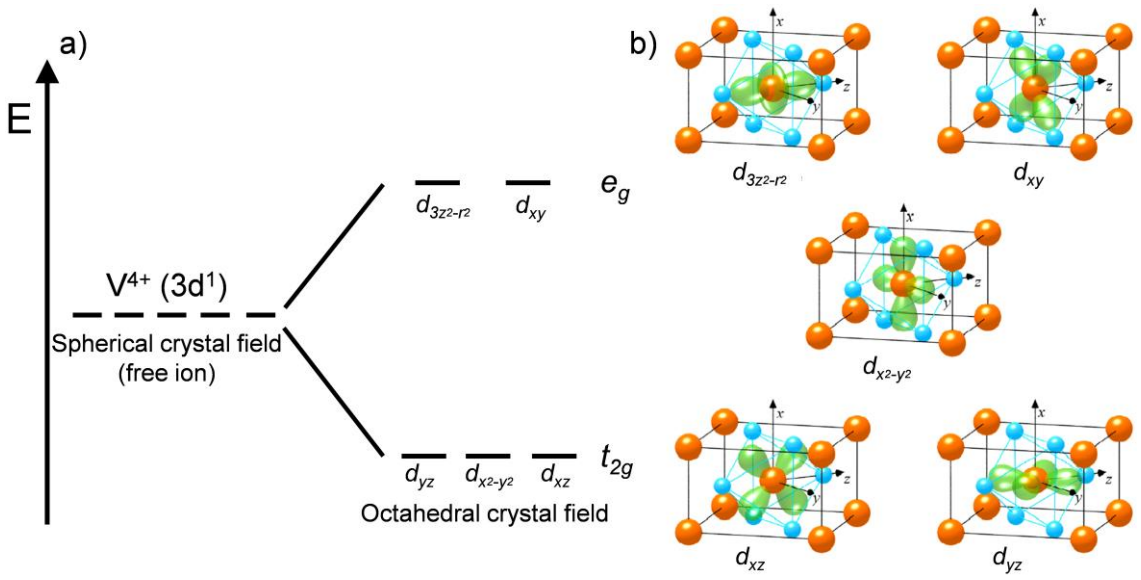

Figure 1.5 a) Crystal-field splitting of the $V^{4+}(3d^1)$ energy levels. b) Angular part of the d orbitals (modified from [41]).

In VO_2(R), the band structure consists of oxygen *2p* bands well below the Fermi level, as well as vanadium *3d* t_{2g} and e_g bands. The band near the Fermi energy (E_F) contains the $d_{\parallel}$

states parallel to the characteristic V chains and the π* bands (Figure 1.6). The vanadium atoms form straight lines with a uniform V-V distance of 2.88 Å. In this case, the V-V distance is shorter than the critical interaction distance (2.94 Å) [61]. Hence, the overlapping of orbitals is possible (electrons flow freely between the atoms) giving conductive characteristics to this phase. During the MIT, the distortion of the rutile structure to form the monoclinic one comes with the formation of metal-metal zigzag pairing along a_M (c_R) axis, with two alternate V-V distances of 2.619 and 3.164 Å. The displacement of the cations lifts the π^* bands above the E_F, and the V-V pairing splits the $d_{\parallel}$ band in two (Figure 1.6), as a consequence, appears a bandgap of about 0.7 eV. In this case, one of the V-V distance is higher than the critical interaction distance, resulting in the localization of *d*-orbital electrons (electrons are trapped and cannot move inside the crystal), which leads to the insulating behavior of VO_2(M).

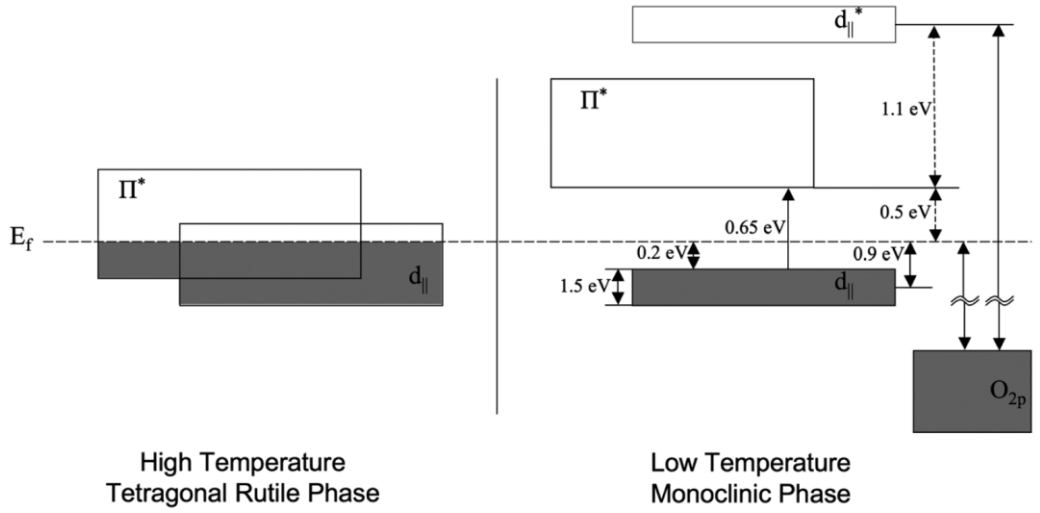

Figure 1.6 Schematic energy diagram of the *3d* bands around the Fermi level for VO_2. The hybridization of the V *3d* and O *2p* levels reflects the symmetries of the atomic arrangement in the crystal lattice [62].

1.4 The VO_2 phase transition

The origin of the VO_2 phase transition is an object of debate in the scientific community. The two models applied to explain this transition are: the Mott-Hubbard transition and the Peierls transition.

1.4.1 The Mott-Hubbard transition

This model proposes that at temperatures lower than T_{MIT} the electron-electron interactions are strong enough to localize the electrons in the atoms [60,63]. Hence, there are not movements of electrons from one site to another. These electronic correlations, related to the carrier density (a function of temperature), create a gap, and VO_2 is in an insulator state. The temperature increase gives the required energy to overcome the strong Coulomb interaction, becoming a free conducting electron. Continue increasing the temperature leads to a critical charge-density value where the energy gap reduces to zero, and therefore an insulator-to-metal transition occurs.

Several theoretical and experimental investigations indicate the Mott-Hubbard transition as the mechanism for the VO_2 MIT. For instance, Zayed *et al*. performed first-principle DFT calculations to investigate the electronic structure and optical properties of the VO_2 (M) phase. The need to include the Hubbard potential to reproduce the VO_2 properties indicates that the transition is of the Mott-Hubbard type [64]. On the other hand, Morrison *et al*. reported on combined ultrafast electron diffraction and infrared transmissivity experiments in PLD-grown VO_2 samples. The results demonstrate a photoinduced transformation to a long-lived state with metal-like mid-IR optical properties and agree with the Mott-Hubbard transition [65]. This model also describes the transition from $VO_2(M_2)$ to the rutile phase [66].

1.4.2 The Peierls transition

In 1955, Peierls published a solid-state physics textbook in which he pointed out that a one-dimensional metal coupled to the underlying lattice is not stable at low temperatures [67]. The ground state of the coupled electron-phonon system is characterized by a gap, thus behaving as an insulator. Later the metal-to-insulator transition was verified in one-dimensional conductors or layered structures [68,69]. This transition is now called Peierls transition. In these systems, one-dimension chains are responsible for the electrical conductivity. At high temperature, the atoms are equidistant, and it is possible to transfer the thermal energy of electrons from one atom to another (metallic state). As the temperature drops below a critical value, the structure is distorted. The distance between the atoms changes, the electron localization occurs due to

the decrease in energy, leading to an insulating state. The Peierls transition is a thermodynamic transition in which the gap disappears by a distortion applied to the lattice that facilitates orbitals overlapping.

In this case, numerous theoretical and experimental investigations agree with the idea that VO_2 follows a Peierls transition. Wentzcovitch *et al*. carried out a theoretical study about the electronic and structural properties of VO_2 across its MIT. They conclude that there is enough energy gain to account for the metal-insulator transition through strengthening the vanadium *d-d* bonds (reorganizing states near the Fermi level) [70]. Furthermore, Okazaki *et al*. made a detailed temperature-dependent photoemission study of VO_2 single crystals in the insulating phase. The results revealed a shift of the top of the O *2p* and the V *3d* bands toward the Fermi energy as the temperature increases. They suggest that the metal-insulator transition of VO_2 is driven by the electron-phonon interaction [71].

1.4.3 Debate about the phase transition

There are numerous theoretical and experimental works devoted to unraveling the details of the mechanism responsible for the MIT of VO_2. Yet, there is not consensual approval whether the driving force causing the MIT is a Mott-Hubbard or a Peierls transition. However, a relatively new possibility advocates that the VO_2 phase transition has the contribution from both models. For instance, Baum *et al.* reported a femtosecond electron diffraction study on the phase transition of VO_2 single crystals. The results displayed different time scales. It begins with a fs motion along the a_M axis (direction of the V–V bond in the VO_2(M), see Figure 1.4). Afterward, a local rearrangement of the VO_6 octahedra changing to a more rutile-like geometry occurs on a ps scale [72]. These two steps caused by electron interactions agree with the Mott-Hubbard model. It ends with a long-range shear motion on the scale of hundreds of picoseconds (distortions supported by Peierls transition). Therefore, in the description of the structural pathway, the two mechanisms were involved [72]. On the other hand, Weber *et al*. studied the VO_2(M) phase using first principle calculations as a function of the disorder. Their results show that a large *3d-3d* Coulomb interaction alone is insufficient to generate the bandgap for VO_2. Hence, the disorder due to imperfections of the crystal, or self-trapping caused by the strong

electron-phonon coupling could be relevant. They propose a new mechanism for the VO_2 phase transition based on an orbital selective Mott transition, assisted by the Peierls distortion: the Peierls instability involves an orbital selection, and bonds the d_{xy} and d_{xz} orbitals along the rutile axis, filling each orbital with one electron, and in turn generates a Mott instability [73]. These research studies may suggest that the MIT problem in VO_2 is closer to resolution.

1.5 Physical properties of VO_2

The metal-insulator transition of VO_2, described in the section before, is accompanied by an abrupt change in the electrical and optical properties of the material as a function of the temperature. In 1959, Morin revealed the first order MIT in single crystals of VO_2 by measuring the dependence of the electrical conductivity with temperature [74]. As already mentioned, at low temperatures the VO_2 behaves as a semiconductor with a monoclinic structure, while at temperatures higher than T_{MIT} it changes to a metallic state with a rutile-type structure. This change may result in a resistivity variation of several orders of magnitude [75–77]. However, the magnitude, sharpness, and transition temperature have a dependence on different parameters like substrate temperature during the deposition [78,79] and average grain size (grain boundaries density) [80].

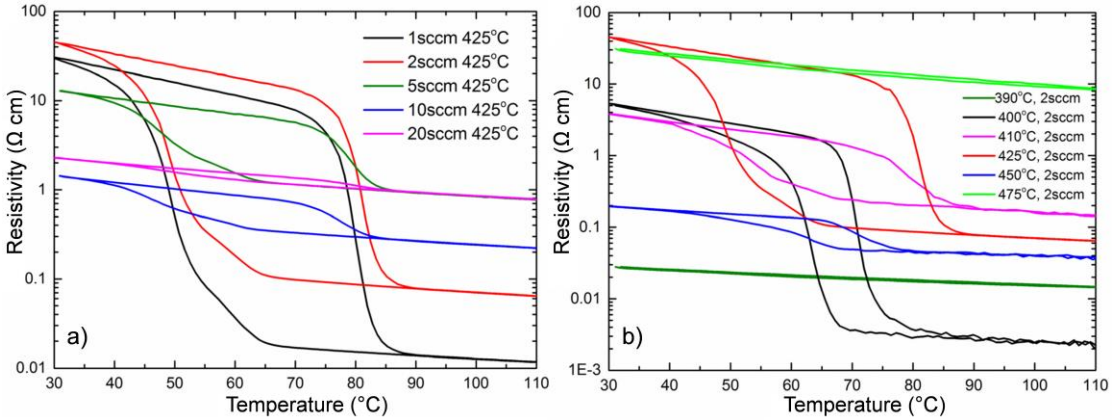

Figure 1.7 Resistivity as a function of temperature for films oxidized at a) 425 °C with different oxygen flow rate and b) at different oxidation temperatures from 390 to 475 °C at fixed oxygen 2 sccm flow rate. Modified figure from [81].

Nevertheless, these are not the only significant parameters. In 2017, Yu *et al*. performed the oxidation of sputter-deposited 100 nm V films varying the oxygen flow rate from 1 sccm to 20

sccm and the air-annealed temperature from 390 to 475 °C [81]. The resistivity changed from almost imperceptible for the oxidized film with 20 sccm of oxygen flow rate at 425°C to more than three orders of magnitude for the oxidized sample with 1 sccm of oxygen flow rate at 425°C (Figure 1.7 a)). Figure 1.7 b) depicts the resistivity change as a function of temperature for samples oxidized at different temperatures with a fixed oxygen flow rate. The results exhibit a non-thermochromic performance for the films annealed at 390 and 475°C. On the contrary, just a 10°C increment is sufficient to obtain an intense hysteresis with a variation of more than three orders of magnitude for the resistivity (Figure 1.7 b)). These findings evidence the importance of controlling the oxidation parameters during the annealing process to form VO_2 with excellent thermochromic behavior.

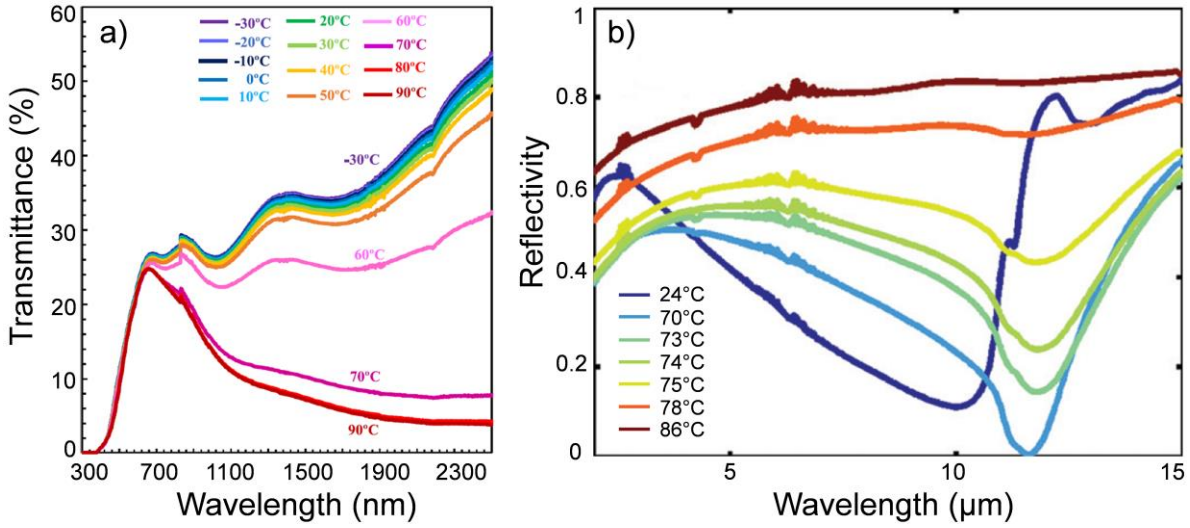

Figure 1.8 a) Transmittance temperature dependence (from -30 to 90°C) in the 300-2500 nm wavelength range of sputtered VO_2 film on ZnO-buffered glass (modified figure from [44]). b) Reflectivity spectrum at temperatures from 24 to 86°C in the 2-15 μm wavelength range of sputtered VO_2 film on c-plane sapphire substrate . At 70°C, the reflectivity drops to ~0.0025 at λ =11.6 μm (modified figure from [82]).

Moreover, transmittance, reflectance, refraction index and emissivity show a dramatic change with temperature. Figure 1.8 a) displays the transmittance as a function of the wavelength in the 300-2500 nm range at different temperatures for a VO_2 film deposited on ZnO-buffered glass. The transmittance of VO_2 is independent of temperature change in the visible region. However, in the IR domain, the transmittance exhibits changes of about 50% at 2500 nm [44]. The reflectivity could also be tuned with temperature in the IR domain. For

instance, Kats *et al.* demonstrate the possibility to obtain an almost perfect absorber at λ =11.6 μm by varying the temperature near the MIT temperature (Figure 1.8 b)). The experiments were carried out in a 180 nm VO_2 film deposited on the *c*-plane sapphire substrate [82]. The optical modulation properties in the IR domain of VO_2 are modified with diverse parameters like substrate bias during deposition [44], film thickness [83], and the IR optical properties of the substrate [84].

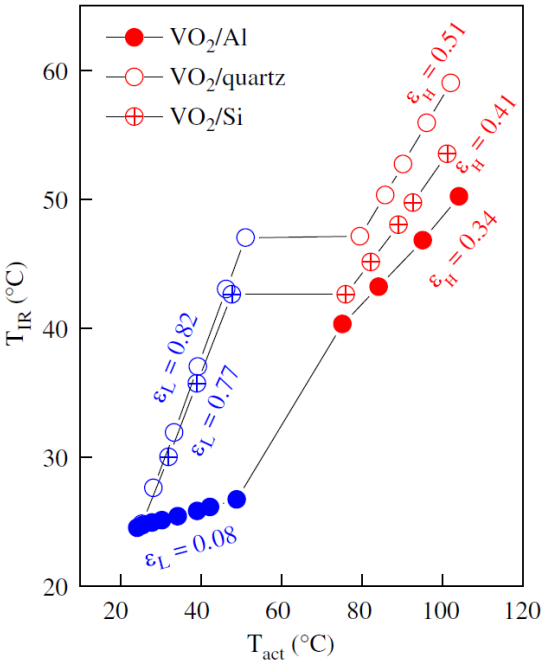

Figure 1.9 Temperature determined from IR camera (T_{IR}), as a function of actual temperature (T_{act}) of VO_2 films deposited on Si, quartz, and Al substrates [84].

The study carried out by Benkahoul *et al.* in thermochromic VO_2 thin films deposited on quartz, Si, and Al was critical to understand the influence of the IR optical properties of the substrate in the response of the VO_2/substrate system. They demonstrate that emissivity dependence on temperature for the VO_2 film deposited on IR reflective substrate (Al) is opposite to that of VO_2 deposited on an IR transparent substrate (quartz and Si), as shown in Figure 1.9. The difference is attributed to the higher IR reflective properties of Al in comparison to quartz and Si [84]. These results suggest that the VO_2/Al system could be employed as a smart radiator device while the VO_2/Si and VO_2/quartz systems are interesting for furtivity applications.

1.6 Possible applications of VO_2

In the previous section, it was illustrated how increasing (decreasing) the temperature above (below) the transition temperature of VO_2 drastically changes its physical properties. Moreover, this transition can be triggered by diverse external stimuli including, photons, electrochemical, magnetic field, temperature, stress and electric field (Figure 1.10) [85]. All the stimuli and their corresponding responses provide broad possibilities for industrial applications, like smart radiator devices [86], thermal rectification [87], smart windows [88], memory devices [89], thermal solar collectors [90], among others.

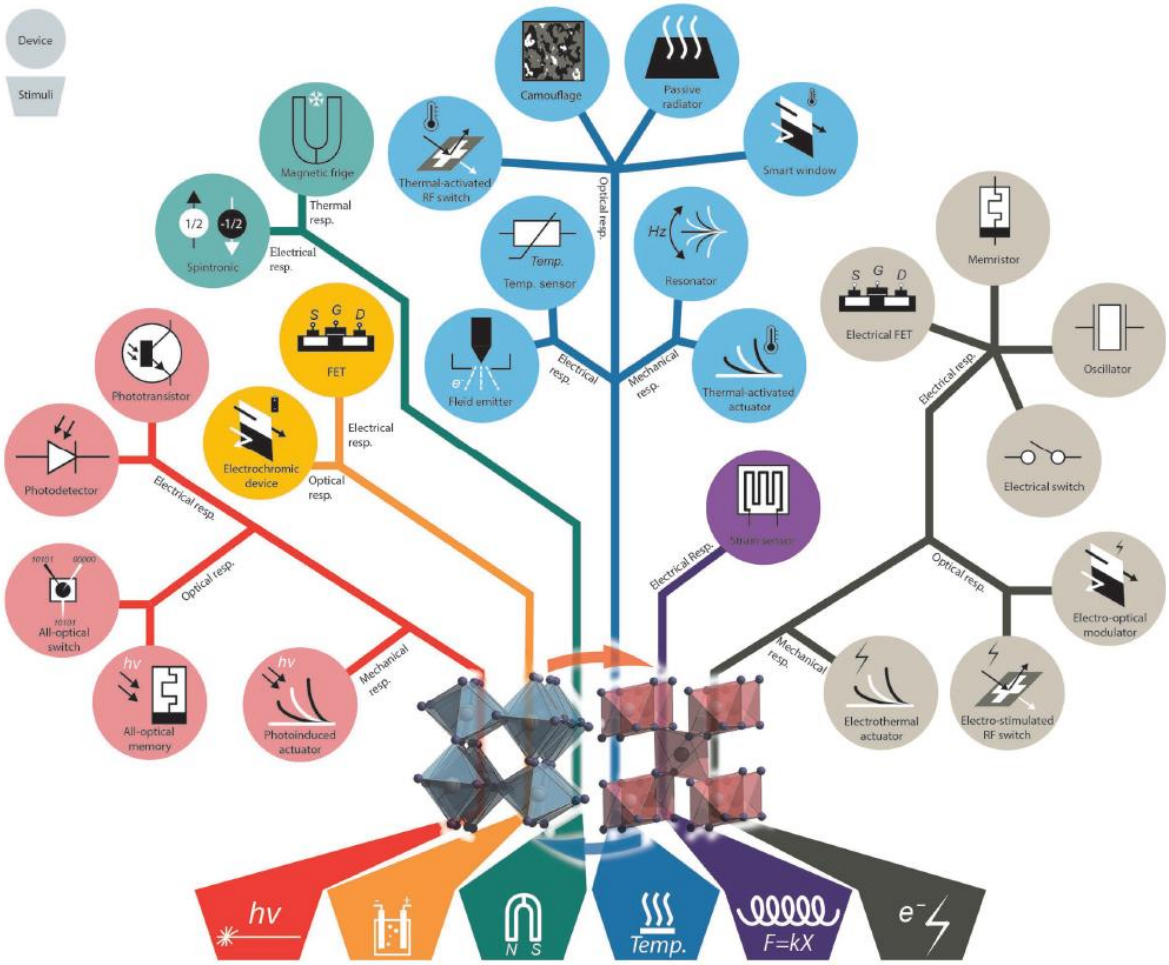

Figure 1.10 Scheme for the VO_2 based devices, its respective input stimuli, and output response. The color represents the category of input stimuli and output response of the device [85].

Since temperature is the stimulus used in this thesis to activate the MIT in the VO_2 films, we will briefly describe one possible application related to this stimulus, the smart radiator devices (SRDs) in spacecraft or satellites.

Spacecraft and satellites in orbit run into large temperature fluctuations depending on their exposure to solar energy (it could be from about -150 to 150°C). Nevertheless, the internal temperature needs to be regulated to an optimal operating range (generally ranging from 0 to 40°C). This is a crucial issue to keep the electronic structures working under stabilized conditions and avoid impacts on the performances and life endurance of the systems. The unique way to heat regulation is radiative heat transfer into deep space [91]. One possibility is to use different types of electromechanical louvers (macro and micro-scale louvers) that are opened and closed to regulate the radiation to dark space [92]. The correct control of these louvers involves complex, heavy and expensive structures for the spacecraft and satellites [93].

Another interesting possibility is the use of the so-called smart radiator devices (SRD), which can control the temperature inside the satellites or spacecraft without complementary systems. The principal advantages of the SRD temperature-control system are its simplicity, low cost and low weight. The operating principle of an SRD is supported by the fact that the heat exchange between the satellite and its environment is primarily controlled by radiation. A SRD must have low emissivity at low temperatures (to preserve the desired temperature) and a high emissivity at high temperatures (to dissipate the extra unnecessary heat), therefore keeping the system working under the optimal operating range [93]. VO_2 thanks to the emissivity changes during the MIT transition is an ideal candidate for thermal regulation in spacecraft and satellites.

Yet, there are tasks to address before the real use of the VO_2 based SRD system. First, the $\Delta\varepsilon = \varepsilon_{HT} - \varepsilon_{LT}$ (emissivity switch at high and low temperatures) must be positive. The higher the $\Delta\varepsilon$ the better the SRD performance. Second, it is crucial to achieving high values of ε_{HT} to enhance the thermal power emitted by the radiator, thus reducing the size and weight of the satellite [93,94].

Hendaoui *et al.* studied the capabilities for SRD application of a 260 nm VO_2 deposited on mirror-like polished Al substrates using of reactive pulsed laser deposition (RPLD). The best values of ε_{HT} and $\Delta\varepsilon$ for the VO_2/Al system were found in the vicinity of the MIT. They explained this phenomenon thanks to the high absorption generated by the coexistence of both insulating and metallic phases of VO_2. They also demonstrated, theoretically and

experimentally, that it is possible to increase ε_{HT} values, above the upper limit allowed for the VO_2/Al system, by adding an appropriate top a-Si:H/SiO_2 λ/4 stack layer on the VO_2/Al system. The thickness of these additional layers (approx. 450 nm for the hydrogenated amorphous silicon (a-Si:H) layer and approx. 100 nm for the SiO_2) were chosen to produce a broadband destructive interference of the reflectance close to the maximum of the blackbody spectrum at 100°C when the VO_2 is in the metallic state. The ε_{HT} and $\Delta\varepsilon$ values enhanced from 0.29 and 0.21, respectively for the VO_2/Al system to 0.62 and 0.38, respectively, for the a-Si:H/SiO_2/VO_2/Al structure.

In the same year, the same group of authors published two more papers about the use of VO_2 as SRD in spacecraft thermal control. In the second paper, the multilayer structure was different. First, a 350 nm thick Au IR-high reflecting layer was deposited on a quartz substrate by RF magnetron sputtering. Second, an 850 nm SiO_2 layer was grown by plasma-enhanced chemical vapor deposition (PECVD). Third, the VO_2 30 nm layer was deposited by RPLD. Note that in this case, the SiO_2 layer has the same function as the a-Si:H/SiO_2 λ/4 stack layer in the previous study, resulting in a higher value of ε_{HT} thanks to the broadband destructive interference for temperatures above T_{MIT}. The ε_{HT} and $\Delta\varepsilon$ values are 0.71 and 0.49 [94]. Both values are higher than the previously reported for the a-Si:H/SiO_2/VO_2/Al structure suggesting that this new VO_2 multilayer system is better for the passive control of the internal temperature of the spacecraft. However, it will be interesting to include a top antireflective layer to the VO_2/SiO_2/Au/ quartz structure to avoid further oxidation of VO_2 and consequently degradation of the thermochromic performance.

Finally, in the third paper, Hendaoui *et al.* optimized the SiO_2 thickness to achieve the best possible value of ε_{HT} and $\Delta\varepsilon$ in the same VO_2 multilayer structure studied in the previous paper. Moreover, they doped the VO_2 with W to decrease the T_{MIT}, which is critical since the spacecraft generally work around room temperature. Two sets of samples were prepared: the first one comprises a top 30 nm of VO_2 with numerous intermediate SiO_2 layer thicknesses (460, 720, 1030, 1360 and 1570 nm) employing Au as an infrared-reflective layer on top of the quartz substrate. The second one contains a top approx. 30 nm thick undoped and W-doped VO_2 layer deposited on a SiO_2 1340 nm-thick layer and Al film as infrared reflecting layer growth on

quartz substrate. For the first sets of samples, the variation of SiO_2 layer thickness enables to increase the ε_{HT}, however, ε_{LT} also increases due to the presence of SiO_2 absorption bands. The higher values of ε_{HT} and $\Delta\varepsilon$ were 0.81 and 0.46. These values correspond to the sample with a 1360 SiO_2 intermediate layer. For the second sets of samples, the undoped VO_2-based SRD displayed a sharp transition at 68°C, $\varepsilon_{HT} = 0.8$ and $\Delta\varepsilon = 0.48$, almost identical values to the best of series one. For the doped films, the emissivity switching properties were strongly affected. The transition temperature decreased with the W content at a rate of 16.5°C per at.%, achieving a minimum at 19.5°C for the 2.9% W content film [95]. On the other hand, the ε_{HT} was not affected by the doping, however, ε_{LT} increase with W content, consequently decreasing $\Delta\varepsilon$. Doping with W donors enhanced the carrier concentration causing a rise of the absorption in the semiconductor state and therefore ε_{LT} [96,97]. The best compromise between emissivity performance and transition temperature was detected for the $V_{0.979}W_{0.021}O_2$-based SRD, characterized by T_{MIT} = 31.5°C, $\varepsilon_{HT} = 0.81$ and $\Delta\varepsilon = 0.43$ [95].

In conclusion, these three works exhibit the potentialities of VO_2 based multilayer structure as an SRD for energy-efficient thermal control of spacecraft. The use of VO_2 in thermal solar collectors is another interesting application in which the MIT is triggered by temperature. In the last eight years, two PhD theses were developed around this topic in our group, one of them with a successful industrial transfer. More details can be found in references [52,98].

1.7 VO_2 thin films growth methods

Driven by potential industrial applications coupled with scientific research on the VO_2 phase transition, the scientific literature on this material has increased significantly in the last decades. Different deposition techniques have been employed to deposit VO_2 with excellent thermochromic behavior, such as sol-gel [99], chemical vapor deposition (CVD) [100], molecular beam epitaxy (MBE) [101,102], atomic layer deposition (ALD) [103], pulsed laser deposition (PLD) [104–106], magnetron sputtering [84,107,108], among others. However, it is still a defiance to grow pure VO_2 on large surfaces caused by the large amounts of oxides in the V-O system.

MBE is a well-known technique used for the growth of high-quality homogeneous epitaxial crystal layers. Fan et al. prepared VO_2 epitaxial film by MBE on two-inches Al_2O_3 (0001) substrate. The stoichiometry film displays a change of the resistance of more than four orders of magnitude. They tuned the MIT temperature along with the resistance change by the modification of oxygen vacancies content during the deposition [101]. Moreover, Paik *et al.* reported the MBE growth of VO_2 films as thin as 1.5 nm with abrupt and reproducible MIT on (001) TiO_2 substrate [102]. Although the excellent control of VO_2 stoichiometry, the low deposition rate of MBE is a major drawback for the use of this technique for large-surface industrial applications.

PLD is another deposition technique suitable for the growth of epitaxial VO_2 with excellent thermochromic properties. This method enables precise control of the VO_2 stoichiometry. For instance, Kim and Kwok disclosed the deposition of VO_2 thin films on (0001) and $(10\bar{1}0)$ sapphire substrates. The films present outstanding electrical modulation properties with electrical resistance ratio between the low and high temperature as large as $4.0\ 10^4$ and 10^5 for the films on (0001) and $(10\bar{1}0)$, respectively [109]. PLD has higher deposition rates than MBE and guarantees exceptional thermochromic performance. However, it is not suitable for deposition on large surfaces as required for industrial applications since the laser beam is focused on a small area.

On the other hand, magnetron sputtering is a deposition technique that facilitates the growth of films on large surfaces with a high deposition rate. There are several approaches to obtain VO_2, within them, reactive sputtering in Ar and O_2 gas mixture without a post-annealing procedure is extensively applied [84,108,110,111]. For example, Yuce *et al.* deposited VO_2 thin films on *c*-cut sapphire (0001). The substrate temperature and the oxygen-argon gas mixture pressure during deposition were fixed at 550°C and 0.85 Pa, respectively. They studied the effect of oxygen concentration during the deposition and thickness (deposition duration) on the properties of the obtained films [108].

Table 1.2 Deposition parameters of samples in [108].

Sample	Oxygen to argon ratio (%)	Deposition time (min)	Thickness (nm)
A	2.00	45	310
B	2.00	22.5	120
C	2.25	22.5	125
D	2.50	22.5	124
E	3.00	22.5	127

The Raman spectra display that only sample A presents pure VO_2, while the other films show a mixture of VO_2 and V_2O_5 (Figure 1.11). The only difference between films A and B is the deposition time (Table 1.2). The authors claimed that decreasing the time leads to reduce the reactions of scattered V atoms with oxygen atoms, forming a mixture of vanadium oxide phases, instead of pure VO_2 [108]. Samples A and C are the only ones to present thermochromic performance (Figure 1.12), illustrating the significance to control these parameters during deposition.

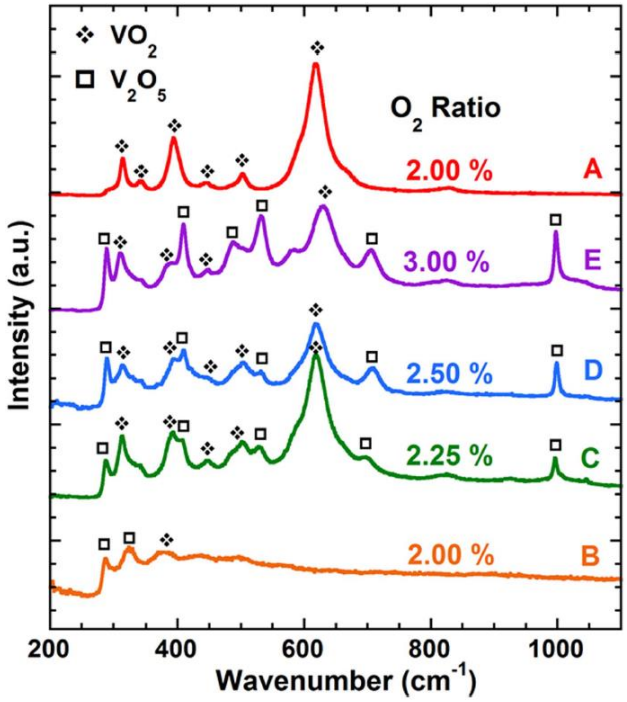

Figure 1.11 Raman spectra of thin films deposited at different O_2/Ar flow rate ratios. Note that sample A is thicker than the rest of the samples [108].

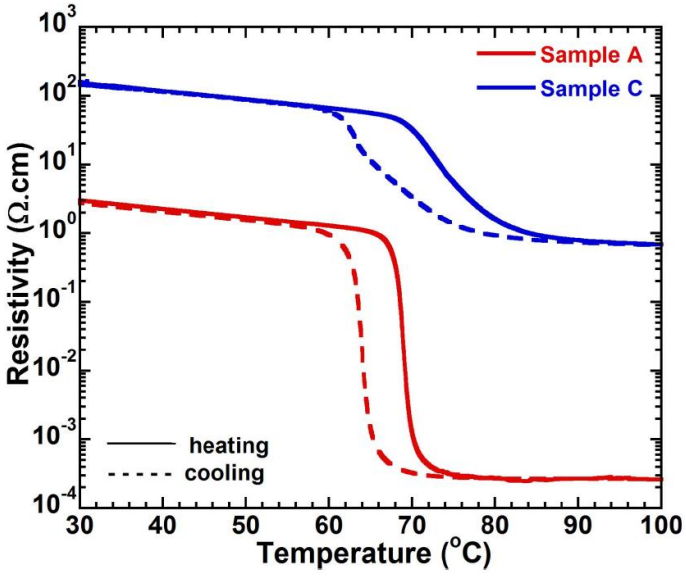

Figure 1.12 Thickness dependence of resistivity change across the MIT for sample A (310 nm) and C (125 nm) [108].

Moreover, Zhao *et al.* studied the influence of growth temperature on the structural, electrical, and optical properties of a series of seven 120 nm thick VO_2 films grown on *c*-plane (0001) sapphire substrates by reactive DC magnetron sputtering in Ar/O_2 ambient. The total gas mixture pressure was kept constant at 0.4 Pa with an 11% O_2/Ar flow rate ratio. All seven samples were grown under the same conditions but with substrate temperatures between 550 and 700°C with steps of 25°C. The results showed stoichiometry variations in the predominant VO_2 phase with the change of deposition temperature. The lower growth temperatures introduce V vacancies leading to hole doping and V^{5+} valence state formation. Therefore, the resistivity increases in both the insulating and the metallic phases. The higher growth temperatures introduce a relatively large density of O vacancies leading to V^{3+} valence state formation. Thus, the resistivity decreases in the monoclinic phase and increases in the metallic phase [110].

In general, the VO_2 crystallinity requires high deposition temperatures during the deposition. This constitutes a disadvantage for the large-scale production of the VO_2 films because of the high energy consumption and the difficulty to guarantee temperature homogeneity over large substrate surfaces. Moreover, it could cause the diffusion of substrate atoms into the films. Therefore, it eliminates the use of some temperature-sensitive substrates. A possibility to overcome this drawback is to employ reactive high-power impulse magnetron sputtering (HiPIMS) with pulsed O_2 flow rate control to deposited the VO_2 films. The highly

ionized fluxes of particles with high fractions of ionized sputtered metal atoms onto the substrate enable to reduce the deposition temperature to 300°C and still obtain VO_2 films with good thermochromic performance [112–114]. Furthermore, Loquai *et al*. demonstrated that VO_2 films deposited by HiPIMS exhibit better environmental stability than conventional magnetron sputtering-prepared VO_2 samples (approx. three times longer) thanks to the higher density and larger average grain size of the HiPIMS films [115].

Another approach is to apply a post-annealing process to enhance the thermochromic performance of the deposited films [116–118]. Melnik *et al*. reported the growth of 100 nm VO_2 thin films on glass substrates. The deposition parameters were 5% of O_2 in Ar at a total gas pressure of 0.4 Pa, and the substrate temperature close to 200 °C. The deposited films were further annealed at 300°C in air for their crystallization [116]. This second step is essential for the crystallization of the films (Figure 1.13), changing from amorphous (before annealing) to well crystalline films (after annealing) with a change in resistance of about four orders of magnitude [116].

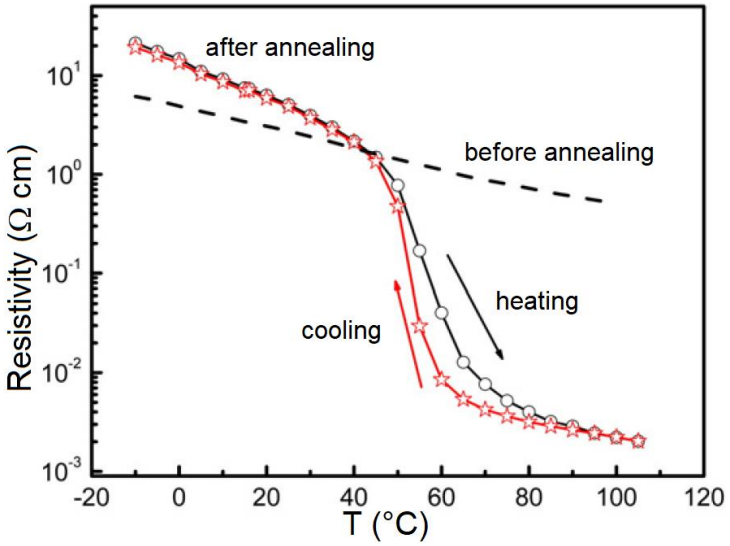

Figure 1.13 Temperature dependence of resistivity for synthesized VO_2 films before (dashed lines) and after annealing. Modified figure from [116].

Nevertheless, it is critical to choose proper conditions for the post-annealing procedure. Dou *et al*. have deposited high-quality VO_2 films on *m*-, *a*-, and *r*-plane sapphire substrates under identical conditions by DC magnetron sputter deposition. The deposition was performed in an Ar-O_2 mixture containing 2 % of O_2 at a total deposition pressure of 1 Pa and 550°C of substrate

temperature. Then the films were annealed to crystallize them at 500°C for 400 s with a pressure of 220 Pa atmosphere by a rapid thermal annealing system. After this procedure, all of the samples exhibit resistance change of more than four orders of magnitude, and good IR optical modulation efficiencies at the transition temperature. Thereafter, the samples were heated up to 450°C in 8 s and kept in air at 450°C for 200, 400, 600, 800 and 1000 s under atmospheric pressure, respectively [118]. After this last annealing, all the samples suffered a decrease in the resistance change and in the IR optical modulation properties with prolonging the oxidation time. These findings suggest progress in the annealing evolution of the films from VO_2 to V_2O_5 [118].

An alternative two-step proposal to produce VO_2 is the reduction of previously obtained V_2O_5 in ammonia [119], vacuum [120], or hydrogen [121]. The reduction of the V_2O_5 + C mixture in a dynamic vacuum system is also reported [122]. Furthermore, there is an additional two-step procedure, in which a vanadium film is deposited and then annealed in an air or oxygen-controlled atmosphere to form thermochromic VO_2. This process could be found in the literature under the name of thermal oxidation method [107,123,124] or sputtering oxidation coupling (SOC) method [125,126]. Xu *et al*. sputter-deposited V films (85 nm) on *c*-plane sapphire substrates. Thereafter, the samples were oxidized in a furnace under air atmosphere at 470°C with a different duration between 250 and 325 s [125]. Their results indicate a transformation of the amorphous vanadium into crystalline VO_2 in the 250 - 285 s range. The optimum oxidation time was 285 s with a resistance change of almost three orders of magnitude. Further oxidation of the films for more than 285 s led to the formation of V_2O_5 affecting the thermochromic behavior of the samples [125]. One year later, the same group found that the logarithm of the optimal oxidation time ($\ln(t)$) as a function of the reverse temperature ($1/T$) of vanadium films (100 nm) under air atmosphere satisfies a linear relationship when the temperature ranges from 430 to 510°C [126]. Using this two-step method, Yoon *et al*. grew 100 nm vanadium films on $(11\bar{2}0)$ sapphire substrates. Their samples were annealed for 10 min at different oxygen pressures ranging from 200 to 600 Pa and temperatures from 510 to 600 °C [107]. The results display a strong dependence of the electrical properties of the VO_2 films

(resistivity ratio and sharpness of the MIT) on the annealing temperature and oxidation pressure (Figure 1.14).

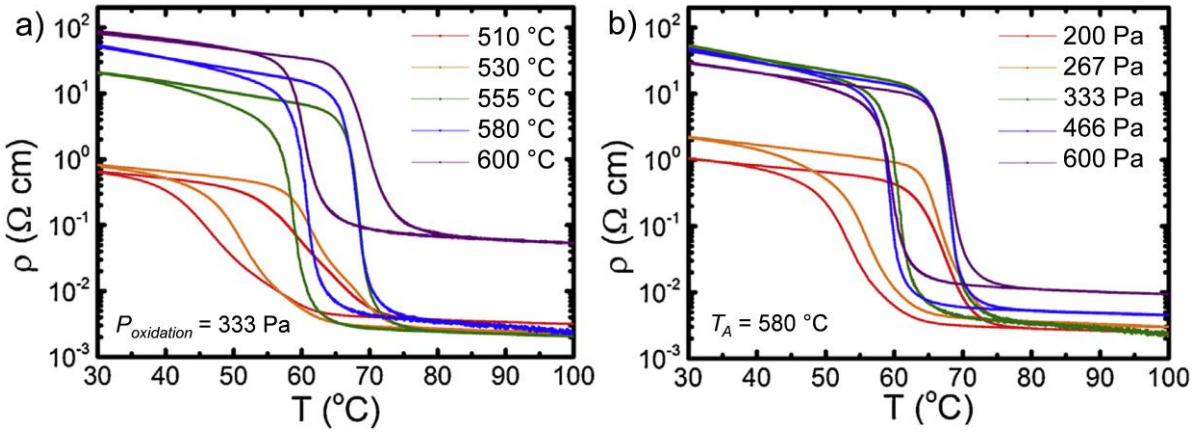

Figure 1.14 Temperature dependence of the resistivity of the VO_2 films oxidized at (a) various oxidation annealing temperatures ranging from 510 to 600°C at fixed oxygen pressure ($P_{oxidation}$) of 333 Pa and b) various oxidation annealing pressures ranging from 200 to 600 Pa at a fixed oxidation annealing temperature of 580°C. Modified figure from [107].

These reports illustrate that the possibility to regulate the temperature and duration along the oxidation process makes the two-step procedure suitable for achieving high-quality VO_2 films over large surfaces. In this thesis we use this method to obtain thermochromic VO_2, yet, we change the precursor. First, we deposit VN or V_2N films by reactive magnetron sputtering. Second, the as-deposited samples are air annealed in a preheated furnace under atmospheric pressure. It is relevant to stress the freedom in the choice of parameters when using a two-stage procedure. The thickness of the precursor film is determined during the deposition process. Afterward, the temperature and duration of the oxidation step depend on the initial thickness of the as-deposited films. Hence, these three parameters are the key to the successful oxidation of VN or V_2N into thermochromic VO_2. Failure to optimize these parameters may lead to the formation of other oxides, such as the Magnéli phases V_nO_{2n-1} (V_4O_7, V_5O_9…) [127–129] and Wadsley phases V_nO_{2n+1} (V_4O_9, V_6O_{13}…) [129–132].

1.8 Chapter conclusions

In this chapter, the different oxides of the V-O system have been exposed with an emphasis on thermochromic VO_2. The crystallographic and band structure of thermochromic VO_2 has

been described, together with comments on the mechanism of the MIT of this material. The change in the physical properties of VO_2 and some possible applications were discussed. Finally, a brief illustration of different methods to obtain a high-quality thermochromic VO_2 was displayed. A more detailed discussion on the magnetron sputtering technique was depicted, with particular attention to smart two-step procedures. The difficult task of obtaining a pure VO_2 phase on large surfaces has been presented. The major influence of the deposition parameters (deposition temperature, oxygen partial pressure…) and oxidation conditions (temperature, oxygen pressure and duration) on the properties of VO_2 was also highlighted.

The following chapter will present the oxidation process carried out to produce the VO_2 thermochromic films. The basic principles of the main characterization techniques and the particular parameters used for the analysis of the samples will be specified.

Chapter 2

Sputter deposition process and characterization techniques

Abstract

In this chapter, we describe the magnetron sputtering techniques used throughout this thesis for the growth of VN and V_2N thin films. We compare the two sputtering machines employed: the in-line semi-industrial machine and the standard laboratory one. We present a simple approach that allows us to obtain analogous samples on both machines. The oxidation process employed to achieve the VO_2 thermochromic films is described. The basic principles of the main characterization techniques used in this thesis are also specified. Moreover, the particular parameters adopted for the analysis of the samples are displayed.

Contents

2.1 Introduction

In this thesis, VN and V_2N films were grown by reactive magnetron sputtering. We discussed the principal features of the two different sputtering machines employed: the in-line semi-industrial machine and the standard laboratory one. We present a simple approach that allows us to obtain analogous films on both machines. We also described the oxidation protocol followed to achieve the VO_2 thermochromic films. X-ray diffraction, Raman spectrometry, scanning electron microscopy (SEM), transmission electron microscopy (TEM) and secondary ions mass spectrometry (SIMS) were performed for structural, microstructural, physico-chemical characterizations and qualitative elemental depth profiles of the oxidized films. The thermally-induced properties of the oxidized VN and V_2N films were analyzed, in the 30-120°C temperature range, in terms of their electrical resistance through the four-point probe method and their emissivity modulation properties by infrared camera. Thermogravimetry analysis was employed to understand the impact of water vapor on the oxidation process. In this chapter, we present the general characteristics of the experimental techniques used throughout this thesis. In addition, we comment on each technique, the particular parameters employed for the analysis of the samples.

2.2 Magnetron sputtering deposition process

2.2.1 Sputtering: Basic principles

Physical vapor deposition (PVD) methods define several vacuum deposition techniques employed to produce thin films and coatings. Each of them is characterized by the generation of a vapor from a source material (generally denominated as target), which is condensed into a thin film on a substrate. All PVD processes differ from the others in the way the vapor is generated from the target. Throughout this thesis, we used sputtering (more specific magnetron sputtering) to synthesize the desired materials.

Sputtering is a process in which the atoms of a solid target are evaporated by bombarding it with energetic ions present in the plasma. This is due to collisions between the ions and the atoms of the target. To achieve this process, in a rarefied atmosphere of inert gas, generally Ar,

a potential difference is applied between a cathode (the target) and an anode (the reactor's grounded chamber walls). Hence, an electrical discharge is originated between the target and the reactor chamber walls resulting in the ionization of the inert gas. Thanks to the electrical potential difference, the positive ions are accelerated towards the target. Figure 2.1 schematically represents the different processes that could occur during the ion bombardment of the target: (1) ejection of target atoms, (2) reflection of the incident ion by the target surface which is neutralized after the charge transfer, (3) stimulate the emission of secondary electrons that helps to sustain the plasma discharge, and (4) implantation of the incident ion into the target. It should be pointed out that the sputtering phenomenon requires that the energy of the incident ions needs to be higher than a threshold energy for each studied target. It must be higher than the binding energy of the source material. This threshold energy is between 15-30 eV for most of the metals.

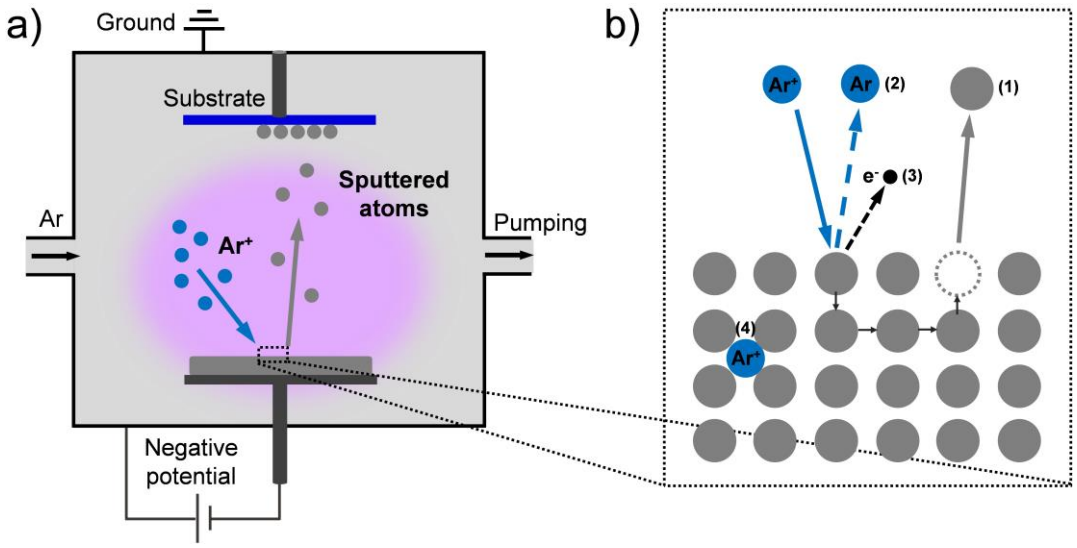

Figure 2.1 a) Scheme of the sputtering process. b) Principal mechanisms resulting from the interaction between the Ar^+ ions and the target atoms.

An important parameter in the sputtering process is the sputtering yield $Y(E)$, which is the mean number of ejected atoms per incident ion. In the case of low energetic incident ions ($E < 1\ keV$) and perpendicular bombardment, $Y(E)$ could be written as [133,134]:

$$Y(E) = \frac{3\alpha}{\pi^2}\frac{m_1 m_2}{(m_1+m_2)^2}\frac{E}{U_S} \qquad 2.1$$

where α is a dimensionless function of the mass ratio between the incoming particle and the target atom, m_1 and m_2 are the atomic masses of the ion and the target, E is the energy of the incident ion and U_S the surface binding energy.

2.2.2 Magnetron sputtering

In the previous section we described the classical sputtering process (diode sputtering). The main problem with this method remains the low ionization rate of the discharge leading to work at high pressures to sustain the plasma. As a consequence, the sputtered atoms suffer several collisions before arriving at the substrate, forming porous films with a low deposition rate. To avoid these drawbacks the target is provided with a magnetron device [135,136]. It consists of two concentric magnets of opposite polarities, as shown in Figure 2.2. This results in a generation of a magnetic field in the vicinity of the target, trapping secondary electrons, thus increasing the probability of a collision with an argon atom in an ionizing interaction. Hence a dense plasma is created near the target, increasing the ionization rate and the ion bombardment of the target, and subsequently the deposition rate. Moreover, under these conditions, it is possible to decrease the working pressures achieving the deposition of denser films.

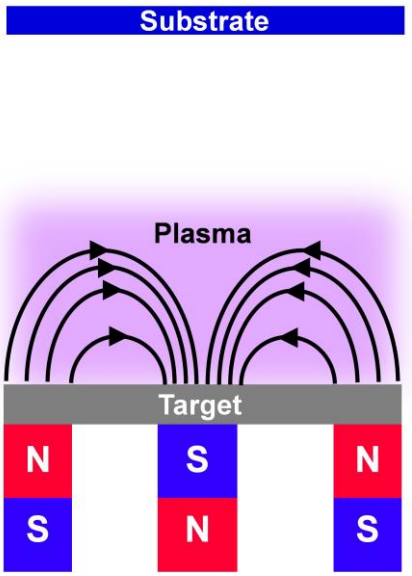

Figure 2.2 Scheme of the magnetic configuration and plasma confinement in a magnetron sputtering source.

2.2.3 Reactive magnetron sputtering

In the previous section, we have described how the sputtering process could be used to synthesize metallic films from metallic targets. However, it is also possible to deposit more complex compounds such as oxides, nitrides, carbides... The use of ceramic targets is one approach to synthesize these compounds [137–141]. Nevertheless, this is a more challenging process due to the charge accumulation on the surface of the insulating targets, and the consequently arcs formation. These obstacles are overcome by employing the radio-frequency (RF) magnetron sputtering mode. Yet, the alternate voltage applied during the RF mode decreased the sputtering rate compared to direct current magnetron sputtering (working with the same power). Besides, ceramic targets are more expensive than metallic ones. Since ceramic targets are brittle, the heating of the target due to the ion bombardment induces a thermal gradient in the target and its cracking. Thus, another approach has to be used to deposit ceramics thin films.

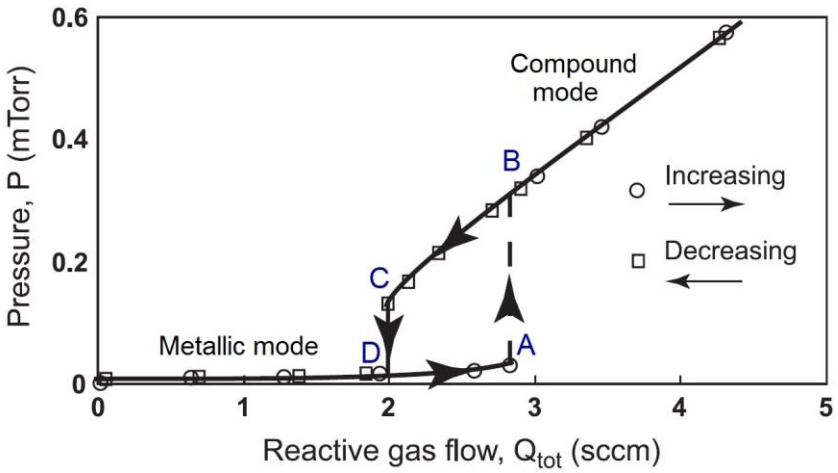

Figure 2.3 Typical experimental curve for the reactive sputtering of a highly reactive metal. The partial pressure, *P*, of the reactive gas as a function of the reactive gas flow. Q_{tot} is expressed in standard cubic centimeters per minute (sccm). 1 mTorr is approx 0.133 Pa. Modified figure from [46].

Reactive magnetron sputtering is another procedure to synthesize compound materials. In this mode, a reactive gas is introduced in the chamber, forming a mixture with the Ar gas. The addition of a reactive gas has a significant influence on the sputtering process. For instance, the deposition rate and the composition of the films are dependent on the reactive gas flow [142,143].

Figure 2.3 shows a typical experimental processing curve for the partial reactive pressure as a function of the reactive gas flow rate for a reactive sputtering process (carried out with a constant target current during processing) [46]. It is important to note that the curve does not follow the same path for the increase of the reactive gas flow rate than for the decrease, displaying a hysteresis behavior. In the beginning, for small values of the reactive gas flow rate, the partial pressure is nearly zero. Almost all the reactive gas is absorbed by the sputtered atoms that condensate on the chamber walls and at the substrate surface (getter effect of the metallic flux). From zero to position A, the target operates in the metallic mode called elemental sputtering mode (ESM). After the critical point A, the chamber walls are saturated (a film is formed on the whole wall), a small increase of the reactive gas flow rate drives to a considerable increase in the partial pressure (range A-B in Figure 2.3). This new value of partial pressure (point B) is high enough to form a compound at the entire surface target. From this position, the target is in poisoned or compound mode. Generally, the binding energy increases when metal is transformed into a compound. As a result, the sputtering yield of the target declines when compared to the elemental target material, and the deposition rate decreases. Since less metal is sputtered after point B, the excess of reactive gas will increase the partial reactive pressure. The process is then working in the compound sputtering mode (CSM). In CSM, when the reactive gas flow rate begins to decrease, the partial reactive pressure becomes different than during the increase of the flow rate, due to the remaining saturation of the walls. This process happens until the compound layer on the surface of the target is removed (decontamination of the target), and metal is sputtered once more (region C-D). In this stage, the reactive gas consumption increases, and the deposited film is in the metallic mode again.

The hysteresis effect is one of the central problems in experimental reactive sputtering systems. It can be avoided in some systems with low reactivity for gas/target material combination. For instance, Schulte *et al.* showed that the small hysteresis effect and not avalanche-like transitions are observed in the Al/N system [144]. On the other hand, the pumping speed of the vacuum system influences the hysteresis effect. The higher the pumping value, the less pronounced the hysteresis. For high enough pumping values, it could even disappear[145,146]. Methods such as plasma emission monitoring (PEM) can be used to work

in the instability zone to deposit ceramic films with high deposition rate. PEM method is mainly used for the deposition of oxides. For the deposition of transition metal nitrides, such equipment is not mandatory due to the quite high deposition rate of such materials.

2.3 Magnetron sputtering depositions machines

During this work, all the VN and V_2N samples were deposited using two different sputtering machines. Both deposition chambers are connected to the IJL "TUBE" equipment. This unique tool combines 25 thin film deposition/growth analysis and post-deposition treatment techniques, all connected under Ultra High Vacuum (10^{-9} Pa), see Figure 2.4. In this configuration, as-deposited samples are transported to an analysis chamber, without exposing them to the air, protecting the films from undesired effects (like oxidation). In the following subsections, we will describe the principal characteristics of each machine.

Figure 2.4 a) Transfer Technology Office (TTO) part of the TUBE. b) Semi-industrial and standard sputtering machine connected to the TUBE.

2.3.1 Description of the semi-industrial sputtering machine

This "in-line" prototyping reactor has two chambers, the load-lock, and the deposition chamber (Figure 2.5). Both of them provide with a turbo-molecular pump to achieve a pressure up to 10^{-5} Pa. The load-lock chamber allows a fast transfer of samples to the deposition chamber without venting every time a new film is synthesized. Substrate cleaning is performed in the load-lock chamber using a microwave plasma combined with a negative bias of the substrate in DC-pulsed mode. This machine is coupled to the standard sputtering chamber (see section 2.3.2) and to the Tube via a UHV load-lock chamber.

The sputtering chamber has two Flecher Plasma Technich rectangular cathodes placed side by side (with the possibility to install a third cylindrical cathode). The cathodes (330 x 50 x 6 mm^3) are powered with a pulsed-DC Pinnacle+ generator from Advanced Energy (5kW, 5-350 kHz, τ_{ON} from 60 to 100%) allowing process regulation in current, power or voltage. The two cathodes are water-cooled. The volume of the deposition chamber is around 350 L. The substrate holder offers the possibility to coat samples with a 29 x 19 cm^2 surface.

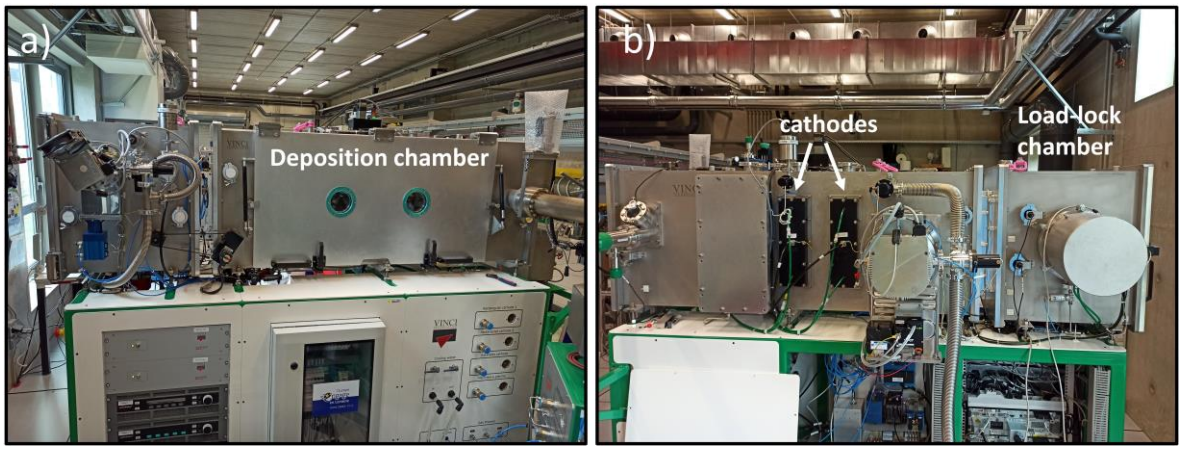

Figure 2.5 a) Front view and b) rear view of the semi-industrial sputtering reactor connected to the TUBE.

The substrate holder does not rotate in this machine. In this case, it moves back and forth on a rail in front of the cathode that is used. In co-sputtering mode, the substrate holder crosses in front of each of the cathodes. The raster scanning speed is adjustable from 0 to 300 cm/min. The target-substrate distance is fixed to 5 cm. A Brooks mass flow meter controls each of the three available gas: argon (0-98 sccm), nitrogen (0-18 sccm), and oxygen (0-18 sccm). This sputtering machine allows neither the synthesis of biased films nor in-situ heating of the substrates. A PC-controlled regulation VAT valve allows precise control of the working pressure in opening or pressure mode.

2.3.1.1 VN thin films deposition in the semi-industrial sputtering machine

The first step before the deposition was to clean the substrates with ethanol. Afterward, the cleaning process continued in the load-lock chamber with the introduction of Ar gas, then the application of 500 Watts to the Magdrive microwave generator to form a plasma. The Ar^+ ions bombarded the negatively biased substrate holder (-280 Volts applied to the pulsed-DC

Pinnacle+ generator) for 90 seconds. After this process, the substrate holder was transferred to the deposition chamber. VN thin films were deposited on Al and undoped (100) silicon substrates by reactive magnetron sputtering of a metallic vanadium target (99.95% purity) in an Ar-N_2 mixture with flow rates of 30 and 5 sccm, respectively. The deposition pressure was fixed to 1 Pa. A pulsed-DC power supply, working on a set current of 1.5 A, provided power to the V target. The frequency of DC-pulses and their off-time were kept at 50 kHz and 4 μs, respectively. The substrate is composed of a Si wafer (four inches diameter) fixed on an Al foil (29 x 19 cm^2). It is important to remark that thanks to the size of the substrate holder, in the same deposition, VN thin films were synthesized on Al and Si substrates. The substrate holder moved back and forth in front of the V target (to ensure film homogeneity) at a speed of 50 cm/min for 1 h. The films deposited with these parameters have a thickness of approx. 175 nm. All the results detailed in chapters 3 and 4 have been obtained from the oxidation of these samples.

2.3.2 Description of the standard sputtering machine

The standard laboratory sputtering reactor (Figure 2.6) has two chambers, the load-lock, and the deposition chamber. The load-lock chamber, equipped with a primary pump allows a fast transfer of samples to the deposition chamber without venting every time a new film is synthesized. A turbo-molecular pump in the deposition chamber guarantees a pressure up to 10^{-6} Pa. The volume of the deposition chamber is around 70 L. The machine is attached to the sputtering chamber of semi-industrial size and to the Tube via a UHV load-lock chamber, pumped by an ion/sublimation pump.

There are 3 Meivac cathodes (two inches diameter) in confocal "sputter-up" configuration. Each cathode is equipped with a different power supply: RF (Seren R300 of 300 W), DC Maxim1000 (1 kV), and pulse DC Advanced Energy Pinnacle+ (5 kW, 5-350 kHz, τ_{ON} from 60 to 100%). The chamber wall, as well as the three cathodes, are water-cooled. The substrate holder is a two inches diameter Inconel molybloc. The device used to manipulate the molybloc allows at the same time, the rotation of the substrate (0-50 rpm), its RF bias, as well as its heating by Joule effect (up to 800°C). The homogeneous deposition zone is the entire surface

of the molybloc. The target-substrate distance is adjustable from 9 to 19 cm. A Brooks mass flow meter controls each of the three available gas: argon (0-98 sccm), nitrogen (0-18 sccm), and oxygen (0-18 sccm).

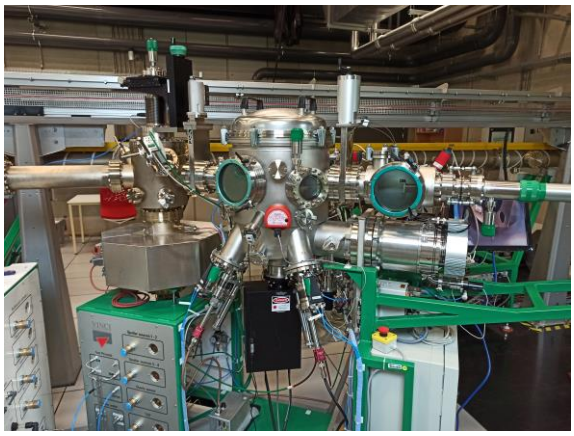

Figure 2.6 Standard sputtering chamber connected to the TUBE.

2.3.2.1 VN, V_2N and epitaxial VN thin films deposition in the standard sputtering machine

In this section, we described the conditions to deposited VN, V_2N, and the epitaxial growth of VN in the standard sputtering machine. There are significant differences between these depositions. However, let's first discuss the mutual parameters.

All the films were deposited by reactive magnetron sputtering of a metallic vanadium target (99.95% purity). A pulsed-DC power supply, working with discharge current regulation, provided power to the V target. The frequency of DC-pulses and their off-time were kept at 50 kHz and 4 μs, respectively. The distance between the target and substrate was 9 cm. During the deposition, the substrate holder was in rotation mode (5 rpm) to guarantee a good homogeneity of the films.

In Table 2.1 we present the parameters that differed in the growth of VN, V_2N and epitaxial VN films in the standard sputtering machine. In the case of VN and V_2N samples, the substrates were cleaned with ethanol before the introduction in the load-lock chamber. Once inside the deposition chamber, the substrate's surface was etched by Ar^+ ions using a RF Seren R300 power supply at 50 W for 3 minutes at 1 Pa.

On the other hand, the MgO wafers with orientation (100), polished, and dimensions 20 x 20 x 0.5 mm^3 followed a completely different process. Before using the MgO substrate, it was

kept inside a glove box under an Ar atmosphere and individually sealed in a sack to reduce the exposure to moisture while storing. Then it was mounted in the substrate holder and introduced into the TUBE to be cleaned it before the deposition. To achieve epitaxial growth the substrate-cleaning process is crucial. Annealing at high temperatures removes the organic contaminants and changes the surface by atomic reconstruction of the surface [147]. The thermally degassed process usually lasts one hour and is performed at different temperatures, for instance, 800°C [148,149] and 900°C [150]. In our case, the process is carried out for about 45 min at 1000°C. As mentioned before, the standard sputtering machine allows the heating of the substrate holder up to 800°C. Hence, the MgO substrate was thermally degassed in the MBE machine connected to the TUBE. This chamber is equipped with a reflection high-energy electron diffraction (RHEED) device to study the surface state of the samples. We will discuss in more details the RHEED technique in section 2.6.2. Afterward, the cleaned substrate was transferred from the MBE to the sputtering chamber where the deposition process begins using the conditions described in Table 2.1.

Table 2.1 Growth conditions of the VN, V_2N and epitaxial VN thin films obtained in the standard sputtering machine.

	VN	**V_2N**	**Epitaxial VN**
Substrate	Si, Al	Si	MgO (100) single crystal
Pressure (Pa)	0.22, 0.56, 0.83	0.22	0.22
Deposition temperature (°C)	No intentional heating (T< 55°C)	450	450
V target curent (A)	0.5	0.7	0.5
Ar flow rate (sccm)	30	33.5	30
N flow rate (sccm)	5	1.5	5

2.4 First approach to compare the deposition conditions used in the two sputtering chambers

The goal of this section is to obtain a simple criterion that allows us to compare the films synthesized on one machine with the ones obtained on the other. In our model, strong assumptions have been made. We will not consider:

- the difference in volume between the deposition chambers,

- the different pumping speeds in each machine,

- the size of the magnetron,

- the difference in the flow of sputtered atoms to reach the substrate in each deposition chamber.

We will assume that the fundamental parameter that governs the growth of thin films is the energy at which the sputtered atoms arrive on the substrate. Hence, the criterion to have analogous films from both machines is that the sputtered atoms coming from the target arrive with the same energy at the substrate.

During the sputtering process, the atoms leaving the surface of the target will lose energy due to collision with the Ar atoms in the plasma. The energy of the atoms arriving at the film surface (E_F) is strongly dependent on the pressure and the target-substrate distance, and can be estimated from [151]:

$$E_F = \left(E - k_B T_g\right) e^{\left[n \ ln\langle \frac{E_f}{E_i} \rangle\right]} + k_B T_g, \qquad 2.2$$

where E is the energy of the sputtered atoms as it leaves the target, k_B is Boltzmann constant, T_g is the sputtering gas temperature and n is the number of collisions that take place before reaching the substrate. When considering a hard-sphere interaction between a particle with energy E, mass m_s and stationary Ar atoms of mass m_g, the average ratio of energy of the sputtered particle after a collision is given by [152]:

$$\langle \frac{E_f}{E_i} \rangle = 1 - \frac{\gamma}{2}, \qquad 2.3$$

where E_i, E_f are the energies before and after the collision and γ is the kinetic energy mass transfer defined as:

$$\gamma = 4\frac{m_g\, m_s}{(m_g+m_s)^2}. \qquad 2.4$$

The number of collisions $n = d/\lambda$ depends on the target-substrate distance d and the mean free path of the sputtered particle λ. The latter can be written as:

$$\lambda = \frac{k_B T_g}{\sqrt{2}\pi d_s^2 P}, \qquad 2.5$$

where P is the sputtering gas pressure and d_s is the diameter of the sputtered particle. In our case, we use a vanadium target, where $d_s = 0.264$ nm [153].

To calculate the energy of the V atoms arriving at the film surface E_F, a Maxwell-Boltzmann (MB) distribution at $T_g = 300\ K$ is assumed for the Ar gas. Moreover, following the Sigmund-Thompson theory for sputtering [133,154], the most-likely energy of the sputtered atoms is in the peak of the energy distribution, which corresponds to $E_{SB}/2$, where E_{SB} is the surface binding energy. We will consider that $E = E_{SB}/2$. In the case of vanadium, $E_{SB} = 5.31\ eV$ [155].

It is important to note that we did not change the parameters for the VN deposition in the semi-industrial machine (see section 2.3.1.1). Moreover, we fixed the target-substrate distance in the standard deposition reactor to 9 cm (see section 2.3.2.1). Therefore, using equations (2.2)-(2.5) we determined the value of pressure (0.56 Pa) to obtain analogous films in the standard sputtering machine. We will use these results in Chapter 5 for the oxidation of different VN films.

As our principal goal is to compare energy values for both machines, working with $E = E_{SB}/2$ seems relevant. This assumption allows us to calculate the most-likely energy with which the sputtered atoms reach the surface of the substrate. However, equation (2.2) could be used for most general and accurate predictions. In this case, the calculus is repeated for each E in the distribution of sputtered atoms and weighted by the collision probability. This probability is the product of the sputtering distribution $f(E)$ and the value of the MB distribution at T_g [151]. This results in the energy distribution of the sputtered particles arriving at the substrate, and most crucial, it provides the average energy value of the atoms reaching the surface's substrate. Therefore, one can compare this adatom's average energy values with the energy order of different surface processes (chemisorption, physisorption, and diffusion)[156].

This criterion has a significant drawback, related to the non-rotation of the substrate holder of the semi-industrial machine. When using one target, as in our case, the as-deposited films are homogeneous. Nevertheless, while working with two targets (La and Co) in the co-sputtering mode a multilayers structure was obtained [6]. This multilayer structure affects the properties of the films. On the other hand, no multilayer structure was formed with the standard sputtering reactor [6]. To avoid the formation of a multilayer structure during depositions that involved two targets one should increase the raster scanning speed of the substrate holder and decrease the flux of particles from both targets.

2.5 Thin film oxidation

Once the VN and V_2N films are obtained, the second step is their oxidation to form VO_2. In this thesis, we used two equipments to oxidize the VN thin films: a furnace under atmospheric pressure and a thermogravimetry analysis chamber. During this work, the furnace was the most used equipment to oxidize the samples. On the other hand, the thermogravimetry was used to analyze the role of water vapor in the oxidation.

2.5.1 Carbolite HRF 7/45 furnace

The modified Carbolite HRF 7/45 furnace is equipped with a quick sample tray loader to prevent a huge drop in the temperature when the sample is introduced (Figure 2.7 a)). It has a maximum operating temperature of 750°C and a volume of 45 liters. Figure 2.7 b) schematically represents a top-view scheme of the furnace. It is equipped with a motor/fan unit mounted at the rear of the chamber (1) and heating elements located on the side of the furnace (2). The fan mixes the heated air, equalizing its temperature, and providing a high uniform volume within the chamber.

In this thesis, we used the furnace working under atmospheric pressure at a preheated temperature (450, 525 and 550°C) and various durations (from a few minutes up to 50 min). The as-deposited films were labeled VN or V_2N, and "VN_temperature_time" or "V_2N_temperature_time" for the oxidized films at various temperatures and annealing duration.

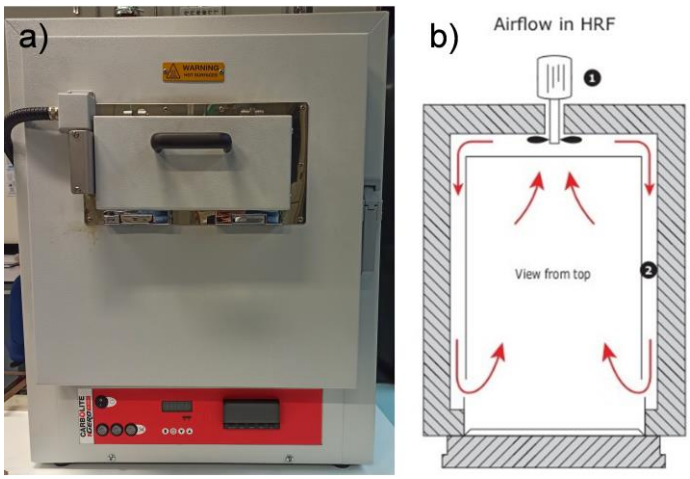

Figure 2.7 a) Front-view picture of the HRF 7/45 furnace. b) Top-view scheme of the HRF 7/45 furnace.

2.5.2 Thermogravimetry analysis (TGA)

Thermogravimetric analysis (TGA) is a technique which measures the mass change of a sample as a function of temperature or time, under a programmed temperature regime, in a controlled atmosphere. Besides, it can be coupled with other methods of analysis to perform simultaneous measurements. The most frequently used complementary techniques are

- differential scanning calorimetry,
- differential thermal analysis,
- separation techniques: mass spectrometry, chromatography.

The most common instruments operate at atmospheric pressure or under vacuum, in isothermal mode, or programmed temperature mode. Therefore, TGA can be applied to any samples that will undergo a mass variation over time due to the effect of temperature in a given atmosphere. Evaporation, sublimation, oxidation are among the transformations that will be detected by thermogravimetry [157].

In our work, we study the oxidation of VN and V_2N on the isothermal mode. Moreover, for the oxidation of the films, we used "dry air" (AlphaGaz 1) or "humid air" (AlphaGaz 1 + 10% absolute humidity). In both cases, the sample was heated at a rate of 20 °C/min up to 450°C in Ar atmosphere. Once the desired temperature was achieved, the Ar gas valve was closed, and simultaneously the dry air (or humid air) valve was opened. After the oxidation time finished, the sample was cooled at a rate of 20 °C/min until reached room temperature.

We used a 1750 Simultaneous symmetrical thermoanalyser (SETARAM) for the oxidation of the films in dry air. On the contrary, a Setsys Evolution 1750 SETARAM coupled with a humidity Wetsys (SETARAM) equipment was employed for the oxidation of the films in the humid air.

2.6 Thin film characterization

2.6.1 X-ray diffraction (XRD)

Over the years, X-ray diffraction (XRD) has become an essential technique for the structural characterization of materials. The phenomenon of diffraction occurs when a wave deviates from its trajectory upon encountering an obstacle. It only takes places when the length of the wave is of the same order of magnitude of the scattering object. Therefore, when studying crystalline structures with interatomic distances between 0.5 and 2.5 Å, X-rays are used. When a monochromatic X-ray beam interacts with a crystalline solid, it is scattered by the atoms forming the solid. The resulting scattered waves (with the same wavelength) interfere each other by adding their amplitudes, producing a diffraction pattern. If the scattered waves are completely out-of-phase, they will extinguish one another (destructive interference). On the contrary, if the scattered waves are completely in-phase, the resulting wave has its amplitude doubled (constructive interference). Bragg's law describes the condition where constructive interference is achieved (see Figure 2.8 a)) [158]:

$$n\lambda = 2d_{hkl} \sin\theta, \qquad 2.6$$

where n is an integer determining the order of reflection, λ is the wavelength of the incident radiation, d_{hkl} is the distance between crystallographic planes with Miller indices h, k and l, and θ is the diffracting angle.

For the most commonly used Bragg–Brentano (or $\theta - 2\theta$) geometry, the X-ray source is fixed, while the sample and detector change their positions at a rate $\dot{\theta}$ and $2\dot{\theta}$, respectively. Figure 2.8 a) presents a schema of this configuration. Under this configuration, only the crystallographic planes parallel to the sample surface are in constructive interference condition. Hence, these are the only peaks observed in the diffractogram.

Figure 2.8 b) displays X-ray diffractograms for VN and V_2N deposited by magnetron sputtering on Si substrate. Structural and microstructural information is extracted from the diffractograms. The peak position enables us to calculate the interplanar distance d_{hkl} using Bragg's law (equation 2.6). These results, coupled with the Powder Diffraction File (PDF) database are used to identify the crystalline structure of the samples. The peak intensity helps to determine if there is a preferred crystallographic orientation. In the case of single crystalline or textured films, the only peaks detected corresponds to the same family of planes. In opposition, in non-textured-polycrystalline films, several peaks are identified since the grains are oriented in different directions in the sample. The diffractograms displayed in Figure 2.8 b) are polycrystalline showing (111) and (200) Bragg reflection for the VN sample, and $(2\bar{1}1)$ and (112) for the V_2N one. Yet, the (111) intense peak in the VN sample and the $(2\bar{1}1)$ in the V_2N one indicate a preferred crystallographic orientation. Furthermore, peak shape provides information about the microstructure. It is correlated with defects present in the structure, non-uniform deformations, and crystallite size (coherently scattering domains).

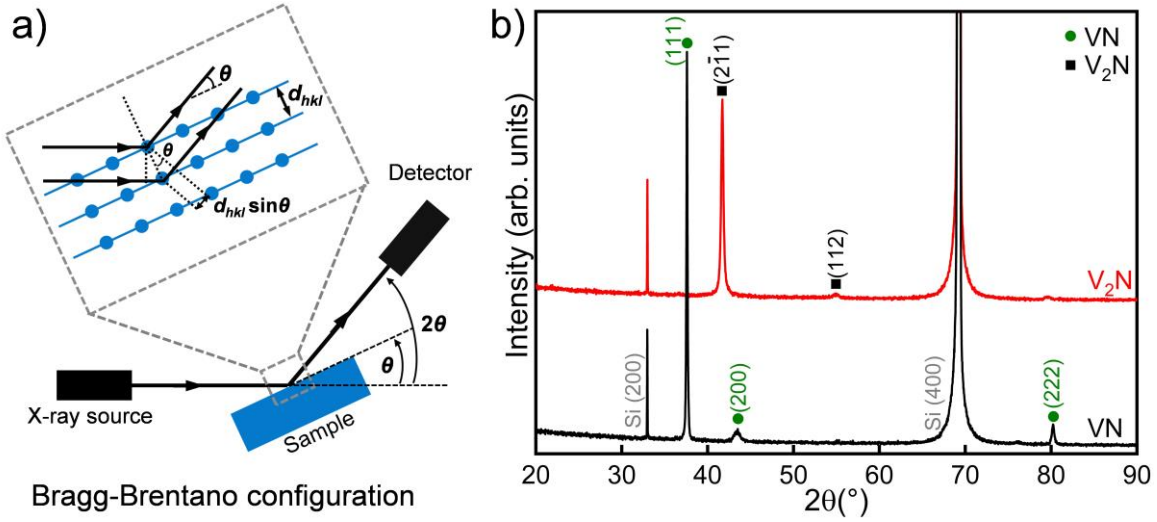

Figure 2.8 a) Schematic representation of Bragg's law and the Bragg-Brentano configuration. b) X-ray diffractogram of VN and V_2N films deposited on Si substrate.

In the Bragg-Brentano configuration, Scherrer's equation (2.7) yields an estimation of the coherent length D in the direction perpendicular to the sample surface [159].

$$D = \frac{K\,\lambda}{\beta\,\cos\theta}, \qquad 2.7$$

where β is full width at half maximum (FWHM), and K is a constant that depends on the particle geometry (0.829 for spherical particles) [159]. Furthermore, micro-strain induces a broadening of the peak. However, equation 2.7 does not consider this contribution to the FWHM of the peak. As a consequence, Scherrer's equation gives a lower limit for the crystallite size.

In this thesis, an AXS Bruker D8 Advance diffractometer in the Bragg-Brentano configuration with Cu $K_{\alpha 1}$ radiation (λ = 1.5406 Å) was used to perform all the XRD measurements.

2.6.2 Reflection high-energy electron diffraction (RHEED)

Reflection high-energy electron diffraction (RHEED) is a technique employed to characterize the surface of crystalline materials during and after the growth. The principle is the same as in X-ray diffraction. In this case, a monochromatic beam of electrons (0 to 40 keV) is sent onto the sample. Incident electrons diffract from atoms at the surface of the sample, at specific angles, a small fraction of the diffracted electrons interfere constructively and form regular patterns on the detector. Figure 2.9 depicts two RHEED patterns acquired on a epitaxially-growth VN on MgO substrate from two different angles.

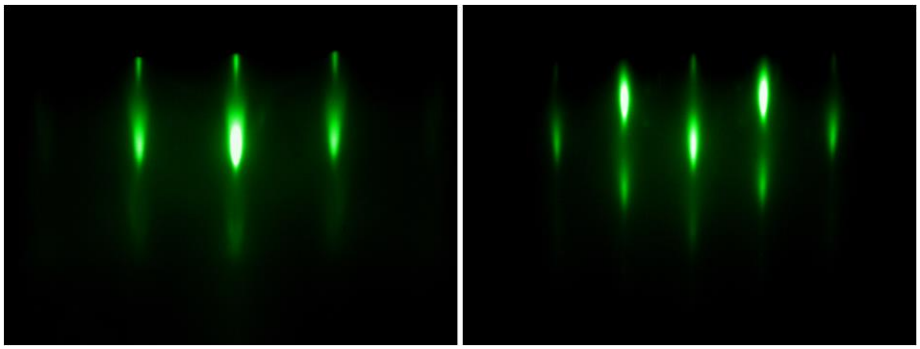

Figure 2.9 RHEED patterns recorded on an epitaxially-growth VN on MgO substrate (after a thermally degassed process at 1000°C) from two different azimuths.

To ensure the proper study of the surface's sample is mandatory to fulfill the following conditions [160]:

- the chamber must be in UHV (to avoid contamination of the studied surface),

- the electron beam hits the sample at an extremely low angle (approx. 1°) relative to the sample surface (to guarantee that diffraction occurs just at the surface of the sample).

RHEED's principal advantage over other surface techniques is the possibility to monitor the growth evolution of the sample during the deposition [160]. The initial goal of electron diffraction was to explore the surface structures and growth process of single-crystalline films (especially in Si and GaAs epitaxial growth). However, this is a quick and powerful technique to determine the crystalline order in thin films. Indeed, very different RHEED patterns are obtained for an amorphous film (continuous background)), a polycrystalline film (rings as in X-ray powder diffraction), or a single-crystalline film (pattern with straight streaks when the beam is aligned with atomic lines). Consequently, a simple look at the RHEED pattern just after the growth process allows the experimentalist to immediately determine the crystalline order range (at least qualitatively). In this thesis, a RHEED (Riber manufacturer) set-up available in the MBE chamber close to the sputtering one (in the TTO part of the TUBE) was employed to investigate the surface of the epitaxial films.

2.6.3 Raman spectroscopy

Raman spectroscopy is a non-destructive analysis technique based on the detection of inelastically scattered photons as a result of the interaction between a laser and a sample. When the electromagnetic radiation interacts with a material, the energy may be transmitted, absorbed, or scattered. Commonly, the radiation frequency of the laser is lower than the electronic frequencies but is much higher than the vibrational frequencies [161]. The rotational and vibrational energy of the molecule does not change in an elastic collision. Hence, the frequency of the scattered photon is the same as the incident photon. This phenomenon is called Rayleigh scattering, and it is by far the highest component of the scattered radiation. On the contrary, an inelastic collision between the incident photon and the material results in a change of the vibrational or rotational energy of the bonds. In this case, this phenomenon is named Raman effect. Thanks to energy conservation, there are two cases for the frequency of the scattered photon. First, the frequency of the scattered photon is smaller than the incident frequency, giving rise to the Stokes lines in the Raman spectrum. Second, the frequency of the scattered

photon is higher than the incident frequency, giving rise to the anti-Stokes lines in the Raman spectrum. At ordinary temperatures, most of the materials exist in the ground state and therefore Stokes lines have greater intensities than anti-Stokes lines which originate from an excited level with a lower population [161]. A Raman spectrum contains several bands, characteristics of each chemical compound that are employed as a "fingerprint" to distinguish one compound from another.

In this thesis, Raman spectra of samples were acquired on a Horiba Jobin-Yvon LabRAM HR800 spectrometer. The films were excited by a Nd:YAG laser (532 nm) with a spot size of around 1.5 µm. The laser beam is focused on the samples' surface using a microscope objective with a magnification of x100. The laser power (approx. 10 mW) was low enough to avoid any heating effect (such as oxidation from VO_2 to V_2O_5). Each spectrum was recorded with an acquisition time of 60 seconds.

2.6.4 Secondary ion mass spectrometry (SIMS)

Secondary ion mass spectrometry (SIMS) is a technique employed to investigate the composition of solid surfaces and thin films. It works by sputtering the studied surface with a focused energetic ion beam (commonly between ~0.1 and 50 keV). These ions (called primary ions) produce the ejection of atoms and molecules from the solid's surface, a small percentage of them are in the ionized state. The emitted ions (referred to as secondary ions) are then collected and transferred through a mass spectrometer. Figure 2.10 displays a well-simplified schema of the main components of SIMS.

This technique can identify all elements, including hydrogen. Moreover, it holds the highest sensitivity among the surface analysis methods, with elemental detection limits ranging from parts per million to parts per billion [32]. There are two distinct modes in SIMS analysis. Dynamic SIMS provides the elemental and (or) molecular distributions over numerous atomic layers (in-depth). In this mode, SIMS data are typically presented in three formats: mass spectra, spatial image, and depth profiles (Figure 2.10). Mass spectra display secondary ion intensity as a function of mass to charge ratio. Ion images show secondary ion lateral distribution. Depth profiles exhibit secondary ion intensity as a function of depth into the sample. On the other

hand, the second mode is named Static SIMS, the difference with Dynamic SIMS is that this method is only suitable for surface analysis (depth profile is not possible).

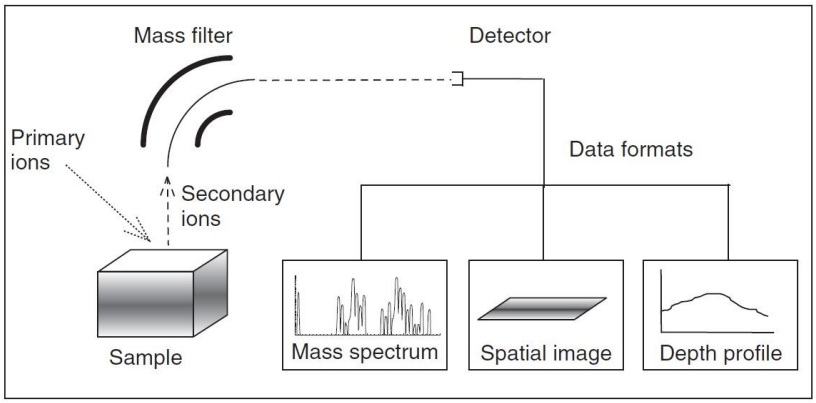

Figure 2.10 Schematic of the major components found in a SIMS instrument along with the common data output noted in Dynamic SIMS. For the sake of simplicity, the additional primary ion beams, lenses, deflectors, apertures, and secondary ion energy filters, which are present in all SIMS instruments, are not shown [162].

In this work an IMS 7F Cameca secondary ions mass spectrometry system was used to obtain the compositional profiles of the VN oxidized films as a function of depth. The instrument was configured to have Cs^+ primary ion energy of 5 keV, secondary ion energy of 2 keV, a primary beam intensity of 10 nA, a raster size of 100 μm and an analyzed area of 33 μm^2.

2.6.5 Scanning electron microscopy (SEM)

Scanning electron microscopy (SEM) is a widely employed technique to achieve high-quality topographical images of the studied material. A focused beam of high-energy electrons (accelerated by a voltage of a few kV) scans the surface of a sample. When the electrons beam hit the atoms elastic and inelastic interactions occur. The collisions produce a variety of signals: secondary electrons (SE), backscattered electrons (BSE), diffracted backscattered electrons (EBSD), characteristics X-rays, among others. Secondary electrons (from the conduction or valence band) have low energy and are generated close to the surface. Hence, these are the electrons use to achieve high-quality topographical images. On the other hand, BSE arises from a deeper region in the pear-shaped interaction volume (see Figure 2.11). The higher the atomic number of the element the higher the scattered signal. Therefore, the image from BSE displays

composition information. EBSD is used to determine crystal structures and orientations of the studied sample. Moreover, a chemical analysis (using the X-rays emitted during the interactions) could be performed if an energy-dispersive spectroscopy (EDS) system is installed in the microscope.

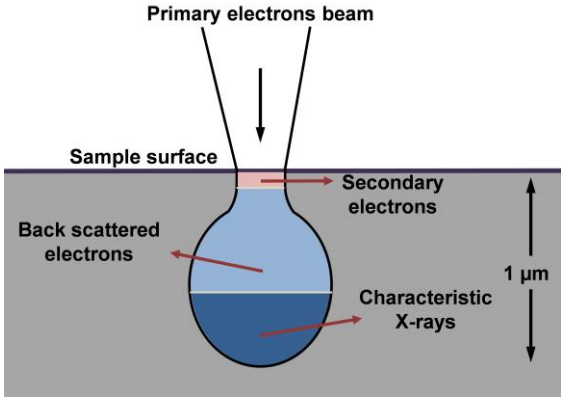

Figure 2.11 Schematic presenting components of the signals generated in pear-shaped interaction volume between the electron beam and the sample surface.

Figure 2.12 a) presents top-view SEM images of a V_2N thin film. The thickness of the films could be determined by the cross-sectional SEM images shown in Figure 2.12 b).Two microscopes were used in this work to investigate the morphology of the samples. A Philips XL-30 S-FEG scanning electron microscope was employed in chapter 4. In chapters 3, 5 and 6, samples were studied with a ZEISS GeminiSEM 500.

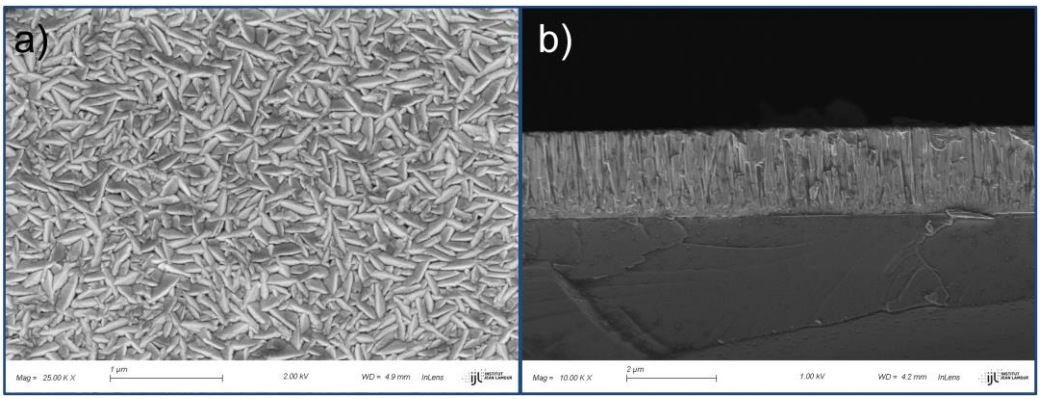

Figure 2.12 a) Top-view and b) cross-sectional images of a V_2N thin film.

2.6.6 Transmission electron microscopy (TEM)

Transmission electron microscopy (TEM) is a unique characterization technique that provides structural and microstructural information about the studied sample. A high-energy

electron beam of 80 - 200 kV is accelerated onto a thin sample (less than 100 nm). The signal collected from the transmitted electrons is used to form a 2D (high-resolution) image of the film.

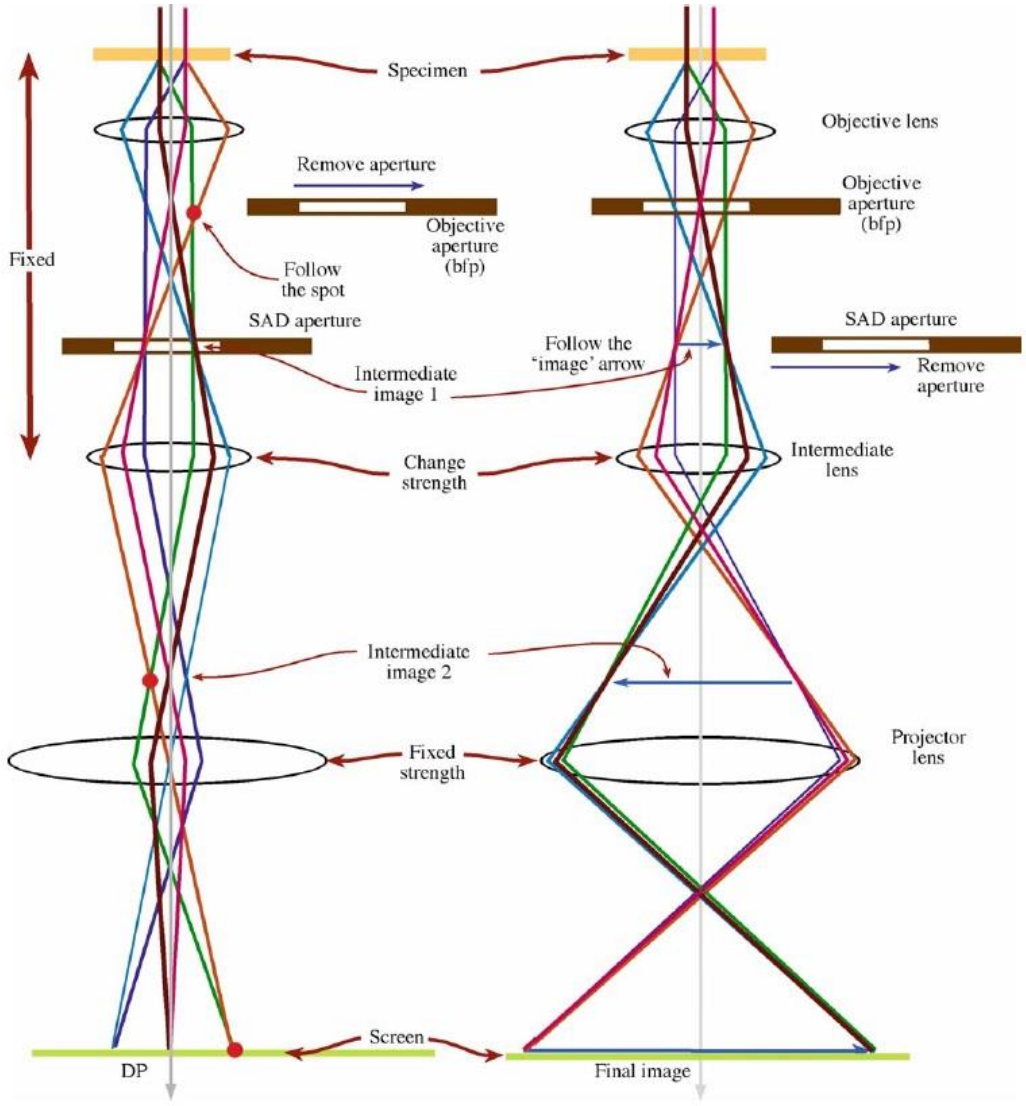

Figure 2.13 Schematic of the two basic operation modes in TEM. In diffraction mode (left) the diffraction pattern (DP) is projected onto the screen and in image mode (right) the image is projected onto the screen. In each case the intermediate lens selects either the back focal plane (left) or the image plane (right) of the objective lens as its object. Image taken from [163].

Diffraction and image modes are the two basic operation modes in TEM (Figure 2.13) [163]. In diffraction mode, the lenses are adjusted in such a way that the back focal plane of the objective lens acts as the object plane for the intermediate lens. Then the diffraction pattern presenting information about the crystalline structure of the sample is projected onto the viewing screen. Single crystals render a pattern of spots, every spot represents a specific

crystallographic plane in the direct space. In the case of polycrystalline and amorphous materials, the diffraction pattern yields a series of rings (wide and diffuse for amorphous films). A fast Fourier transform (FFT) applied to a high-resolution TEM (HRTEM) micrograph gives the same crystallographic information.

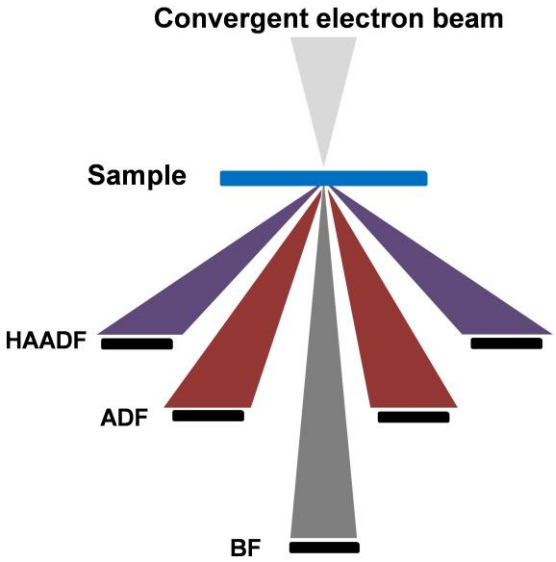

Figure 2.14 Schematic of the STEM configuration detectors, on-axis detector for BF images and off-axis annular detectors for DF images.

On the other hand, in the image mode, the intermediate lens is readjusted so that its object plane is the image plane of the objective lens. Then the image is projected onto the screen. In Scanning TEM mode (convergent beam + scan), diffused electrons are collected to form images (see Figure 2.14): bright-field (BF) and high angle annular dark-field (HAADF). BF images are obtained from the electrons that are transmitted through the sample without much deflection (close to the direct beam). Hence, brighter areas correspond to the presence of lighter elements (the electron beam does not suffer much deviation). On the contrary, darker areas correspond to heavy elements, thicker regions of the sample. In the case of the HAADF images, the image is formed from electrons that are diffused with a high angle from the optical axis of the microscope. In such circumstances, bright regions correspond to heavy elements, and also to grains that are under the selected diffraction conditions.

Electron Energy Loss Spectroscopy (EELS) is a technique associated with STEM. In EELS an electron spectrometer directly records the energy loss experienced by the electron beam incident on the sample. These energy-loss events provide information about the chemistry and

the electronic structure of the specimen atoms. These results could reveal significant sample information such as the bonding/valence state, the nearest-neighbor atomic structure, their dielectric response, the free electron density, the band gap (if there is one), and the specimen thickness [163]. Figure 2.15 a) displays a high angle annular DF image of a VN sample deposited on Si substrate. Figure 2.15 b) depicts the EELS spectra recorded in four zones (labeled from 1 to 4) of Figure 2.15 a). In the four zones there are only peaks corresponding to V (V_{L3} =513 eV and V_{L2}= 521 eV) and N (N_K =401 eV), suggesting that the sample is homogeneous.

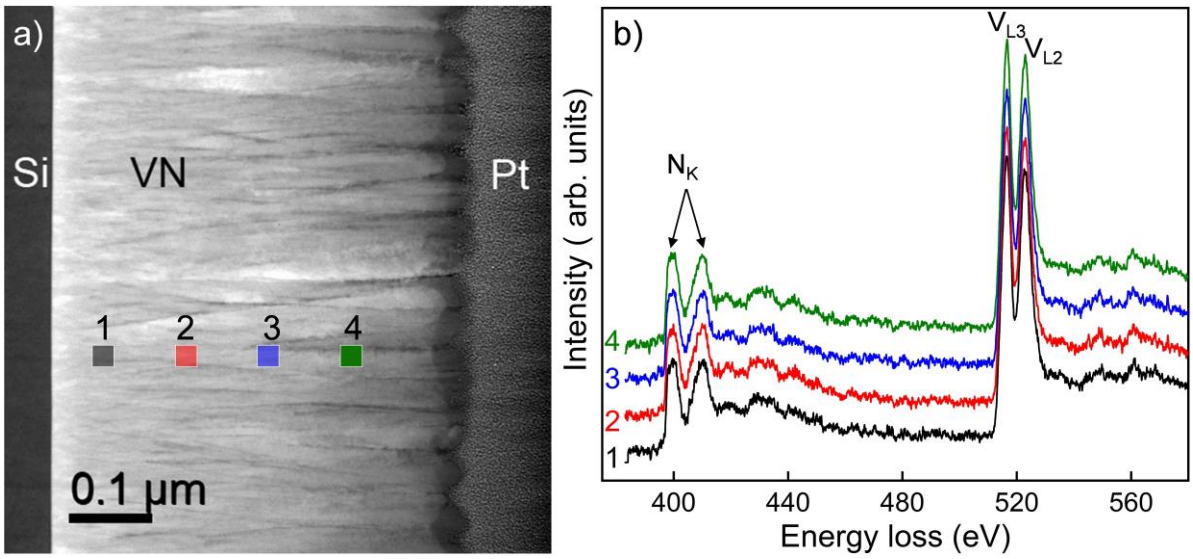

Figure 2.15 a) High angle annular dark field image of a VN sample deposited on Si substrate, EELS characterization was performed in the four zones (labeled from 1 to 4). b) EELS spectra of the four different zones of Figure 2.15 a). The color of each curve corresponds to the area of the same color where the spectrum was conducted.

In this thesis, TEM studies were carried out with a JEOL ARM 200-Cold FEG (point resolution 0.19 nm). The cross-section TEM samples were prepared by a focused ion beam (FIB)-SEM dual beam system (FEI Helios Nanolab 600i). The lift-out technique was used to obtain the samples. An acceleration voltage of 30 kV was applied during the preparation and thinning process. However, during the last step of the thinning, the acceleration voltage was reduced to 5kV, to decrease the possibility of ion implantation and amorphization. EELS experiments were performed in scanning electron transmission microscopy mode (STEM). The spectrometer was set to an energy dispersion of 0.1 eV/channel. The camera length, the pixel

time, and the diaphragm were set to 2 cm, 1 second, and 5 mm, respectively. Finally, the resolution of the full width at half maximum (FWHM) of the zero-loss peak was 0.7 eV.

2.6.7 Infrared thermal camera

One approach to characterize the thermochromic behavior of the VO_2 films is to study the difference of the optical properties with the temperature. The determination of the emissivity change from the semiconductor state to the metal state is a practical method to accomplish this task. We can define the emissivity (ε) as the ratio of the thermal radiation from a surface to the radiation from an ideal black body surface at the same temperature, therefore, ε is a value between 0 and 1.

During this thesis, we employed an infrared thermal camera[1] FLIR 325sc that yields a cumulative response in the of 7.5-13 μm range together with a Prazitherm heater system to calculate the emissivity switch of the samples. The measurements were taken in the 30-120°C range, with approximately 55 cm between the camera and the sample. The camera forms an angle of around 57° relative to the sample surface. The IR camera provides the measure of the infrared temperature (T_{IR}) of the sample while the heater gives the actual temperature of the sample (T_S).

To calculate the emissivity, we follow the procedure employed by Benkahoul *et al*. [84]:

$$\varepsilon = \varepsilon_{ref} \frac{T_{IR}}{T_S}, \qquad 2.8$$

where ε_{ref} represents the emissivity of a blackbody reference. It is relevant to note that we do not have a proper blackbody reference in the 30-120°C range. For this reason, we will use throughout the entire thesis $\varepsilon_{ref} = 1$.

[1] An infrared camera is a device that creates an image using infrared radiation, similar to a common camera that forms an image using visible light. However, infrared cameras are sensitive to wavelengths from 1-14 μm. A major difference with optical cameras is that the focusing lenses cannot be made of glass, as glass blocks long-wave infrared light. The main components are a lens that focuses IR onto a detector, plus electronics and software for processing and displaying the signals and images.

Figure 2.16 displays T_{IR} versus T_S during heating and cooling for a VN film on Si substrate oxidized 25 minutes at 450 °C. The emissivity at low temperature (ε_{LT}) and high temperature (ε_{HT}) was calculated from the slope of the temperature measured using the IR camera as a function of the real temperature of the sample (equation 2.8). These values serve to calculate the emissivity change ($\Delta\varepsilon$) and thus to evaluate the thermochromic performance. The highest the $\Delta\varepsilon$ the better the thermochromic properties.

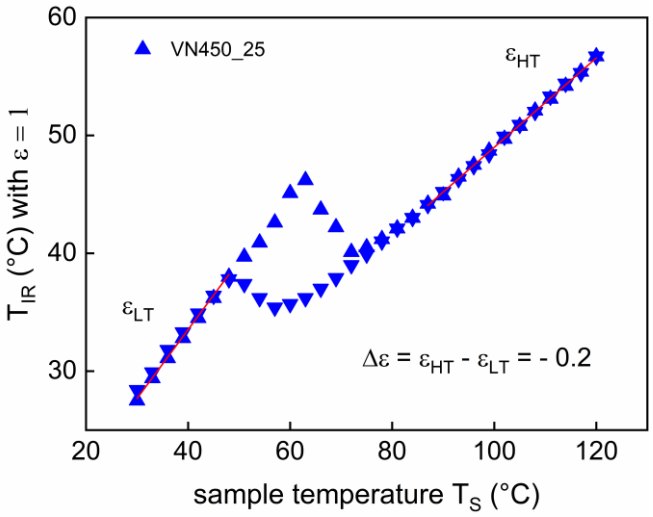

Figure 2.16 Thermal camera measurements of apparent infrared temperatures (T_{IR}), as a function of sample temperature (T_S) for a VN film on Si substrate oxidized 25 minutes at 450°C. Up and down triangles represent the profiles for temperature ramping up and down, respectively. The red lines obtained by a linear fitting in the low temperature (LT) and high temperature region (HT) enabled the determination of emissivity values before and after MIT.

2.6.8 Four-point probe method

A four-point probe is a technique to measure the resistivity of a material. It consists of four in a line equidistant electrical probes (Figure 2.17). It operates by applying a current (I) on the two outer probes and measuring the resultant voltage drop (ΔV) between the two inner probes. In this configuration, the wire resistances and the contact resistances do not contribute to the measurement. This is an advantage for the precise measurement of low resistance values. The sheet resistance (SR) is determined by:

$$SR = C\frac{\Delta V}{I}, \qquad 2.9$$

where C is a geometry constant. When the thickness of the sample (t) is significantly smaller than the distance between the probes, $C = 4.53$. If the thickness is known, the resistivity (ρ) can be calculated by $\rho = SR * t$.

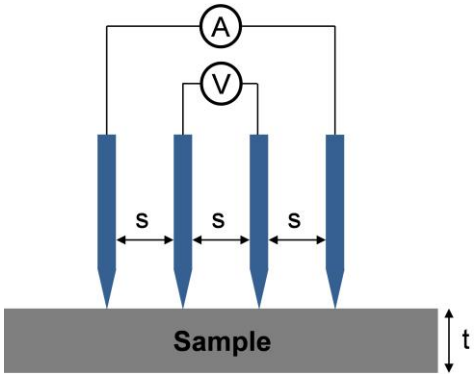

Figure 2.17 Schematic of the four-point probe method.

In this work, we coupled a Linkam® HFS600E heating plate with a Jandel four-point probe head (spacing (S) of 1 mm between the probes) to study the dependence with the temperature of the electrical properties of the samples. This configuration allows us to sweep a range of temperatures ranging from 30 to 120°C while measuring the sheet resistance of the films. For instance, Figure 2.18 displays the dependence of SR with temperature for a VO_2 obtained after the oxidation of a VN film for 25 minutes at 450°C. It is clearly shown the change in electrical properties when the VO_2 undergoes the phase transition.

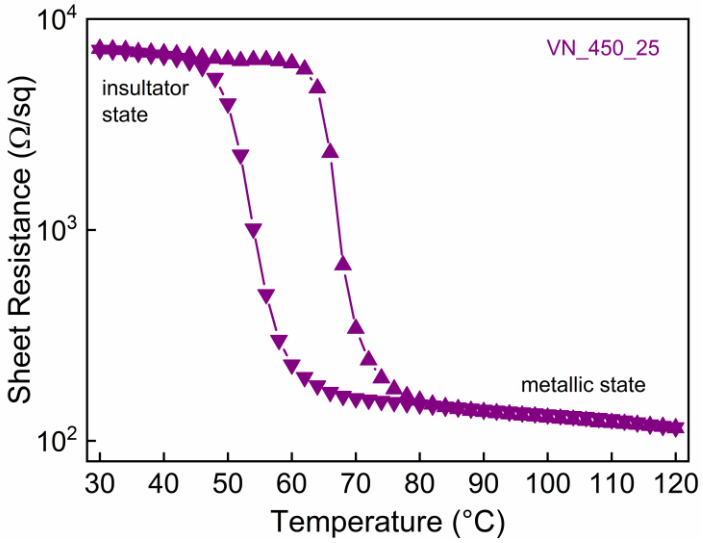

Figure 2.18 Sheet resistance (SR) as a function of the temperature for an oxidized VN films deposited on silicon substrate at 450 °C during 25 minutes.

2.7 Chapter conclusions

In this chapter, we have depicted the essential features of the magnetron sputtering technique. We have also displayed the principal characteristics of both sputtering reactors employed and the growth conditions of the deposited films. Furthermore, we have described the characterization techniques utilized throughout the thesis and detailed the parameters used for each procedure. In the coming chapters, we will present the main results of the work, for instance, chapter 3 will be dedicated to the effect of the oxidation duration on the thermochromic performance of VO_2 obtained by the oxidation of VN thin films in the semi-industrial machine.

Chapter 3

Oxidation of sputter-deposited vanadium nitride as a new precursor to achieve thermochromic VO_2 thin films

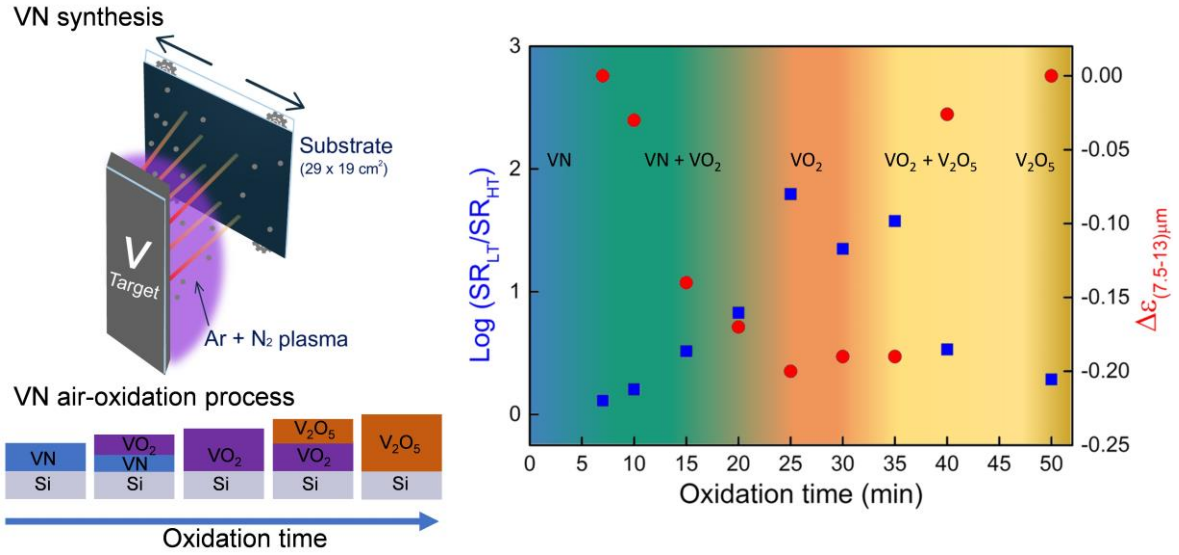

Abstract

In this chapter, we propose vanadium nitride (VN) as a new precursor to obtain thermochromic VO_2. VN films were reactively sputter-deposited on Si substrates by using an in-line semi-industrial machine. The films of 175 nm thickness were submitted to an air-annealing process implemented at different durations at 450°C. X-ray diffraction and Raman spectrometry were performed for structural characterizations of the oxidized films showing the presence of monoclinic VO_2 in a wide range of oxidation time. As the annealing time increased, V_2O_5 appeared to affect the performance of the oxidized films. The TEM analysis carried out on the oxidized sample for 25 minutes showed that there is an abrupt interface between VN and VO_2. The thermal-induced properties of the studied films were analyzed in terms of their electrical resistance employing a four-point probe method and their emissivity modulation properties by infrared camera. The results showed a thermochromic behavior for the samples oxidized in the range of 15-35 min. On the contrary, the presence of residual VN layers in samples oxidized for less than 15 min and V_2O_5 in the ones annealed for more than 35 min hindered the

thermochromic behavior of these films. Bringing together all the characterization techniques used a phase diagram of VN oxidation was plotted.

Contents

3.1 Introduction

In 1959, Morin demonstrated that vanadium dioxide (VO_2) exhibits a reversible metal-insulator transition (MIT) approximately at T_{MIT} = 68°C [74]. At low temperature, VO_2 behaves as a semiconductor with a monoclinic structure, high transmittance in the infrared region and high electrical resistivity, while at temperatures higher than T_{MIT} a transition to a metallic tetragonal rutile structure occurs and VO_2 exhibits low transmittance and low electrical resistivity. The change of these properties during the phase transition of VO_2 makes this material convenient for several applications, such as infrared modulation in smart windows [164–170], thermal solar collectors [90,171], dynamic thermal control of spacecraft [84,93–95], ultrafast electronic devices [172,173] and many others. Although the research on this material has been carried on for several decades, the synthesis of VO_2 films with good thermochromic properties on large surfaces still remains a challenge. The reason behind this defiance is the imperative need to avoid several other phases in the vanadium-oxygen system [174].

Magnetron sputtering is one of the most used methods to produce VO_2. Among the different approaches to obtain VO_2, reactive sputtering in a mixture of Ar and O_2 without a post-annealing process is one of the most used [84,108,110,111,175,176]. However, the need to properly control the O_2 flow rate makes this method not suitable on large surfaces. On the other hand, a post-annealing process in air or oxygen is commonly used to improve the quality of the deposited films [116–118]. Other interesting and simple proposals are the so-called sputtering oxidation coupling (SOC) method and the thermal oxidation method. These are a two-stage procedures, in which a vanadium film is deposited and then annealed in a furnace outside of the deposition chamber [123,125]. The possibility to regulate the temperature and duration during the oxidation process makes this method suitable and attractive for the industrial process.

In this work, we chose to modify these two-stage procedures using an original precursor: vanadium nitride (VN). At room temperature, the NaCl-like structure of the VN phase is more resistant to oxidation than the body-cubic centered of the V one [177,178]. Besides, several studies have shown that the oxidation of VN at elevated temperatures resulted in the formation of a series of vanadium oxides, which significantly improved the tribological properties of the

film [179,180]. Nevertheless, to the best of our knowledge, controlled oxidation of VN has never been performed to produce thermochromic VO_2.

In this chapter, VN thin films are reactively sputter-deposited on Si substrates by using an in-line semi-industrial machine. A second step consists of air-oxidation of the VN films to form vanadium oxide films. The as-deposited VN films are annealed under atmospheric pressure at 450°C during different durations 7, 10, 15, 20, 25, 30, 35, 40 and 50 minutes. The films are labeled "VN" for as-deposited vanadium nitride films and "VN_time" for the oxidized films for various annealing durations. The air-oxidation conditions of these films have been optimized. The results will indicate that VN is an interesting new precursor to synthesize high-quality thermochromic VO_2 films.

3.2 Microstructure and morphology of oxidized samples

The X-ray diffractograms for as-deposited and air annealed VN films deposited on silicon are shown in Figure 3.1 (the deposition conditions of the VN films are described in Chapter 2). VN films (175 nm thick) exhibit two diffraction peaks located at approx. 37.9° and 80.3° corresponding to (111) and (222) planes of the face-centered cubic VN structure (PDF no.00-035-0768), respectively. No other peak is detected except those of silicon substrate. Figure 3.1 also presents diffractograms for the films after air-annealing at 450°C during different durations in the 7-50 min range. For the lowest duration, the monoclinic VO_2 phase is not detected. However, the intensity of the VN peaks diminishes, which indicates that the oxidation process has effectively begun. In addition, these peaks are shifted to higher angles because of stress relaxation during the oxidation process. As the annealing time increases, the VN peaks intensity decreases even more and the main (111) peak is noticed up to 25 min, indicating the presence of a remaining layer of vanadium nitride. Monoclinic VO_2 is detected for the first time after 10 min of air oxidation. The most significant peaks corresponding to m-VO_2 are located at 2θ = 37.1, 42.3 and 72.1° (PDF no. 04-003-2035), showing that the oxide layer corresponds to an equiaxed structure (i.e. that it does not grow with a strong preferred orientation). The most intense peak of VO_2 appears at 30 min of oxidation and the VN peak completely disappears at the same time. In this sample (VN_30), two new peaks with a low intensity corresponding to

orthorhombic V_2O_5 phase are detected (PDF no. 00-041-1426). For oxidation times higher than 30 min, the peaks corresponding to VO_2 decrease in intensity while the opposite occurs with the peaks of V_2O_5. For the VN_50 sample, the VO_2 vanishes, leading to the V_2O_5 being the only crystalline phase present. These results show oxidation from V^{4+} state to V^{5+} state as the oxidation time increases and are consistent with the findings of several authors [118,181].

Due to the overlapping of the diffraction peaks of the various vanadium oxide phases, X-

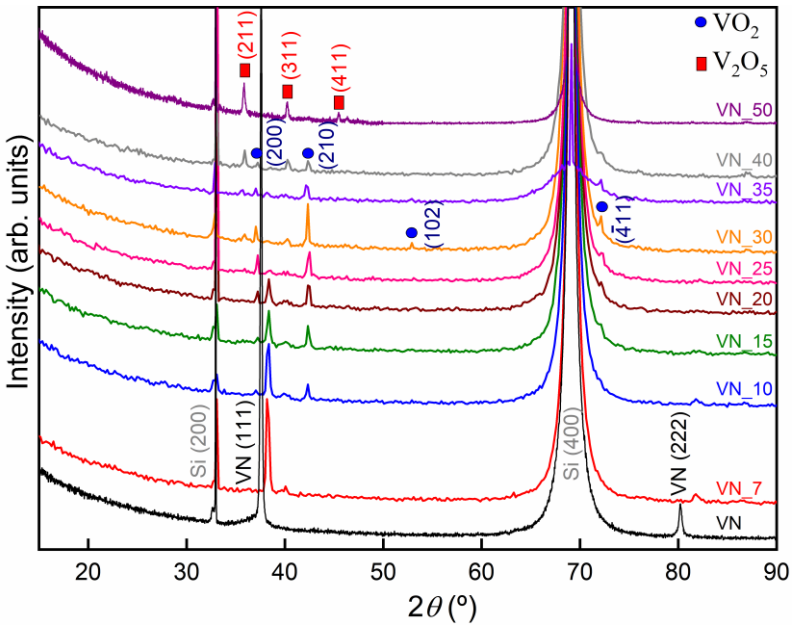

Figure 3.1 X-ray diffractograms of as-deposited VN film on silicon substrate and the resulting oxide films after air-oxidation at 450°C for various durations.

ray diffraction is not the most powerful method to evince the formation of a pure VO_2 phase. To verify the formation of VO_2, cross-examination with Raman spectrometry is carried out for all oxidized films. Figure 3.2 presents room-temperature Raman spectra of the oxidized VN films, deposited on silicon substrates.

The Si substrate signal (520.7 cm^{-1}) is barely visible until 10 min of oxidation, thanks to the presence of the VN film that exhibits metallic behavior. As the oxidation time increases the Si signal becomes more perceptible indicating a decrease of the VN layer thickness. From sample VN_25, the peak at 520.7 cm^{-1} is intense; suggesting that the sample is almost completely oxidized, as shown by XRD. Thus, the evolution of the Si Raman band is a powerful tool to monitor the VN oxidation.

Oxidized samples in the range of 10 to 25 min show relatively similar vibration bands, with most of the peaks (located at approx. 192, 223, 264, 296, 331, 389, 499 and 622 cm^{-1}) assigned

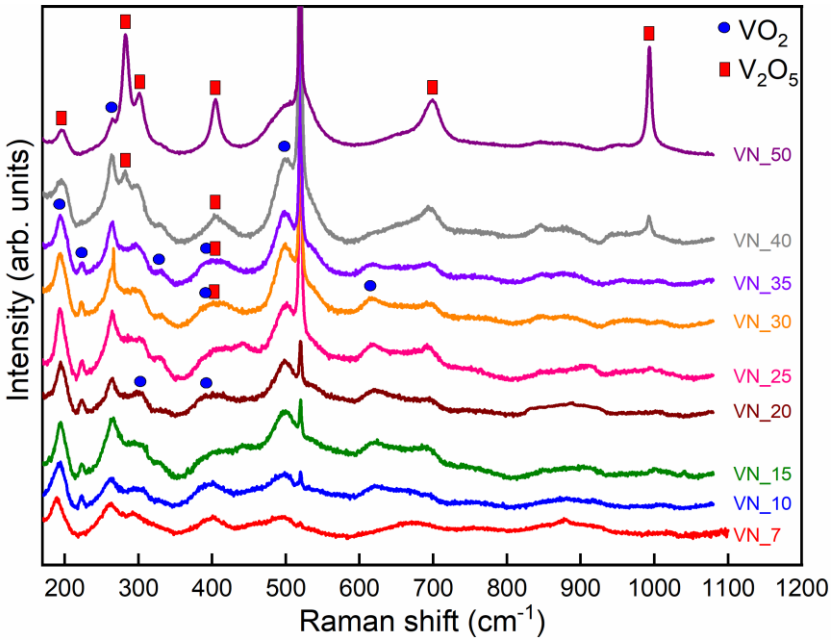

Figure 3.2 Raman spectra of air-oxidized VN films at 450°C for various durations.

to m-VO_2 phase, in accordance with literature data [182–185].

In the case of the oxidized films during 40 and 50 minutes, the shape of the spectra is different from the other samples. The vibration bands detected at approx. 195, 284, 303, 405, 528, 701 and 992 are readily assigned to the V_2O_5 phase [182,186].

The simultaneous presence of VO_2 and V_2O_5 is detected by X-ray diffraction results in oxidized samples between 30 and 40 min. Although several bands may overlap, it is difficult to notice a big change in the spectrum of these samples. However, one can notice a slight shift of the band located at 389 cm^{-1} (VN_20 sample) until reaching 405 cm^{-1} (VN_40 sample). The Raman results confirm the formation of VO_2 and V_2O_5 as shown by the X-ray results.

Figure 3.3 shows the top view SEM images of six relevant samples: the as-deposited VN films and samples oxidized during 10, 20, 25, 30 and 50 min, respectively. The VN film exhibits a surface morphology with small pyramidal-shaped grains in agreement with the [111] preferred orientation observed by XRD. Throughout the oxidation process, a drastic change in the morphology of the samples is noticed when compared to as-deposited VN films. After 10 minutes of oxidation (Figure 3.3 b)), the surface changes and the pyramidal-shaped grains of

VN are not perceived anymore. The oxidized VN grains coalesce into an elongated structure, increasing grain size. As oxidation continued, the morphology of the samples does not change significantly and the grain size continues to grow. In all the images, the grain boundaries are clear and well defined.

Figure 3.4 a) shows transmission electron microscopy micrograph for the VN_25 sample. The figure displayed that there is no well-defined shape for the "supposed" VO_2 grains (two

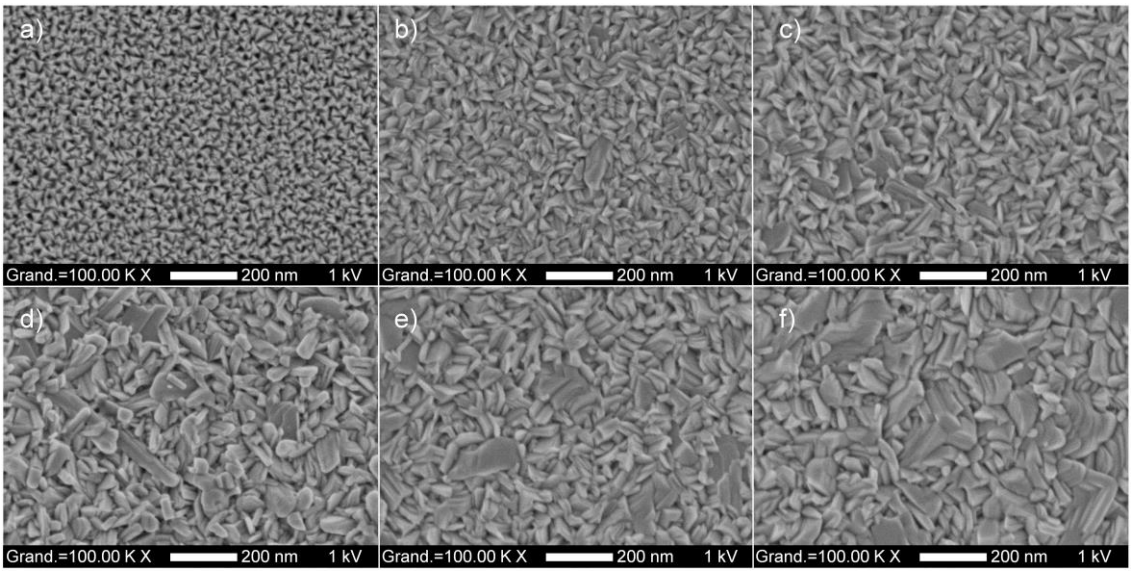

Figure 3.3 Top-view SEM images corresponding to a) the as-deposited VN films and sample oxidized during 10, 20, 25, 30 and 50 min for b), c), d), e) and f) respectively.

regions with different morphologies) and there is still residual VN, as observed in XRD. Moreover, the presence of vanadium nitride is not continuous on the surface of the sample. To check the presence of VO_2 in the sample, a high-resolution TEM (HRTEM) micrograph with the corresponding fast Fourier transform pattern (FFT) investigation is conducted in the area enclosed in red in Figure 3.4 a) and Figure 3.4 b), respectively. It was possible to identify the (111), (010) and (101) planes of VO_2. The obtained interplanar distances are 0.229, 0.452 and 0.484 nm for the (111), (010) and (101) planes, respectively, in agreement with those reported for monoclinic VO_2 (PDF no. 04-003-2035).

From Figure 3.4 one cannot discern whether areas with different colors and shapes belong to the same compound. To better elucidate this, an EELS characterization is performed in a region of the sample where VN and VO_2 coexist (Figure 3.5 a)). The high angle annular dark

field image shows different morphologies and colors. VN with a columnar structure is evidenced close to the substrate. The region adjacent to the VN presents a light gray color and an almost rectangular shape; it was already proved that corresponds to VO_2. On the other hand, the region close to the film surface has a dark grey color and contains elongated grains. These grains present two pronounced differences concerning the morphology of the VN: they are thicker and are not perpendicular to the substrate, indicating that during the oxidation process a coalescence of the oxide grains occurs.

EELS spectra are recorded in four zones (labeled from 1 to 4) of Figure 3.5 a), the results are shown in Figure 3.5 b). In zone 1 there are only peaks corresponding to V (V_{L3} = 513 eV and V_{L2} = 521 eV) and N (N_K = 401 eV), confirming the presence of a remaining vanadium

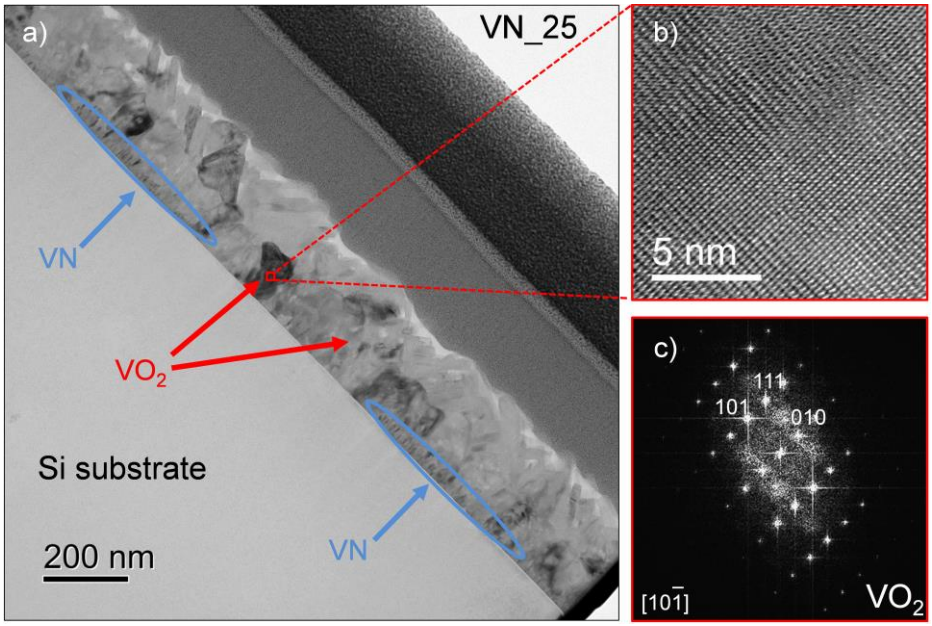

Figure 3.4 a) TEM cross-sectional image of sample VN_25. b) HRTEM image of the highlighted red area in Figure 3.4 a). c) FFT from the region of Figure 3.4 b)

nitride layer. It is important to notice that region 3 is at the interface between the areas with different shapes and intensities of grey. In zones 2, 3 and 4 the spectra are very similar. Since the ratio of the V/O peaks intensity and as well as the peak position are constant, the zones labeled 2, 3 and 4 seem to contain the same oxide phase that corresponds to VO_2.

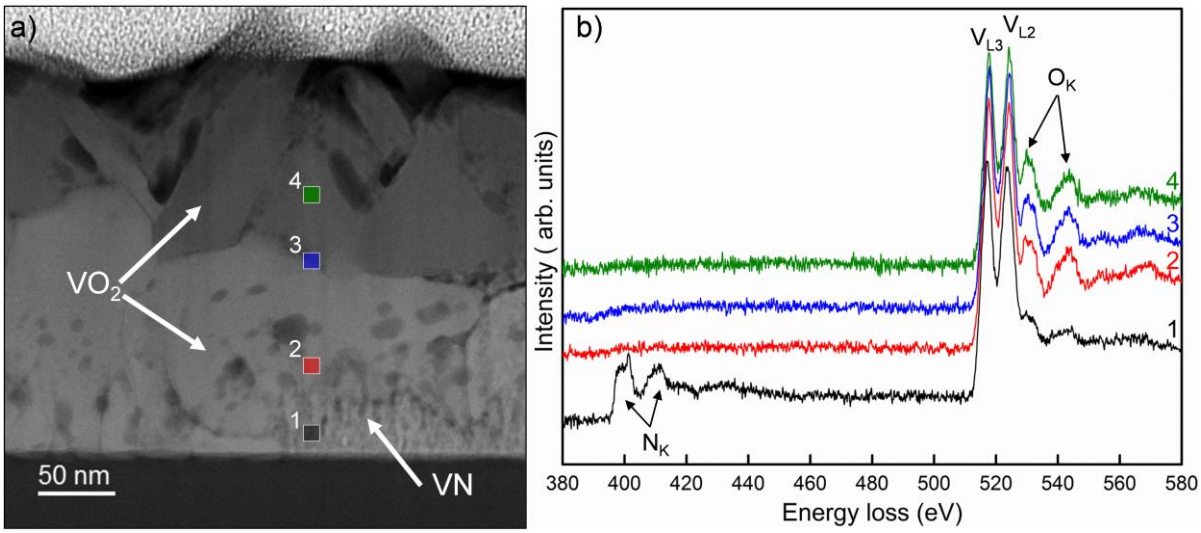

Figure 3.5 a) High angle annular dark field image of the sample VN_25, EELS characterization was performed in the four zones (labeled from 1 to 4). b) EELS spectra of the four different zones of Figure. 3.5 a). The color of each curve corresponds to the area of the same color where the spectrum was conducted.

3.3 Optical and electrical properties of oxidized samples

Near the MIT transition of VO_2, some physical properties present a hysteresis between the heating and cooling cycles. Within these properties, changes in electrical resistivity and emissivity at low and high temperatures are considered as indicators of VO_2 quality [107,126,187]. The higher the difference, the better the thermochromic properties.

For all oxidized samples, the optical modulation properties in the infrared (IR) domain are studied using an infrared camera. Figure 3.6 represents apparent infrared temperature (T_{IR}) of samples monitored versus the sample temperature (T_S) during both, heating and cooling for the studied films. All the films in Figure 3.6 exhibit hysteresis loops near the MIT region. Samples oxidized for 10 minutes or less show no representative thermochromic behavior ($\Delta\varepsilon_{VN_{10}} = -0.03$). This is due to the presence of a considerable residual layer of VN. Figure 3.7 presents a cross-section SEM image of the VN_10 sample. Two different layers are evidenced. On the silicon surface substrate, a thick residual layer of VN is covered by the VO_2 one. This image proves that at 10 min, the oxidation is not complete, indicating that higher oxidation time is needed to observe a thermochromic behavior. Furthermore, a thermochromic effect is not observed for samples oxidized for a duration longer or equal to 40 min, $\Delta\varepsilon_{VN\_40} = -0.03$. In

this case, this is attributed to the increased formation of the V_2O_5 phase with oxidation time. On the contrary, for samples oxidized in the range of 15 and 35 minutes, a thermochromic behavior with values of $\Delta\varepsilon$ between -0.14 and -0.20 is evidenced, confirming the presence of m-VO_2 consistent with XRD and Raman results.

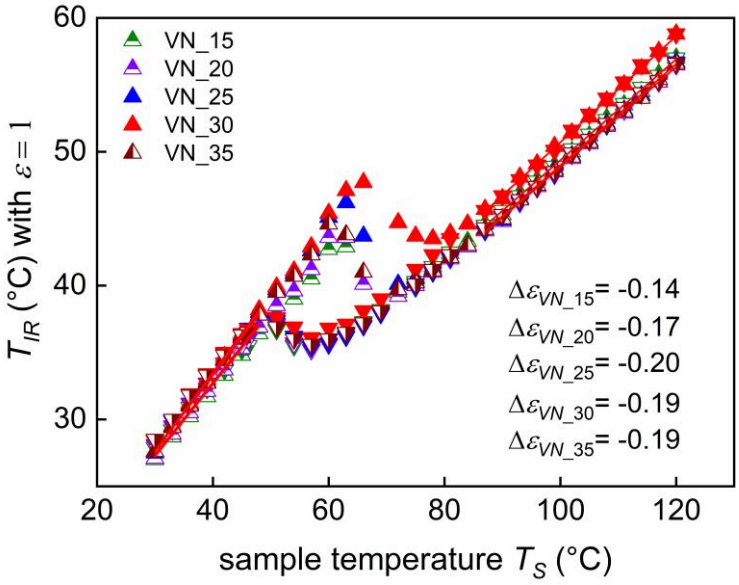

Figure 3.6 Thermal camera measurements of apparent infrared temperatures (T_{IR}), as a function of sample temperature (T_S) for VN films oxidized between 15 and 35 minutes. Measurements are carried out by considering $\varepsilon = 1$ irrespective to the sample. Up and down triangles represent the profiles for temperature ramping up and down, respectively. The red lines obtained by a linear fitting in the low temperature (LT) and high temperature region (HT) enabled the determination of emissivity values before and after MIT.

Nevertheless, the emissivity contrast obtained from our samples is lower than that reported in the literature. For example, Benkahoul et al. found $\Delta\varepsilon = -0.36$ in 300 nm thick VO_2 film deposited on Si [84]. Emissivity switching properties can be improved by doping [90,95,164], or thickness changes [111,188]. Moreover, modifying the temperature and duration of the air-annealing process could play a significant role in the optical properties of the oxidized films. Figure 3.8 a) (Figure 3.8 b)) displays the optical modulation properties for identical raw VN films oxidized at 550°C between 2.5 and 4.5 minutes (at 525°C between 4 and 7 minutes). The experiment was performed under the same conditions that Figure 3.6 and the films were labeled "VNtemperature_time" for the oxidized films for various temperature and annealing durations.

The maximum value of the emissivity switch for the three oxidation temperatures (450, 525 and 550°C) is different. The highest value of $\Delta\varepsilon$ in the oxidized sample at 525°C (550°C) increased by 25% (45%) when compared to the highest value in the oxidized sample at 450°C. These results confirm the influence of this parameter on the thermochromic performance. In the next chapter, we will discuss in more detail the relationship between oxidation parameters and the optical properties of oxidized samples.

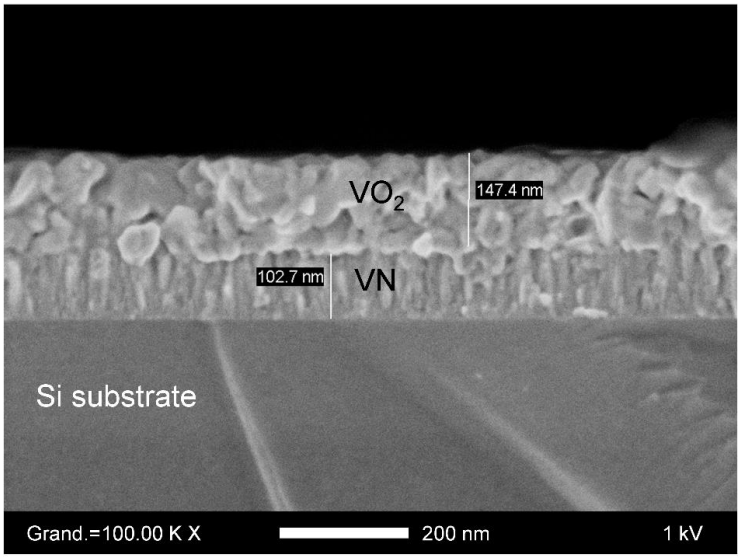

Figure 3.7 SEM cross-section image for the sample VN_10. Two different layers are evidenced. On the silicon surface substrate, the remaining VN layer is covered by the VO_2 one. This image shows an thick residual layer of VN, proving that at 10 min the oxidation is not complete.

Figure 3.9 shows the evolution of the sheet resistance (SR) as a function of the temperature for oxidized samples at 450°C during both heating and cooling. In this study, sheet resistance is calculated rather than the resistivity, due to the presence of the remaining metallic VN layer for films oxidized for less than 25 minutes. Up and down triangles in Figure 3.9 represent the profiles for temperature ramping up and down, respectively. The samples oxidized during 7 and 50 min do not evidence any hysteresis. For the low time oxidation duration (7 minutes) there is no remarkable change between low and high temperatures sheet resistance values, this is due to the presence of a remaining layer of VN. On the other hand, the sample oxidized for a long duration (50 minutes) displays no sign of VO_2, only V_2O_5.

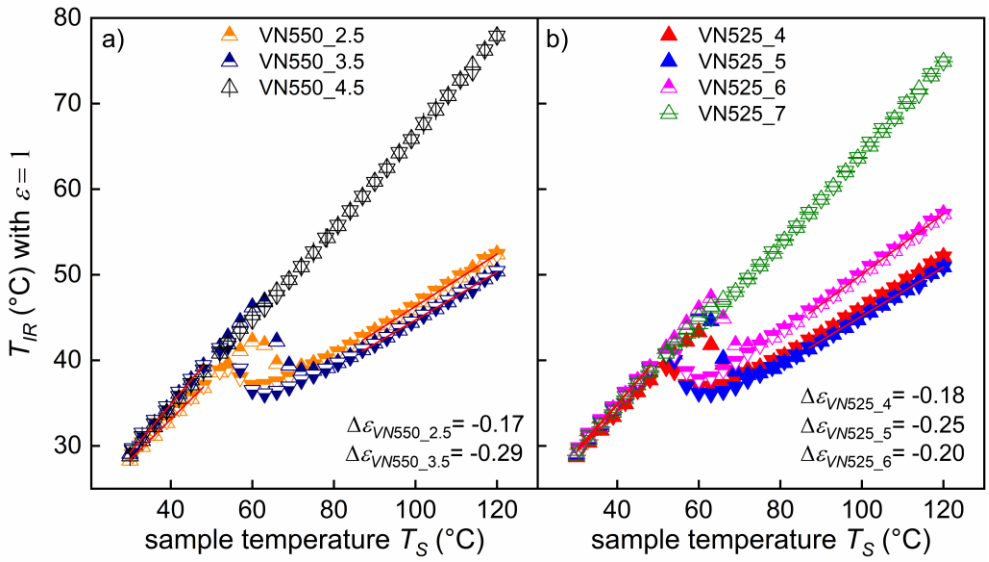

Figure 3.8 Thermal camera measurements of apparent infrared temperatures (T_{IR}), as a function of sample temperature (T_S) for samples oxidized between a) 2.5 and 4.5 minutes at 550°C and b) 4 and 7 minutes at 525°C. Measurements were carried out by considering an emissivity equal to 1 irrespective to the sample. The films were labeled "VNtemperature_time" for the oxidized films for various temperature and annealing durations.

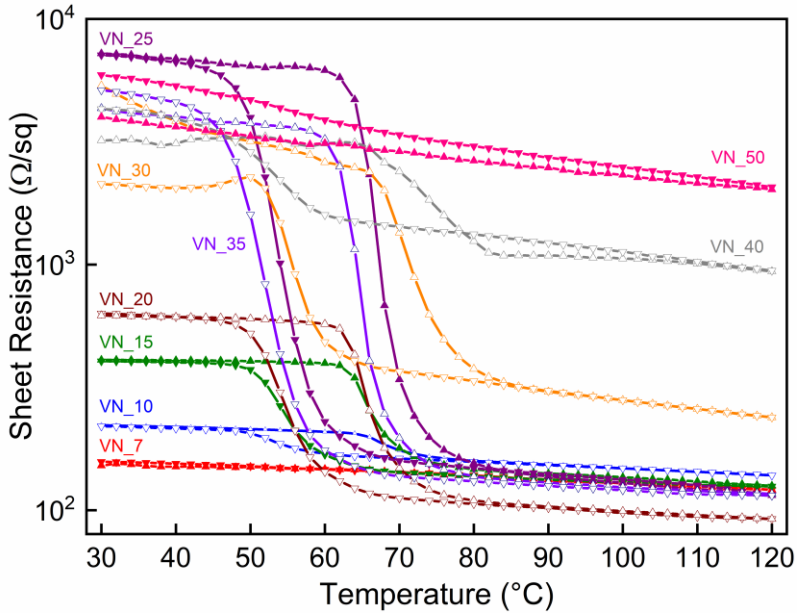

Figure 3.9 Sheet resistance (SR) as a function of the temperature for all oxidized VN films deposited on silicon substrate at 450°C.

All other studied samples exhibit hysteresis loops in the near MIT region with different magnitudes: from a feeble smoothed hysteresis for VN_10, that rises to maximum marked hysteresis curves for VN_25 and then decreases again until an almost imperceptible hysteresis

for VN_50. The enlarging presence of V_2O_5 in the samples oxidized for more than 25 minutes, is the reason for the reduction of the difference between the values of sheet resistance at low and high temperatures. These hysteresis loops are an intrinsic feature of thermochromic VO_2 MIT and, again confirm the XRD, Raman and IR thermometry results for the series of studied samples.

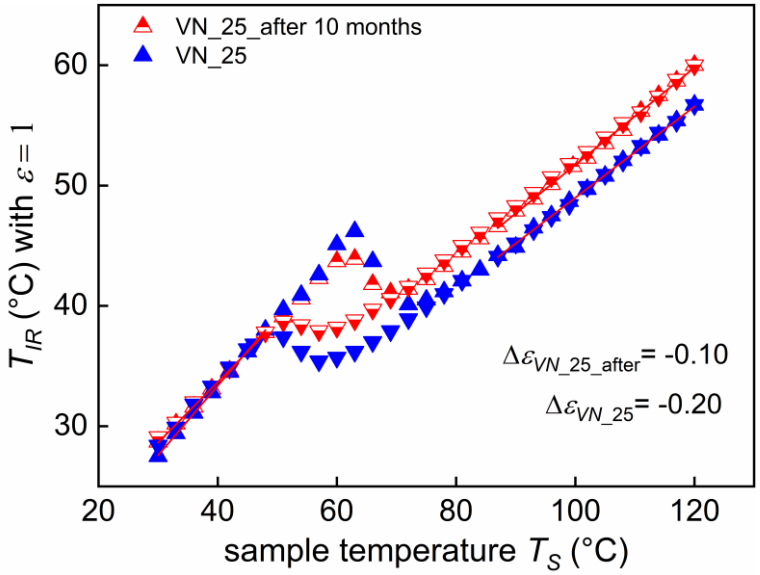

Figure 3.10 Thermal camera measurements of apparent infrared temperatures (T_{IR}), as a function of sample temperature (T_S) for VN film oxidized during 25 minutes at 450°C. The experiment was conducted on the same sample 10 months later.

The thermochromic behavior of oxidized samples will be affected if they remain exposed to air-open contact because the oxidation process continues. Infrared camera measurements of the oxidized sample 25 minutes at 450°C were repeated 10 months later, showing a significant decrease (50%) in the absolute value of the emissivity switch (Figure 3.10). Measurements were performed under the same conditions, aimed to examine the performance of the samples after prolonged air open contact. To protect the films for further and undesired oxidation anti-reflective layers such as TiO_2 [189,190], SiO_2 [191], AZO [192] and SiN_x [193] are used.

3.4 Phase diagram of VN oxidation at 450°C

Gathering the results of XRD and Raman, as well as the study of optical and electrical properties, it is possible to obtain a phase diagram of VN oxidation [194].

In Figure 3.11 is displayed on the left axis (blue squares) the logarithm of the ratio between the sheet resistance at low (SR_{LT}, measured at 30°C), and at high temperatures (SR_{HT}, measured at 120°C) as a function of the oxidation time for all the oxidized samples. The right axis (red circles) of the same figure shows the dependence of the emissivity switch with the oxidation time for all studied samples.

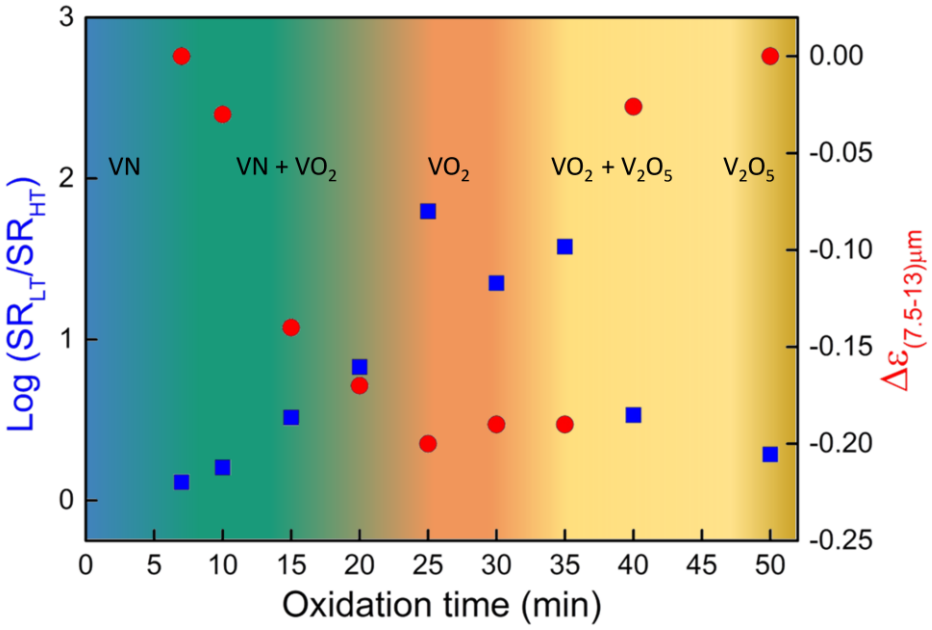

Figure 3.11 Logarithm of the ratio of sheet resistance at low and high temperature (left axis, blue squares), emissivity switch (right axis, red circles) as a function of oxidation time. We used a color gradient to illustrate the different five regions for the structure of oxidized films at 450 °C.

A color gradient is used in Figure 3.11 to illustrate the five different regions that exist in the oxidation of VN at 450 °C. The first region is a VN predominant zone. As the oxidation time progresses, a region with the coexistence of VN and VO_2 appears. By increasing the annealing duration in this region, the ratio between SR_{LT} and SR_{HT} (the emissivity switch) increases (decreases) due to the competing effect of VO_2 formation with simultaneous VN degradation. During the interval between 25 and 30 min, there are the best thermochromic properties due to the almost complete oxidation of VN, where VO_2 is the predominant compound. Beyond 30 min, the amount of VO_2 declines and begins the formation of V_2O_5. Continuing with the oxidation process in this region, thermochromic performance decays as the amount of VO_2 diminishes while the presence of V_2O_5 rises. This reduction of thermochromic behavior is

evident at 40 min of oxidation. Finally, as oxidation time continues to increase, there is a region where V_2O_5 is the only compound because of the over-oxidation of the samples.

3.5 Chapter conclusions

This chapter provides an initial insight into the air-controlled oxidation of VN films deposited on Si substrates. We reveal, for the first time, that VN is a new efficient precursor to achieve a high-quality monoclinic VO_2 using a two-step procedure.

During the oxidation process at 450 °C, there are only two phases corresponding to the V-O system, VO_2 and V_2O_5. The first oxide formed is VO_2, several techniques (XRD, Raman, IR thermometry and four-point probe method) allow us to confirm that m-VO_2 is present in numerous samples oxidized between 10 and 40 min. Furthermore, V_2O_5 is only detected after the total oxidation of VN. The amount of V_2O_5 presents on the samples increases with the oxidation time (after 30 min) and affects the thermochromic performance of the oxidized films. After 50 min of oxidation, the only phase identified is V_2O_5 and not thermochromic conduct is perceived.

On the other hand, the best thermochromic behavior is accomplished in the oxidized samples in the range between 25-35 min. However, it is important to point out that in these samples two phases coexist:

1- VN and VO_2 in the sample VN_25,

2- VO_2 and V_2O_5 in samples VN_30 and VN_35.

In both cases, VN and V_2O_5 represent a small fraction compared to the VO_2 content. Therefore, we could expect to obtain a sample with only VO_2 in the range between 25-30 minutes of oxidation, which could present a better thermochromic behavior.

The TEM analysis performed on the oxidized sample for 25 minutes shows that there is an abrupt interface between VN and VO_2.

Finally, a phase diagram of VN oxidation is displayed showing the formation of the different phases as a function of the oxidation time at 450°C. These results are the first indication that during the VN oxidation process, several phases can coexist. Hence, the

importance of optimizing the annealing duration to obtain thermochromic vanadium dioxide is verified, in correspondence with previous studies of oxidation of vanadium films.

In this chapter, the oxidation of VN films was performed at one specific temperature (450°C). Furthermore, the first findings of optical modulation properties for films oxidized at 525 and 550°C are revealed. In the next chapter, we will study the effect that could have three different oxidation temperatures on the optical properties of the oxidized films deposited on Al substrates.

Chapter 4

Surface morphology-optical properties relationship in thermochromic VO_2 thin films obtained by air oxidation of vanadium nitride

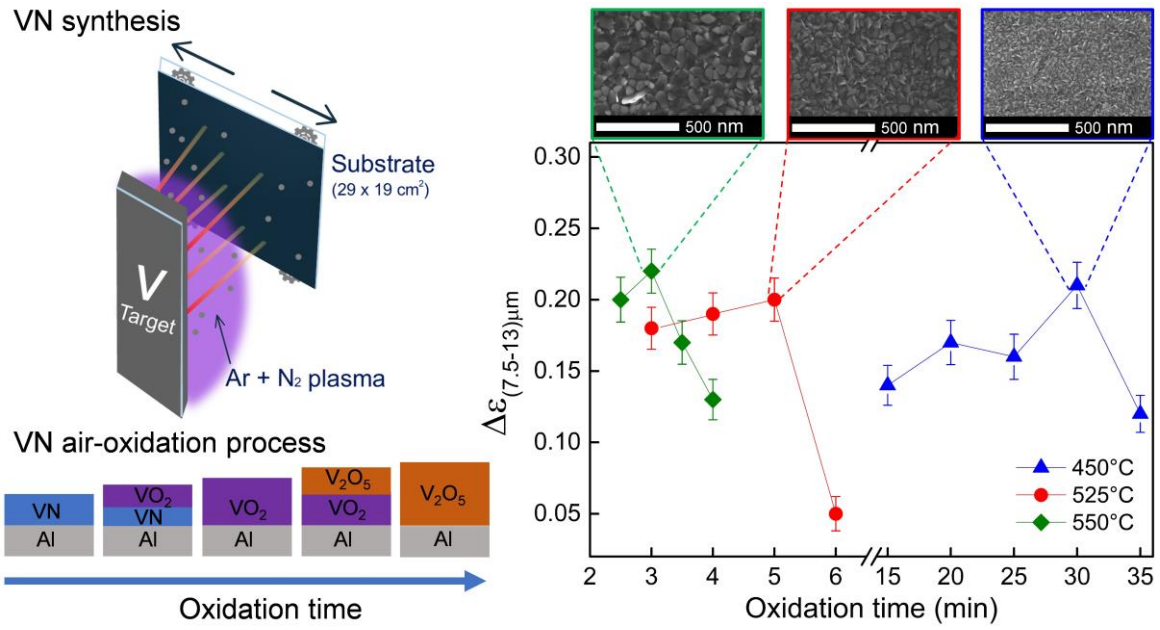

Abstract

In this chapter, vanadium nitride (VN) thin films have been deposited on Al substrates by reactive magnetron sputtering. Thermochromic VO_2 films have been obtained by air oxidation of VN samples performed at three temperatures (450, 525 and 550°C) at various durations (lower than 50 min). X-ray diffraction and Raman spectrometry of the VN oxidized films indicate that VO_2 and V_2O_5 are the only phases produced during the oxidation process. As a function of the oxidation duration, vanadium dioxide is the first oxide formed. It coexists with VN in a long period at 450°C or suddenly disappears at 525 and 550°C. Whatever the temperature, V_2O_5 is exclusively detected after the total oxidation of VN. This oxide is detrimental to the thermochromic performance of films. The emissivity-switching properties of the oxidized films were analyzed by infrared camera in the 7.5-13 µm range. The comparison among all the samples exhibiting a thermochromic behavior shows that the maximum

emissivity switch is independent of the oxidation temperature and the surface morphology of the samples. These results could open a new strategy in the investigation of VN oxidation as a method to obtain VO_2, along with an insight into the correlation between surface morphology and optical properties.

Contents

4.1 Introduction

Vanadium dioxide (as we mentioned before) has been one of the most studied thermochromic materials since its discovery by Morin in 1959 [74]. The significant change in optical transmittance and reflectance (during the metal-insulator transition), particularly in the infrared (IR) region makes this material suitable for numerous applications, for instance as, smart radiator devices for spacecraft [84,91,95,195,196], IR bolometers detectors [197,198], infrared camouflage [199–202]...

However, to employ VO_2 as smart coating some challenges need to be overcome. For example, in the case of smart windows: the luminous transmittance (T_{lum}) and solar transmittance modulation (ΔT_{sol}) have to be high. On the other hand, the transition temperature of the material should be close to room temperature, therefore, the T_{MIT} of the VO_2 should be lowered [164]. There are different strategies to improve the thermochromic performance of VO_2 thin films. The selection of the substrate can influence the switching performance of the material [203,204]. Nevertheless, the substrate choice is linked directly to the desired application. Elemental doping is one of the most practical and feasible methods to tune the optical properties of VO_2 films as well as change T_{MIT}. It has been shown that W is one of the most successful elements to reduce T_{MIT} of VO_2 films [205,206]. On the contrary, Krammer *et al.* proved that T_{MIT} could be increased to approx. 94°C by Ge doping [207]. Several dopants (Mg, Ca, Sr, Ba, Al, Sn, among others) have been studied as an effective way to enhance the optical properties of VO_2 films [90,164,165,208–210]. Moreover, it has been proven that some anti-reflective coatings can improve the optical properties of VO_2 films (ZrO_2 [211], TiO_2 [188,189]). Furthermore, anti-reflective layers such as TiO_2 [189,190], SiO_2 [191], AZO [192] and SiN_x [193] have been used to prevent further oxidation (in case the films continue to be in air-direct contact).

Although great advances have been made in the thermochromic properties of VO_2, the synthesis of this material on large surfaces is still an issue. In chapter 3, we proposed a new strategy to obtain high-quality VO_2 films by the controlled oxidation of vanadium nitride films (VN) deposited on Si substrate [194].

In the present chapter, VN thin films were reactively sputter-deposited on Al substrates by using an in-line semi-industrial machine. The air oxidation of VN samples is performed at three temperatures (450, 525 and 550°C) and several durations up to 50 min. The films were labeled "VN" for as-deposited vanadium nitride films (as in chapter 3) and "VNtemperature_time" for the oxidized films at various temperatures and annealing duration. We study the effect of the temperature and the oxidation duration on the formation of VO_2 films. We aim to determine the influence of the oxidation parameters on the functional properties of the obtained VO_2 films.

4.2 Thermochromic behavior of oxidized VN samples at 450°C

VN precursor thin films (175 nm thick) have been deposited by the sputtering of a vanadium target in a reactive Ar-N_2 atmosphere on Al substrate (the deposition conditions of the VN films are described in Chapter 2). The films have been air oxidized at 450°C during different durations. As-deposited VN films exhibit two peaks corresponding to (111) and (222) planes of the face-centered cubic VN structure (PDF no.00-035-0768), located at approx. 37.9° and 80.3°, respectively (Figure 4.1). No other peaks are detected except those coming from the aluminum substrate.

The X-ray results for films annealed at 450°C during various durations in the 7-50 min range are also presented in Figure 4.1. After 7 min of annealing, the VO_2 phase is not detected. Nevertheless, the oxidation process started, as evidenced by the decline of the VN peak intensity. Besides, these peaks are shifted to higher angles due to stress relaxation during the oxidation process. VN peaks intensity continues to decrease as the annealing time increases, and the main (111) peak disappears at 25 min, indicating that the sample is completely oxidized. On the other hand, after 10 min of air oxidation, a first peak corresponding to the $(\bar{2}12)$ monoclinic(m)-VO_2 is detected close to 42.0°for the first time. As oxidation continues, other peaks located at approx. 2θ = 27.8, 33.3, 36.7, 60.3 and 71.4° (PDF no. 04-003-2035) emerge belonging to m-VO_2. The intensities of these different peaks indicate that the oxide layer does not grow with a strong preferred orientation. Since the as-deposited VN films exhibit a texture along the [111] direction and because the m-VO_2 grains present several diffraction peaks, it may be concluded that there is no structural relationship between the VN and the m-VO_2 grains.

Results between 10 and 25 min suggest that within this period m-VO_2 is formed from the VN precursor oxidation. The most intense peak of VO_2 appears at 30 min of oxidation when there is no VN peak anymore (see Figure 4.2).

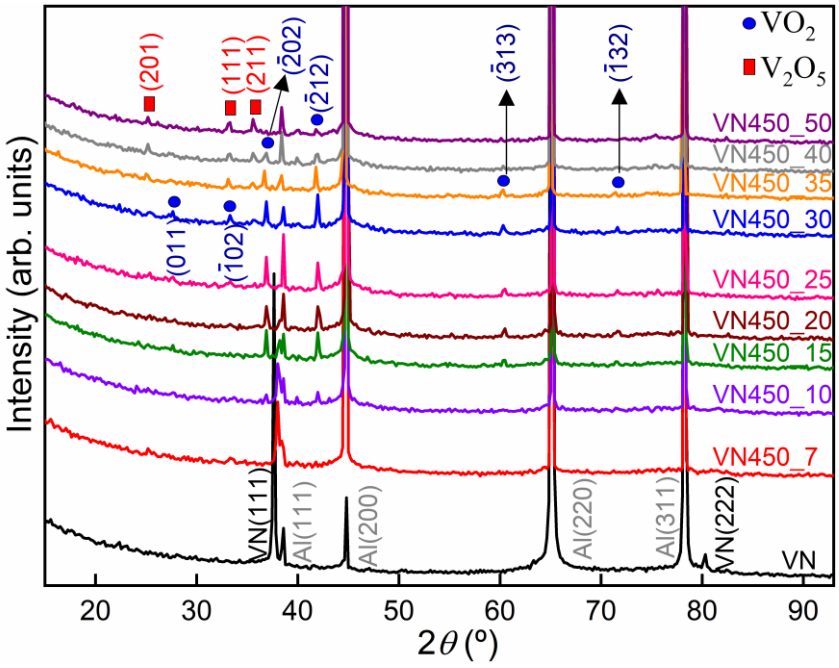

Figure 4.1 X-ray diffractograms of as-deposited VN film on aluminum substrate and the resulting oxidized films after air annealing at 450°C for various durations.

SIMS is a well-known surface analysis technique suitable to obtain composition depth profiles. The SIMS capability of depth profiling with high resolution turns out useful to check the presence of a possible residual layer of VN between the substrate and the formed VO_2 layer. Figure 4.2 shows the SIMS depth profiles of samples VN450_15 and VN450_30. Starting from the surface the signal intensities for V, N, O and Al elements are displayed as a function of etching time in each of the two samples. The twenty first seconds of the analyses (until V and O lines cross each other) can be omitted, it corresponds to the depth needed to reach an equilibrium state. In Figure 4.2 a), the intensity of V and O is quite constant during the first 400 s, suggesting the presence of vanadium oxide. On the contrary, in the same range, the amount of N is negligible due to the oxidation process. After 400 s intensity of these three elements changes, the amount of O decreases while an increase is noticed for V and N. This indicates the presence of a residual layer of VN on the VN450_15 sample. In the case of sample VN450_30 (Figure 4.2 b)), V and O signals are almost constant throughout all the depth profile. Besides,

the intensity of N is imperceptible when compares to those of V and O, showing that this sample is fully oxidized. These findings are in agreement with the X-ray diffraction results of Figure 4.1.

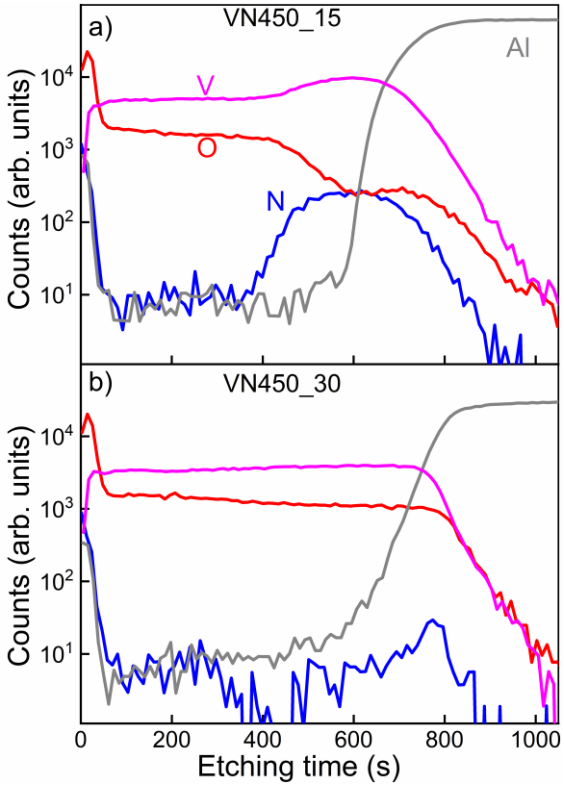

Figure 4.2 SIMS depth profile of samples oxidized at 450°C during a) 15 and b) 30 minutes.

Back to the Figure 4.1, all samples oxidized more than 35 min show three peaks that correspond to the orthorhombic V_2O_5 phase (PDF no. 00-041-1426). Once again there is a competition between phases, in this case, the over-oxidation of VO_2 leads to the formation of the most stable phase of the V-O system i.e., V_2O_5. For the VN450_50 sample, the VO_2 diffraction peaks almost disappeared, and V_2O_5 becomes the predominant crystalline phase. These results are in agreement with our previous work on silicon substrate [194] and also with several authors who already proved the transition from V^{4+} state to V^{5+} state as the oxidation time increases [118,181].

Among the exciting changes in properties during the phase transition on VO_2, the emissivity switch provides an excellent idea of the thermochromic response of the films. The higher the difference in emissivity between the monoclinic and the tetragonal phase of VO_2, the better the thermochromic properties. Figure 4.3 a) shows the apparent infrared temperature as a function

of the real temperature of two samples oxidized during 30 min at 450°C on different substrates (Al and Si). Both samples present a good thermochromic performance. There are two important features to discuss in this figure: first the difference in sign in the emissivity switch. Benkahoul *et al.* disclosed that VO_2 deposited on highly IR-reflective substrates such as Al exhibits opposite behavior to VO_2 deposited on IR-transparent substrates such as Si and quartz [84]. Hence, the choice of the substrate is directly related to the desired application (applications in the solar thermal domain required a highly IR-reflectivity substrate). Second, the significant difference in the hysteresis width of both systems is mainly driven by the distinct substrates [212], which could be connected with the VO_2 film grow orientation (compare Figure 3.1 and Figure 4.1) and the surface morphology.

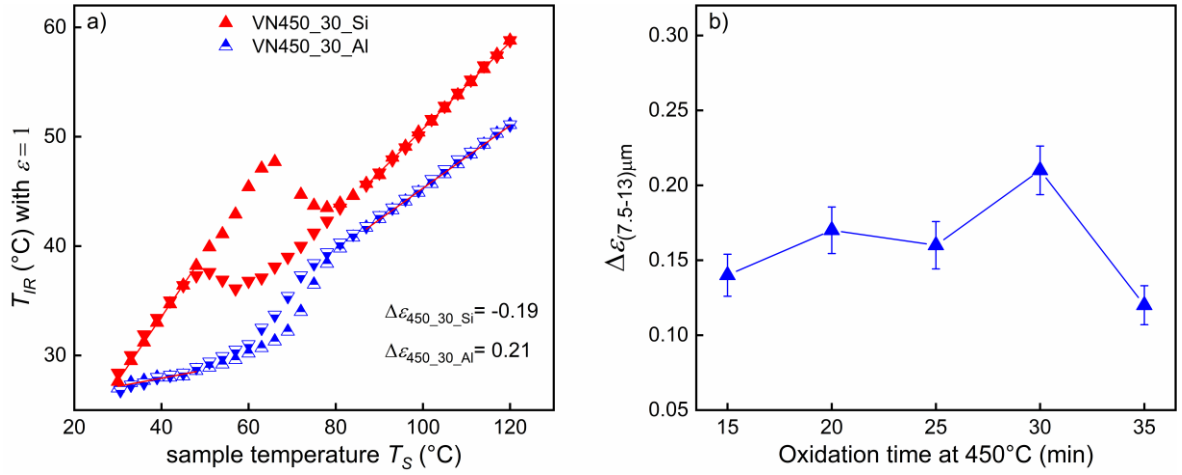

Figure 4.3 a) Thermal camera measurements of apparent infrared temperatures (T_{IR}), as a function of sample temperature (T_S) for VN films on Al and Si substrates oxidized during 30 min at 450 °C. Up and down triangles represent the profiles for temperature ramping up and down, respectively. The red lines obtained by a linear fitting in the low-temperature (LT) and high-temperature region (HT) enabled the determination of emissivity values before and after MIT. b) Dependence of the emissivity switch (in the range of 7.5-13 µm) with the oxidation time at 450°C for samples on Al substrates showing a thermochromic behavior.

Figure 4.3 b) displays the dependence of the emissivity switch in the 7.5-13 µm range as a function of the annealing duration at 450°C for films deposited on aluminum substrates. The values of $\Delta\varepsilon$ are ranging from 0.12 to 0.21 (see Figure 4.4). A tendency to increase the $\Delta\varepsilon$ until a maximum value at 30 min of oxidation is the result of the competing effect of VN oxidation

and the growth of VO_2. However, with higher oxidation duration the formation of V_2O_5 starts and affects the thermochromic effect. Following the same line of thought due to the increasing (decreasing) presence of V_2O_5 (VO_2) samples with 40 and 50 min of oxidation do not exhibit thermochromic response anymore. Moreover, samples oxidized less than 15 min with an important residual VN layer (see Figure 4.2 a)) present a poor thermochromic performance. These findings are in agreement with XRD and also with our previous results (chapter 3). The difference between the present chapter and the previous one corresponds to the nature of the substrate: Al vs. Si. The type of substrate does not modify the vanadium oxides phases found in the films. Thermochromic behavior is obtained for both substrates for very close annealing durations. The main difference is related to the sign of the emissivity switch that is positive using a reflective substrate (Al) and negative using an IR-transparent substrate (Si).

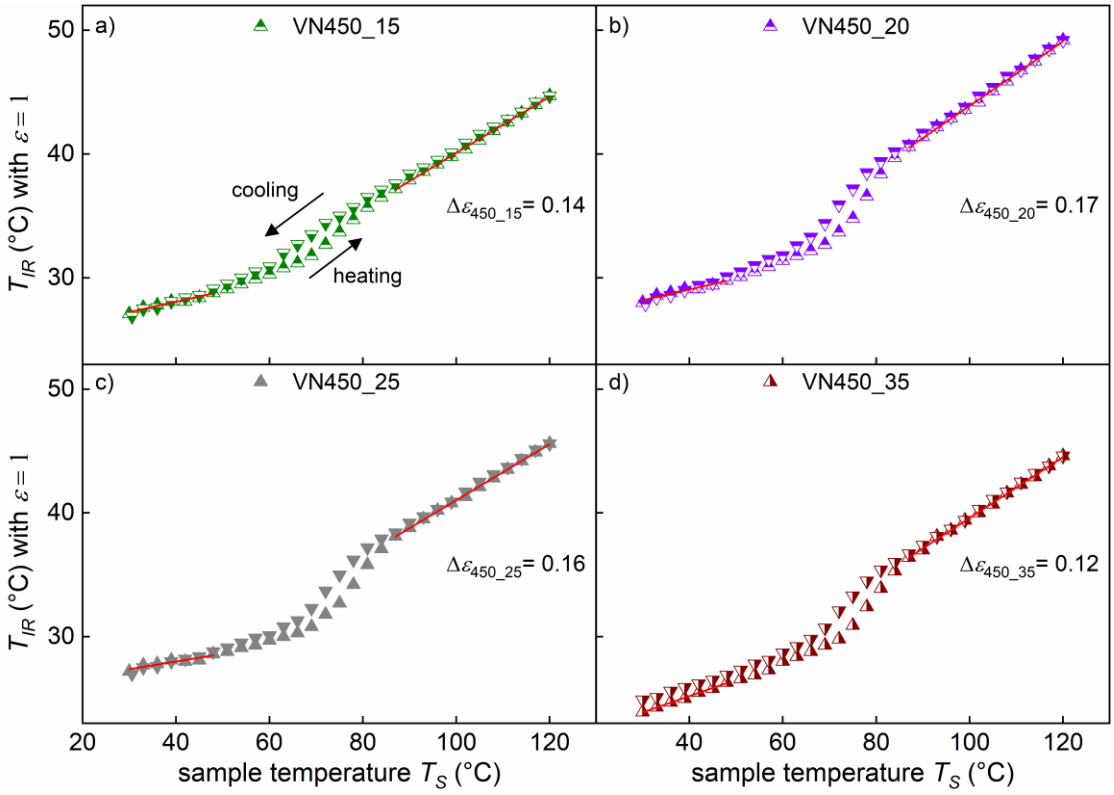

Figure 4.4 Thermal camera measurements of apparent infrared temperatures (T_{IR}), as a function of sample temperature (T_S) for samples oxidized during 15, 20, 25 and 35 minutes at 450°C. Measurements were carried out by considering an emissivity equal to 1 regardless of the sample. The red lines obtained by a linear fitting in the low temperature (LT) and high temperature region (HT) enabled the determination of emissivity values before and after MIT.

4.3 Thermochromism performance on oxidized VN samples at 525°C and 550°C

To study the effect of air oxidation at higher temperatures on the thermochromic behavior, VN precursor thin films were annealed at 525°C and 550°C during distinct durations. Compared to section 4.2, the annealing temperature has been increased, as a consequence, the annealing duration has been reduced to take into account the increase of the oxidation kinetics. Figure 4.5 a) (Figure 4.5 b)) depicts the diffractograms for samples oxidized at 525°C (550°C) between 3-7 min (2-5 min). The corresponding XRD results for VN film (identical to those displayed in Figure 4.1) are included as a guideline for a better comparison of the oxidation process. Sample VN525_3 displays several peaks corresponding to m-VO_2 and the signal of VN does not disappear, indicating that the oxidation is not complete. VO_2 is the only oxide presents on the samples oxidized between 3-5 min, besides VN peaks completely vanished at 5 min. The maximum intensity of VO_2 peaks is detected after 5 min; following the oxidation process, these peaks rapidly decrease in intensity and almost fade away after 7 min. In contrast, after 5 min of oxidation, intense peaks of V_2O_5 emerge caused by the over-oxidation of m-VO_2. Interestingly, a monoclinic V_2O_5 phase (PDF no. 00-061-0027) is revealed together with the already detected orthorhombic V_2O_5 phase (PDF no. 00-041-1426). The peaks of the m-V_2O_5 are situated around 2θ = 17.8, 26.8 and 61.4° and identified with an asterisk (*) in the figure.

The X-ray diffractograms of samples oxidized at 550°C, Figure 4.5 b) are close to those reported at 525°C (Figure 4.5 a)). The only phase of the V-O system detected between 2 and 3 min is m-VO_2. For higher durations, peaks corresponding to the monoclinic and orthorhombic V_2O_5 phase arise due to the over-oxidation of VO_2. During this period the intensity of the peaks belonging to m-VO_2 starts to decrease inducing a vanishing of this phase after 5 min of oxidation. For the films oxidized at 550°C, the V_2O_5 phase appears after 3.5 min of annealing, while 6 min at 525°C are required to overoxidize the VO_2.

The X-ray results for the three studied temperatures suggest that the VN oxidation occurs on the same stages. The first phase of the V-O system detected is m-VO_2 that could coexist with VN. The second and third phases are orthorhombic and monoclinic V_2O_5, which always

appeared only when there is no signal of VN anymore. Yet again, these results illustrate the change from the V^{4+} state into the V^{5+} state with the oxidation time increase and are consistent with the findings of previous studies [118,181,194].

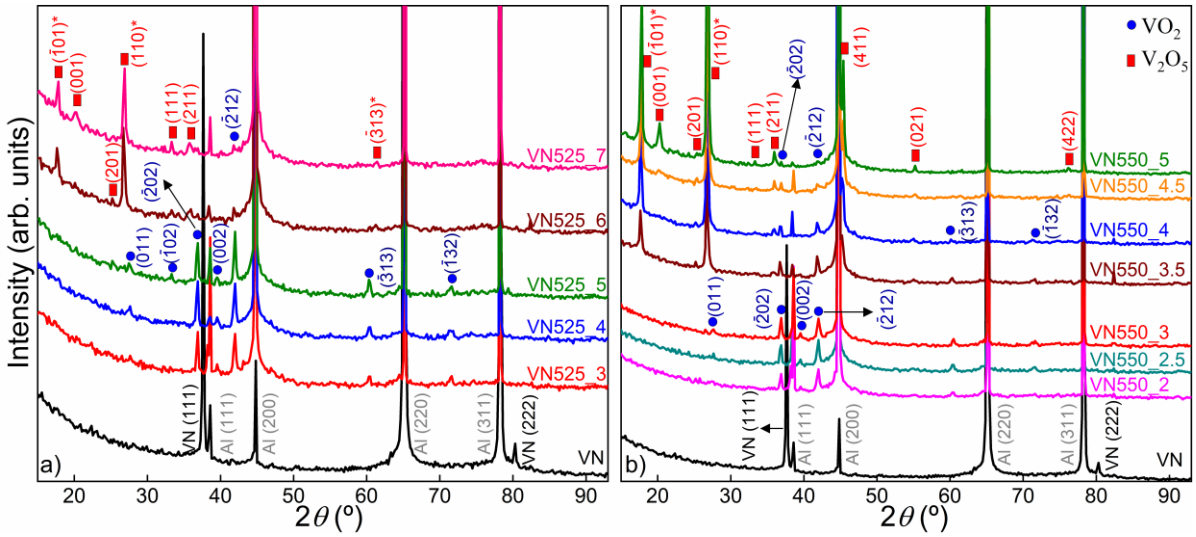

Figure 4.5 X-rays diffractograms of as-deposited VN film on aluminum substrate and the resulting oxide films after air oxidation at a) 525°C and b) 550°C for various durations.

Oxidation kinetics seems to be the main difference in the annealing process between 525°C and 550°C, according to X-ray results. The phases belonging to the binary V-O system crystallize in structures with low symmetries giving a high amount of diffraction peaks. The application of the sole XRD method to characterize the oxide layer may induce some mistakes in the film structure determination. Thus, the use of a second characterization method is mandatory. Within this objective, we have employed Raman spectrometry. Figure 4.6 presents room-temperature Raman spectra of oxidized VN films between 3 to 5 min at 525°C and 550°C.

The samples annealed at 525°C and the VN550_3 one show similar vibration bands (located at approx. 194, 224, 263, 389 and 624 cm^{-1}) that can be assigned to m-VO_2 phase, in agreement with the literature [182–185]. In the case of the oxidized films at 550°C during 4 and 5 min, the shape of the spectra is different from the other samples. Some vibration bands still correspond to VO_2, yet new bands are detected at approx. 195, 282, 301, 405 and 532 cm^{-1} that are readily ascribed to the orthorhombic V_2O_5 phase [182,186]. These findings confirm the simultaneous presence of VO_2 and V_2O_5 in VN550_4 and VN550_5 samples as well as the only existence of

m-VO_2 in samples oxidized between 3 and 5 min at 525°C and 3 min at 550°C as shown by the X-ray results.

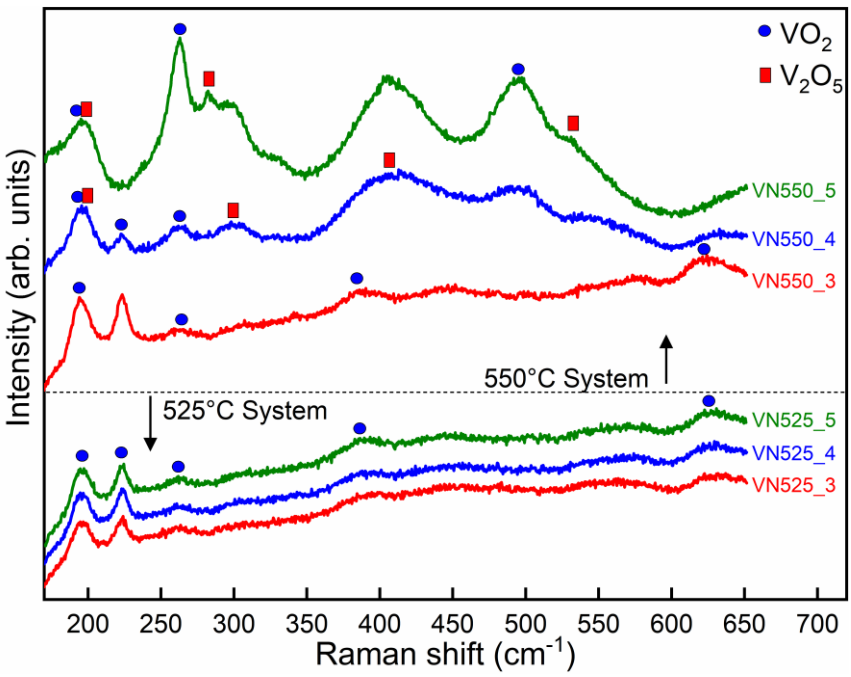

Figure 4.6 Raman spectra of air-oxidized VN films during 3 to 5 min at 525°C and 550°C.

Figure 4.7 a), c) and d) show the SIMS depth profile of samples oxidized at 525°C for 3, 4 and 5 min respectively. Starting from the sample surface the signal intensities for V, N, O and Al elements are displayed as a function of etching time in each of the three samples. Once again; the twenty first seconds of the analyses (until V and O lines cross each other) can be omitted, it corresponds to the depth needed to reach an equilibrium state. The signal corresponding to V and O in Figure 4.7 a) is relatively constant during the first 400 s, suggesting the presence of vanadium oxide with a constant composition. During this period the amount of N is negligible thanks to VN oxidation. On the contrary, after 400 s the intensity of these three elements changes, the signal of O drops while the opposite occurs for V and N. The latter evince the presence of a remaining VN layer in the VN525_3 sample.

Figure 4.7 b) shows a transmission electron microscopy cross-section of the VN525_3 sample. The figure depicts close to the Al substrate an uninterrupted columnar VN layer of approx. 90 nm thick and above a VO_2 layer of approx. 140 nm thick (corresponding to the oxidation of a 85 nm thick VN layer). This TEM cross-section image confirms the results obtained by XRD and SIMS. From Figure 4.7 a) and b) it can be concluded that the sample

VN525_3 is not completely oxidized. Concerning the VN525_4 sample, the behavior of V, N and O signals from Figure 4.7 c) are equivalent to those of Figure 4.7 a). However, the thickness of the remaining VN layer is lower compared to the sample VN525_3. Moreover, V and O signals are rather constant throughout all the depth profile of sample VN525_5 (Figure 4.7 d)) and the N amount is negligible, suggesting that the sample is fully oxidized. The SIMS analysis corroborates the X-ray results of Figure 4.5 a) showing the growing presence of VO_2 caused by the air oxidation of VN.

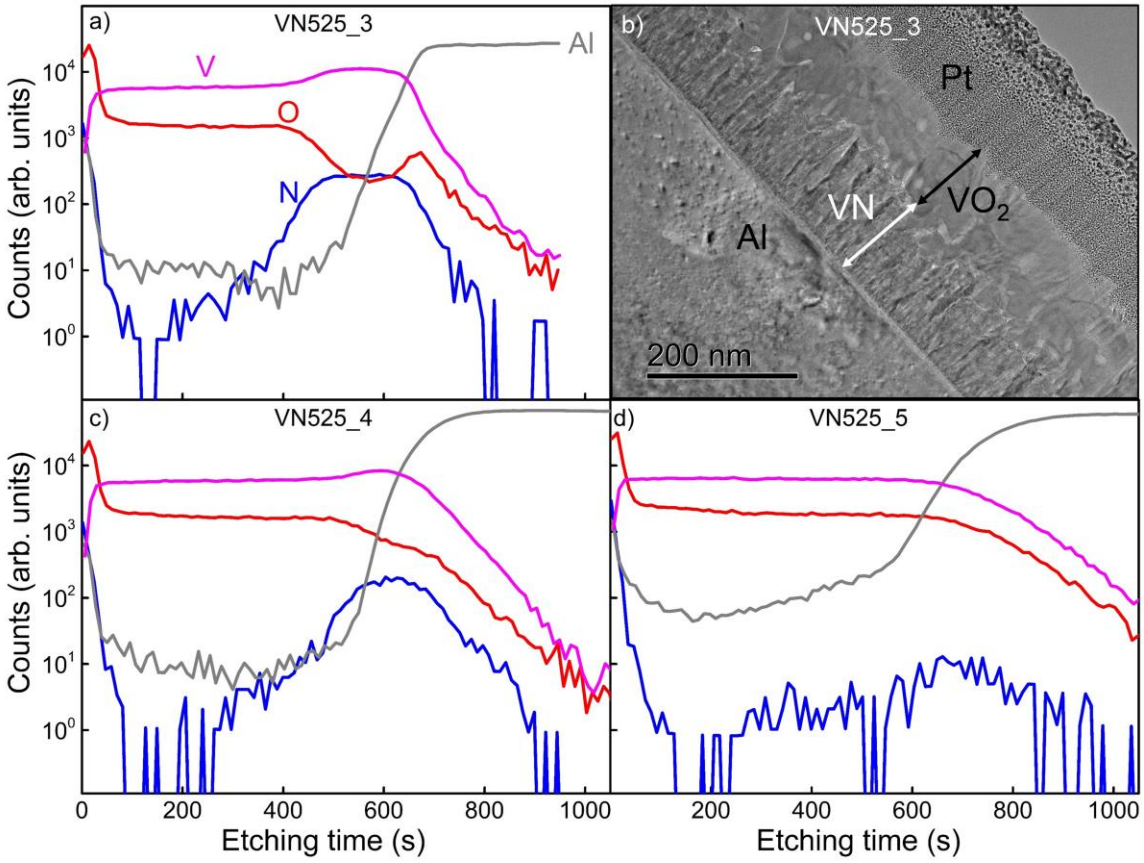

Figure 4.7 SIMS depth profiles of samples oxidized at 525°C during 3, 4 and 5 min for a), c) and d), respectively. The etching time indicates the depth of the sample from the surface. b) TEM cross-section image of sample VN525_3.

Figure 4.8 depicts the top view SEM images of six noteworthy samples: the as-deposited VN films and samples oxidized during 15, 30 min at 450°C, 4, 5 min at 525°C and 3 min at 550°C. Note that all the images have not the same magnification, but all of them except the as-deposited VN were acquired with identical acceleration voltage. The as-deposited VN film exhibits a surface morphology with small pyramidal-shaped grains in agreement with the [111]

preferred orientation evidenced by XRD (as the VN films on Si substrate [194]). Along the oxidation process, the morphology of the oxidized samples considerably changes when compared to the VN films. After 15 min of oxidation at 450°C (Figure 4.8 b)), the oxidized VN grains merge into an extended structure, enlarging grain size. Increasing the annealing time at the same temperature leads to the growth of the grains (Figure 4.8 c)). Samples VN525_4 (Figure 4.8 d)) and VN525_5 (Figure 4.8 e)) present different morphology than samples oxidized at 450°C, the grains are bigger and more rounded. In the case of Figure 4.8 f) (VN550_3) the grains are equiaxed and are the largest among all the images. It is noteworthy that despite drastic different morphology and grain size the images of Figure 4.8 c), e) and f) correspond to samples completely oxidized, in which the only phase detected is m-VO_2.

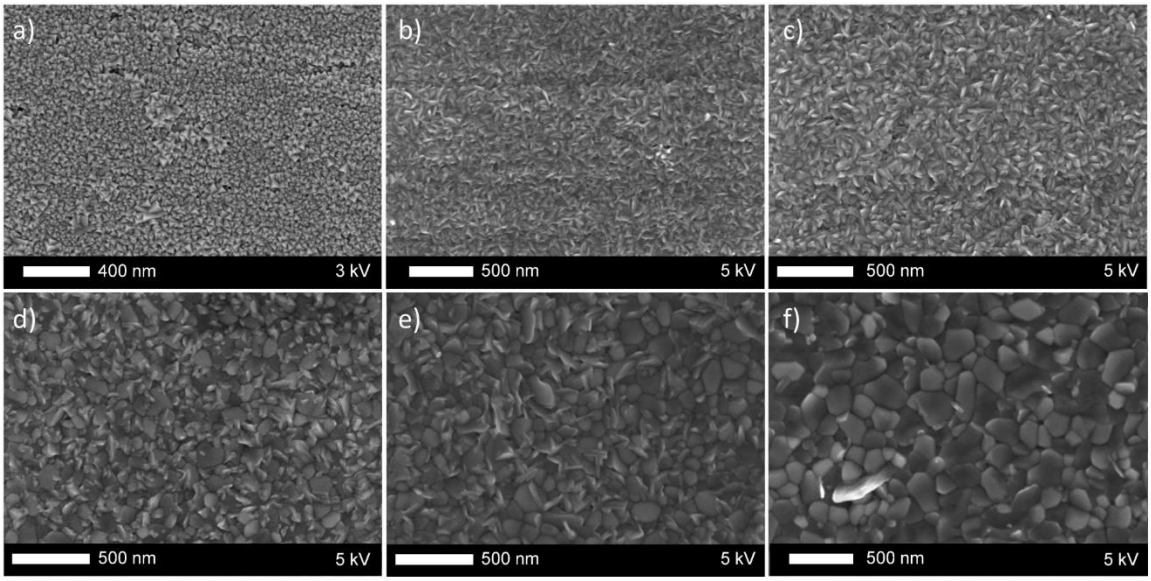

Figure 4.8 Top-view SEM images corresponding to a) the as-deposited VN films and samples VN450_15, VN450_30, VN525_4, VN525_5 and VN550_3 for b), c), d), e) and f), respectively. Note that the magnification is different, as indicated in each image, besides the image of the as-deposited VN was acquired with a lower acceleration voltage.

The optical modulation properties for samples oxidized at 525°C in a range of 3 to 6 min are studied with an infrared camera (Figure 4.9 a)). Air-annealed samples between 3 and 5 min display hysteresis loops near the MIT region, a characteristic thermochromic signal. The corresponding values for the emissivity switch for these samples slightly increase with oxidation time. This is a consequence of the continuous growth of VO_2 from the oxidation of

VN, reaching a maximum after 5 min. However, the $\Delta\varepsilon$ value of VN525_6 drops drastically to 0.05 (75% less when compared with the VN525_5 sample) caused by the over-oxidation of VO_2 to V_2O_5. This behavior is in total accordance with X-ray (Figure 4.5 a) and Raman results (Figure 4.6).

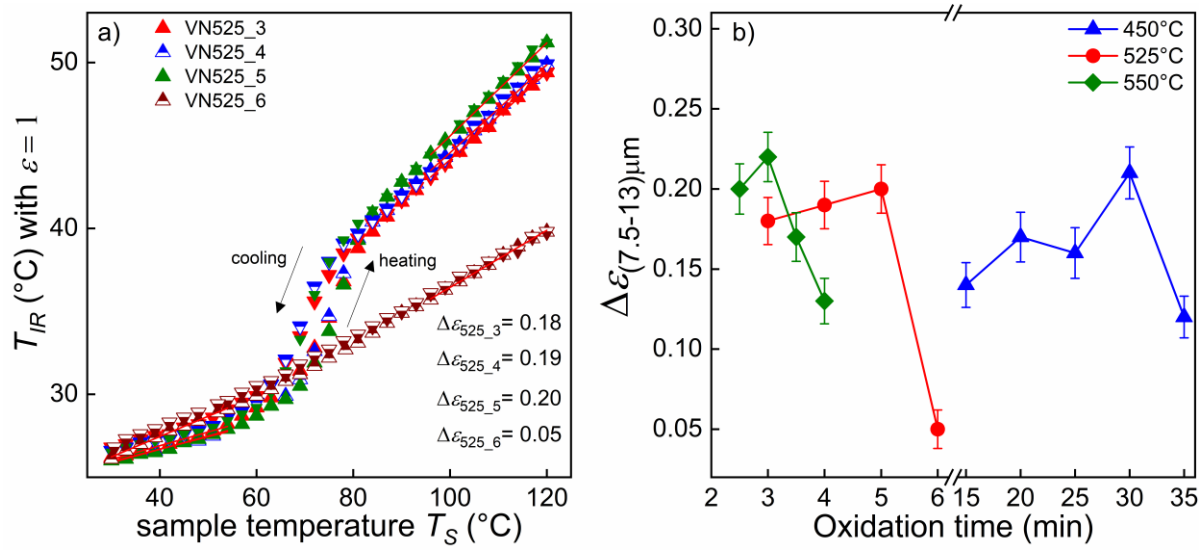

Figure 4.9 a) Thermal camera measurements of apparent infrared temperatures (T_{IR}), as a function of sample temperature (T_S) for VN films oxidized at 525°C between 3 and 6 min. Measurements are carried out by considering $\boldsymbol{\varepsilon = 1}$ irrespective to the sample. Up and down triangles represent the profiles for temperature ramping up and down, respectively. The red lines obtained by a linear fitting in the low temperature (LT) and high temperature region (HT) enabled the determination of emissivity values before and after MIT. b) Dependence of the emissivity switch (on the range of 7.5-13 µm) with the oxidation time for the three studied systems (450, 525 and 550°C).

Figure 4.9 b) displays the dependence of the emissivity switch with oxidation time for the three studied systems (see Figure 4.10 for the 550°C system). All systems have similar dynamics. The $\Delta\varepsilon$ values increase smoothly when VN and VO_2 phase coexist, until reaching a maximum value when VO_2 is the predominant phase and the precursor is completely oxidized. Further increase of the oxidation time induces a decrease of $\Delta\varepsilon$ due to the over-oxidation of VO_2 and the consequent growth of V_2O_5. The optical modulation properties' findings are in full agreement with XRD and Raman results.

Several stimulating conclusions can be drawn from Figure 4.9 b). First of all, the maximum values of $\Delta\varepsilon$ are similar (between 0.20 to 0.22) for the three different systems suggesting that

they are independent of the oxidation temperature. These results could be related to the fact that all the precursor VN samples have the same thickness. The amount of VN which can be transformed into VO_2 is the same, independent of the air-annealed temperature. Nevertheless, the results shown (in chapter 3) in oxidized VN samples on Si substrate are different, with an increase of the maximum $\Delta\varepsilon$ with the oxidation temperature. This difference requires further study. The emissivity contrast values found in this paper are in the same range as those reported in the literature in the same IR domain. For instance, Benkahoul *et al.* found $\Delta\varepsilon$ = 0.26 in 300 nm thick VO_2 film deposited on Al using an infrared camera in the 8-14 µm range [84].

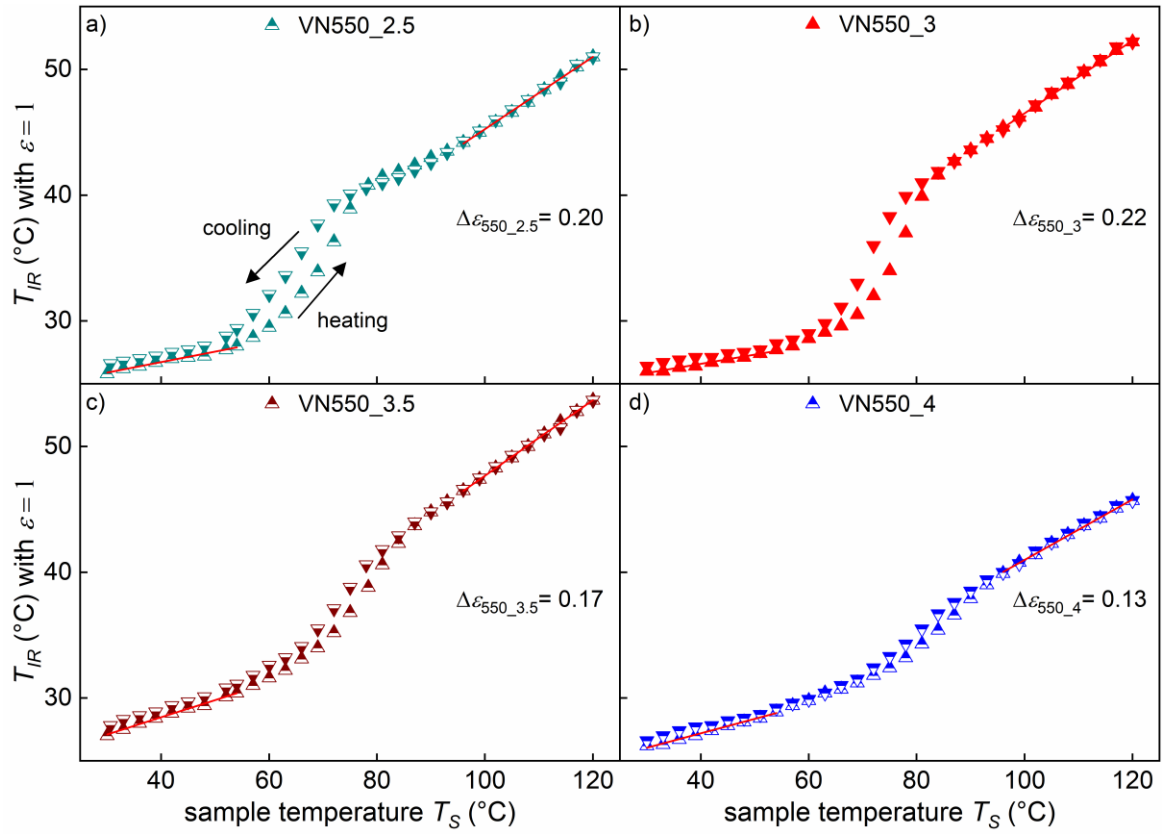

Figure 4.10 Thermal camera measurements of apparent infrared temperatures (T_{IR}), as a function of sample temperature (T_S) for VN film oxidized during 2.5, 3, 3.5 and 4 minutes at 550°C. Measurements were carried out by considering an emissivity equal to 1 regardless of the sample. The red lines obtained by a linear fitting in the low temperature (LT) and high temperature region (HT) enabled the determination of emissivity values before and after MIT.

It is well reported in the literature the close correlation between electrical properties with the surface morphology of VO_2 [81,107,111]. However, the morphology of the samples with the highest emissivity switch (VN450_30, VN525_5 and VN550_3) in the different studied

systems is remarkably different (Fig. 4.8 c), e) and f) respectively). These results suggest that the optical properties are independent of the VO_2 surface morphology, at least in the 7.5-13 μm IR range.

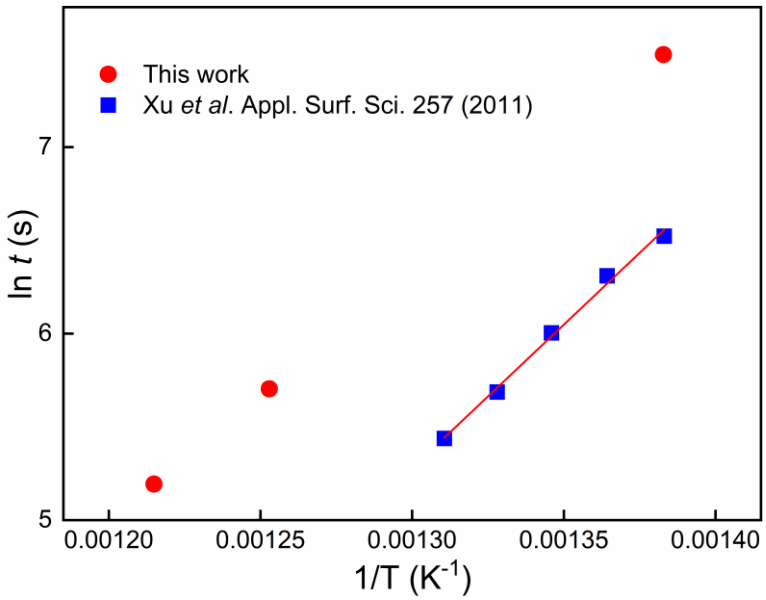

Figure 4.11 Relationship between optimal oxidation time and temperature. In red circles the corresponding values for this work and blue squares for the results of Xu *et al.*[126].

One more interesting result is related to the best-oxidation time for each studied temperature. Xu *et al.* [126] reported an optimal oxidation time at different temperatures to obtain high-quality VO_2 films by oxidation of 100 nm thick vanadium films (using the Sputtering Oxidation Coupling method [125]). Figure 4.11 displays the optimal oxidation time (ln *t*) expressed as a linear function of the reversed temperature (1/*T*). In red circles the results of our work and in blue square the results of Xu *et al*. In the latter, the fit serves to obtain the diffusion activation energy and also to predict theoretical optimal oxidation time at other temperatures. A direct evaluation of both works shows that the values of activation energy are similar. Yet, the most important result from the comparison is that the time required to obtain the best VO_2 is larger in VN than in V films, indicating that it is easier to control the oxidation of VN.

4.4 Chapter conclusions

In this chapter, we study the effect of three oxidation temperatures (450, 525 and 550°C) on the optical properties of the VN oxidized films. The results indicate that for all studied systems the VN oxidation occurs on the same stages. The first oxide formed is VO_2, it coexists with VN in a long period at 450°C or suddenly disappeared at 525 and 550°C. Furthermore, V_2O_5 is detected after the total oxidation of VN. These findings confirm the oxidation from the V^{4+} state into the V^{5+} state with the annealing time increase and correspond with the results of previous studies.

Concerning the optical properties of the oxidized films, the best emissivity switch in each system is quite similar (between 0.20 and 0.22), whatever the oxidation temperature. On the other hand, the film morphology is strongly dependent on the oxidation temperature. Nevertheless, the change of the surface morphology does not influence the optical properties of the films. This indicates that the optical properties of VO_2 in the 7.5-13 µm range are independent of the surface morphology.

In chapters 3 and 4, we have shown a simple method to deposit VN on large surfaces and different substrates. The VN oxidized films display good optical modulation properties at different temperatures and durations. These reasons make the VN oxidation process encouraging for the production of high-quality thermochromic VO_2 films for several applications as furtivity and smart radiator devices.

In the next two chapters, we will use a standard sputtering machine. In chapter 5, we will deposit epitaxial VN films. The oxidation of these films will be performed with the best oxidation conditions found in chapters 3 and 4. Furthermore, we will compare the samples obtained in the two different sputtering reactors.

Chapter 5

Oxidation of sputter-deposited vanadium nitride epitaxial films: a novel approach to obtain VO_2

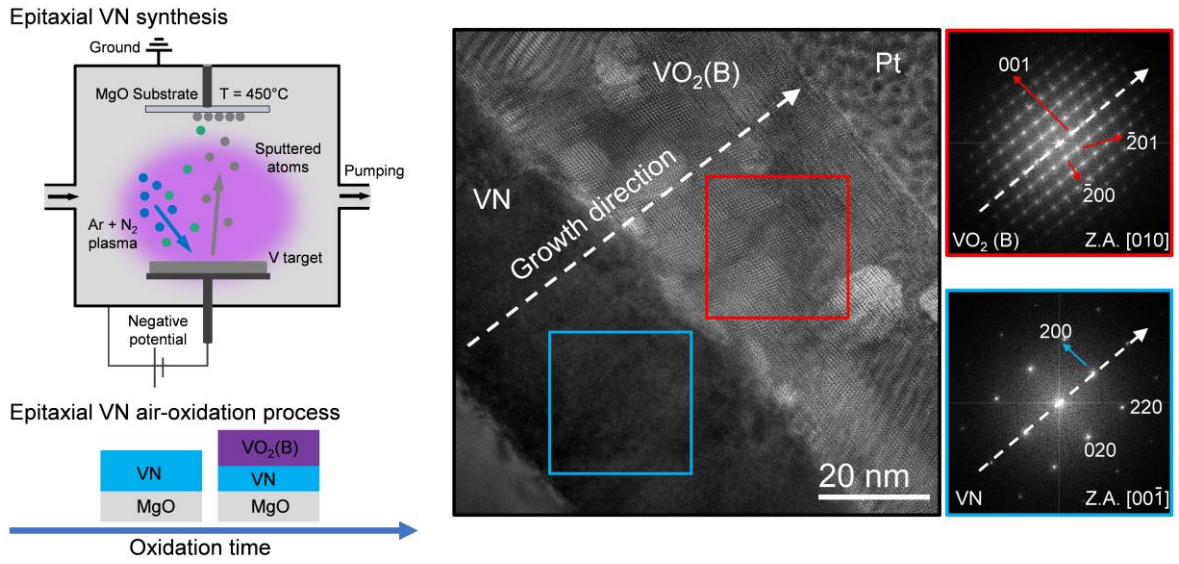

Abstract

In this chapter, epitaxial VN thin films were deposited on MgO single crystalline substrates by reactive magnetron sputtering. The results from XRD, RHEED, EBSD and HRTEM microscopy analyses prove that VN are epitaxial single crystals which grow cube-on-cube with respect to the substrate: VN (100) || MgO (100) and VN [010] || MgO [010]. The epitaxial as-deposited VN films were annealed in a pre-heated furnace at different durations and three temperatures in the range of 450-550°C. The XRD and Raman results depict a mixture of phases, with VO_2(B) as the predominant compound. The TEM findings exhibits an epitaxial growth between VO_2(B) and VN with the following relationships: VO_2(B) (001) || VN (200) out-of-plane and VO_2(B) (200) || VN (020) in-plane orientation. SEM images and the AFM results illustrates the growth of VO_2(B) nanorods perpendicular to the substrate. Finally, we apply a criterion to transpose the deposition conditions between the two sputtering machines used in the thesis: the semi-industrial one (chapters 3 & 4) and a lab-scale one used in the

present chapter. Only the oxidized films deposited with the analogous conditions show thermochromic performance.

Contents

5.1 Introduction

In the previous chapters, we have shown that VN can be considered as a new precursor to produce thermochromic VO_2 thin films. The VN films were oxidized under certain specific conditions to achieve VO_2 as the predominant compound on the sample. We have illustrated that the choice of proper oxidation parameters (temperature and oxidation duration for a given thickness) is crucial to reach the desired final phase [194,213].

Doping can be considered as an alternative strategy to improve the properties of VO_2 resulting from the oxidation of vanadium nitride. It has been reported a successful addition of Cr and Al into the VN structure. In both cases, the sputtered-deposited doped films form a solid solution and retain the rocksalt-like structure of VN [17,214]. On the other hand, Cr and Al are well-known doping elements for VO_2. Brown *et al.* and Zou *et al.* showed that doping with Cr ions gradually increased the metal-insulator transition temperature of the films, meanwhile, the electrical and optical modulation properties decreased with the amount of Cr [215,216]. On the contrary, Al doping increases luminous transmittance, improves solar modulation ability, and efficiently reduces the phase transition temperature to 45°C [164]. Moreover, Mercs *et al.* reported a new generation of thermochromic thermal solar collectors based on the oxidation of VO_x/SiO_2 layers on aluminum. The air oxidation of Al-doped film (8 at. %) during 3.5 minutes at 550°C gives a thermochromic selective absorber ($VO_2/V_nO_{2n\pm1}/Al_2O_3/SiO_2$) that guarantees a lifetime of at least 25 years without significant change of its optical properties [90]. These results illustrate that doping the VN could be a compelling strategy to enhance the thermochromic performance of the conceived VO_2.

The change of the VN deposition parameters (deposition temperature, operating pressure, nitrogen partial pressure, substrate bias, among others) represents another attractive approach. For instance, Chu *et al.* displayed that the change of nitrogen partial pressure on the sputter-deposited VN films controlled the formation of different phases (from V metal to cubic VN_x with other compounds in between) [217]. In 2019, Wu *et al.* optimized the deposition conditions to sputter-deposit VN films. The optimum conditions were: − 90 V for the substrate bias, 2.5 sccm nitrogen flow rate, a substrate temperature of 300°C and a substrate rotational speed of

20 rpm. The achieved VN film presented an exceptional combination of properties, including high hardness, low residual stress and low electrical resistivity [218].

Based on the above results, we decided to enhance the quality of the VN precursor. The idea is to obtain epitaxial VN, then oxidize these high-quality films to synthesize improved thermochromic VO_2 (first and second sections of the chapter). Several substrates are used to deposit epitaxial VN, such as $SrTiO_3$ [219,220], Pt [221] and MgO [148,222–224]. MgO has a small lattice mismatch of less than 2% to that of VN. Furthermore, the thermal expansion coefficient of MgO and VN are similar (i.e., $\alpha_{MgO} \approx 13 \times 10^{-6}$ K^{-1} [225], $\alpha_{VN} \approx 9.7 \times 10^{-6}$ K^{-1} [226]). Hence MgO is a suitable substrate for the epitaxial growth of VN. In our case, we operated with MgO (100), the parameters of the deposition are listed in section 2.3.2.1 (Chapter 2).

All the results depicted in chapters 3 and 4 were from the oxidation of polycrystalline VN deposited on the semi-industrial machine. In this chapter, we will use a lab-scale sputtering machine with 2" target diameter. The change of reactor and the VN deposition conditions should lead to a variation of the film microstructure and then to the oxidation parameters to get high-performance thermochromic VO_2.

Furthermore, the deposition of similar films using different sputtering machines must be an even more difficult task. In the final section of the chapter, we will discuss about a simple criterion to obtain similar VN films between the two sputtering reactors employed throughout the thesis. Moreover, three series of samples with different working pressures were deposited. We study the oxidation of the three series of VN films. The results display that the only oxidized films that present thermochromic performance are the ones with the parameters obtained from our criterion.

5.2 Deposition and characterization of epitaxial growth VN thin films

All the studies performed in chapters 3 and 4 employed the semi-industrial machine to deposit the VN films. As mentioned in chapter 2 (section 2.3.1), this machine is not equipped to heat the substrate holder. The growth of epitaxial VN films has been reported in high-energy deposition conditions, with deposition temperatures higher than 430°C to form stoichiometry

epitaxial VN on MgO substrates [148,222]. Thus, we have to use another sputtering chamber. The lab-scale machine connected to the TUBE allows the deposition at temperatures as high as 800°C. Using the TUBE it is possible to transfer the samples (raw and VN-coated MgO substrates) to the RHEED setup to check the surface structure. We will exploit this possibility as a benefit to obtain VN films with higher quality.

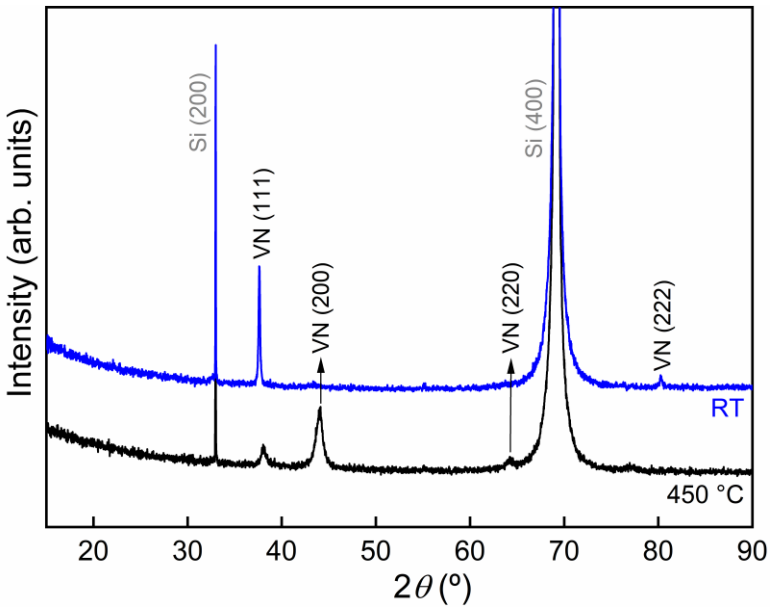

Figure 5.1 X-ray diffractograms of as-deposited VN thin films on Si substrate at room temperature and at 450°C. Both samples were deposited with the same parameters (current applied to the target of 0.5 A, working pressure 0.22 Pa, deposition time 30 min and Ar and N_2 flow rate of 30 and 5 sccm, respectively) except the substrate holder temperature.

Figure 5.1 displays the diffractograms of VN films deposited on Si substrates with the same Ar and N_2 flow rates as in previous chapters (30 and 5 sccm, respectively) during 30 minutes at 0.22 Pa. The films grown at room temperature (RT) present the same preferred orientation that in preceding chapters as illustrated in Figure 5.1 (peaks located at approx. 37.9° and 80.3° corresponds to (111) and (222) planes of the fcc VN structure (PDF no.00-035-0768)). Nevertheless, once the substrate holder is heated (at 450°C), the (111) peak intensity decreases and the preferred orientation changes; the (200) peak becomes more intense than the (111) one. When heating the substrate holder, the adatom's energy increases, thus the adatom's mobility enhances stimulating the formation of the (100) orientation [227]. This change in the texture is employed as an advantage for the growth of high-quality epitaxial VN thin films. The increase

of the deposition temperature also comes with an enlargement of the diffraction peak, suggesting a grain size decrease. This phenomenon could be due to an increase in the nucleation site density with increasing deposition temperature. Huang *et al.* have also reported a grain size decrease when changing the texture from (111) to (200) [227].

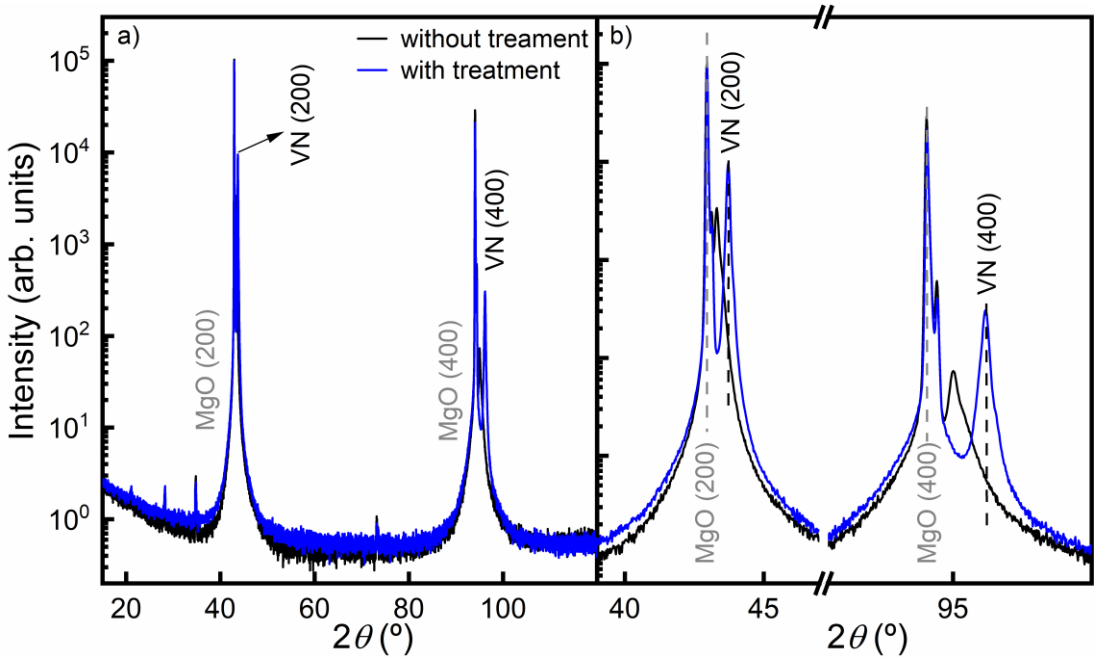

Figure 5.2 X-ray diffractograms of epitaxial growth VN thin films on MgO substrate at 450°C in the 2θ region from a) 15 to 120 and b) zoom in the region with peaks. The blue and black curves represents the diffractograms for a sample that follow a thermal treatment right after the deposition and for the one who doesn't follow it, respectively.

The X-ray diffractograms of the VN films deposited on MgO substrates are shown in Figure 5.2 (details about the preparation of the MgO substrates are given in section 2.3.2.1). The films were grown with the same parameters as samples in Figure 5.1. There are four diffraction peaks, two corresponds to the (200) and the (400) planes of the MgO substrates located at 42.9 and 94.0°, respectively (PDF no.00-004-0829). The other two peaks are assigned to the (200) and the (400) planes of the fcc VN structure (PDF no.00-035-0768). Once the deposition finished, every sample went again to the MBE machine to study the surface by RHEED (Figure 5.3). The samples characterized in Figure 5.2 differ from a thermal treatment following the PVD deposition: one was submitted to a thermal treatment at 990 °C during 45 minutes (blue curve) and the other one was not submitted to thermal treatment (black curve). The thermal treatment may induce some changes in the film due to the stress relaxation or to a change of the nitrogen

content. Since this treatment is performed in the MBE reactor at high temperature under ultra-high vacuum, no oxidation of the film surface has been noticed. The use of such a high temperature (990 °C) may also induce some diffusional steps generating a flattening of the film surface. The sample that did not follow the thermal treatment present peaks displaced at angles lower than the theoretical VN values. On the contrary, the sample that was thermally treated shows diffraction peaks at 43.7 and 96.2° in agreement with theoretical values for the (200) and the (400) planes of the fcc VN structure (PDF no.00-035-0768), respectively. From now on, all the epitaxial VN films presented in the thesis underwent a thermal treatment.

Figure 5.3 illustrates the RHEED patterns for an epitaxial VN growth on MgO substrate along two different azimuths. The straight lines in both patterns indicate that the surface of the epitaxial VN corresponds to a single-crystalline film.

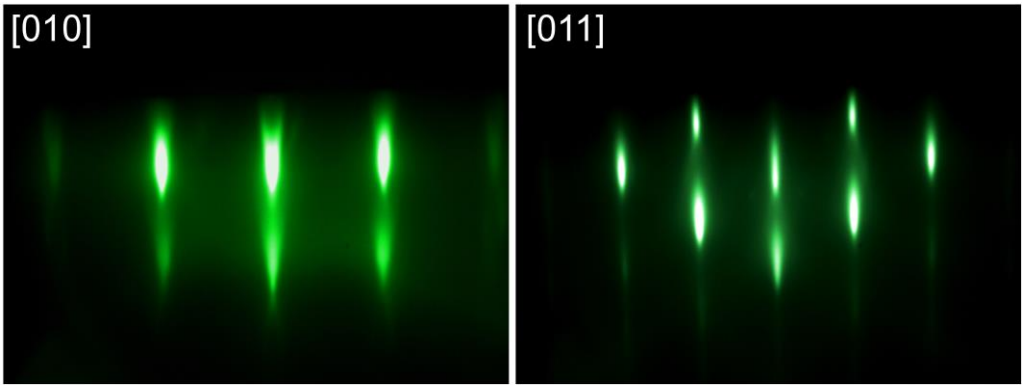

Figure 5.3 RHEED patterns recorded on an epitaxially-growth VN on MgO substrate after thermal treatment at 990°C under ultra-high vacuum along two different azimuths.

To corroborate the RHEED results, we performed an electron backscatter diffraction (EBSD) study of an epitaxial growth VN film. Figure 5.4 exhibits two EBSD maps from the same sample collected at two different angles, in a) at the [100] direction and in b) at the [110] direction. A first result to point out is that in the analyzed volume there are no grain boundaries, this states that we are in the presence of a single-crystalline film. Besides, in both cases, the X-axis indicates the [100] direction, which is consistent with the texture deduced from the XRD results. On the other hand, the results of the Y and Z axis change with the orientation of the sample in front of the detector. Yet, the results in Figure 5.4 a) and Figure 5.4 b) for the Y and Z axis show the same color in the whole analyzed surface (either all red or all green). Therefore,

the RHEED and EBSD results confirm that the epitaxial VN film is a single crystal with [100] growth direction.

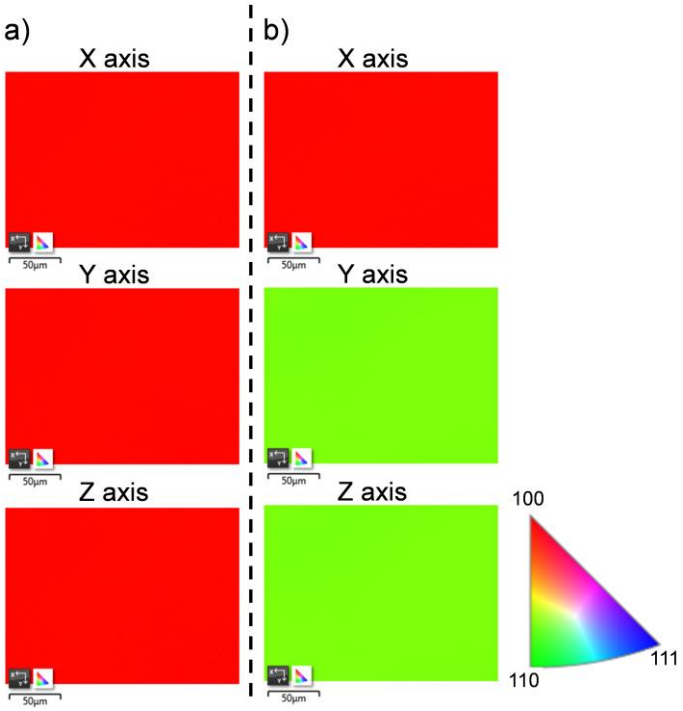

Figure 5.4 Electron backscatter diffraction images of an epitaxially-growth VN on MgO substrate when the sample was placed in front of the detector in a) the [100] direction and b) the [110] direction.

A high-resolution cross-sectional transmission electron image displaying the film-substrate interface is shown in Figure 5.5 a). The higher average atomic number of VN compared to MgO enables to distinguish between the film and the substrate due to the contrast differences in the lattice images. No grain boundary is evidenced in the VN film. This result differs from that obtained on VN grown on Al substrates at room temperature (Figure 4.7 b)). Figure 5.5 b) and c) represents the FFT pattern performed in the enclosed areas of Figure 5.5 a). It was possible to identify the (200), (220) and (020) planes of the VN and MgO. The obtained interplanar distances are 0.207, 0.147 and 0.206 nm for (200), (220) and (020) planes, respectively, in agreement with those reported for the fcc VN (PDF no. 00-035-0768). Both substrate and VN film exhibit the same FFT pattern. The combination of XRD, RHEED, EBSD and HRTEM microscopy analyses prove that VN films grow with film/substrate epitaxial relationships: VN (100) || MgO (100) and VN [010] || MgO [010].

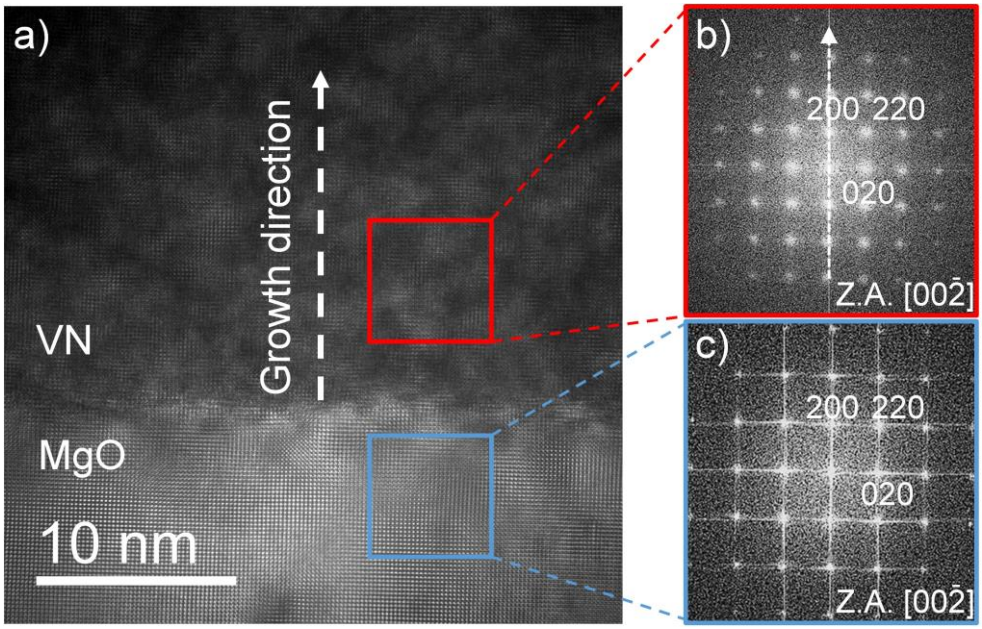

Figure 5.5 a) HRTEM micrograph acquired near the VN/MgO(100) film-substrate interface. FFT from the region highlighted in b) red (VN) and c) blue (MgO) of Figure 5.5 a).

5.3 Oxidation of epitaxially growth VN thin films as a new possible route to achieve thermochromic VO_2

Once the deposition of epitaxial VN on MgO is demonstrated, we can focus our work on the controlled oxidation of such highly crystallized nitride. Thus, the second step consists of the air-oxidation of these films to obtain VO_2. We have chosen the best oxidation conditions found in chapters 3 and 4 for polycrystalline VN films deposited on Si and Al substrates (25, 5, and 3 minutes at 450, 525, and 550°C, respectively). Figure 5.6 shows the X-ray diffractograms for as-deposited epitaxial VN (around 150 nm thickness) and air-annealed epitaxial VN films deposited on MgO substrate. The three oxidized films present numerous peaks, two of them correspond to the (110) and ($\bar{2}$22) planes of the m-VO_2(M) (PDF no. 04-003-2035) located at approx. 26.8° and 55.2°. Besides, one peak at 45.4° corresponds to the (411) plane of orthorhombic V_2O_5 (PDF no. 00-041-1426). For the first time, the oxidation of VN films reveals several peaks assigned to another oxide phase, namely m-VO_2(B) (PDF no. 04-007-0514) located at 2θ =17.7, 28.9, 35.9, 44.1 (shoulder of the (200) peak of VN, see Figure 5.6 b)), 49.5, 50.4 and 59.9°. Figure 5.6 b) displays a zoom in the region around the (200) VN peak, the most striking result is that the intensity of the VN peaks slightly decreases after this oxidation test.

Compared to the films elaborated at room temperature on Si or Al substrates, the epitaxial VN layer is still evidenced after the oxidation test. Hence, the oxidation of epitaxial VN films exhibits a slower kinetics than that observed for the polycrystalline films (with similar thickness) studied in Chapters 3 and 4.

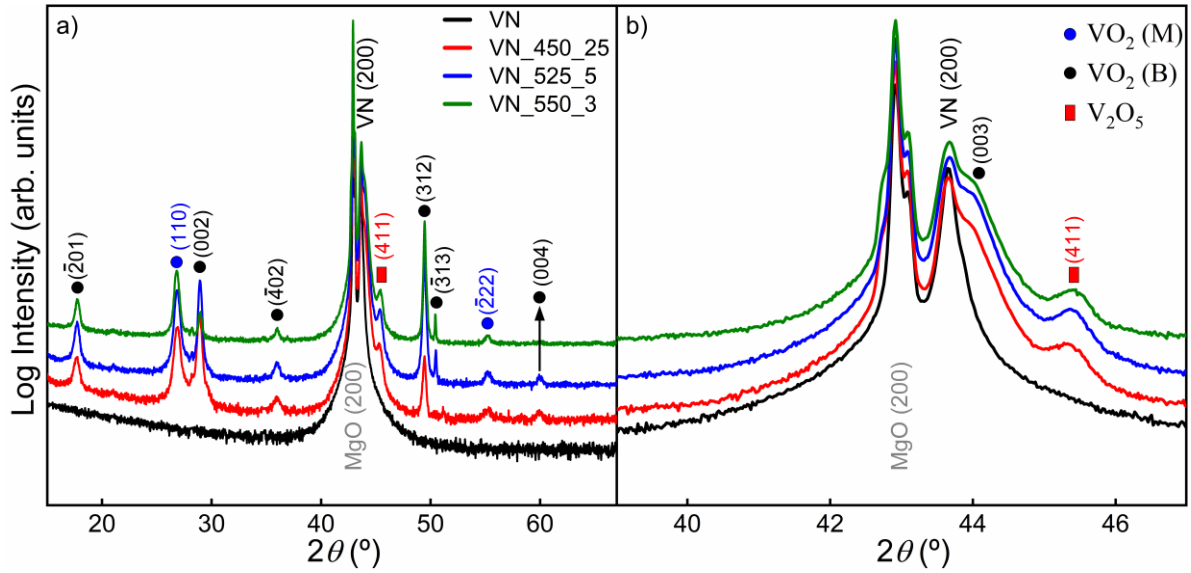

Figure 5.6 a) X-ray diffractograms of as-deposited epitaxial VN films (approx. 150 nm) on MgO substrate and the resulting oxide films after air-oxidation at three different temperatures for various durations. b) Zoom in the region where the Mg(200) and VN(200) are located.

For the sake of clarity in the notation throughout the thesis, from now on, we will use VO_2(M) when we refer to m-VO_2 that we have been studying so far. On the other hand, VO_2(B) will be adopted to designate the phase detected after oxidation of epitaxial VN films.

One approach to continue studying the oxidation of VN epitaxial films is to decrease the deposition time. In this way, there will be less matter to convert into VO_2. Therefore, we will continue the analysis with single-crystalline VN thin films of about 55 nm. Once again, the film is oxidized for 25 min at 450°C. Figure 5.7 exhibits the X-ray diffractograms of the as-deposited VN epitaxial films and the oxidized film on MgO substrate. The annealed epitaxial VN films in Figure 5.6 and Figure 5.7 exhibit similar diffractograms. The only discrepancy is that the oxide diffraction peak intensities are different in both figures, which is related to the grain size, crystallinity and the amount of oxide phase presented in the film. The thickness of the initial epitaxial VN films is quite different in both cases (almost three times higher for the samples oxidized in Figure 5.6) that explains the change in intensity in the diffractograms. Over again,

the (200) VN peak is still intense, which indicates that a significant residual VN layer is still present. This result confirms that the single-crystalline VN oxidizes in a completely different route than the polycrystalline VN films. A characteristic feature in a single crystal is the absence of grain boundaries, which play a crucial role in the oxidation of the VN samples. We believe that the nonexistence of grain boundaries on these films is the principal reason for the distinctive oxidation pathway. Indeed, the diffusion of oxygen species at the grain boundaries is not possible anymore.

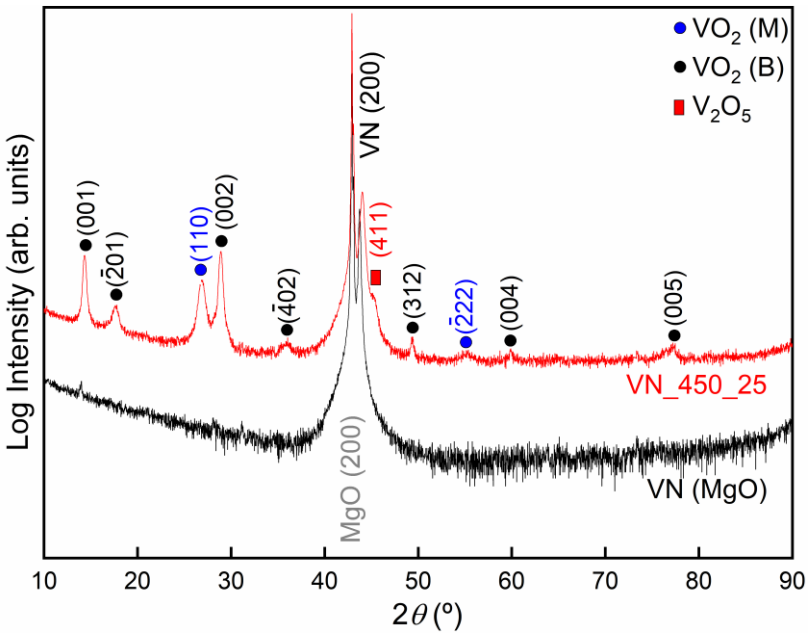

Figure 5.7 X-ray diffractograms of as-deposited and oxidized (450°C during 25 minutes) VN films (55 nm thickness) on MgO substrates.

Figure 5.8 depicts the room temperature Raman spectrum of the 55 nm VN epitaxial oxidized sample recorded to corroborate the XRD results shown in Figure 5.7. The spectrum features a mixture of phases; vibration bands located at 102 and 303 cm^{-1} are assigned to orthorhombic V_2O_5, whereas the bands detected at 133 and 416 cm^{-1} correspond to V_6O_{13} [228,229]. Yet, the V_6O_{13} phase was not detected by X-ray diffraction, suggesting that the amount of this phase is too low or that this oxide is amorphous. Moreover, the vibration bands located at 188, 265 and the enlarged one at 666 cm^{-1} are attributed to VO_2(B) [230,231]. Finally, the band at 500 cm^{-1} corresponds to VO_2(M) [184,232]. As already pointed out (Figure 3.2), several bands of different compounds may overlap, as could be the case, for instance, in the regions between 220 to 360 cm^{-1} and 360 to 480 cm^{-1}. To clarify a possible conflict, Figure 5.8

b) and c) depict the deconvolution performed in both regions revealing the accuracy of the results shown above. The Raman results confirm that there is a mixture of phases in the VN_450_25 (MgO) film.

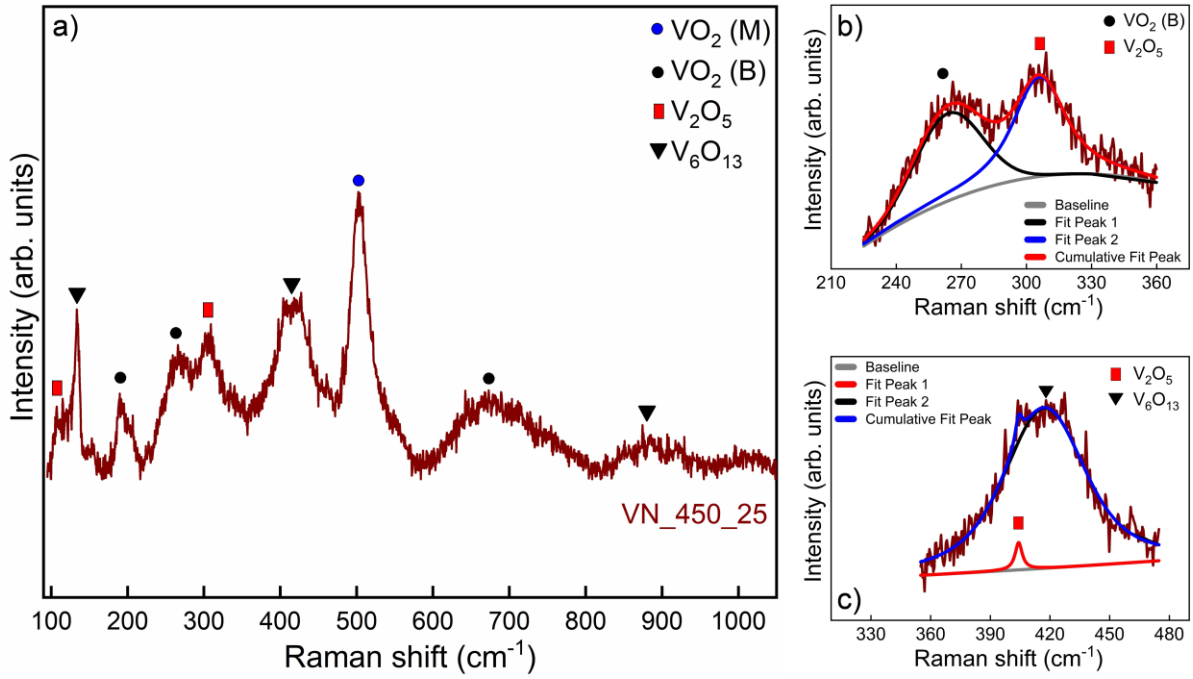

Figure 5.8 a) Raman spectra of air-oxidized (during 25 min at 450°C) VN film deposited on MgO; b) and c) depict the deconvolution of the vibration bands located between 220 to 360 cm^{-1} and 360 to 480 cm^{-1}, respectively.

The morphology of the oxidized epitaxial VN film is different from all that we have studied until now (Figure 5.9 a)). The surface resembles a grid of nanorods that form a right angle between them. In the left zone, the rods are bigger and in certain places form clusters that lose the order of the grid (not shown). However, in general, the sample has a typical surface as shown in Figure 5.9 b) (zoom in the center of Figure 5.9 a)). On the other hand, scattered throughout the sample appear structures without a well-defined shape that can be distinguished in the SEM image by its light color. Figure 5.9 c) depicts an AFM image on the same sample with a roughness of (2.60 ± 1.00) nm. The "light" colored structures from the SEM images also appear in the AFM, this is highlighted in Figure 5.9 d), where a height profile performed in one of these structures provides a value of 31 nm height with a 145 nm length. The AFM image indicates that the "light" colored structures are nanorods that grow perpendicular to the surface. In summary, in the vast majority of the sample, the surface is formed by a grid of nanorods

forming a right angle to each other, with additional nanorods coming out perpendicular to the surface.

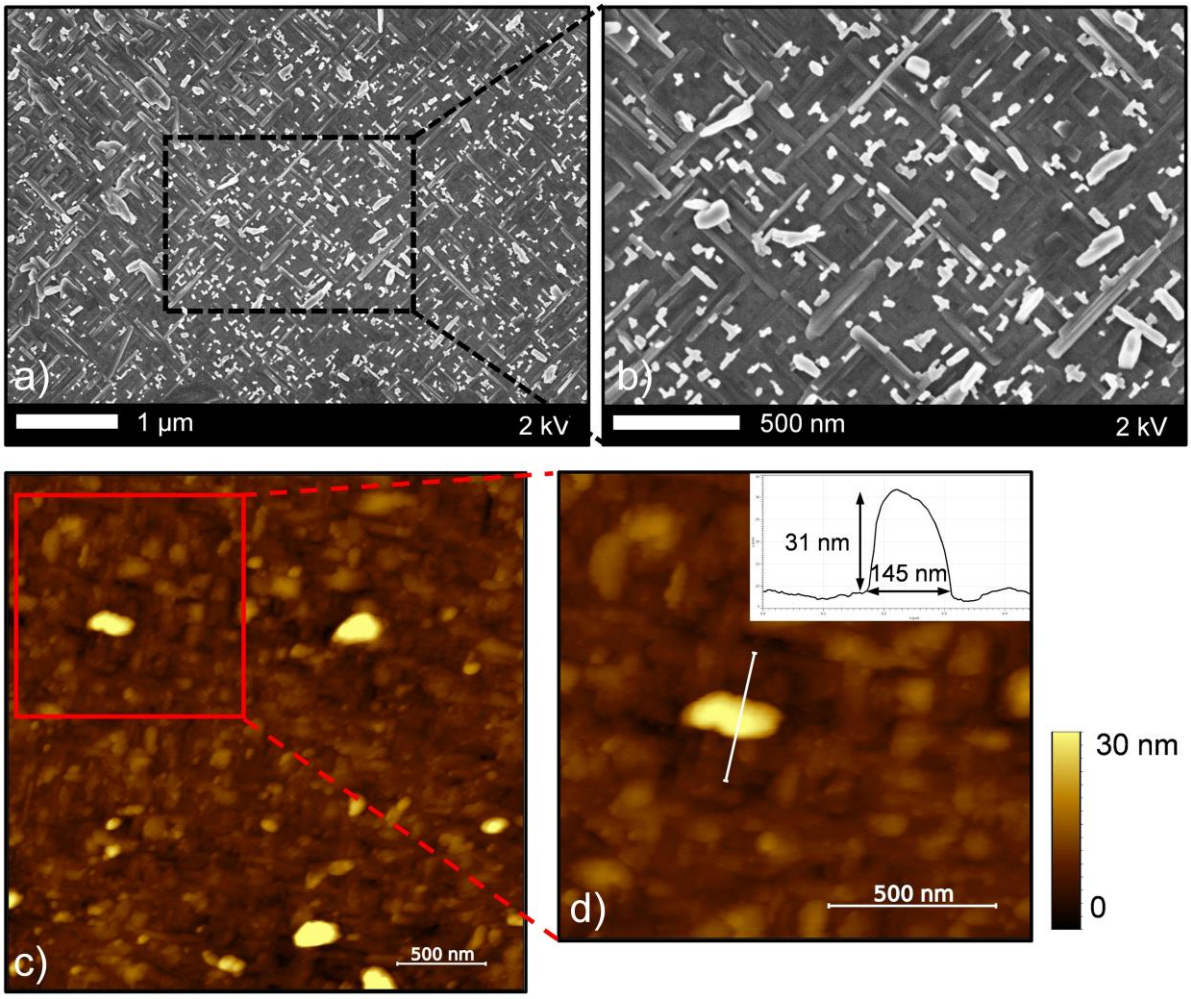

Figure 5.9 a) Top-view SEM image for the epitaxial VN film oxidized at 450°C during 25 minutes. b) zoom in the highlighted area of Figure 5.9 a). c) AFM image of the same sample and d) AFM image of the highlighted area in c).

X-ray diffraction and Raman results manifest a mixture of compounds in the oxidized VN epitaxial sample at 450°C for 25 minutes. From one side, the diffractogram displays a higher number of peaks corresponding to the VO_2(B) phase. Meanwhile, the Raman spectrum is different from the typical spectrum of the VO_2(M) and V_2O_5 phases shown so far. As previously stated, the morphology of this sample is unusual from that depicted so far. For all these reasons, we decided to perform a TEM analysis in the predominant area of the film (similar to the one shown in Figure 5.9 b)).

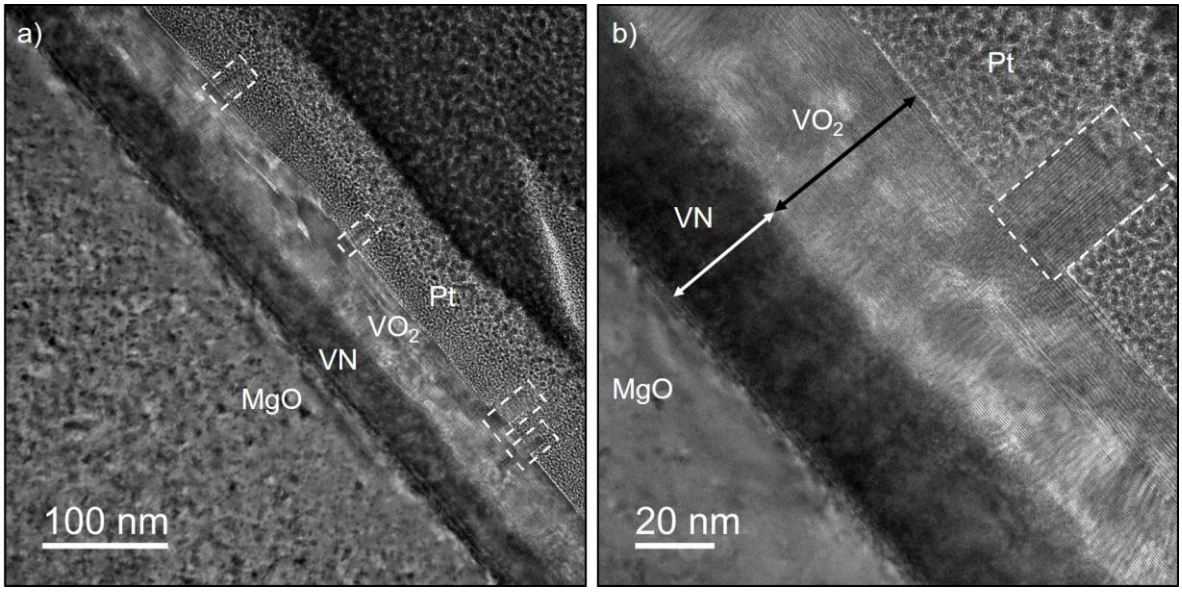

Figure 5.10 a) TEM cross-sectional image of the epitaxial VN oxidized at 450°C during 25 minutes. b) TEM cross-sectional image of the same film in an area where a nanorod perpendicular to the sample surface is clearly depicted. In both images the white-dashed rectangles highlight the nanorods perpendicular to the surface.

Figure 5.10 exhibits a TEM cross-sectional micrograph for the VN_450_25 (MgO) film, where two distinct layers are well defined. The first one corresponds to residual VN (as detected by XRD) with a thickness of around 35 nm. The second layer (approx. 55 nm thick) seems to be epitaxially grown on VN and presents the same growth direction. Nevertheless, there are defects throughout this layer, which could be dislocations and/or stacking faults, specific analysis (STEM images in a zone axis) is needed to corroborate this hypothesis. Furthermore, enclosed in white-dashed rectangles are found the nanorods perpendicular to the surface. Figure 5.10 b) depicts an image with a higher magnification that enables to distinguished the perpendicular nanorods. Since most of the peaks in XRD and vibration bands in Raman belong to VO_2, we believe that this oxide layer may match with VO_2(M) or VO_2(B). To clarify which VO_2 polymorph corresponds to the oxide layer an FFT pattern was performed on a HRTEM image in each of the layers and the interface, as shown in Figure 5.11.

The FFT pattern of the blue square has an excellent match with the $[00\bar{1}]$ zone axis of VN (Figure 5.11 c)). For the FFT pattern in the red square, corresponding to the oxide, the (001), $(\bar{2}00)$ and $(\bar{2}01)$ planes of VO_2(B) were identified. The measured interplanar distances are 0.619, 0.580 and 0.494 nm for the (001), $(\bar{2}00)$ and $(\bar{2}01)$ planes, in agreement with those

reported for VO_2(B) (PDF no. 04-007-0514). One interesting result is that both remaining VN layer and the oxide one exhibit a preferred growth orientation. On the other hand, Figure 5.11 d) represents the FFT pattern performed in the interface between the VN and the oxide (green square). The third point from the center to the growth direction matches the (003) plane for the VO_2(B) and the (200) plane for the VN. The interplanar distance obtained is 0.204 nm, in agreement with the theoretical values of 0.205 for the (003) plane of the VO_2(B) and 0.207 nm for the (200) plane of the VN. The results indicate that the predominant oxide layer on the film corresponds to VO_2(B) that grows with epitaxial relationships: VO_2(B) (001) || VN (200) out-of-plane and VO_2(B) (200) || VN (020) in-plane orientation.

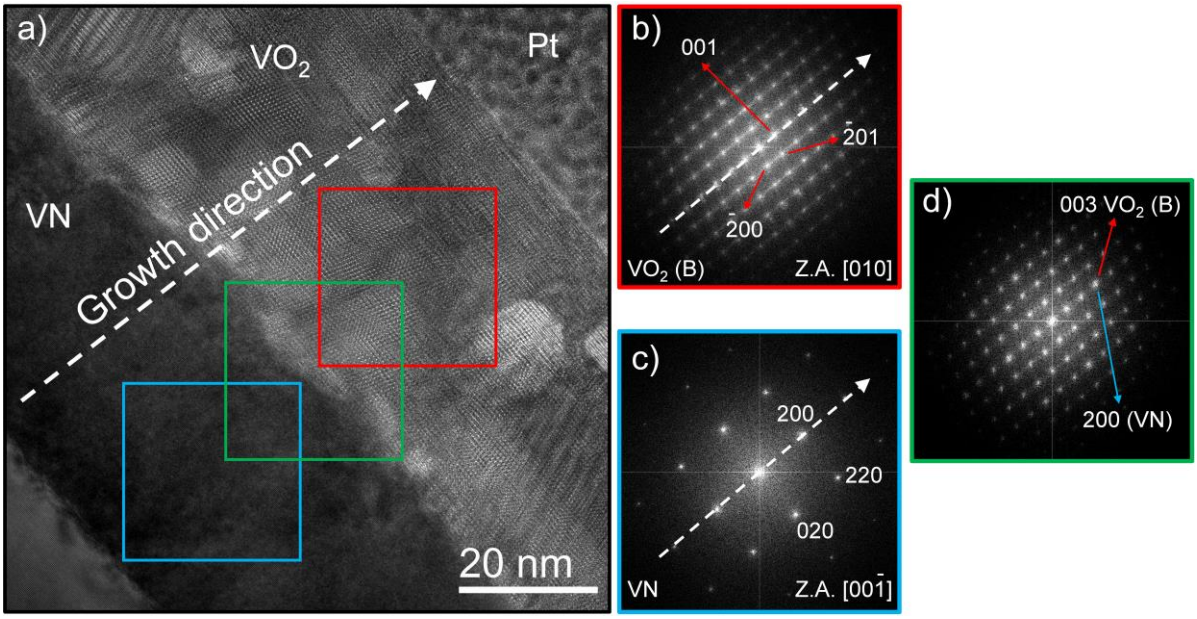

Figure 5.11 a) High-resolution TEM (HRTEM) micrograph for the VN_450_25 (MgO) film. FFT pattern of the region enclosed in the b) red square, c) blue square and d) green square.

However, there is still the inquiry about the phase that corresponds with the perpendicular nanorods. To better elucidate this, an EELS characterization is performed in two regions of the sample, one without and one with the presence of the perpendicular nanorods, corresponding to Figure 5.12 a) and Figure 5.12 b), respectively. In both images, there are four distinct regions equivalent to MgO, VN, VO_2(B) and Pt. EELS spectra recorded in six zones (labeled from 1 to 6) between the two images cover the VN zone (1 and 4), the VO_2(B) region (2, 3 and 5) and the Pt (6). In Figure 5.12 b), the white-dashed rectangles represent the zones with perpendicular

nanorods, in particular, the EELS spectra no. 6 is conducted in one of these regions. Figure 5.12 c) and Figure 5.12 d) exhibit the results for the EELS characterization in each of the six regions.

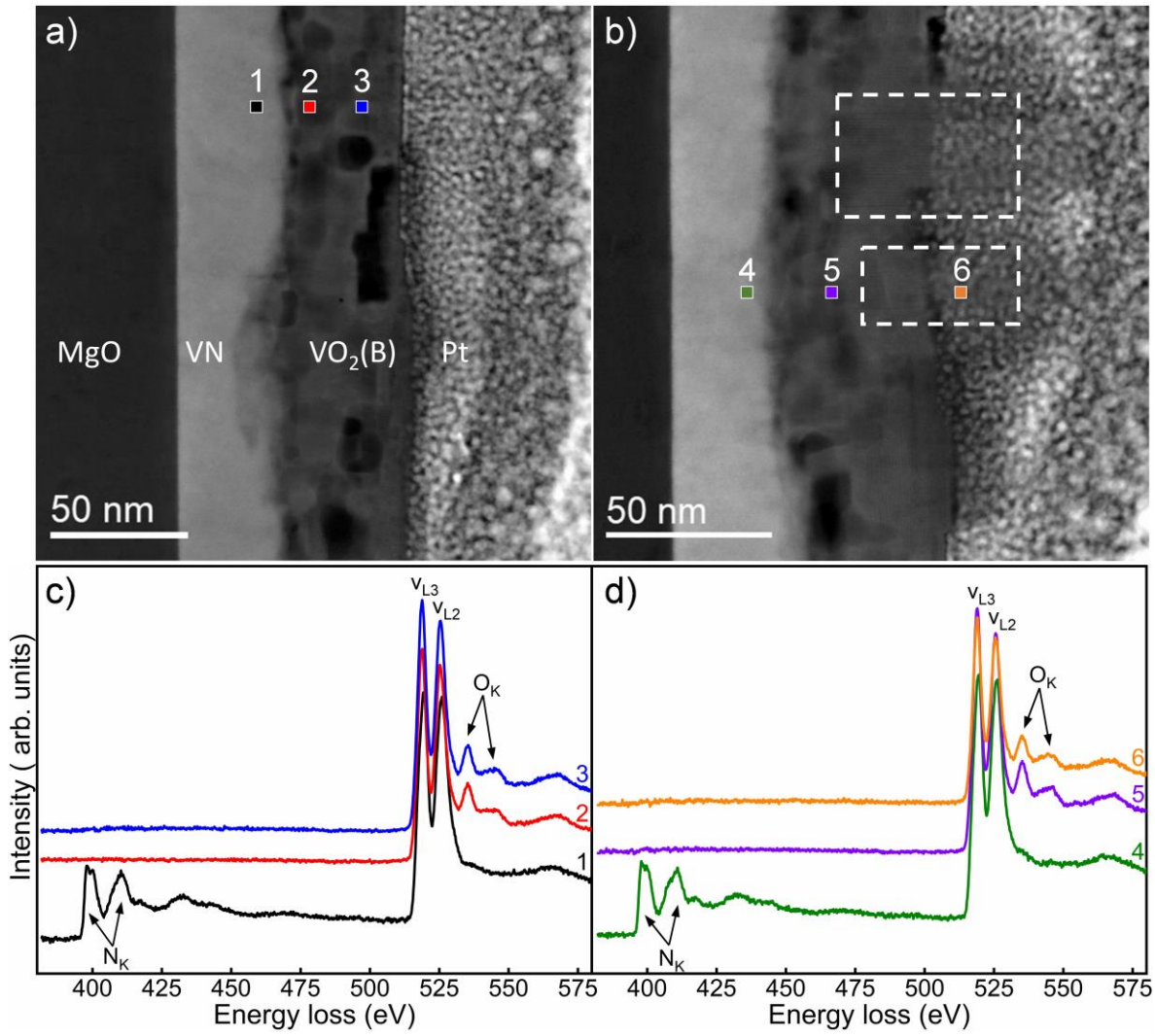

Figure 5.12 High angle annular dark field image of the sample VN_450_25 (MgO) in two different regions: a) without and b) with the presence of the perpendicular nanorods. EELS characterization was performed in three zones in each image labeled from 1 to 3 (Figure 5.12 a)) and from 4 to 6 (Figure 5.12 b)). c) and d) illustrates the EELS spectra of the three different zones of Figure 5.12 a) and b), respectively. The color of each curve corresponds to the area of the same color where the spectrum was conducted.

There are two differences between the EELS spectra concerning the VO_2(B) and VO_2(M) phases (see Figure 5.12 c) and Figure 5.12 d) for the VO_2(B), and Figure 3.5 b) for the VO_2(M) phase). The first is a shift of approximately 5 eV towards higher energies of the first O peak in VO_2(B) concerning the equivalent one in VO_2(M). The other difference is that the intensity of the second O peak (located approx. at 545 eV) is higher in the VO_2(M) phase. Furthermore, it

is relevant to mention, that in the EELS spectra, the chemical environment of the atom determines the shape, position, and intensity of the peaks related to each element. For example, V_{L3} = 513 eV and V_{L2}= 521 eV refer to metallic V, N_K = 401 eV and O_K= 532 eV indicate nitrogen and molecular oxygen. Yet, these values change when the elements form a compound. To our knowledge, there is no literature reporting the difference between the EELS spectra of VO_2(B) and VO_2(M). Therefore, it may be relevant to continue the study on this topic as a possible way to distinguish between these two VO_2 polymorphs.

Figure 5.12 c) and d) display that in zone 1 and 4 there are only peaks of V (V_{L3} and V_{L2}) and N, as expected for the remaining vanadium nitride layer. In zones 2, 3, 5 and 6, the spectra are equivalent (there are no peaks of N). The only difference between the spectrum of zone 6 with the spectra recorded in zones 2, 3 and 5 is the intensity of V and O peaks. This could be explained due to the presence of a sole nanorod in the Pt analyzed volume. Since the V and O peaks position, as well as the V/O peaks-intensity ratio, are constant, the labeled zones 2, 3, 5 and 6 corresponds to the same phase, VO_2(B). This result indicates that the perpendicular nanorods are also VO_2(B).

Once that VO_2(B) is confirmed as the predominant compound in the VN_450_25 (MgO) sample, it is crucial to check the optical properties. Figure 5.13 displays apparent infrared temperature (T_{IR}) of the VN_450_25(MgO) sample versus the sample temperature (T_S) during heating and cooling for the studied films. There is no thermochromic behavior since the slope does not change. The results of the thermal camera are in agreement with all the evidence presents so far, since the VO_2(B) is the predominant phase in the sample VN_450_25(MgO).

Although VO_2(B) is not thermochromic, it is possible to convert this phase into VO_2(M) by thermal treatment in Ar [34,35] or N_2 [36] atmospheres. We believe that conducting this process in our VO_2(B) films will lead to VO_2(M) with bigger grains than the polycrystalline VO_2(M) obtained in chapters 3 and 4, hence with better thermochromic performance. In the future, further investigation should be focused on this topic.

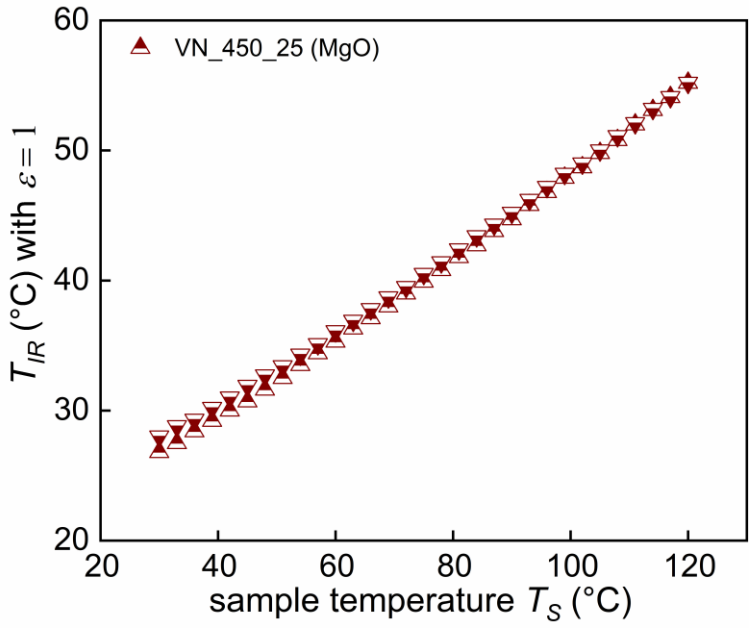

Figure 5.13 Thermal camera measurements of apparent infrared temperatures (T_{IR}), as a function of sample temperature (T_S) for the VN_450_25(MgO) films. Measurements are carried out by considering $\varepsilon = 1$ irrespective to the sample. Up and down triangles represent the profiles for temperature ramping up and down, respectively.

All the results concerning the annealing of epitaxial VN thin films display a distinct oxidation route compared with the findings in polycrystalline VN thin films from the semi-industrial machine. As previously mentioned, we consider that the nonexistence of grain boundaries on the epitaxial films is the principal reason for the distinctive oxidation pathway. However, it is vital to address that the deposition of the epitaxial VN films was conducted on a lab-scale sputtering machine under different conditions than those obtained from the semi-industrial reactor. For these reasons, VN films are deposited on Si substrate with the equal thickness (about 55 nm) on the lab-scale machine. The samples were grown with the same conditions as the epitaxial ones (applied current to the target 0.5 A, working pressure 0.22 Pa and Ar and N_2 flow rate of 30 and 5 sccm, respectively) except the deposition temperature (no intentional heating in the case of Si and 450°C for the MgO). Furthermore, it is worthy to note that both VN samples (on Si and MgO substrate) were oxidized simultaneously.

Figure 5.14 a) exhibits the X-ray diffractograms of the as-deposited VN on Si substrate and the oxidized film at 450°C for 25 minutes. The VN film features the (200) peak stronger than the (111) one. All the TEM studies performed in VN samples deposited on Si substrate have

always shown near the film-substrate interface a polycrystalline layer of around 20-40 nm thick composed of small VN grains with preferential orientation along the [200] direction. Vanadium crystallizes in the bcc structure, in which (110) is one of the densest planes with lower surface energy than other planes. Thus, at the beginning of the deposition, the vanadium adatoms tend to form clusters with (110) plane configuration on the substrate. Then, the nitrogen atoms occupy the four interstitial sites between the V atoms and settle the (200) plane of the fcc VN structure [227]. It has been suggested that low adatom mobility (low substrate bias and deposition temperature) is the key to obtain (111) texture [227]. In our case, the depositions are carried out at room temperature and with no substrate bias. Hence, the first stage (200) texture is followed by a (111) texture with increasing deposition time for VN films under these growing conditions. TEM analysis for films with higher thickness proves that the growth is columnar with large grains exhibiting a [111] preferred orientation (not shown). On the other hand, the oxidized VN film of Figure 5.14 a) displays that all diffraction peaks correspond to orthorhombic V_2O_5 (PDF no. 00-041-1426) with no sign of VN or VO_2, indicating that the sample is completely oxidized.

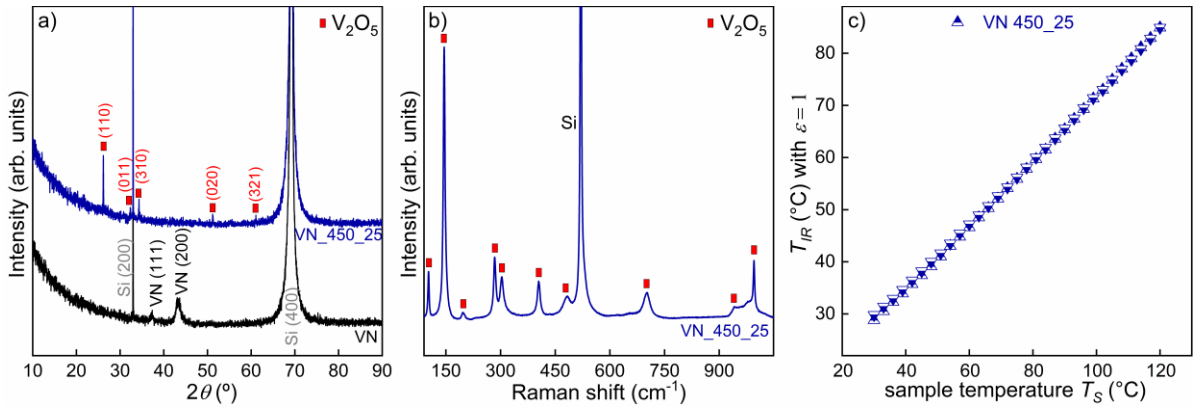

Figure 5.14 a) X-ray diffractograms of a VN film deposited on Si substrate at 0.22 Pa and the resulting oxide film after air-oxidation for 25 minutes at 450°C. b) Raman spectra for then oxidized film at 450°C for 25 minutes. c) Thermal camera measurements of apparent infrared temperatures (T_{IR}), as a function of sample temperature (T_S) for the VN_450_25 (Si) film. Up and down triangles represent the profiles for temperature ramping up and down, respectively.

Figure 5.14 b) depicts the Raman spectra recorded at room temperature on the VN_450_25 (Si) sample. The spectrum for the sample deposited on Si shows that the only phase identified is orthorhombic V_2O_5, with several bands detected at approx. 102, 145, 195, 282, 303, 405, 483,

701 and 995 cm^{-1} [182,183,186,228]. On the other hand, Figure 5.14 c) shows the IR thermal camera measurement for the VN_450_25 (Si) sample in the 30-120°C range. There is no change in the slope of the curve, therefore, not thermochromic behavior. The results from XRD, Raman and IR camera are in agreement and illustrate that V_2O_5 is the only phase present in the VN_450_25 (Si) sample.

The findings on the oxidized sample on Si substrate are dissimilar that the ones obtained in chapter 3 for samples oxidized under the same conditions. One possible reason is the distinct precursor initial thickness, around 175 nm for the films from the semi-industrial machine and 55 nm for those deposited on the lab-scale chamber. Nevertheless, we believe that the main difference comes from the deposition in two distinct sputtering chambers under dissimilar conditions. Hence, the next section will be dedicated to the possible relation between the deposition in different sputtering machines.

5.4 Impact of VN deposition conditions on its oxidation to obtain thermochromic VO_2: theoretical approach and experimental verification

In the previous section, we have exposed that even by applying the "best oxidation conditions" (found in chapters 3 and 4) to polycrystalline VN films (grown in the lab-scale sputtering machine) we are not able to reach the formation of VO_2(M). In this section, we will employ the criterion developed in section 2.4 to transpose the results found from one sputtering machine to another. The purpose is to determine the deposition conditions used in the lab-scale sputtering chamber to synthesize similar polycrystalline VN films to those deposited in the semi-industrial chamber. Within this objective, we should be able to oxidize these films with the already well-known oxidation conditions to form thermochromic VO_2.

It is worth to mention that the criterion established in section 2.4 to grow analogous films from different sputtering chambers is that the sputtered atoms coming from the target arrive with the same energy on the substrate surface. In our case, the deposition conditions of the semi-industrial machine are fixed. From equations (2.2)-(2.5), it is possible to calculate the values of working pressure (P) and target-substrate distance (d) to obtain the conditions to deposit similar

VN in the standard sputtering chamber. In the lab-scale machine, *d* was fixed to 9 cm, which represents the closest possible distance. In the semi-industrial chamber, the *P.d* value corresponds to a pressure of 0.56 Pa in the lab-scale chamber (*d* being 9 cm). Thus, we chose to conduct three sets of depositions in the lab-scale machine with different working pressure. Series I, with 0.22 Pa, the same value as the applied to obtain the epitaxial VN. The series II, with the corresponding working pressure (0.56 Pa). Finally, 0.83 Pa (series III), to also have a higher value than the expected (less dense films). Thereby the criterion will be evaluated.

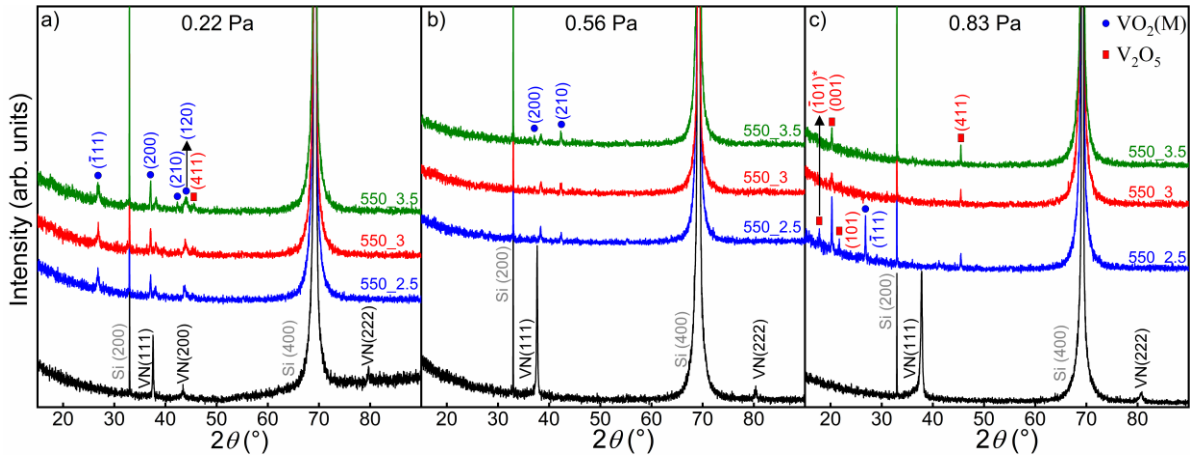

Figure 5.15 X-ray diffractograms of as-deposited VN films and the resulting oxide films after air-oxidation at 550°C during 2.5, 3 and 3.5 minutes for the three sets deposited with different working pressure a) 0.22 Pa (series I), b) 0.56 Pa (series II) and c) 0.83 Pa (series III).

Figure 5.15 depicts the X-ray diffractograms for as-deposited VN samples and air annealed films at 550°C during 2.5, 3 and 3.5 minutes deposited at three working pressures: 0.22, 0.56 and 0.83 Pa (Figure 5.15 a), b) and c), respectively). The thickness of the VN films are about 140, 150 and 170 nm for the different set of samples I, II and III, respectively. The oxidation conditions (time and duration) were based on those giving VO_2 with high thermochromic behavior from the oxidation of VN films (175 nm) obtained in the semi-industrial chamber . Moreover, under these conditions, the VN was completely oxidized. There are several differences in the oxidation of the samples coming from the three series. For the annealed films of series I (Figure 5.15 a)) and II (Figure 5.15 b)), the VN peaks intensity decreases but it is still evidenced even after 3.5 minutes of oxidation. This suggest that there is still a residual layer of VN nitride in all of these samples. On the contrary, none of the films belonging to the

series III (Figure 5.15 c)) exhibits a peak related to VN, which is an indication that the films are completely oxidized.

Concerning the oxides formed during oxidation, in Figure 5.15 a) the oxidized films present four peaks corresponding to VO_2(M) and one to orthorhombic V_2O_5. Thus, the results suggest the coexistence of three phases VN, VO_2(M), and V_2O_5, where VO_2(M) is the predominant compound. In the series II samples depicted in Figure 5.15 b), VO_2(M) is the only oxide phase detected. Finally, in Figure 5.15 c), VO_2(M) is identified only in the sample oxidized 2.5 minutes. All other peaks are assigned to V_2O_5. As the oxidation time increase the VO_2(M) disappears, thanks to the over oxidation, to form V_2O_5. These findings indicate that the only phase present after 3 minutes of oxidation is V_2O_5.

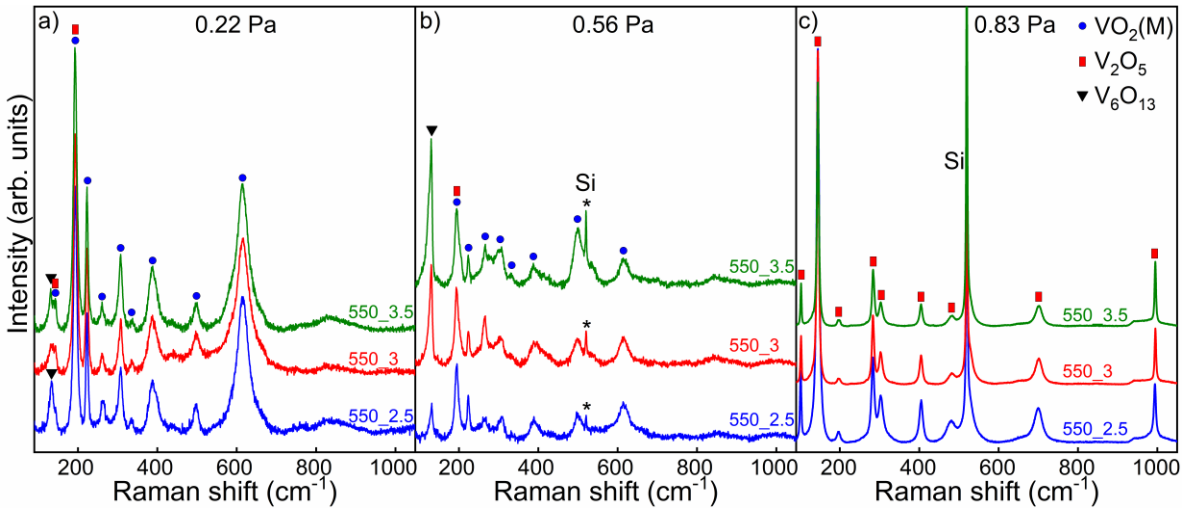

Figure 5.16 Raman spectra of air-annealed VN films at 550°C during 2.5, 3 and 3.5 minutes deposited with different working pressure a) 0.22 Pa, b) 0.56 Pa and c) 0.83 Pa.

Raman spectrometry is performed in all the oxidized films to corroborate the XRD results (Figure 5.16). As mentioned in chapter 3, the presence and intensity of the Si vibration band (520.7 cm^{-1}) is a powerful tool to monitor VN oxidation. None of the series I samples in Figure 5.16 a) present the Si band, then, a significant layer of VN must be still present in the films. On the other hand, all the series II films exhibit the Si band, indicating the thickness of the remaining VN films is small. However, the Si band intensity is quite low for the sample oxidized for 2.5 minutes. As the oxidation time increases, the signal becomes pronounced, indicating a decrease of the residual VN layer thickness. For the films displayed in Figure 5.16

c), the Si band is more intense than all the other vibration bands, which is associated with the complete oxidation of the VN layer.

All the spectra in Figure 5.16 a) are similar, with most of the vibration band located at 222, 260, 308, 337, 388, 500 and 613 cm^{-1} assigned to VO_2(M) [182–184,232]. Besides, there is a band in 133 cm^{-1} that corresponds to V_6O_{13} [228,229]. This vibration band slightly change for the samples oxidized 3 and 3.5 minutes, attributed to a new band at 143 cm^{-1} ascribed to VO_2(M) or orthorhombic V_2O_5 [182,183,186,228]. On the three samples, there is also a band at 195 cm^{-1} that matches either with VO_2(M) or orthorhombic V_2O_5 [182–184,186,228]. The spectra of Figure 5.16 b) and Figure 5.16 a) are alike (except for the band at 143 cm^{-1}), yet with different intensities. The predominant phase is also VO_2(M). On the contrary, the films of Figure 5.16 c) depict equivalent spectra among them, yet completely different from the ones of Figure 5.16 a) and Figure 5.16 b). The only phase identified is orthorhombic V_2O_5, with several bands detected at approx. 102, 145, 195, 282, 303, 405, 481, 700 and 995 cm^{-1} [182,183,186,228].

The XRD and Raman results evidence the difference in the VN oxidation for each working pressure. When the films deposited at 0.22 Pa are oxidized, there is a coexistence of phases: an important residual layer of VN and VO_2(M). The samples grown at 0.56 Pa and oxidized, must have a thinner layer of VN and VO_2(M) appears as the predominant phase. Finally, the samples deposited at 0.83 Pa and then air-annealed, are entirely oxidized, with orthorhombic V_2O_5 as the principal compound.

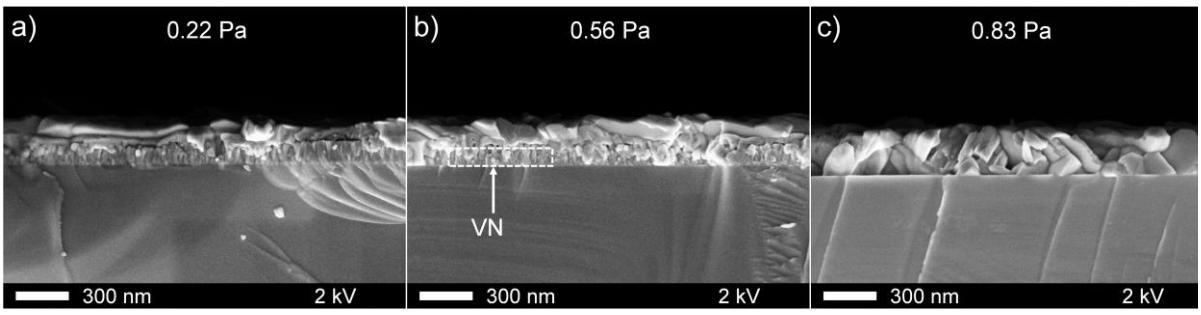

Figure 5.17 SEM cross-section images for VN samples deposited at different working pressure a) 0.22, b) 0.56 Pa and c) 0.83 Pa and afterwards oxidized at 550°C during 3.5 minutes.

Figure 5.17 depicts a SEM cross-section image performed on each of the samples oxidized during 3.5 minutes at 550°C for the three working pressure. Figure 5.17 a) exhibits on top of the Si substrate a continuous columnar VN layer and above a coating with different morphology

(possibly VO_2(M)). Figure 5.17 b) displays enclosed in a dashed-white rectangle a discontinuous VN layer. It is important to mention that the presence of a VN layer is irregular. On top of the VN layer, there is a film with a distinct morphology that should correspond to VO_2(M)). On the contrary, Figure 5.17 c) depicts that there is no VN, the films characterized by big grains with different shapes correspond to orthorhombic V_2O_5. Figure 5.17 validates the results obtained by XRD and Raman spectrometry suggesting that the remaining VN layer is only observed with a deposition pressure of 0.22 and 0.56 Pa.

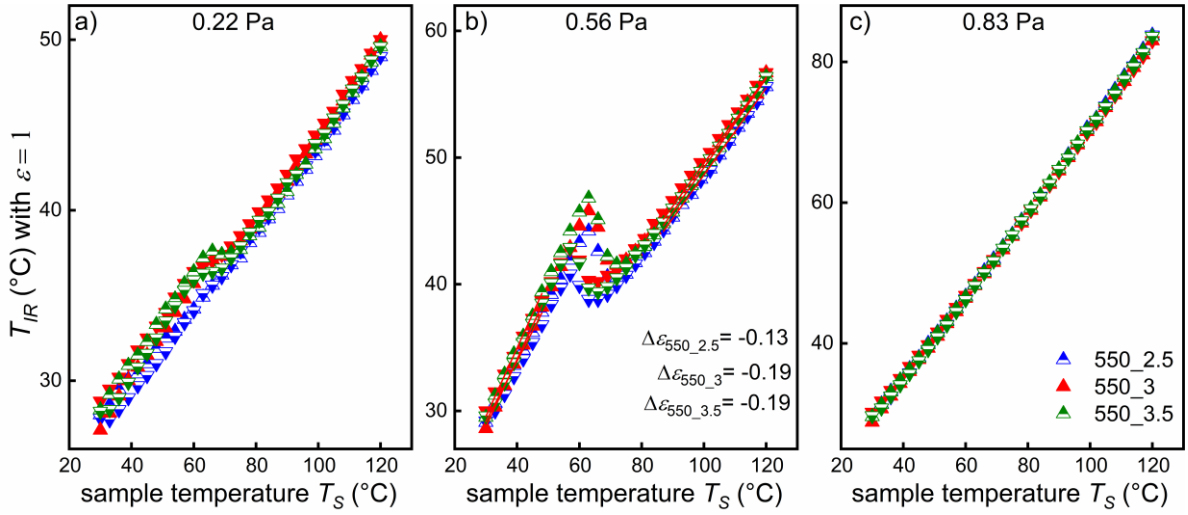

Figure 5.18 Thermal camera measurements of apparent infrared temperatures (T_{IR}), as a function of sample temperature (T_S) for films of the three different series a) I, b) II and c) III oxidized between 2.5 and 3.5 min at 550°C. Up and down triangles represent the profiles for temperature ramping up and down, respectively. Measurements were carried out by considering an emissivity equal to 1 irrespective to the sample.

To verify the thermochromic performance of the films, the optical modulation properties in the infrared domain are studied using an infrared camera. Figure 5.18 represents the apparent infrared temperature (T_{IR}) of samples monitored versus the sample temperature (T_S) during both, heating and cooling for the three series of oxidized films. None of the oxidized samples illustrated in Figure 5.18 a) and Figure 5.18 c) exhibits neither hysteresis loop characteristic of a thermochromic behavior nor change in the slope. In Figure 5.18 a), this is the result of the residual VN layer found in the samples. For the films presented Figure 5.18 c), it is due to the complete conversion of the VN into V_2O_5. On the other hand, all samples displayed in Figure 5.18 b) show thermochromic performance, even with a residual VN layer.

These results evidence the influence of the VN deposition pressure on its oxidation behavior to form a thermochromic VO_2(M) phase. As predicted, the only samples that display a thermochromic behavior are the ones deposited at 0.56 Pa, even with the presence of a residual VN layer. Samples deposited with lower pressure (0.22 Pa) are denser and more difficult to oxidize. On the contrary, films deposited with higher pressure (0.83 Pa) are less dense and easy to oxidize. These findings reveal the relevance of our criterion to produce analogous films through different sputtering machines. The conditions obtained could be employed as initialization parameters to transpose deposition from one sputtering chamber to another (even to industrial scale). Moreover, it could be used to reproduce results from other articles.

Although the encouraging results, the final films (series II) were not completely oxidized. Therefore, it is necessary to improve the criterion. The idea is to include a term without excessively increase the criterion complexity. Under this condition, we should first check the current density (j) applied to each target. The racetrack surface in each target is different, approx. 58.6 cm^2 for the semi-industrial target and 10.7 cm^2 for the 2" target diameter. The calculated values for each target (semi-industrial and lab-scale) are $j^{semi-ind} = 25.6\ mA/cm^2$ and $j^{std} = 46.7\ mA/cm^2$, with a ratio of $\frac{j^{std}}{j^{semi-ind}} = 1.8$. Therefore, the V flux is higher for the films deposited in the lab-scale machine, while the N_2 flow rate is the same for both depositions (see Table 2.1). Hence, the concentration of V is more important in the films deposited in the lab-scale machine than the ones produced in the semi-industrial chamber, as a consequence, the oxidation step is different. In future works, we will include the equality of the current density to validate this assumption. Such a conclusion may also be useful to study the oxidation of epitaxial VN films but keeping in mind that the absence of grain boundaries strongly influences the oxidation kinetics.

5.5 Chapter conclusions

In this chapter, we deposit epitaxial VN on MgO substrate in the lab-scale sputtering machine. The epitaxial films have been submitted to a thermal treatment after their deposition to obtain stoichiometric VN films. The results from XRD, RHEED, EBSD and HRTEM

microscopy analyses prove that VN films grow with film/substrate epitaxial relationships: VN (100) || MgO (100) and VN [010] || MgO [010].

The VN epitaxial films oxidize within the conditions determined in chapters 3 and 4, follow a completely different oxidation pathway. Even a thin VN layer (about 55 nm) is very difficult to oxidize, which could be caused by the absence of grain boundaries in the epitaxial layers. The XRD and Raman results display a mixture of phases, with VO_2(B) as the predominant compound. Remarkably, oxidation leads to epitaxial growth between VO_2(B) and VN with the following relationships: VO_2(B) (001) || VN (200) out-of-plane and VO_2(B) (200) || VN (020) in-plane orientation, as shown by the TEM results. Moreover, the SEM images and the AFM results depict a completely different surface morphology for the VO_2(B) phase, with nanorods perpendicular to the substrate. As expected, the VO_2(B) phase does not exhibit a thermochromic behavior, corroborated by the IR camera findings.

In the last section of the chapter, we apply a criterion to compare the deposition conditions between the two sputtering machines used in this thesis. Three sets of VN films were deposited, series II with the equivalent conditions of the semi-industrial chamber, series I with lower working pressure and series III with higher working pressure. All films were oxidized at 550°C for up to 3.5 minutes. The XRD, Raman and SEM results display that:

- The oxidized VN samples of series I (0.22 Pa) present a significant VN residual layer, with VO_2(M) phase as the predominant oxide.
- The air-annealed VN films of series III (0.83 Pa) are completely oxidized, with V_2O_5 as the only phase present.
- The oxidized VN samples of series II are not completely oxidized. However, there is less VN than in the air-annealed films of series I. The principal phase of these films is the VO_2(M) phase.

None of the VN oxidized samples deposited at 0.22 and 0.83 Pa evidence thermochromic properties. For the series I films, it is a consequence of the residual VN layer found in the samples. For series III, it is due to the complete conversion of the VN into V_2O_5. Only the oxidized films deposited with the analogous conditions (series II) show thermochromic

performance, even with a residual VN layer. Our criterion evinces that it is possible to transpose deposition from one sputtering chamber to another (even to an industrial scale).

Chapter 6

Second example of new precursor for the VO_2 synthesis: V_2N a promising material to get tunable emissivity switch

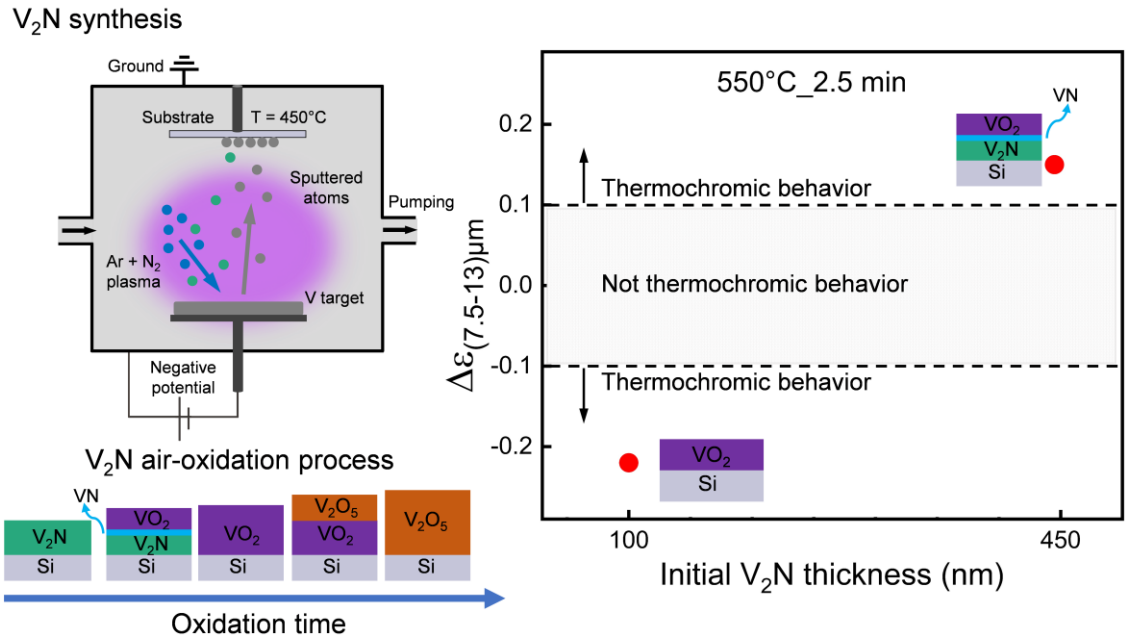

Abstract

In this chapter we present a second new precursor for the synthesis of VO_2 thin films after controlled oxidation. V_2N thin films have been deposited on Si substrates by reactive magnetron sputtering and their properties have been compared to the well-know VN phase: structure, mechanical, electrical and optical properties. The results evidence that the EELS spectra could be used as a fingerprint to distinguish between both phases. Thermochromic VO_2 films have been obtained by air oxidation of V_2N samples performed at two temperatures (450 and 550°C). X-ray diffraction and Raman spectrometry of the V_2N oxidized films evidence that VO_2(M) and V_2O_5 are the only phases obtained throughout the oxidation process. VO_2(M) is the first oxide formed, it coexists with V_2N for a long time at 450°C or swiftly vanished at 550°C. EELS results show that the oxidation of V_2N to VO_2(M) shows a special feature. Indeed, the oxidation of V_2N induces the release of nitrogen that is either evacuated in the gas phase or is used to

fully nitride the remaining V_2N layer inducing the formation of VN at the interface between V_2N and VO_2. When the oxidation duration exceeds a critical value, V_2O_5 is formed, diminishing the thermochromic performance of the films. A very interesting result has been obtained as a function of the thickness of the initial V_2N layer. When it increases from about 100 nm to 445 nm, the optical modulation properties of the formed VO_2(M) films change from a negative value of $\Delta\varepsilon$ to a positive value. These results may pave the way for future research on the oxidation of V_2N as a new precursor to form high-quality thermochromic VO_2(M).

Contents

6.1 Introduction

The attractive physical properties of transition metal nitrides (TMN), such as high hardness and high melting points, are of great interest in numerous industrial applications. When used as protective coatings on cutting tools and other mechanical components, they provide resistance to wear and extended life. The crystallographic phase, morphology, and chemical composition of the TMN determine their mechanical and electronic properties.

It is reported that most of the equiatomic TMN crystallize in the well-known NaCl-type structure. However, there is also a stable hexagonal phase for some nitrides, such as Cr_2N, Ta_2N, V_2N, δ-MoN [233–235]. In the particular case of V_2N, there are not as numerous studies on its properties and possible applications as for VN. One of the first studies carried out by Christensen and Lebech in 1979 described the formation of V_2N by melting single crystals of the cubic phase $VN_{0.74}$ in nitrogen at 1 MPa [18]. X-ray diffractograms indicate that the center of the sample was almost pure V_2N and that the surface contained a minor fraction of VN [18].

In 1996 Chu *et al*. deposited polycrystalline VN films onto M2 steel substrates by sputtering a vanadium target in an Ar + N_2 atmosphere. The dominant parameter for the formation of different compounds (crystalline V metal, hexagonal V_2N_x, cubic VN_x, amorphous V–N solid solution, and their mixtures) was the nitrogen partial pressure. Among these phases, V_2N exhibits the highest hardness. Thus, these authors studied the effect of substrate bias by fixing the nitrogen partial pressure. The XRD results depicted that the crystallinity was modified with higher substrate bias, although the crystal structure remained the same. They also detected that increasing the target power (keeping the nitrogen flow rate and the substrate bias constant) changed the phases from VN to V_2N, maybe due to the decreasing nitrogen partial pressure in front of the target with increasing target power [217].

Recently, Wu *et al.* performed an optimization of deposition conditions to obtain high-quality VN thin films [218]. The samples were deposited on Si (100) substrates by magnetron sputtering. The selected processing parameters were substrate bias, nitrogen flow rate, substrate temperature and substrate rotational speed. They found V and V_2N as the main phases when the N_2 flow rate was at the minimum value (1 sccm), substrate bias was -65 or -90 V, and the

deposition temperature was either 300 or 450°C. Once again, V_2N exhibited the highest values of hardness than VN films.

Based on our success to obtain VO_2 films from the oxidation of VN and since another nitride is known in the binary V-N system, the objective of this chapter is first to deposit pure V_2N phase on Si (100) substrates (see chapter 2 for more details in the deposition conditions). Second, to study the ability of V_2N to become a precursor for VO_2 synthesis. We also compare the structure, microstructure, optical and electrical properties of VN and V_2N films. Finally, the last section of this chapter is devoted to the study of the effect of the initial V_2N thickness in the optical modulation properties of the VO_2.

The films are labeled "V_2N" for as-deposited films and "V_2N_temperature_time" for the films oxidized at various temperatures and annealing durations.

6.2 Comparison of structure, microstructure, optical and electrical properties of VN and V_2N thin films

The X-ray diffractograms of VN and V_2N thin films prepared by reactive sputtering in the lab-scale chamber are depicted in Figure 6.1. The deposition parameters of this series of three samples are shown in Table 6.1. The total amount of flow rate gases (Ar + N_2) remains unchanged for each of the three depositions. Sample S1 presents peaks located at approx. 37.6, 43.5 and 80.2° corresponding to (111), (200) and (222) planes of the face-centered cubic VN structure (PDF no.00-035-0768), respectively. Note that S1 was deposited with the same parameters as non-epitaxial VN films (see first section of chapter 5).

Table 6.1 Growth conditions of samples S1, S2 and S3 shown in Figure 6.1 obtained in the lab-scale sputtering machine.

Sample	Thickness (nm)	V target current (A)	Pressure (Pa)	Ar flow rate (sccm)	N_2 flow rate (sccm)	Deposition temperature (°C)
S1	520	0.5	0.22	30	5	RT
S2	430	0.7	0.22	33.5	1.5	RT
S3	450	0.7	0.22	33.5	1.5	450

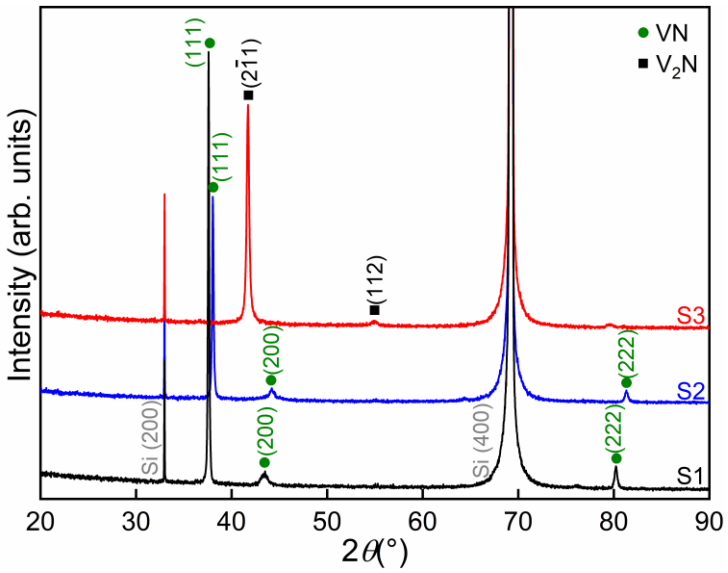

Figure 6.1 X-ray diffractograms of as-deposited VN and V_2N films on silicon substrate at room temperature and at 450°C. The deposition parameters of the three samples are shown in Table 6.1.

The first step towards the deposition of V_2N was to increase the V target current and decrease the amount of nitrogen flow rate (see sample S2 in Table 6.1). However, the diffractogram of S2 (Figure 6.1) exhibits the VN peaks shifted to higher angles indicating that changing these parameters is not enough to form V_2N. The peak position shift may come from the variation of the film stoichiometry or to the stress level. The only relevant parameter that can be modified is the deposition temperature (compared to the work of Wu *et al*. [218]). The sample S3 deposited at 450 °C displays new peaks detected at approx. 41.7 and 54.9° ascribed to the (2$\bar{1}$1) and (112) planes of the hexagonal V_2N phase (PDF no.00-033-1439), respectively. These peaks cannot be assigned to VN diffraction peaks. No other peak is noticed except those of silicon substrate, which indicates that the sample S3 only contains the crystalline V_2N phase.

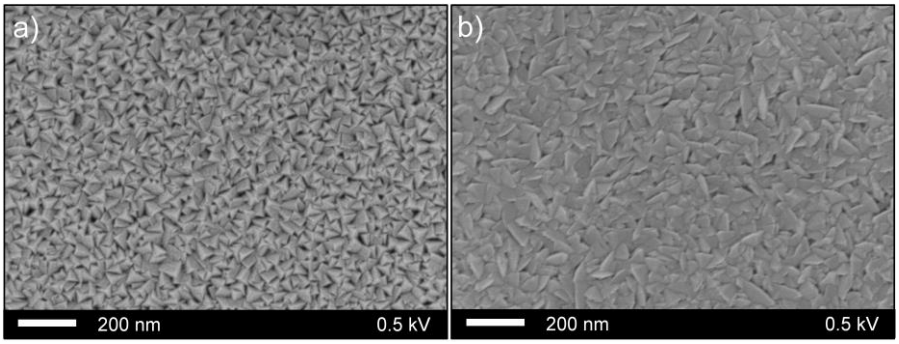

Figure 6.2 Top-view SEM images corresponding to the as-deposited a) VN film (sample S1) and b) V_2N film (sample S3).

We will continue the analysis with samples S1 and S3 since they only feature the VN and V_2N phases, respectively. Figure 6.2 depicts the surface morphology of sample S1 and S3. As already presented, the VN film (Figure 6.2 a)) shows small pyramidal-shaped grains in agreement with the [111] preferred orientation observed by XRD. On the other hand, V_2N displayed in Figure 6.2 b) exhibits an elongated structure, with bigger grains than the one of VN. In both images, the grain boundaries are clear and well defined.

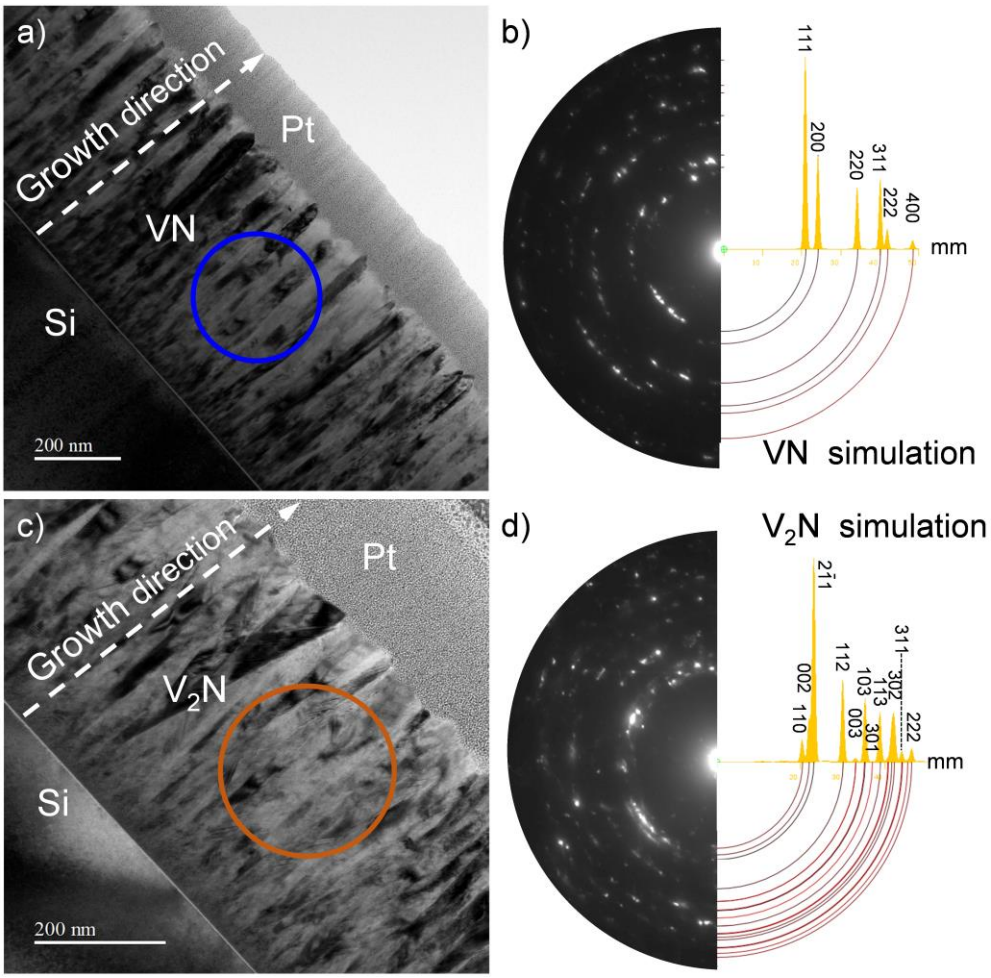

Figure 6.3 TEM cross-sectional images of a) S1 and c) S3 samples. SAED pattern performed at c) the blue circle for the S1 film and d) the orange circle for the S3 film. The simulation carried out for each SAED pattern is also shown in the right region of the pattern.

TEM analysis carried out on the S1 and S3 films (Figure 6.3 a) and c), respectively) illustrates that both samples present a columnar microstructure. Figure 6.3 b) and d) show the selected area electron diffraction (SAED) patterns performed in a region of the films (blue and orange circle in Figure 6.3 a) and c)) reveals that both samples are polycrystalline. Only VN is detected in the sample S1 while V_2N is the only phase detected in sample S3. The recorded

SAED patterns match well with the simulation ran for each compound as depicted in Figure 6.3 b) and d). These SAED results agree well with the XRD ones.

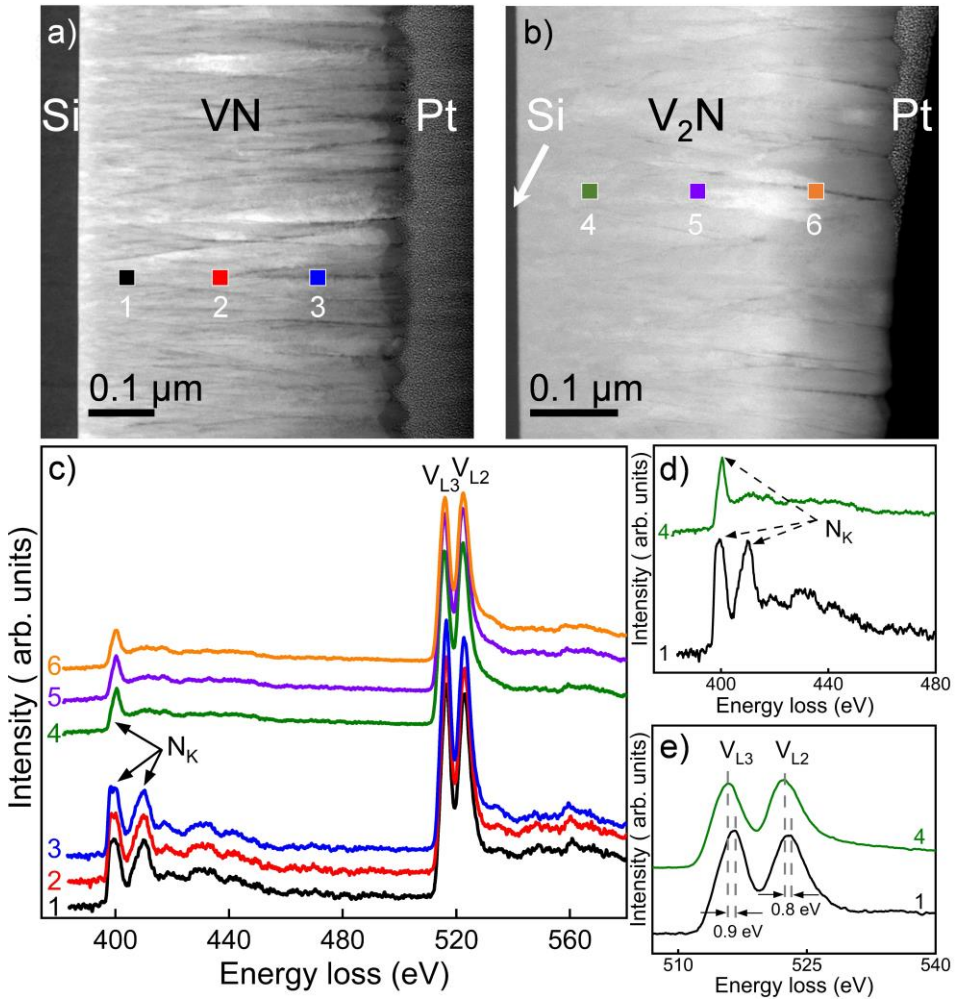

Figure 6.4 High angle annular dark-field image of the samples a) S1 and b) S3. c) EELS spectra of the three highlighted zones in each image labeled from 1 to 3 and from 4 to 6. d) and e) illustrate a zoom for the zone 1 and 4 in the specific range of nitrogen peaks (N_K) and vanadium peaks (V_{L3} and V_{L2}), respectively. The color of each curve corresponds to the area of the same color where the spectrum was conducted.

Figure 6.4 a) and b) show a high angular annular dark-field image (HAADF) of samples S1 and S3, respectively. In both images, there are three distinct regions equivalent to Si, VN (Figure 6.4 a)) or V_2N (Figure 6.4 b)), and Pt. Figure 6.4 c) illustrates EELS spectra recorded in both films (labeled from 1 to 6). Spectra from 1 to 3 cover the VN region, and spectra from 4 to 6 denote the V_2N one. There are remarkable differences in the results for the VN and V_2N compounds. The VN spectrum exhibits two clear peaks corresponding to nitrogen (N_K), while

only one peak is evidenced for the V_2N phase. Besides, the VN displays a less intense and broad peak around 430 eV, which is not present in the V_2N spectrum (Figure 6.4 d)). The presence of one or two peaks for the nitrogen element has been already found in CrN and Cr_2N [234,236,237], and also in VN and V_2N [238,239]. The differences concerning the V peaks (V_{L3} and V_{L2}) lie in the position and the ratio between the intensities of both peaks. For the VN, the V_{L3} peak intensity is always higher than the V_{L2} one. For the V_2N, the intensity ratio between the V peaks is the opposite of the VN results, which is different from the reported results by Hofer *et al*. [239]. These features in the VN and V_2N spectra could be used as a fingerprint to distinguish both compounds at the TEM scale.

Table 6.2 Hardness and Young's modulus of samples S1 and S3.

Sample	Hardness (GPa)	Young's Modulus (GPa)
S1 (VN)	4.0 ± 0.1	96 ± 1
S3 (V_2N)	9.5 ± 0.3	139 ± 3

Once we illustrate how the structure and microstructure of VN and V_2N differ, we perform complementary measurements to compare the mechanical, optical and electrical properties of both compounds. The hardness and Young's modulus of the studied films were measured by an Anton Paar Ultra Nano-Hardness Tester ($UNHT^3$) equipped with a Berkovich diamond indenter head. To control the penetration depth to less than one-tenth of the film thickness, which avoids the substrate effect, the applied loads were 0.8 mN (VN) and 1.4 mN (V_2N). At least 15 indentations were conducted for both samples, and the average values are shown in Table 6.2. The Young's modulus and hardness of the V_2N film are higher than the VN, in agreement with the literature [217,218,240]. An attractive topic for future works is to improve the hardness of V_2N by applying a substrate bias during deposition.

To compare the optical properties of both compounds, reflectance measurements were carried out in the 250-2500 nm range using a Varian Cary 7000 UV-vis-NIR spectrophotometer with a coupled integrating sphere. Figure 6.5 a) illustrates the total reflectance for the S1 and S3 samples. Moreover, the specular and diffuse reflectance are depicted in Figure 6.5 b) and c), respectively. The sample S1 exhibit a minimum of the total reflectance at approx. 250 nm that is related to the plasmon absorption of VN [241]. Within the studied wavelength range, the

position of the absorption band of V_2N cannot be estimated. The S3 (V_2N) specular reflectance is higher than the S1 (VN) in the 250-815 nm range. Above 815 nm, the VN sample becomes more reflective than the V_2N one. The specular reflectance for the VN (V_2N) is in the scope of 13% at 250 nm to 34% at 2500 nm (17% at 250 nm to 32% at 2500 nm). The diffuse reflectance exhibits the same behavior for both films, suggesting that the samples' roughness is quite similar. This indicates that the difference in the total reflectance for both compounds is given entirely by the behavior of the specular reflectance.

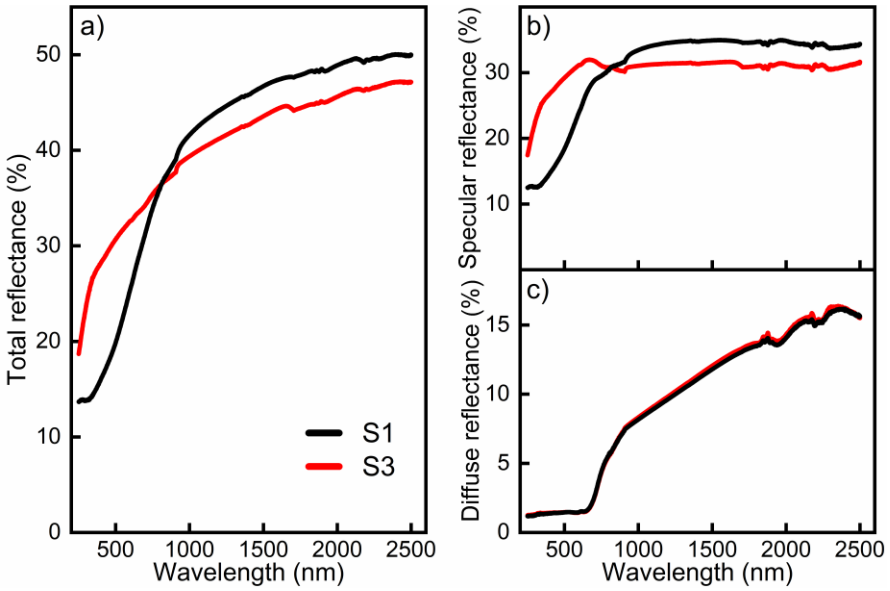

Figure 6.5 a) Evolution of a) total, b) specular and c) diffuse reflectance spectra at normal incidence as a function of the wavelength for samples S1 and S3.

Figure 6.6 depicts the dependence of resistivity with temperature for the S1 and S3 films in the 30-120°C range. The resistivity for both samples increases linearly with temperature as expected for metallic conductors. The values at 30°C are $\rho_{VN} = 178.4$ μΩ cm and $\rho_{V_2N} = 185.7$ μΩ cm, indicating that both materials exhibit quite the same electrical properties. The temperature coefficient of resistance defined as $TCR = \frac{1}{\rho}\frac{d\rho}{dT}$ is dissimilar for both films $TCR_{VN} = 3.7\ 10^{-4}$ K^{-1} and $TCR_{V_2N} = 2.0\ 10^{-4}$ K^{-1}. Note that the sample with higher resistivity (S3) shows lower total reflectance in the near infrared region, in agreement with theory and literature [242,243].

In this section, we have illustrated the required changes in the films deposition conditions to obtain V_2N. It is mandatory to decrease the amount of nitrogen, increase the V target current

and the deposition temperature. However, the application of a negative bias to the substrate is not necessary. Besides, the principal differences between VN and V_2N are shown. The next section is dedicated to the study of the V_2N oxidation.

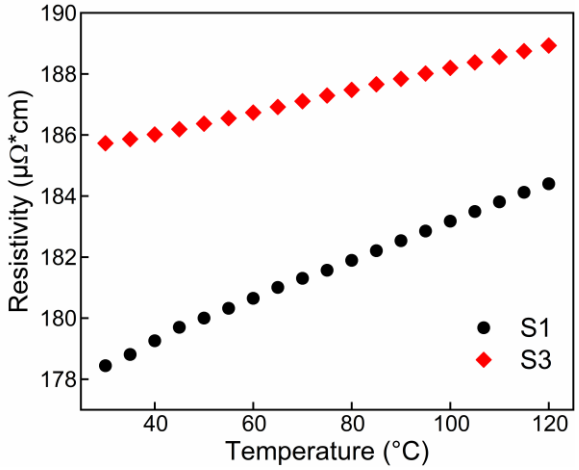

Figure 6.6 Resistivity evolution of samples S1 and S3 with the temperature in the 30-120°C range.

6.3 Oxidation of V_2N thin films as an original precursor to form thermochromic VO_2

At the end of the previous chapter, we discussed the effect of the VN deposition conditions on the film oxidation behavior. The V_2N phase has a higher amount of vanadium than the VN films, which makes its oxidation different. Thus, to form thermochromic VO_2 from the V_2N oxidation with the same conditions as before, it should be necessary to decrease the film thickness.

The V_2N samples (approx. 100 nm) were oxidized at 450 and 550°C during different durations. Figure 6.7 a) (Figure 6.7 b)) depicts the X-ray diffractograms for the air-annealed films at 450°C (550°C) between 20-30 min (2.5-3.5 min). The XRD results for the as-deposited V_2N film show a broad peak detected at approx. 42.1°, between the theoretical values of the (200) and the $(2\bar{1}1)$ planes of the V_2N phase (PDF no.00-033-1439). Therefore, it is ascribed to the $(2\bar{1}1)$ plane to be consistent with the diffractogram in Figure 6.1. No other peak is noticed except those of silicon substrate. Sample V_2N_450_20 displays several peaks corresponding to VO_2(M), and the broad peak of V_2N disappeared (Figure 6.7 a)). The peak at approx. 28.5° attributed to the (101) plane of the V_2N phase indicates that the oxidation is not complete. This

unexpected result suggests that during the annealing process, the V_2N microstructure change, forming bigger grains with a distinct orientation. Regarding the sample oxidized 25 min, only VO_2(M) peaks are perceived (the V_2N peak completely vanishes), suggesting its complete oxidation. A broad peak located at 44.8° in the V_2N_450_30 film could be composed of a mixture of VO_2(M), orthorhombic V_2O_5 or monoclinic V_6O_{13} (PDF no.00-027-1318). Further oxidation will lead to a complete transformation of VO_2(M) into V_2O_5, as we have witnessed in the case of VN oxidation. As for the VN films, the oxidation at 550°C occurs in a much shorter time. The V_2N_550_2.5 depicts no sign of V_2N and only peaks of VO_2(M) are detected (Figure 6.7 b)). Nevertheless, the increase of the oxidation duration of 30 seconds induces drastic changes in the diffractograms. Samples V_2N_550_3 and V_2N_550_3.5 exhibit intense peaks corresponding to monoclinic (PDF no. 00-061-0027) and orthorhombic V_2O_5 phases. The peaks of the m-V_2O_5 are located at approx. 17.8, 24.5 and 26.9° and identified with an asterisk (*) in Figure 6.7 b). The X-ray results illustrate that the V_2N oxidation is similar to VN polycrystalline oxidation. In the first stage, VO_2(M) is the only detected phase and in the second stage, the V_2O_5 appears due to over-oxidation of the VO_2.

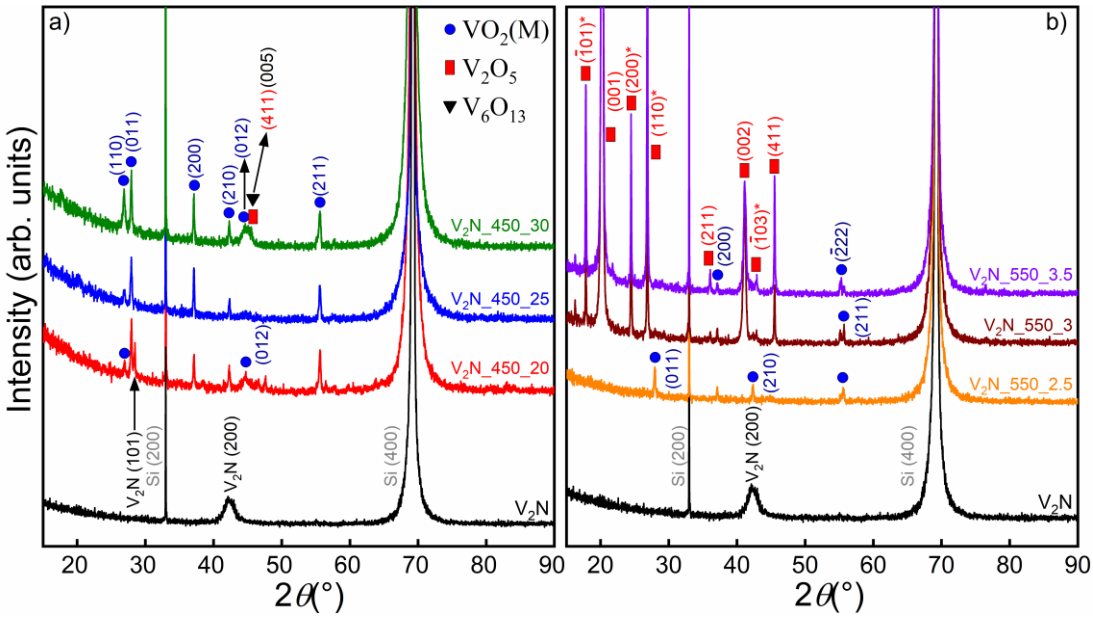

Figure 6.7 X-rays diffractograms of as-deposited V_2N film on Si substrate and the resulting oxide films after air oxidation at a) 450°C and b) 550°C for various durations.

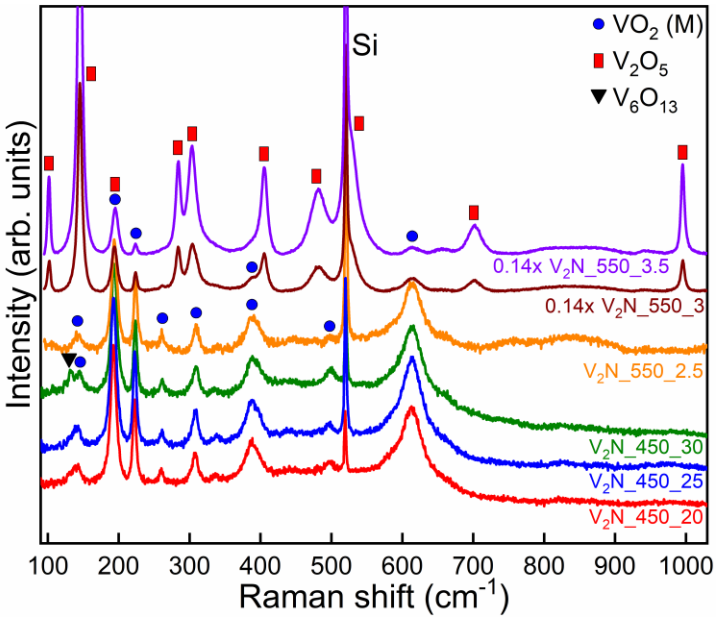

Figure 6.8 Raman spectra of air-annealed V_2N films at 450 and 550°C during different durations. The V_2N_550_3 and V_2N_550_3.5 film spectra were multiplied by 0.14 to fit in the same figure as the other studied samples.

Raman spectrometry (Figure 6.8) was performed on the oxidized samples to compare with the XRD results. The films annealed at 450°C and the V_2N_550_2.5 exhibits similar spectra, with vibration bands (located at approx. 142, 194, 222, 262, 308, 388, 500 and 613 cm^{-1}) assigned to VO_2(M), in agreement with the literature [182–185]. The V_2N_450_30 film displays a vibration band at 132 cm^{-1}, which corresponds to the V_6O_{13} phase [228,229], caused by the ongoing oxidation of VO_2(M). The presence and intensity of the Si vibration band (520.7 cm^{-1}) have been used as an indicator of VN oxidation (chapters 3 and 4), and it will be employed likewise for the V_2N oxidation. From Figure 6.8, one can notice that the Si band intensity on the V_2N_450_20 film is lower than the other samples. Hence, this sample is the only one not completely oxidized, in agreement with the XRD results. On the other hand, the V_2N_550_3 and V_2N_550_3.5 films display similar spectra but different from the samples oxidized at 450°C and the V_2N_550_2.5. As depicted in Figure 6.8, some vibration bands corresponding to VO_2(M) are still evidenced, yet new bands are detected at approx. 102, 145, 194, 283, 303, 404, 529, 701 and 995 cm^{-1} that are ascribed to the orthorhombic V_2O_5 phase [182,183,186,228].

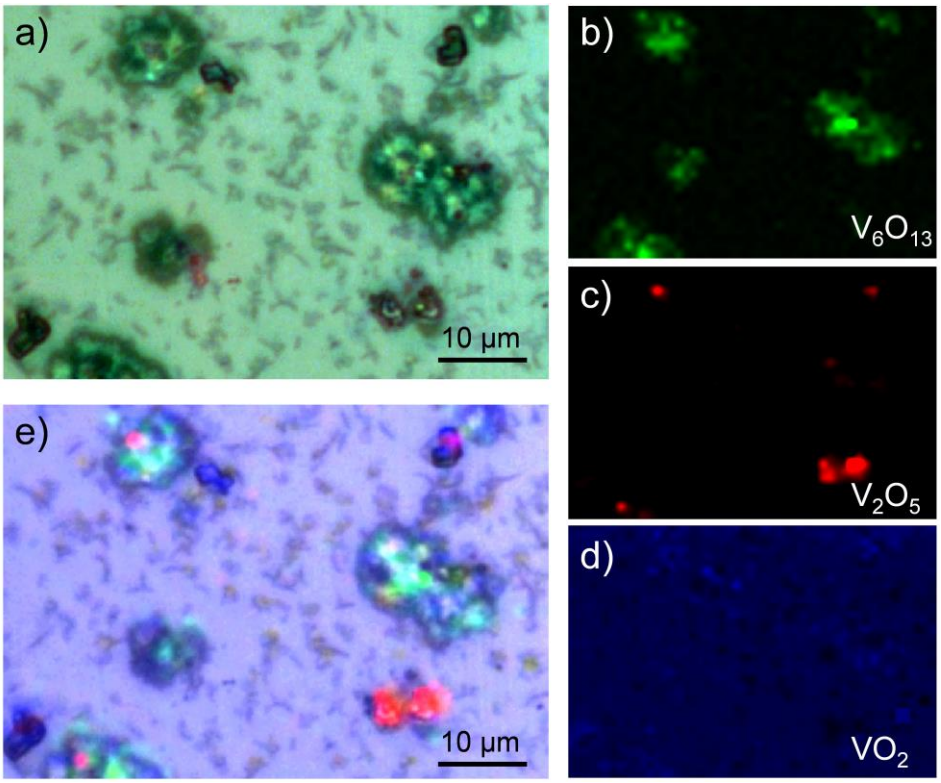

Figure 6.9 a) Image of sample V_2N_450_30 in the area where the 2D Raman mapping was conducted. The image was taken with the CCD camera coupled to the Raman spectrometer. 2D Raman mapping on the b) green, c) red, and d) blue color area indicates the presence of the bands at 845 cm^{-1} band (V_6O_{13} phase), 283 cm^{-1} (V_2O_5 phase) and 222 cm^{-1} (VO_2 phase), respectively. e) Merge of the three 2D Raman mappings in b), c) and d) and superposition on the image of Figure 6.9 a).

For the V_2N_450_30 sample, the XRD results display a peak that could correspond either to the V_2O_5 or the V_6O_{13} compound. The Raman spectrum depicts one band ascribed to the V_6O_{13} phase. To further investigate this topic, a 2D Raman mapping was carried out in a non-homogeneous zone of the film (Figure 6.9 a)). The studied area has dimensions of approx. 42 µm x 62 µm. The inhomogeneities present different shapes with average diameters from 3.5 to 16 µm. The applied laser has a diameter of about 1.5 µm. Each spectrum is registered from 95 to 1100 cm^{-1}, with an X-Y scanning step motion of 0.75 µm between them. To discern between each phase a characteristic band was chosen and associated with a color. The band at 845 cm^{-1} of the V_6O_{13} phase (correlated with the green color) appears only in the prominent inhomogeneous regions (Figure 6.9 b)). The 132 cm^{-1} band of the V_6O_{13} phase was not selected for potential interference from the band at 138 cm^{-1} of the VO_2(M) phase. On the contrary, the band at 283 cm^{-1} of the V_2O_5 (associated with the red color) is detected only in the small

inhomogeneities (Figure 6.9 c)). Finally, the vibration band located at 222 cm^{-1} of the VO_2(M) was associated with the blue color, and it is present in the whole studied zone (Figure 6.9 d)). The merge of the three 2D maps (Figure 6.9 b), c) and d)) in Figure 6.9 e) reveals the growth of the V_6O_{13} and V_2O_5 phases in a VO_2(M) matrix. These results are in agreement with the XRD findings and give extra information to the Raman spectrum shown in Figure 6.8 for the V_2N_450_30 sample.

The Raman mapping could be used as a powerful tool to distinguish which phases are present in each film and to study with more details the oxidation of VO_2. However, a careful analysis must be conducted before reaching important conclusions. For example, depending on the homogeneity of the sample, several Raman mappings in different zones may be necessary. In some cases, it might be essential to complement this study with other characterization techniques, such as XRD, TEM, or even optical and electrical measurements. Another attractive application of 2D Raman mapping is the study of the MIT of VO_2(M) [244,245].

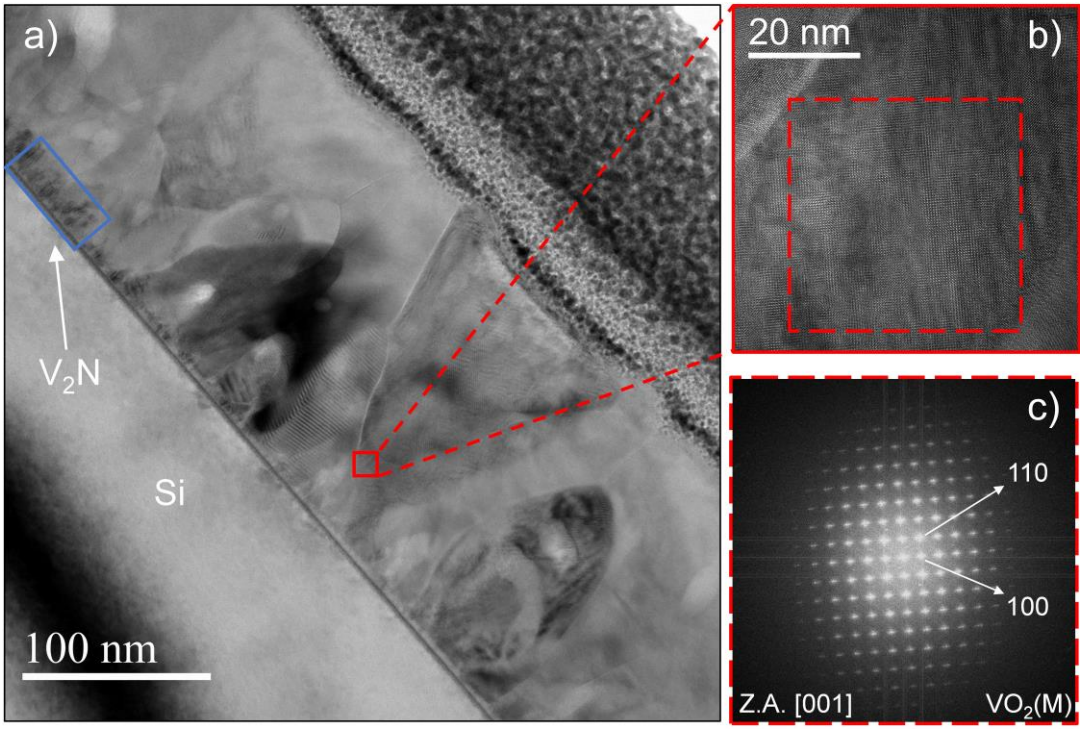

Figure 6.10 a) TEM cross-sectional image of sample V_2N_550_2.5. b) HRTEM image of the highlighted red area in Figure 6.10 a). c) FFT from the region of Figure 6.10 b).

Figure 6.10 illustrates a TEM cross-sectional micrograph for the V_2N_550_2.5 sample. The figure displayed an almost complete oxidized film with a small zone of V_2N. The other layer

(expected to be VO_2(M)) features large grains and a thickness of about 170 nm. To check the presence of VO_2(M) a high-resolution TEM (HRTEM) micrograph with the corresponding FFT pattern investigation is conducted in the area enclosed in red in Figure 6.10 a) (Figure 6.10 b) and Figure 6.10 c), respectively). It was possible to identify the (100) and (110) planes of VO_2(M). The obtained interplanar distances are 0.483 and 0.334 nm for the (100) and (110) planes, respectively, in agreement with those reported for monoclinic VO_2(M) (PDF no. 04-003-2035).

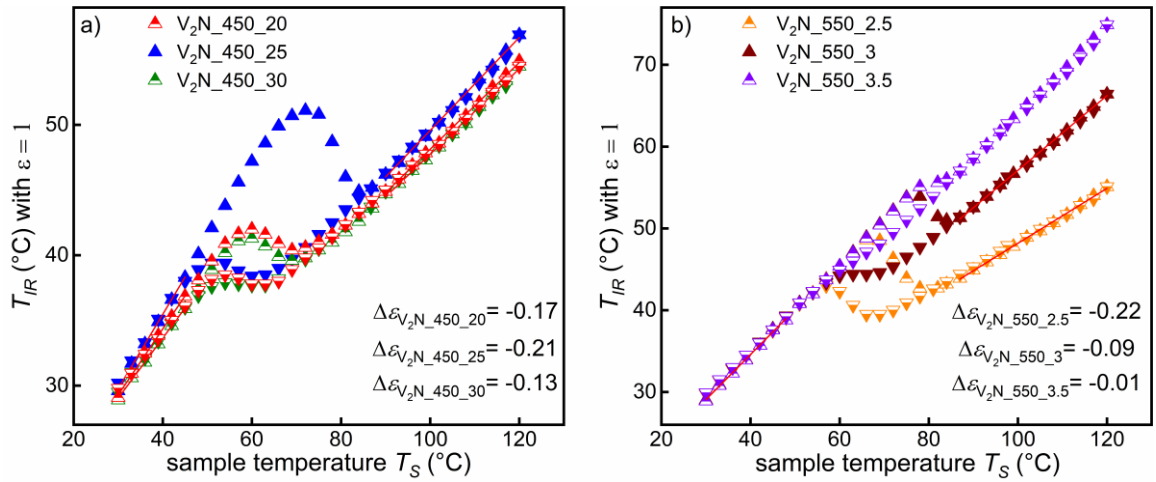

Figure 6.11 Thermal camera measurements of apparent infrared temperatures (T_{IR}) as a function of the sample temperature (T_S) for films oxidized at a) 450 and b) 550°C. Up and down triangles represent the profiles for temperature ramping up and down, respectively. Measurements were carried out by considering an emissivity equal to 1 irrespective to the sample.

To evaluate the thermochromic performance of the oxidized films, optical measurements were performed in the IR domain with an infrared camera. Figure 6.11 displays the evolution of the apparent infrared temperature (T_{IR}) of samples as a function of the actual sample temperature (T_S) during heating and cooling for the oxidized films. The three air-annealed samples at 450°C (Figure 6.11a)) exhibit hysteresis loops and a change in the slope, characteristics of a thermochromic behavior. The values of $\Delta\varepsilon$ are ranging from -0.13 to -0.21. The highest value of emissivity switch ($\Delta\varepsilon = -0.21$) corresponds to the sample oxidized 25 minutes, in which VO_2(M) is the predominant phase. The V_2N_450_20 sample presents a residual V_2N layer, and the V_2N_450_30 one shows signal of over-oxidation of the VO_2(M), with both phases V_6O_{13} and V_2O_5 affecting the thermochromic behavior of the films. For the

samples in Figure 6.11 b), the V_2N_550_2.5 film depicts the best thermochromic performance ($\Delta\varepsilon = -0.22$). The optical modulation properties of the V_2N_550_3 sample decrease to -0.09 (59% less when compared with the V_2N_550_2.5) originated by the over-oxidation of VO_2 into V_2O_5. The film air-annealed 3.5 minutes at 550°C does not evidence a thermochromic performance anymore. These results are in total accordance with X-ray and Raman results.

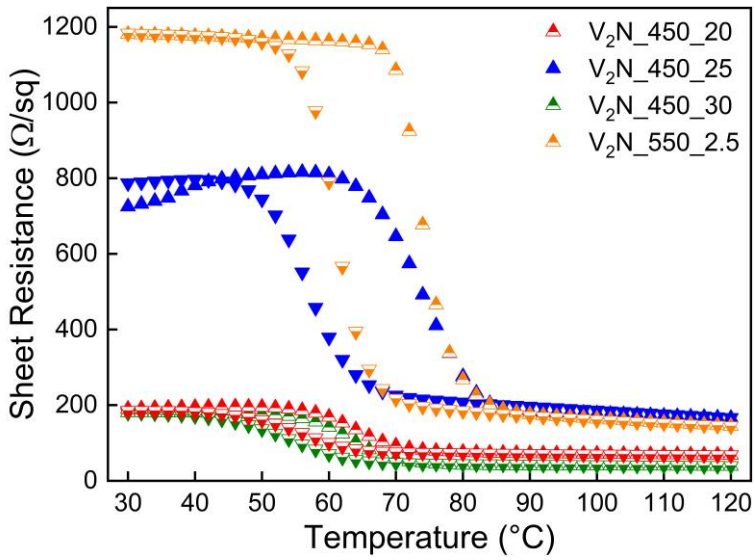

Figure 6.12 Sheet resistance (SR) as a function of the temperature for the V_2N films oxidized at 450°C and during 2.5 min at 550°C. Up and down triangles represent the profiles for temperature ramping up and down, respectively.

Figure 6.12 displays the evolution of the sheet resistance (SR) as a function of the temperature during both heating and cooling for the four films that present a thermochromic effect. For these electrical measurements, we prefer to plot the SR values rather than the resistivity ones. This choice results from the presence of the remaining conductive V_2N layer or the V_6O_{13} and V_2O_5 phases in some samples. For the V_2N_450_20 sample, there is almost no change between low and high temperatures SR values, due to the presence of a V_2N layer. A similar response is observed for the V_2N_450_30 film, caused by the over-oxidation of the VO_2(M). The V_2N_450_25 and the V_2N_550_2.5 films exhibit hysteresis loops in the near MIT region: with a maximum difference in SR values for the V_2N_550_2.5 sample.

These four-point probe results confirm the XRD, Raman, and IR thermometry finding for the studied samples. However, the ratio between the SR values at low and high temperatures is small compared to the results obtained in Chapter 3 for the VN oxidation and the literature data,

this could be caused by the poor crystallinity of the films. Several others parameters affect the electrical modulation properties of VO_2. In 2005, Brassard *et al*. studied the effect of thickness on the resistivity changes of sputter-deposited VO_2(M). They found a link between the film thickness and crystallite size with the transition characteristics. An increase in the film thickness leads to sharper and higher transitions, with the best results for a 350 nm VO_2(M) sample with an abrupt resistivity change of 3.2 decades [111]. Other critical parameters are the annealing temperature and the oxygen pressure during the oxidation. In 2015, Yoon *et al*. achieved a resistivity change at MIT of almost four orders of magnitude by oxidizing 100 nm of V films between 200 to 600 Pa of oxygen pressure and 510 and 600 °C for the annealing temperature [107]. Two years later, Yu *et al*. conducted the oxidation of sputter-deposited 100 nm V films in the 390 to 475 °C temperature range, while the oxygen flow rate was ranging from 1 to 20 sccm. The resistivity change during the metal-insulator transition varies from 0.2 to 4 orders of magnitude depending on the oxidation condition [81]. Based on these results, we consider that we should control the temperature and oxygen pressure during the oxidation process to improve the electrical properties of the achieved VO_2(M).

6.4 On the precursor thickness impact in the optical modulation properties of the formed thermochromic VO_2

In the present manuscript, it has been demonstrated that thermochromic VO_2 can be formed after air oxidation of new precursors: VN and V_2N films. Whatever the oxidation temperature, the performance of the VO_2 layer shows an optimum as a function of the annealing duration. When the duration is lower than the optimized value a remaining VN or V_2N layer has been evidence due to an incomplete oxidation of the precursor. All these results have been obtained using a quite low thickness of the nitride layer (in the 100 – 175 nm range), but we do not study the properties of a VO_2 thin film formed by air oxidation of a thick nitride film. In other words, does the initial nitride thickness layer play a role on the performance of the resulting VO_2 film? The idea is to oxidize a thick film of as-deposited VN or V_2N film on Si substrate. The oxidation should be incomplete and a certain thickness of the precursor should be remaining while the VO_2 phase should be detected on the sample surface. We expect that the combination of the

thick non-oxidized film with Si substrate should behave like a highly IR-reflective substrate such as Al. Hence, the emissivity switch should change to a positive value, rather than a negative one, characteristic of a VO_2 layer deposited on an IR-transparent substrate such as Si or quartz [84,194]. The VN thickness value chosen (350 nm) is twice than that used in chapters 3 and 4. The VN films are grown with two different working pressures: 0.22 and 0.56 Pa (the other parameters remains the same as in chapter 5). For the V_2N, the selected thickness is higher, about 445 nm. To test our hypothesis, both nitride films deposited on Si substrate are oxidized at 550°C for 2.5, 3, and 3.5 minutes.

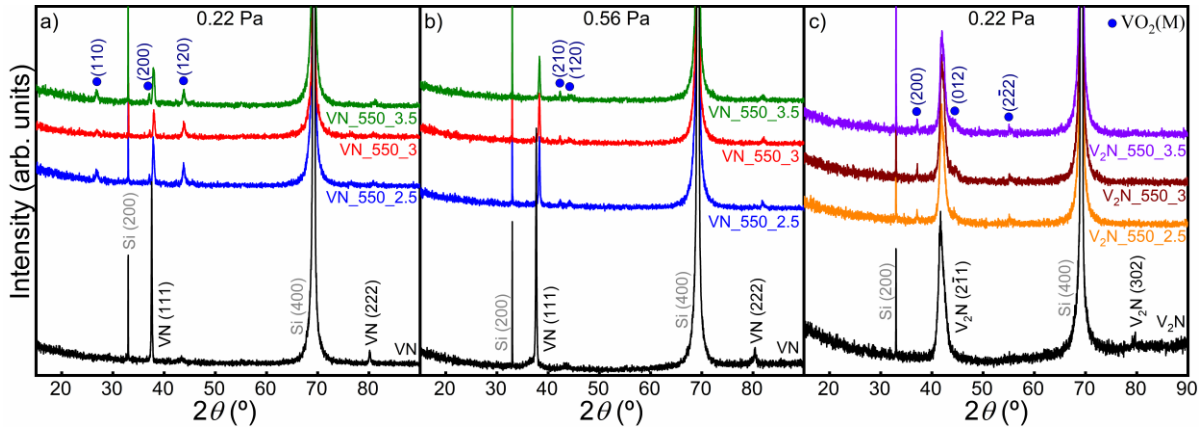

Figure 6.13 X-ray diffractograms of as-deposited VN (350 nm) and the resulting oxide films after air-oxidation at 550°C during 2.5, 3 and 3.5 minutes deposited with different working pressure a) 0.22 Pa and b) 0.56 Pa. c) X-ray diffractograms of as-deposited V_2N (445 nm) and the resulting oxide films after air-oxidation under the same conditions as films in Figure 6.13 a) and b).

Figure 6.13 depicts the X-ray diffractograms for both precursors (VN and V_2N) and the air-annealed films at 550°C for 2.5, 3, and 3.5 min. As expected, the VN films present the usual [111] texture. On the other hand, the V_2N sample exhibits a [2$\bar{1}$1] texture. The oxidation of both precursors is incomplete. There is a VN intense peak in Figure 6.13 a) and Figure 6.13 b), and a V_2N strong peak in Figure 6.13 c). Besides, these peaks are shifted to higher angles due to stress relaxation during the oxidation step. Although the VO_2(M) peaks are not intense, this is the only detected phase of the V-O system in all the oxidized films. These results differ from the one related to the oxidation of thinner films (Figure 5.15). A possible explanation is that in the thinner films the oxygen diffusion is limited, 3.5 min at 550°C are sufficient to entirely oxidize the precursor forming VO_2 and continue the overoxidation reaching V_2O_5. On the other hand, for thicker films, 3.5 minutes at 550°C is not enough to transform all the VN precursor

into VO_2. In this case, oxygen continues to diffuse inside the precursor before begins to overoxidize the already formed VO_2.

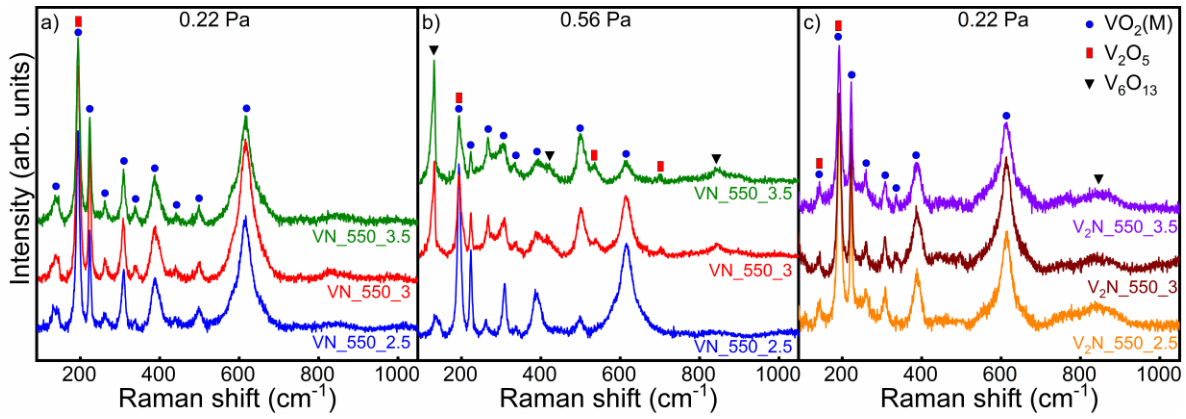

Figure 6.14 Raman spectra of air-annealed VN films at 550°C during 2.5, 3 and 3.5 minutes deposited with different working pressure a) 0.22 Pa and b) 0.56 Pa. c) Raman spectra of air-annealed V_2N films under the same conditions as films in Figure 6.14 a) and b).

To check the VO_2(M) formation, Raman scattering was carried out for all the oxidized films (Figure 6.14). As expected, none of the samples in Figure 6.14 exhibits the Si band. Hence, a significant layer of VN or V_2N must be still present in the films. All the spectra in Figure 6.14 a) are similar, with most of the vibration bands located at 138, 223, 262, 308, 337, 388, 441, 500 and 615 cm^{-1} assigned to VO_2(M) [182–185]. On all the samples, there is also a band around 195 cm^{-1} that matches either with VO_2(M) or orthorhombic V_2O_5 [182–184,186,228]. The spectrum of the VN_550_2.5 film, corresponding to oxidation treatments made for a thick VN synthesized at a higher working pressure of 0.56 Pa, are shown in Figure 6.14 b) and, resembles the ones of Figure 6.14 a), with VO_2(M) as the predominant phase. There are some variations in the spectra of VN_550_3 and VN_550_3.5 samples compared to the one oxidized during 2.5 min (Figure 6.14 b)). First of all, the vibration band at 138 cm^{-1} disappears and a new band rises at 131 cm^{-1} ascribed to V_6O_{13} [228,229]. The bands characteristic of VO_2(M) at 222 and 613 cm^{-1} decrease in intensity with the oxidation time increase. The intensity ratio between the bands at 262 at 308 cm^{-1} also changes. The band at 388 cm^{-1} also decreases in intensity and becomes broader with a contribution of a new band located at 416 cm^{-1}, which corresponds to V_6O_{13} [228]. On the contrary, the band at 500 cm^{-1} grows in intensity and emerges a shoulder attributed to V_2O_5. Finally, two feeble bands arise, one at 700 cm^{-1} and the other one around

845 cm^{-1}, corresponding to V_2O_5 [182,183,186,228,246] and V_6O_{13} [182], respectively. These differences between the samples annealed at 2.5 min and the ones at 3 and 3.5 min (of Figure 6.14 b)) indicates that the oxidation of VO_2(M) continues giving rise to the formation of V_6O_{13} and V_2O_5. The films synthesized at higher pressure (0.56 Pa) are less dense, facilitating the oxidation compared with those deposited at 0.22 Pa. For the V_2N annealed samples all the spectra are equivalent, with most of the vibration bands located at 144, 222, 260, 308, 337, 388 and 613 cm^{-1} that can be assigned to VO_2(M) [182–185] (Figure 6.14 c). The band at 144 cm^{-1} could match either with VO_2(M) or orthorhombic V_2O_5 [182–184,186,228]. Moreover, there is a wide band located around 845 cm^{-1} ascribed to V_6O_{13} [182]. Raman results confirm the formation of VO_2(M) in all the samples and also indicate the emergence of V_6O_{13} and V_2O_5 caused by the over-oxidation of m-VO_2.

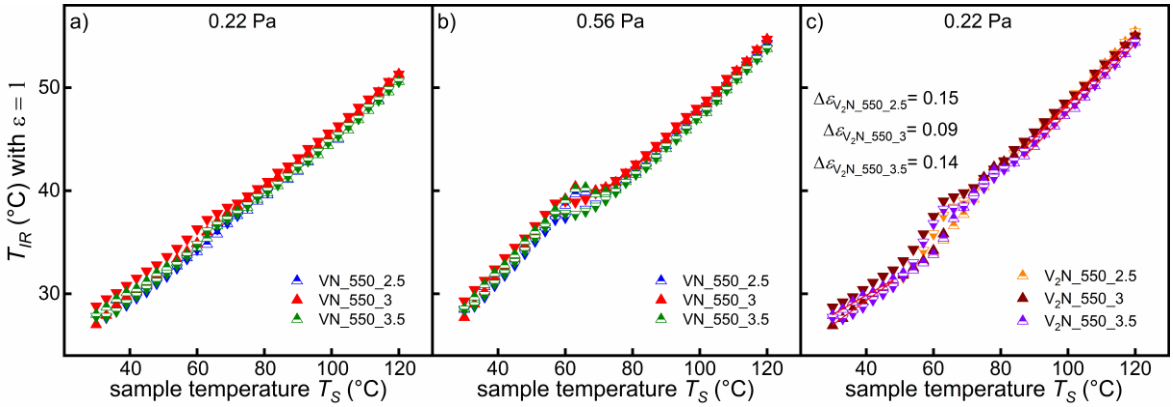

Figure 6.15 Thermal camera measurements of apparent infrared temperatures (T_{IR}), as a function of sample temperature (T_S) for VN films deposited at a) 0.22 and b) 0.56 Pa oxidized between 2.5 and 3.5 min at 550°C. c) Thermal camera measurements of apparent infrared temperatures (T_{IR}), as a function of sample temperature (T_S) for V_2N samples oxidized under the same condition as films in Figure 6.15 a) and b). Up and down triangles represent the profiles for temperature ramping up and down, respectively. Measurements were carried out by considering an emissivity equal to 1 irrespective to the sample.

The emissivity-switching properties of the annealed films in the IR domain are investigated using an infrared camera. Figure 6.15 illustrates the apparent infrared temperature (T_{IR}) of samples monitored versus the sample temperature (T_S) during heating and cooling for the VN and V_2N oxidized films. The films in Figure 6.15 a) do not reveal any change in the slope or any hysteresis loop. On the other hand, the annealed films in Figure 6.15 b) depict negligible

hysteresis and an almost irrelevant slope change (with the highest value $\Delta\varepsilon$ of -0.06 for the VN_550_3 sample). The main drawback is not the small value of $\Delta\varepsilon$, but its negative sign. The results confirm that the oxidation of 350 nm-thick VN cannot change the sign of $\Delta\varepsilon$. Figure 6.15 c) related to oxidized V_2N films evidences a thermochromic behavior for all samples. Besides, an appealing result is obtained on the sign of $\Delta\varepsilon$ that is positive (for 100 nm thick V_2N films oxidized at 550 °C, $\Delta\varepsilon$ is negative (Figure 6.11 b)). The positive value of $\Delta\varepsilon$ means that the combination of the remaining V_2N with the Si substrate behaves as a highly IR-reflective substrate such as Al. The V_2N_550_2.5 film displays the maximum emissivity switch (0.15). Surprisingly, the $\Delta\varepsilon$ value for the V_2N_550_3 sample decrease before increasing again for the V_2N_550_3.5 film. Our results clearly evidence that the sign of the emissivity switch can be tuned according to the thickness of the as-deposited V_2N film. This stimulating new result opens the possibility for applications on tunable furtivity ($\Delta\varepsilon < 0$) or smart radiator devices ($\Delta\varepsilon > 0$).

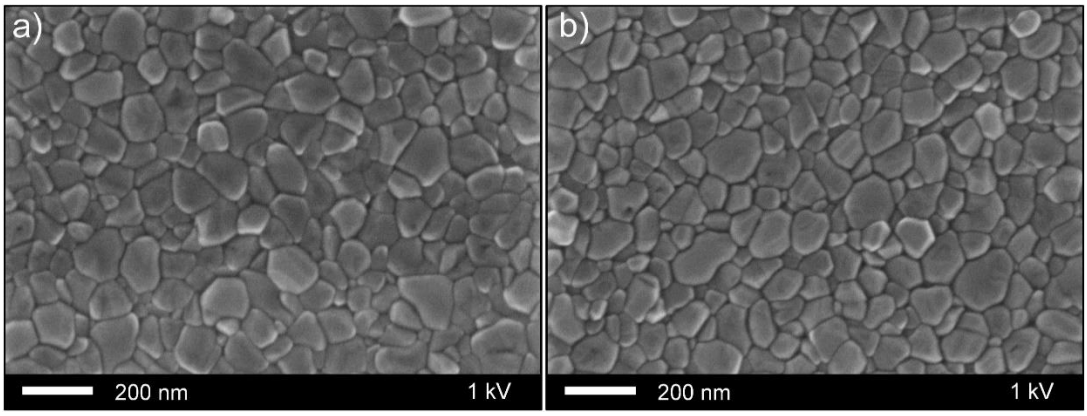

Figure 6.16 Top-view SEM images of films oxidized for 2.5 min at 550°C. The thickness of the V_2N initial films are a) 100 nm and b) 445 nm.

Figure 6.16 displays the surface morphology of samples oxidized during 2.5 min at 550°C for a 100 nm V_2N precursor in Figure 6.16 a) and for a 445 nm V_2N precursor in Figure 6.16 b). Both images are very similar, almost identical. In the two images, the grains have analogous shape and size distribution. More fascinating is the resemblance with Figure 4.8 f), in which also VO_2(M) is the predominant phase on the surface. There are several differences between the three films: the substrate (Si for the images of Figure 6.16 and aluminum for the Figure 4.8 f)), the precursor (V_2N for Figure 6.16 and VN for Figure 4.8 f)). Yet, there are similarities, for instance, all the precursor films present columnar microstructure, and the oxidation conditions

are comparable, 550°C for 2.5 min for the V_2N films and 3 min for the VN one. Gathering all this information, one can "presume" a conclusion: the temperature is the driven parameter for the VO_2(M) surface morphology of the oxidized films. These results also confirm that the surface morphology does not play any role in the emissivity switch as previously discussed in chapter 4.

6.5 First attempt to describe the oxidation mechanism of V_2N films

At this stage, all the results reported indicate that the oxidation of V_2N occurs with the same steps as reported for VN. The first oxide to appear is VO_2(M), which can coexist with V_2N. As the oxidation process continues, VO_2(M) is oxidized into V_6O_{13} and finally into V_2O_5. A significant feature of VN oxidation is the absence of an intermediate layer between VN and VO_2.

To check if this conclusion can also be drawn for the oxidation of V_2N, STEM and EELS analyses have been performed on two oxidized V_2N samples, which present good thermochromic behavior. Figure 6.17 depicts a high angular annular dark-field image of films oxidized for 2.5 min at 550°C from a 100 nm V_2N precursor in Figure 6.17 a) and from a 445 nm V_2N precursor in Figure 6.17 b). There are four distinct regions in Figure 6.17 a) equivalent to Si, a thin layer of less than 5 nm, VO_2(M) and Pt. The 5 nm-thick layer is almost undetectable in Figure 6.10, and it is expected to correspond to a remaining V_2N layer. On the other hand, Figure 6.17 b) exhibits four regions ascribed to Si, V_2N (about 335 nm), VO_2(M) (about 160 nm) and Pt. On these two samples, EELS spectra were recorded on nine zones (labeled from 1 to 9). Spectra from 1 to 4 were registered in Figure 6.17 a), while the ones from 5 to 9 correspond to Figure 6.17 b). The spectra from 2 to 4 are similar and correspond to the VO_2(M) EELS spectra. This result is in agreement with XRD, Raman, TEM and IR camera that evidence the formation of a vanadium dioxide layer. Interestingly, spectrum 1 conducted in the thin layer of Figure 6.17 a) matches the characteristic VN-EELS spectrum. Indeed, it presents two clear N_K peaks and the V_{L3} intensity peak higher than the V_{L2} one.

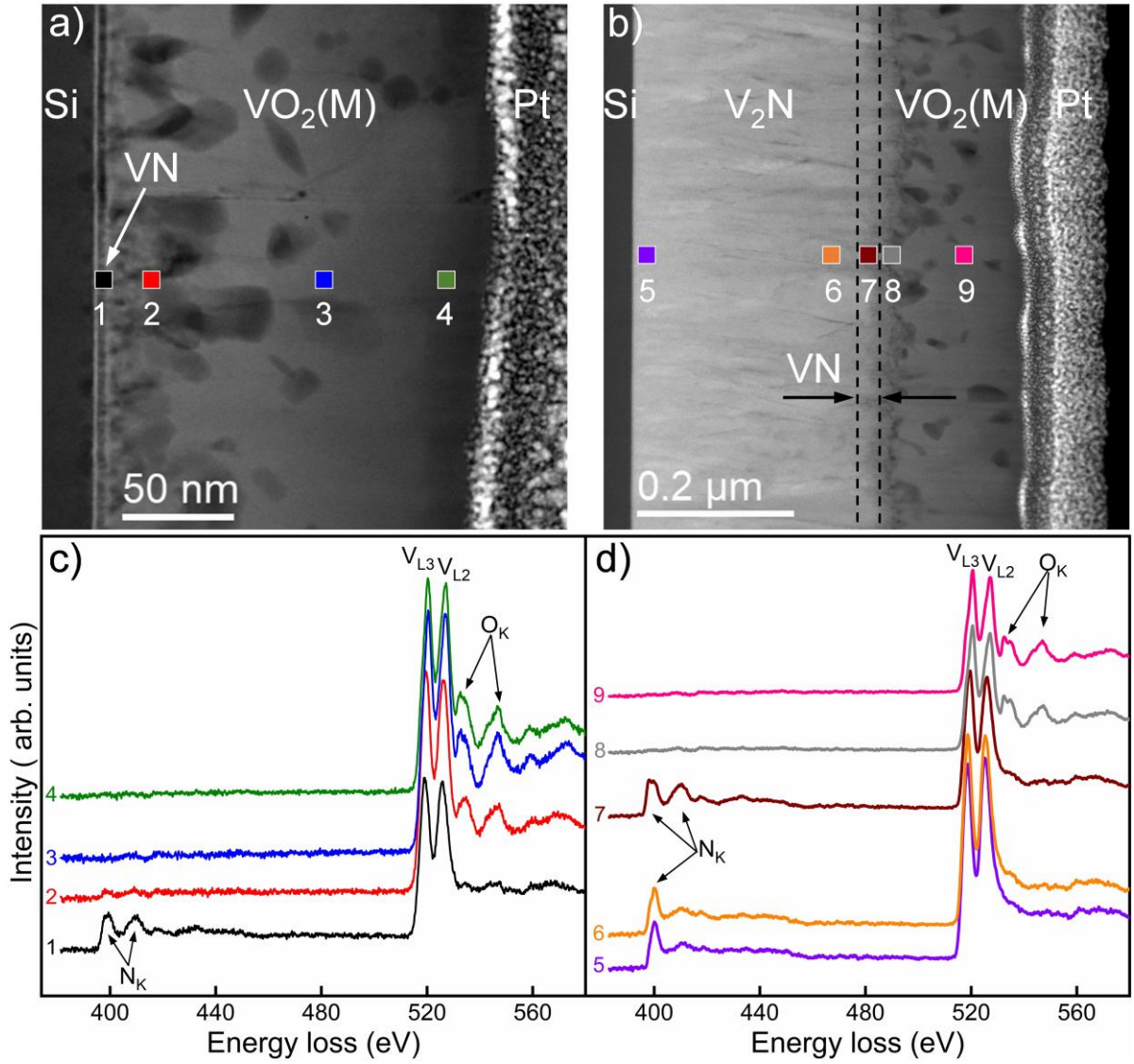

Figure 6.17 High angle annular dark-field image of the samples oxidized for 2.5 min at 550°C from a a) 100 nm V_2N precursor and b) from a 445 nm V_2N precursor. c) EELS spectra of the four highlighted zones in a). d) EELS spectra of the five highlighted zones in b). The color of each curve corresponds to the area of the same color where the spectrum was conducted.

At this stage, two hypotheses can be considered to explain the occurrence of a thin layer of VN at the film-substrate interface. The first one corresponds to the deposition of a thin VN layer before the growth of the V_2N film due for instance to bad control of the deposition process. However, in TEM analysis we have never found such a VN layer. The second hypothesis suggests that this thin VN layer is formed during the oxidation of the V_2N film. To distinguish these two hypotheses, EELS spectra have been also recorded on a thick V_2N oxidized at 550°C for 2.5 minutes (Figure 6.17 d). Spectra 5 and 6 in Figure 6.17 b) corroborate that V_2N is still present in this region. Spectra 8 and 9 are recorded in the second layer of Figure 6.17 b) and

correspond to VO_2(M) phase. The four spectra validate the XRD, Raman and IR camera results previously shown. However, there is a region of about 25 nm thick, highlighted with black dashed lines in Figure 6.17 b), where the EELS spectrum is different from the features of V_2N and VO_2(M) phases. Indeed, spectrum 7 (registered in this transition zone) matches with the VN-EELS spectrum. These results clearly evidence that during the oxidation of V_2N a VN layer is formed at the interface between the remaining V_2N layer and the growing VO_2 one. During the oxidation of V_2N, oxygen diffuses into the growing VO_2 layer and reacts with V_2N at the V_2N-VO_2 interface. This oxidation reaction leads to the release of nitrogen. Up to now, we were considering that nitrogen atoms diffuse outwards of the sample into the VO_2 film and form molecular nitrogen on its surface, contributing to the denitriding of the sample. However, the occurrence of a VN layer at the V_2N-VO_2 interface suggests that a certain fraction of nitrogen diffuses towards the substrate and nitride the V_2N layer to form a thin VN intermediate layer. Thus, from a microscopic point of view, the oxidation of a V_2N layer comes with the formation of an intermediate VN phase, and the growth of the VO_2 layer occurs on this intermediate layer. Similar behavior has been reported for the air oxidation of Cr_2N films in a temperature range between 500 and 1000°C. In the interface between the non-oxidized Cr_2N and Cr_2O_3 oxide, an intermediate CrN layer is detected [247,248].

6.6 Chapter conclusions

This chapter offers an overview of the air-controlled oxidation of V_2N films deposited on Si substrates. In the first section, we compare the structure, mechanical, electrical and optical properties of VN and V_2N compounds. The results depict that the EELS spectra could be used as a fingerprint to distinguish between both phases. The hardness value of V_2N is more than twice that of VN. Both phases have metallic properties, the resistivity being increased with temperature. Nevertheless, VN ($TCR_{VN} = 3.7\ 10^{-4}\ K^{-1}$) has a higher temperature coefficient of resistance than V_2N ($TCR_{V_2N} = 2.0\ 10^{-4}\ K^{-1}$).

We study the oxidation of the V_2N films at two temperatures (450 and 550°C). For the first time, our work shows that V_2N can also be considered as a precursor for the synthesis of thermochromic VO_2. During the oxidation step, VO_2(M) is the first oxide formed, it coexists

with V_2N for a long time at 450°C or swiftly vanished at 550°C. Further increase of the oxidation duration leads to the formation of V_6O_{13} or V_2O_5 phases that do not exhibit thermochromic properties. EELS characterization of thin and thick oxidized V_2N films evidences the formation of a very thin VN intermediate layer (about 25 nm) is formed at the V_2N-VO_2(M) interface. These findings evidence that the oxidation of V_2N to VO_2(M) occurs in two stages. The oxidation of V_2N leads to the release of nitrogen that diffuse in two opposite directions: towards the surface and towards the substrate and contribute to form the intermediate VN layer. For high oxidation duration, the VO_2(M) becomes V_2O_5, which dramatically affects the thermochromic response of the films. The values for the $\Delta\varepsilon$ of the oxidized V_2N films are similar to those obtained from the VN oxidation. However, the films present a feeble change in the sheet resistance values, which is not well understood.

Finally, we provide a first insight into the influence of the V_2N thickness on the optical modulation properties of the formed VO_2(M). We managed to change the sign of the $\Delta\varepsilon$ for the oxidized films by changing the initial V_2N thickness. For the VO_2(M) samples obtained from the oxidation of a 100 nm V_2N film, the $\Delta\varepsilon$ is negative, with the direct effect of the Si substrate. However, for the VO_2(M) films achieved after the air-annealing of a 445 nm V_2N layer, the $\Delta\varepsilon$ is positive. This means that a combination of a thick V_2N layer (at least 335 nm) with the Si substrate behaves as a highly IR-reflective substrate such as Al. We believed that these results may pave the way for future investigations on the oxidation of V_2N as a new precursor to form VO_2(M).

General conclusions

The development of thin film processes for the synthesis of thermochromic vanadium dioxide is crucial for the applications of such material at the industrial scale. The main issue comes from the complex phase diagram of the V-O binary system as presented in chapter 1. In this thesis, we obtained for the first time thermochromic VO_2 from the controlled oxidation of sputter-deposited VN and V_2N polycrystalline films. It was discussed the importance of optimizing the annealing duration in each of the studied oxidation temperatures to achieve high-quality thermochromic VO_2.

During the oxidation process at different temperatures (450, 525 and 550°C) of the polycrystalline VN and V_2N films, we found, in general, only two phases belonging to the V-O system: VO_2 and V_2O_5. As a function of the oxidation duration, the first oxide formed was VO_2. This oxide can coexist with the remaining precursor for a long period at 450°C or suddenly disappeared at 525 and 550°C. The best thermochromic performance was achieved after the almost complete or complete oxidation of the precursor. It was show that a remaining precursor layer affects the thermochromic performance of the films. Above the optimal annealing duration, V_2O_5 appears due to the continued oxidation process, affecting the thermochromic behavior of the films. TEM analyses displayed that the interface between the polycrystalline VN films and the formed VO_2 is abrupt. On the contrary, EELS analyses evidenced that V_2N oxidation occurs in two stages. First, the V_2N turns into VN (approx. 25 nm layer) before its oxidation into VO_2(M).

In the matter of the oxidized polycrystalline VN films on Al substrate at different temperatures, the best emissivity switch in each system is quite similar (between 0.20 and 0.22), whatever the oxidation temperature. On the other hand, the film morphology is strongly dependent on the annealing temperature. The results displayed an independence of the optical modulation properties of VO_2 in the 7.5-13 µm range with the surface morphology.

The oxidation of VN epitaxial films followed a completely different path than polycrystalline VN thin films, which could be caused by the absence of grain boundaries in the

epitaxial layers. Remarkably, oxidation led to the epitaxial growth of the VO_2(B) phase on the single crystalline VN with the following relationships: VO_2(B) (001) || VN (200) out-of-plane and VO_2(B) (200) || VN (020) in-plane orientation, as shown by the TEM results. Moreover, the SEM images and the AFM results depicted a completely different surface morphology for the VO_2(B) phase, with nanorods perpendicular to the substrate.

Furthermore, we applied a simple criterion to transpose the deposition conditions between the two sputtering machines employed in the thesis. Three sets of VN films were deposited using the lab-scale machine: series II with the equivalent conditions of the semi-industrial chamber, series I and III with lower and higher working pressure, respectively. All films were oxidized at 550°C up to 3.5 minutes. The results displayed that: none of the VN oxidized samples of series I and III evidenced thermochromic behavior. For the annealed films of series I, this is due to the residual VN layer found in the samples and for the complete conversion of the VN into V_2O_5 in the annealed samples of series III. Only the oxidized films deposited with the analogous conditions (series II) showed thermochromic performance. Therefore, we assume that it is possible to transpose deposition from one sputtering chamber to another keeping constant the pressure x distance conditions.

Finally, we provided a first insight into the influence of the V_2N thickness on the optical modulation properties of the formed VO_2(M). For the VO_2(M) samples obtained from the oxidation of a 100 nm V_2N film, the $\Delta\varepsilon$ is negative, caused by the direct effect of the Si substrate. Yet, for the VO_2(M) films achieved after the air-annealing of a 445 nm V_2N layer, the $\Delta\varepsilon$ is positive. These findings indicate that a combination of a thick V_2N layer (at least 335 nm) with the Si substrate behaves as a highly IR-reflective substrate such as Al.

This thesis may pave the way for future investigations on the oxidation of VN and V_2N as a new precursors to form high-quality thermochromic VO_2(M).

Perspectives

- Our work was not dedicated to tune the metal insulating transition temperature. However, such an objective could be reached by doping the VN or V_2N films before the oxidation. Indeed, elements such as chromium or aluminum are highly miscible in the vanadium nitrides. The oxidation of such doped nitride films could change the T_{MIT} and improve the optical modulation properties of the obtained VO_2 samples.
- In the literature, the effect of the oxygen pressure during the annealing of V films to achieve thermochromic VO_2 is well established. The same kind of work could be done for the oxidation of vanadium nitrides. The simplest way to achieve it would be to use the heating substrate holder of our deposition chamber to oxidize the films at various oxygen partial pressures.
- The oxidation of epitaxial VN leads to the formation of a VO_2(B) film that is not thermochromic. However the literature reports some works that evidence a possible transformation of VO_2(B) into VO_2(M). Such kind of processes could be studied to get epitaxial VO_2(M) films. An increase of the thermochromic performance is expected.
- Finally, the first experiments of thermogravimetry analyses on the VN and V_2N oxidation suggest that the humidity plays a role on the oxidation kinetics. Further works should be devoted to the study of the water partial pressure on the oxidation step and on the thermochromic performance of the obtained VO_2 films.

Appendix

Oxidation of VN and V_2N films by thermogravimetry analysis

During the thesis, all characterizations have focused on as-deposited and oxidized vanadium nitride films; there is no *in situ* analysis of the oxidation process itself. The annealing of the samples was performed in the air under atmospheric pressure, with no control of the annealing atmosphere. In the literature, several authors have reported the influence of the oxidation atmosphere in the thermochromic performance of the obtained VO_2 films [81,107]. The goal of the appendix is to start a first study on the oxidation of VN and V_2N polycrystalline films with two different atmospheres by thermogravimetric (TGA) analysis.

The oxidation procedure in this study is different than the one used throughout the thesis. First, the sample is introduced in the SETARAM Setsys thermobalance. Afterward, a flow rate of Ar cleans the chamber during six hours before the oxidation. The heating process up to the desired temperature (450°C) is carried out in an Ar atmosphere (AlphaGaz 1) to avoid possible oxidation. This procedure takes approx. 21.5 minutes with a heating rate of 20°C/min. As soon as 450°C is reached, the Ar valve is closed, simultaneously the dry air (or humid air) valve is opened. At the end of the annealing process, the temperature drops to room temperature at the same rate as the heating.

Figure A.1 displays the dependence of the mass gain with time for V_2N films (approx. 1 cm^2 of surface and 440 nm thick) deposited on Si substrate oxidized during 15 hours at 450°C in dry air (AlphaGaz 1) or humid air (AlphaGaz 1 + 10% absolute humidity) atmosphere. The figure shows the first 130 min of the process (including the 21.5 min of the heating procedure), while the inset illustrates the whole process. The mass gain during the heating process is caused by the decrease of the density gas with temperature. It is relevant to mention that it takes around 35-40 min to remove all the Ar in the chamber. Therefore, the mass gain for the first 35-40 min of the annealing process is due to the gas density change (Ar atmosphere to air) and the oxidation process itself. Besides, Figure A.1 depicts that after approx. 17 min of oxidation (38

min in the total) the mass gain for the sample in humid air is higher than for the that in dry air, suggesting an effect of water vapor in the oxidation process. This trend is maintained until the end of the process where both curves merge, which indicates that both samples present the same final compound.

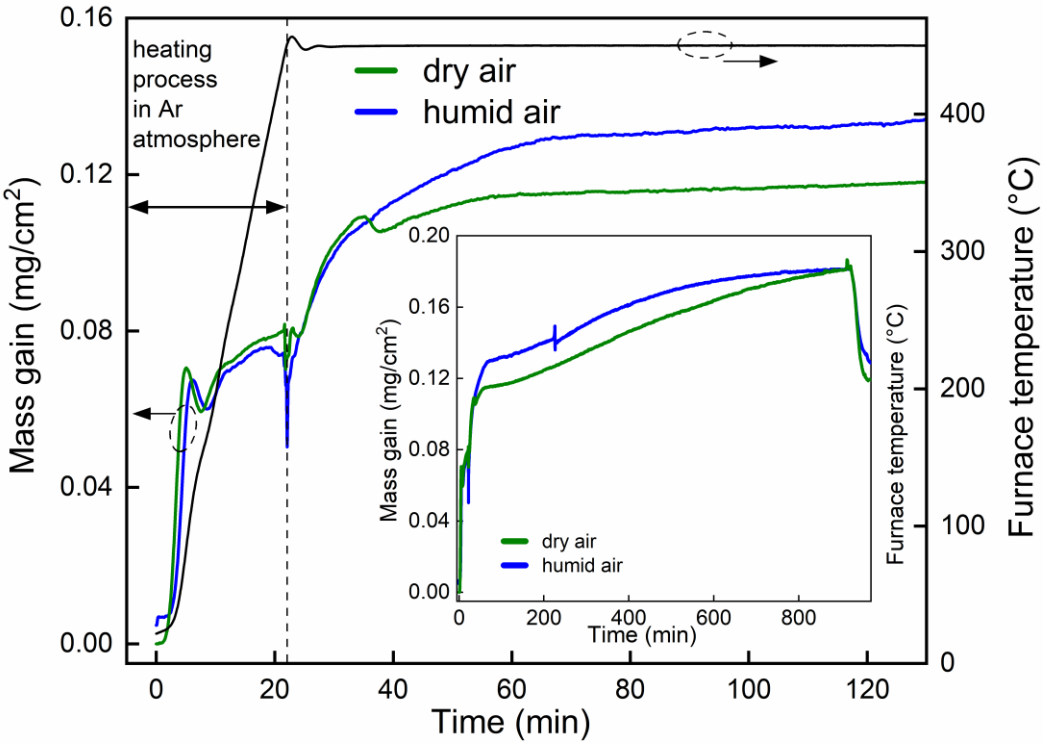

Figure A.1 Mass gain curves as a function of time of the V_2N oxidized samples for 15 hours at 450°C in dry (green curve) and humid (blue curve) atmosphere. The figure depicts the first 130 min of the oxidation process, where the beginning (21.5 min) corresponds to the heating procedure. The inset illustrates the whole process.

Figure A.2 a) displays the X-ray diffractograms of as-deposited V_2N films and the resulting oxides. As expected, after 15 hours of annealing the V_2N is transformed into orthorhombic V_2O_5. The results indicate the formation of a polycrystalline V_2O_5 phase with no preferred orientation. Raman spectra of the oxidized films (Figure A.2 b)) corroborate the XRD results with all the bands ascribed to V_2O_5. This result indicates that the structure of the oxidized films is not influenced by the composition of the oxidizing atmosphere.

Moreover, the surface morphology of both oxidized samples are similar, they may even be considered indistinguishable (Figure A.3). Both films show large grains of approx. 1 µm and a plateau-like growth. This surface morphology is different from that of the films analyzed in the previous chapters.

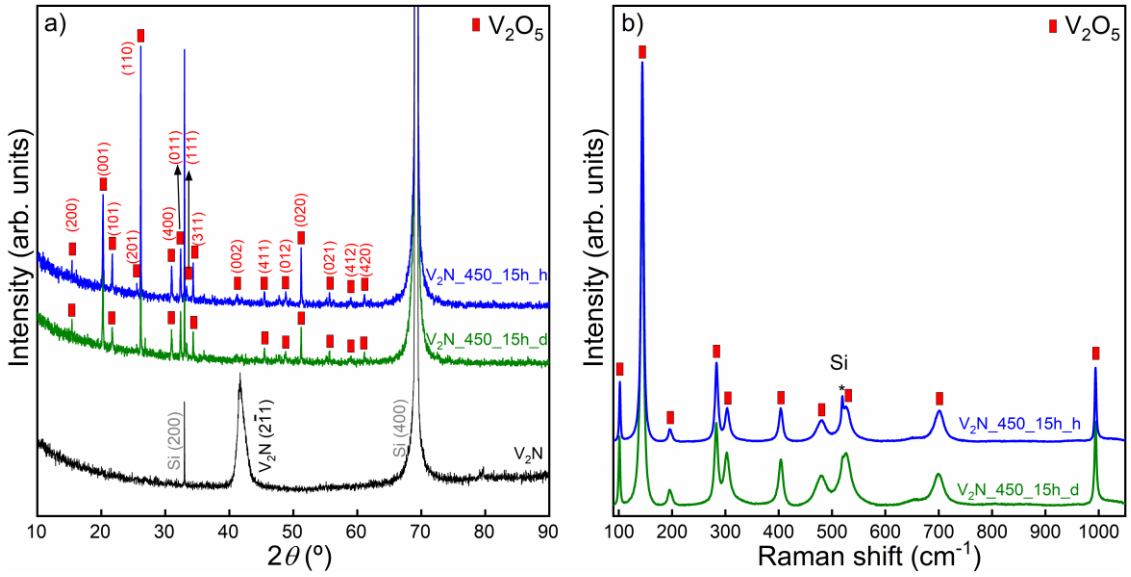

Figure A.2 a) X-rays diffractograms of as-deposited V_2N film on Si substrate and the resulting oxide films after oxidation in dry (green curve) and humid (blue curve) atmosphere at 450°C for 15 hours. b) Raman spectra of the V_2N oxidized films in dry and humid atmosphere at 450°C for 15 hours.

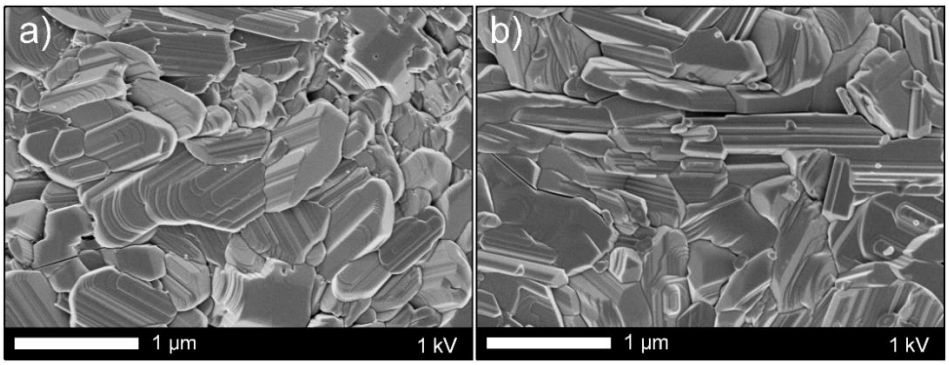

Figure A.3 Top-view SEM images corresponding to the oxidized V_2N films for 15 hours at 450°C in a) humid atmosphere and b) in dry atmosphere.

In this configuration, the possible influence of water vapor at the beginning of the oxidation is disguised because the annealing atmosphere is composed of a gas mixture with different densities. Hence, we change the procedure: the sample is introduced in the SETARAM Setsys thermobalance chamber with an air atmosphere from the very beginning. Therefore, the heating process is carried out in a dry air atmosphere, avoiding the influence of different gases density during the first minutes of the oxidation process. In the new configuration, VN films (around 1 cm^2 of surface and 176 nm thick) deposited on Si substrate at 0.56 Pa are oxidized at 450°C for 90 min in dry air (AlphaGaz 1) or humid air (AlphaGaz 1 + 10% absolute humidity)

atmosphere. Once again, the heating process takes around 21.5 min to achieve the desired temperature of 450°C. The rate of heating and cooling is the same, 20°C/min.

Figure A.4 depicts the mass gain as a function of time for the VN oxidized films in dry air (green curve) and humid air (blue curve) atmosphere. Both curves follow the same path during the whole heating process. Afterward, the sample oxidized in humid atmosphere evidence a slightly higher mass gain than the one annealed under a dry air atmosphere. This behavior persists for around 40 minutes, then both curves merge and reach a plateau, suggesting complete oxidation.

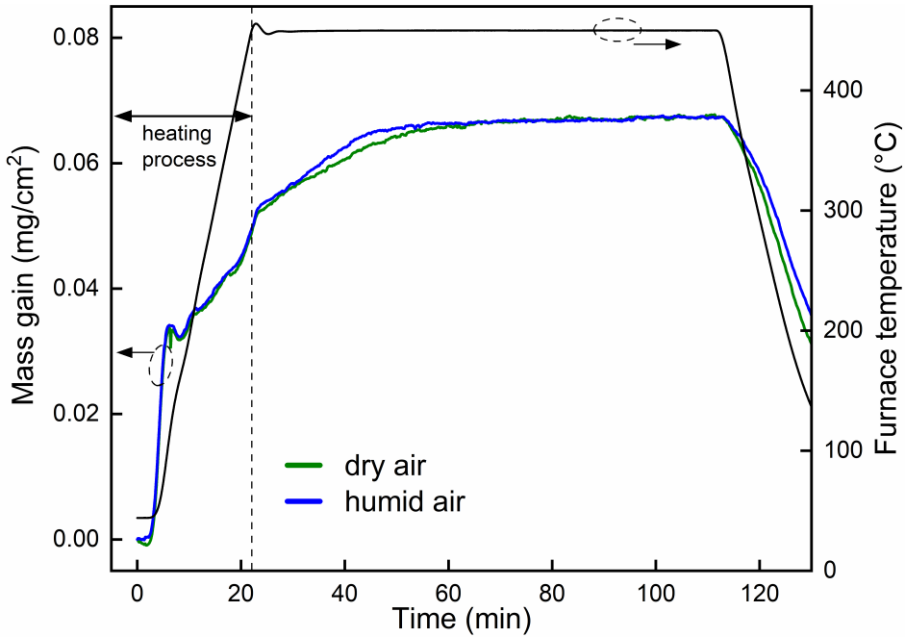

Figure A.4 Mass gain curves as a function of time of the VN oxidized samples for 90 min at 450°C in dry (green curve) and humid (blue curve) atmosphere. The first 21.5 min corresponds to the heating procedure.

To corroborate the TGA findings, XRD analyses are performed on both samples after the annealing procedure (Figure A.5). The as-deposited VN films are also shown as a guideline for a better comparison of the oxidation process. The diffractograms illustrate that V_2O_5 is the only phase present in both oxidized samples, as expected for the plateau at the final stage in Figure A.4. All the peaks in both samples correspond to orthorhombic V_2O_5. However, some peaks only appear in one of the samples. This could refer to a different oxidation process even though the final phase is the same.

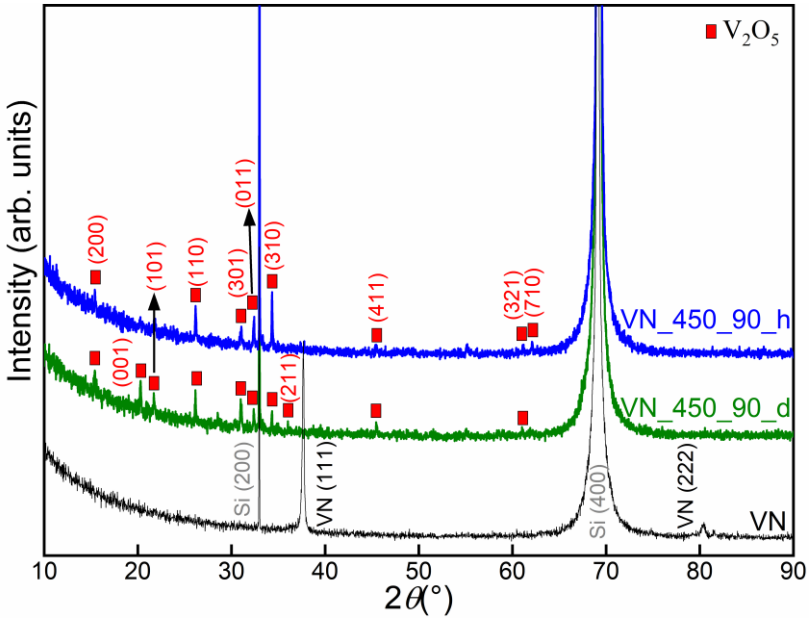

Figure A.5 X-rays diffractograms of as-deposited VN film on Si substrate and the resulting oxide films after oxidation in dry (green curve) and humid (blue curve) atmosphere at 450°C for 90 min.

Although we present just two examples, the preliminary results reveal a possible modification in the oxidation kinetics of VN and V_2N under different atmospheres. The control of the oxidation process is a key step for future industrial applications. The findings exhibited in this appendix expose that TGA is an attractive technique to study the oxidation *in situ* of VN and V_2N films. Nevertheless, to better study the oxidation kinetics a higher mass gain is needed, which means that we must use thicker or larger samples. Also, it will be interesting to perform studies with various amounts of absolute humidity.

Bibliography

[1] C.M. Lampert, Chromogenic smart materials, Mater. Today. 7 (2004) 28–35. https://doi.org/10.1016/S1369-7021(04)00123-3.

[2] I. Bouessay, A. Rougier, P. Poizot, J. Moscovici, A. Michalowicz, J.-M. Tarascon, Electrochromic degradation in nickel oxide thin film: A self-discharge and dissolution phenomenon, Electrochimica Acta. 50 (2005) 3737–3745. https://doi.org/10.1016/j.electacta.2005.01.020.

[3] S.V. Green, E. Pehlivan, C.G. Granqvist, G.A. Niklasson, Electrochromism in sputter deposited nickel-containing tungsten oxide films, Sol. Energy Mater. Sol. Cells. 99 (2012) 339–344. https://doi.org/10.1016/j.solmat.2011.12.025.

[4] C.M. Lampert, Optical switching technology for glazings, Thin Solid Films. 236 (1993) 6–13. https://doi.org/10.1016/0040-6090(93)90633-Z.

[5] C.G. Granqvist, Radiative heating and cooling with spectrally selective surfaces, Appl. Opt. 20 (1981) 2606–2615. https://doi.org/10.1364/AO.20.002606.

[6] D.N. Kharkhan, D. Pilloud, S. Bruyère, S. Migot, S. Barrat, F. Capon, Influence of as-deposited non-uniform stoichiometry on thermochromic properties of LaCoO3 selective layers, J. Appl. Phys. 127 (2020) 015304. https://doi.org/10.1063/1.5121514.

[7] F. Capon, A. Boileau, C. Carteret, N. Martin, P. Boulet, J.F. Pierson, Cation size effect on the thermochromic properties of rare earth cobaltites RECoO3 (RE: La, Nd, Sm), J. Appl. Phys. 114 (2013) 113510. https://doi.org/10.1063/1.4821884.

[8] A. Boileau, F. Capon, P. Laffez, S. Barrat, J.L. Endrino, R.E. Galindo, D. Horwat, J.F. Pierson, Mechanisms of Oxidation of NdNiO3−δ Thermochromic Thin Films Synthesized by a Two-Step Method in Soft Conditions, J. Phys. Chem. C. 118 (2014) 5908–5917. https://doi.org/10.1021/jp4111597.

[9] A. Boileau, F. Capon, S. Barrat, P. Laffez, J.F. Pierson, Thermochromic effect at room temperature of Sm0.5Ca0.5MnO3 thin films, J. Appl. Phys. 111 (2012) 113517. https://doi.org/10.1063/1.4722264.

[10] X. Shen, G. Xu, C. Shao, Influence of structure on infrared emissivity of lanthanum manganites, Phys. B Condens. Matter. 405 (2010) 1090–1094. https://doi.org/10.1016/j.physb.2009.11.011.

[11] M.E.A. Warwick, R. Binions, Advances in thermochromic vanadium dioxide films, J. Mater. Chem. A. 2 (2014) 3275–3292. https://doi.org/10.1039/C3TA14124A.

[12] O.N. Carlson, J.F. Smith, R.H. Nafziger, The vanadium-nitrogen system: a review, Metall. Trans. A. 17 (1986) 1647–1656. https://doi.org/10.1007/BF02817263.

[13] L.E. Toth, C.P. Wang, C.M. Yen, Superconducting critical temperatures of nonstoichiometric transition metal carbides and nitrides, Acta Metall. 14 (1966) 1403–1408. https://doi.org/10.1016/0001-6160(66)90160-X.

[14] N. Fateh, G.A. Fontalvo, G. Gassner, C. Mitterer, Influence of high-temperature oxide formation on the tribological behaviour of TiN and VN coatings, Wear. 262 (2007) 1152–1158. https://doi.org/10.1016/j.wear.2006.11.006.

[15] Y. Qiu, S. Zhang, B. Li, Y. Wang, J.-W. Lee, F. Li, D. Zhao, Improvement of tribological performance of CrN coating via multilayering with VN, Surf. Coat. Technol. 231 (2013) 357–363. https://doi.org/10.1016/j.surfcoat.2012.03.010.

[16] R. Lucio-Porto, S. Bouhtiyya, J.F. Pierson, A. Morel, F. Capon, P. Boulet, T. Brousse, VN thin films as electrode materials for electrochemical capacitors, Electrochimica Acta. 141 (2014) 203–211. https://doi.org/10.1016/j.electacta.2014.07.056.

[17] G. Durai, P. Kuppusami, T. Maiyalagan, J. Theerthagiri, P. Vinoth Kumar, H.-S. Kim, Influence of chromium content on microstructural and electrochemical supercapacitive properties of vanadium nitride thin films developed by reactive magnetron co-sputtering process, Ceram. Int. 45 (2019) 12643–12653. https://doi.org/10.1016/j.ceramint.2019.02.170.
[18] A.N. Christensen, B. Lebech, The structure of β-vanadium nitride, Acta Crystallogr. B. 35 (1979) 2677–2678. https://doi.org/10.1107/S0567740879010141.
[19] Z. Yang, C. Ko, S. Ramanathan, Oxide Electronics Utilizing Ultrafast Metal-Insulator Transitions, Annu. Rev. Mater. Res. 41 (2011) 337–367. https://doi.org/10.1146/annurev-matsci-062910-100347.
[20] F.A. Chudnovskii, E.I. Terukov, D.I. Khomskii, Insulator-metal transition in V3O5, Solid State Commun. 25 (1978) 573–577. https://doi.org/10.1016/0038-1098(78)91492-8.
[21] H.A. Wriedt, The O-V (Oxygen-Vanadium) system, Bull. Alloy Phase Diagr. 10 (1989) 271–277. https://doi.org/10.1007/BF02877512.
[22] C. H. Griffiths, and H. K. Eastwood, Influence of stoichiometry on the metal-semiconductor transition in vanadium dioxide, J. Appl. Phys. 45 (1974) 2201.
[23] W. Brückner, W. Moldenhauer, H. Wich, E. Wolf, H. Oppermann, U. Gerlach, W. Reichelt, The range of homogeneity of VO2 and the influence of the composition on the physical properties. II. The change of the physical properties in the range of homogeneity, Phys. Status Solidi A. 29 (1975) 63–70. https://doi.org/10.1002/pssa.2210290107.
[24] H. W. Liu, L. M. Wong, S. J. Wang, S. H. Tang, X. H. Zhang, Effect of oxygen stoichiometry on the insulator-metal phase transition in vanadium oxide thin films studied using optical pump-terahertz probe spectroscopy, Appl. Phys. Lett. 103 (2013) 151908. https://doi.org/10.1063/1.4824834.
[25] C. Cao, Y. Gao, H. Luo, Pure Single-Crystal Rutile Vanadium Dioxide Powders: Synthesis, Mechanism and Phase-Transformation Property, J. Phys. Chem. C. 112 (2008) 18810–18814. https://doi.org/10.1021/jp8073688.
[26] E. Caruthers, L. Kleinman, Energy Bands of Semiconducting VO2, Phys. Rev. B. 7 (1973) 3760–3766. https://doi.org/10.1103/PhysRevB.7.3760.
[27] S.R. Popuri, M. Miclau, A. Artemenko, C. Labrugere, A. Villesuzanne, M. Pollet, Rapid Hydrothermal Synthesis of VO2 (B) and Its Conversion to Thermochromic VO2 (M1), Inorg. Chem. 52 (2013) 4780–4785. https://doi.org/10.1021/ic301201k.
[28] Y. Oka, S. Sato, T. Yao, N. Yamamoto, Crystal Structures and Transition Mechanism of VO2(A), J. Solid State Chem. 141 (1998) 594–598. https://doi.org/10.1006/jssc.1998.8025.
[29] D. Hagrman, J. Zubieta, C.J. Warren, L.M. Meyer, M.M.J. Treacy, R.C. Haushalter, A New Polymorph of VO2Prepared by Soft Chemical Methods, J. Solid State Chem. 138 (1998) 178–182. https://doi.org/10.1006/jssc.1997.7575.
[30] L. Liu, F. Cao, T. Yao, Y. Xu, M. Zhou, B. Qu, B. Pan, C. Wu, S. Wei, Y. Xie, New-phase VO2 micro/nanostructures: investigation of phase transformation and magnetic property, New J. Chem. 36 (2012) 619–625. https://doi.org/10.1039/C1NJ20798A.
[31] C. Wu, Z. Hu, W. Wang, M. Zhang, J. Yang, Y. Xie, Synthetic paramontroseite VO2 with good aqueous lithium–ion battery performance, Chem. Commun. (2008) 3891–3893. https://doi.org/10.1039/B806009F.
[32] G.A. Horrocks, S. Singh, M.F. Likely, G. Sambandamurthy, S. Banerjee, Scalable Hydrothermal Synthesis of Free-Standing VO2 Nanowires in the M1 Phase, ACS Appl. Mater. Interfaces. 6 (2014) 15726–15732. https://doi.org/10.1021/am504372t.

[33] Y. Oka, T. Yao, N. Yamamoto, Structural phase transition of VO2(B) to VO2(A), J. Mater. Chem. 1 (1991) 815–818. https://doi.org/10.1039/JM9910100815.
[34] Y. Zhang, VO2(B) conversion to VO2(A) and VO2(M) and their oxidation resistance and optical switching properties, Mater. Sci.-Pol. 34 (2016) 169–176. https://doi.org/10.1515/msp-2016-0023.
[35] J.-C. Valmalette, J.-R. Gavarri, High efficiency thermochromic VO2(R) resulting from the irreversible transformation of VO2(B), Mater. Sci. Eng. B. 54 (1998) 168–173. https://doi.org/10.1016/S0921-5107(98)00148-2.
[36] D. Liu, H. Ji, R. Peng, H. Cheng, C. Zhang, Infrared chameleon-like behavior from VO2(M) thin films prepared by transformation of metastable VO2(B) for adaptive camouflage in both thermal atmospheric windows, Sol. Energy Mater. Sol. Cells. 185 (2018) 210–217. https://doi.org/10.1016/j.solmat.2018.05.042.
[37] D.B. McWhan, M. Marezio, J.P. Remeika, P.D. Dernier, X-ray diffraction study of metallic VO2, Phys. Rev. B. 10 (1974) 490–495. https://doi.org/10.1103/PhysRevB.10.490.
[38] S. Westman, I. Lindqvist, B. Sparrman, G.B. Nielsen, H. Nord, A. Jart, Note on a Phase Transition in VO2, Acta Chem. Scand. 1989. 15 (1961). https://doi.org/10.3891/acta.chem.scand.15-0217.
[39] H.S. Choi, J.S. Ahn, J.H. Jung, T.W. Noh, D.H. Kim, Mid-infrared properties of a VO2 film near the metal-insulator transition, Phys. Rev. B. 54 (1996) 4621–4628. https://doi.org/10.1103/PhysRevB.54.4621.
[40] J. Ordonez-Miranda, Y. Ezzahri, K. Joulain, J. Drevillon, J.J. Alvarado-Gil, Modeling of the electrical conductivity, thermal conductivity, and specific heat capacity of VO2, Phys. Rev. B. 98 (2018) 075144. https://doi.org/10.1103/PhysRevB.98.075144.
[41] V. Eyert, The metal-insulator transitions of VO2: A band theoretical approach, Ann. Phys. 11 (2002) 650–704. https://doi.org/10.1002/1521-3889(200210)11:9<650::AID-ANDP650>3.0.CO;2-K.
[42] J.M. Longo, P. Kierkegaard, A Refinement of the Structure of VO2, Acta Chem. Scand. 24 (1970) 420–426. https://doi.org/10.3891/acta.chem.scand.24-0420.
[43] G. Andersson, Studies on Vanadium Oxides. II. The Crystal Structure of Vanadium Dioxide., Acta Chem. Scand. 10 (1956) 623–628. https://doi.org/10.3891/acta.chem.scand.10-0623.
[44] H. Hoshino, K. Okimura, I. Yamaguchi, T. Tsuchiya, Infrared-light switching in highly oriented VO2 films on ZnO-buffered glasses with controlled phase transition temperatures, Sol. Energy Mater. Sol. Cells. 191 (2019) 9–14. https://doi.org/10.1016/j.solmat.2018.10.022.
[45] Y.Y. Luo, L.Q. Zhu, Y.X. Zhang, S.S. Pan, S.C. Xu, M. Liu, G.H. Li, Optimization of microstructure and optical properties of VO2 thin film prepared by reactive sputtering, J. Appl. Phys. 113 (2013) 183520. https://doi.org/10.1063/1.4803840.
[46] S. Berg, T. Nyberg, Fundamental understanding and modeling of reactive sputtering processes, Thin Solid Films. 476 (2005) 215–230. https://doi.org/10.1016/j.tsf.2004.10.051.
[47] M. Marezio, D.B. McWhan, J.P. Remeika, P.D. Dernier, Structural Aspects of the Metal-Insulator Transitions in Cr-Doped VO2, Phys. Rev. B. 5 (1972) 2541–2551. https://doi.org/10.1103/PhysRevB.5.2541.
[48] J.P. Pouget, H. Launois, J.P. D'Haenens, P. Merenda, T.M. Rice, Electron Localization Induced by Uniaxial Stress in Pure V${\mathrm{O}}_{2}$, Phys. Rev. Lett. 35 (1975) 873–875. https://doi.org/10.1103/PhysRevLett.35.873.
[49] Y. Gu, J. Cao, J. Wu, L.-Q. Chen, Thermodynamics of strained vanadium dioxide single crystals, J. Appl. Phys. 108 (2010) 083517. https://doi.org/10.1063/1.3499349.

[50] Switching properties of V1−xTixO2 thin films deposited from alkoxides, Mater. Res. Bull. 32 (1997) 1109–1117. https://doi.org/10.1016/S0025-5408(97)00084-6.
[51] E. Strelcov, A. Tselev, I. Ivanov, J.D. Budai, J. Zhang, J.Z. Tischler, I. Kravchenko, S.V. Kalinin, A. Kolmakov, Doping-Based Stabilization of the M2 Phase in Free-Standing VO2 Nanostructures at Room Temperature, Nano Lett. 12 (2012) 6198–6205. https://doi.org/10.1021/nl303065h.
[52] A. Didelot, Films d'oxydes de vanadium thermochromes dopés aluminium obtenus après un recuit d'oxydation-cristallisation pour applications dans le solaire thermique, PhD dissertation, Université de Lorraine, 2017.
[53] Y. Guo, J. Robertson, Analysis of metal insulator transitions in VO2 and V2O3 for RRAMs, Microelectron. Eng. 109 (2013) 278–281. https://doi.org/10.1016/j.mee.2013.03.015.
[54] C. Wang, X. Liu, J. Shao, W. Xiong, W. Ma, Y. Zheng, Structural transition and temperature-driven conductivity switching of single crystalline VO2(A) nanowires, RSC Adv. 4 (2014) 64021–64026. https://doi.org/10.1039/C4RA12392A.
[55] F. Théobald, R. Cabala, J. Bernard, Essai sur la Structure de VO2(B), J. Solid State Chem. 17 (1976) 431–438.
[56] Ch. Leroux, G. Nihoul, G. Van Tendeloo, From VO2(B) to VO2(R) : Theoretical structures of VO2 polymorphs and in situ electron microscopy, Phys. Rev. B. 57 (1998) 5111–5121. https://doi.org/10.1103/PhysRevB.57.5111.
[57] H. Li, P. He, Y. Wang, E. Hosono, H. Zhou, High-surface vanadium oxides with large capacities for lithium-ion batteries: from hydrated aerogel to nanocrystalline VO2(B), V6O13 and V2O5, J. Mater. Chem. 21 (2011) 10999–11009. https://doi.org/10.1039/C1JM11523E.
[58] H. Liu, Y. Wang, K. Wang, E. Hosono, H. Zhou, Design and synthesis of a novel nanothorn VO2(B) hollow microsphere and their application in lithium-ion batteries, J. Mater. Chem. 19 (2009) 2835–2840. https://doi.org/10.1039/B821799H.
[59] J.B. Goodenough, The two components of the crystallographic transition in VO2, J. Solid State Chem. 3 (1971) 490–500. https://doi.org/10.1016/0022-4596(71)90091-0.
[60] A. Zylbersztejn, N.F. Mott, Metal-insulator transition in vanadium dioxide, Phys. Rev. B. 11 (1975) 4383–4395. https://doi.org/10.1103/PhysRevB.11.4383.
[61] C. Wu, F. Feng, Y. Xie, Design of vanadium oxide structures with controllable electrical properties for energy applications, Chem. Soc. Rev. 42 (2013) 5157–5183. https://doi.org/10.1039/C3CS35508J.
[62] S. Shin, S. Suga, M. Taniguchi, M. Fujisawa, H. Kanzaki, A. Fujimori, H. Daimon, Y. Ueda, K. Kosuge, S. Kachi, Vacuum-ultraviolet reflectance and photoemission study of the metal-insulator phase transitions in VO2, V6O13, and V2O3, Phys. Rev. B. 41 (1990) 4993–5009. https://doi.org/10.1103/PhysRevB.41.4993.
[63] N.F. Mott, The Basis of the Electron Theory of Metals, with Special Reference to the Transition Metals, Proc. Phys. Soc. Sect. A. 62 (1949) 416–422. https://doi.org/10.1088/0370-1298/62/7/303.
[64] M.K. Zayed, A.A. Elabbar, O.A. Yassin, Electronic and optical properties of the VO2 monoclinic phase using SCAN meta-GGA and TB-mBJ methods, Phys. B Condens. Matter. 582 (2020) 411887. https://doi.org/10.1016/j.physb.2019.411887.
[65] V.R. Morrison, Robert.P. Chatelain, K.L. Tiwari, A. Hendaoui, A. Bruhács, M. Chaker, B.J. Siwick, A photoinduced metal-like phase of monoclinic VO revealed by ultrafast electron diffraction, Science. 346 (2014) 445–448. https://doi.org/10.1126/science.1253779.

[66] T.M. Rice, H. Launois, J.P. Pouget, Comment on VO2: Peierls or Mott-Hubbard? A View from Band Theory", Phys. Rev. Lett. 73 (1994) 3042–3042. https://doi.org/10.1103/PhysRevLett.73.3042.
[67] R.E. Peierls, Quantum Theory of Solids, Clarendon Press. Oxford, 1955.
[68] S. Kagoshima, Peierls Phase Transition, Jpn. J. Appl. Phys. 20 (1981) 1617. https://doi.org/10.1143/JJAP.20.1617.
[69] G. Grüner, The dynamics of charge-density waves, Rev. Mod. Phys. 60 (1988) 1129–1181. https://doi.org/10.1103/RevModPhys.60.1129.
[70] R.M. Wentzcovitch, W.W. Schulz, P.B. Allen, VO2: Peierls or Mott-Hubbard? A view from band theory, Phys. Rev. Lett. 72 (1994) 3389–3392. https://doi.org/10.1103/PhysRevLett.72.3389.
[71] K. Okazaki, A. Fujimori, M. Onoda, Temperature-Dependent Electronic Structure of VO2 in the Insulating Phase, J. Phys. Soc. Jpn. 71 (2002) 822–825. https://doi.org/10.1143/JPSJ.71.822.
[72] P. Baum, D.-S. Yang, A.H. Zewail, 4D Visualization of Transitional Structures in Phase Transformations by Electron Diffraction, Science. 318 (2007) 788–792. https://doi.org/10.1126/science.1147724.
[73] C. Weber, D.D. O'Regan, N.D.M. Hine, M.C. Payne, G. Kotliar, P.B. Littlewood, Vanadium Dioxide: A Peierls-Mott Insulator Stable against Disorder, Phys. Rev. Lett. 108 (2012) 256402. https://doi.org/10.1103/PhysRevLett.108.256402.
[74] F.J. Morin, Oxides Which Show a Metal-to-Insulator Transition at the Neel Temperature, Phys. Rev. Lett. 3 (1959) 34–36. https://doi.org/10.1103/PhysRevLett.3.34.
[75] M.M. Qazilbash, M. Brehm, B.-G. Chae, P.-C. Ho, G.O. Andreev, B.-J. Kim, S.J. Yun, A.V. Balatsky, M.B. Maple, F. Keilmann, H.-T. Kim, D.N. Basov, Mott Transition in VO2 Revealed by Infrared Spectroscopy and Nano-Imaging, Science. 318 (2007) 1750–1753. https://doi.org/10.1126/science.1150124.
[76] S. Kumar, F. Maury, N. Bahlawane, Electrical Switching in Semiconductor-Metal Self-Assembled VO2 Disordered Metamaterial Coatings, Sci. Rep. 6 (2016) 37699. https://doi.org/10.1038/srep37699.
[77] J. Givernaud, A. Crunteanu, J.-C. Orlianges, A. Pothier, C. Champeaux, A. Catherinot, P. Blondy, Microwave Power Limiting Devices Based on the Semiconductor–Metal Transition in Vanadium–Dioxide Thin Films, IEEE Trans. Microw. Theory Tech. 58 (2010) 2352–2361. https://doi.org/10.1109/TMTT.2010.2057172.
[78] P. Jin, K. Yoshimura, S. Tanemura, Dependence of microstructure and thermochromism on substrate temperature for sputter-deposited VO2 epitaxial films, J. Vac. Sci. Technol. A. 15 (1997) 1113–1117. https://doi.org/10.1116/1.580439.
[79] D. Ruzmetov, K.T. Zawilski, V. Narayanamurti, S. Ramanathan, Structure-functional property relationships in rf-sputtered vanadium dioxide thin films, J. Appl. Phys. 102 (2007) 113715. https://doi.org/10.1063/1.2817818.
[80] J. Jian, W. Zhang, C. Jacob, A. Chen, H. Wang, J. Huang, H. Wang, Roles of grain boundaries on the semiconductor to metal phase transition of VO2 thin films, Appl. Phys. Lett. 107 (2015) 102105. https://doi.org/10.1063/1.4930831.
[81] S. Yu, S. Wang, M. Lu, L. Zuo, A metal-insulator transition study of VO2 thin films grown on sapphire substrates, J. Appl. Phys. 122 (2017) 235102. https://doi.org/10.1063/1.4997437.
[82] M.A. Kats, D. Sharma, J. Lin, P. Genevet, R. Blanchard, Z. Yang, M.M. Qazilbash, D.N. Basov, S. Ramanathan, F. Capasso, Ultra-thin perfect absorber employing a tunable phase change material, Appl. Phys. Lett. 101 (2012) 221101. https://doi.org/10.1063/1.4767646.

[83] G. Xu, P. Jin, M. Tazawa, K. Yoshimura, Thickness dependence of optical properties of VO2 thin films epitaxially grown on sapphire (0001), Appl. Surf. Sci. 244 (2005) 449–452. https://doi.org/10.1016/j.apsusc.2004.09.157.
[84] M. Benkahoul, M. Chaker, J. Margot, E. Haddad, R. Kruzelecky, B. Wong, W. Jamroz, P. Poinas, Thermochromic VO2 film deposited on Al with tunable thermal emissivity for space applications, Sol. Energy Mater. Sol. Cells. 95 (2011) 3504–3508. https://doi.org/10.1016/j.solmat.2011.08.014.
[85] Y. Ke, S. Wang, G. Liu, M. Li, T.J. White, Y. Long, Vanadium Dioxide: The Multistimuli Responsive Material and Its Applications, Small. 14 (2018) 1802025. https://doi.org/10.1002/smll.201802025.
[86] R. Beaini, B. Baloukas, S. Loquai, J.E. Klemberg-Sapieha, L. Martinu, Thermochromic VO2-based smart radiator devices with ultralow refractive index cavities for increased performance, Sol. Energy Mater. Sol. Cells. 205 (2020) 110260. https://doi.org/10.1016/j.solmat.2019.110260.
[87] I.Y. Forero-Sandoval, J.A. Chan-Espinoza, J. Ordonez-Miranda, J.J. Alvarado-Gil, F. Dumas-Bouchiat, C. Champeaux, K. Joulain, Y. Ezzahri, J. Drevillon, C.L. Gomez-Heredia, J.A. Ramirez-Rincon, VO2 Substrate Effect on the Thermal Rectification of a Far-Field Radiative Diode, Phys. Rev. Appl. 14 (2020) 034023. https://doi.org/10.1103/PhysRevApplied.14.034023.
[88] G. Sun, X. Cao, H. Zhou, S. Bao, P. Jin, A novel multifunctional thermochromic structure with skin comfort design for smart window application, Sol. Energy Mater. Sol. Cells. 159 (2017) 553–559. https://doi.org/10.1016/j.solmat.2016.09.045.
[89] M.-J. Lee, Y. Park, D.-S. Suh, E.-H. Lee, S. Seo, D.-C. Kim, R. Jung, B.-S. Kang, S.-E. Ahn, C.B. Lee, D.H. Seo, Y.-K. Cha, I.-K. Yoo, J.-S. Kim, B.H. Park, Two Series Oxide Resistors Applicable to High Speed and High Density Nonvolatile Memory, Adv. Mater. 19 (2007) 3919–3923. https://doi.org/10.1002/adma.200700251.
[90] D. Mercs, A. Didelot, F. Capon, J.-F. Pierson, B. Hafner, A. Pazidis, S. Föste, R. Reineke-Koch, Innovative Smart Selective Coating to Avoid Overheating in Highly Efficient Thermal Solar Collectors, Energy Procedia. 91 (2016) 84–93. https://doi.org/10.1016/j.egypro.2016.06.177.
[91] H. Kim, K. Cheung, R.C.Y. Auyeung, D.E. Wilson, K.M. Charipar, A. Piqué, N.A. Charipar, VO2-based switchable radiator for spacecraft thermal control, Sci. Rep. 9 (2019) 1–8. https://doi.org/10.1038/s41598-019-47572-z.
[92] R. Osiander, S.L. Firebaugh, J.L. Champion, D. Farrar, M.A.G. Darrin, Microelectromechanical devices for satellite thermal control, IEEE Sens. J. 4 (2004) 525–531. https://doi.org/10.1109/JSEN.2004.830297.
[93] A. Hendaoui, N. Émond, S. Dorval, M. Chaker, E. Haddad, Enhancement of the positive emittance-switching performance of thermochromic VO2 films deposited on Al substrate for an efficient passive thermal control of spacecrafts, Curr. Appl. Phys. 13 (2013) 875–879. https://doi.org/10.1016/j.cap.2012.12.028.
[94] A. Hendaoui, N. Émond, M. Chaker, É. Haddad, Highly tunable-emittance radiator based on semiconductor-metal transition of VO2 thin films, Appl. Phys. Lett. 102 (2013) 061107. https://doi.org/10.1063/1.4792277.
[95] A. Hendaoui, N. Émond, S. Dorval, M. Chaker, E. Haddad, VO2-based smart coatings with improved emittance-switching properties for an energy-efficient near room-temperature thermal control of spacecrafts, Sol. Energy Mater. Sol. Cells. 117 (2013) 494–498. https://doi.org/10.1016/j.solmat.2013.07.023.
[96] B.G. Chae, H.T. Kim, Effects of W doping on the metal–insulator transition in vanadium dioxide film, Phys. B Condens. Matter. 405 (2010) 663–667. https://doi.org/10.1016/j.physb.2009.09.083.

[97] M. Soltani, M. Chaker, E. Haddad, R.V. Kruzelecky, J. Margot, Effects of Ti–W codoping on the optical and electrical switching of vanadium dioxide thin films grown by a reactive pulsed laser deposition, Appl. Phys. Lett. 85 (2004) 1958–1960. https://doi.org/10.1063/1.1788883.
[98] A. Corvisier, Élaboration par pulvérisation magnétron réactive d'une couche thermochrome à base de dioxyde de vanadium. Application à la régulation passive de la température de panneaux solaires, PhD dissertation, Université de Lorraine, 2014. https://www.theses.fr/2014LORR0024.
[99] J. Wu, W. Huang, Q. Shi, J. Cai, D. Zhao, Y. Zhang, J. Yan, Effect of annealing temperature on thermochromic properties of vanadium dioxide thin films deposited by organic sol–gel method, Appl. Surf. Sci. 268 (2013) 556–560. https://doi.org/10.1016/j.apsusc.2013.01.007.
[100] R. Binions, G. Hyett, C. Piccirillo, I.P. Parkin, Doped and un-doped vanadium dioxide thin films prepared by atmospheric pressure chemical vapour deposition from vanadyl acetylacetonate and tungsten hexachloride: the effects of thickness and crystallographic orientation on thermochromic properties, J. Mater. Chem. 17 (2007) 4652–4660. https://doi.org/10.1039/B708856F.
[101] L.L. Fan, S. Chen, Y.F. Wu, F.H. Chen, W.S. Chu, X. Chen, C.W. Zou, Z.Y. Wu, Growth and phase transition characteristics of pure M-phase VO2 epitaxial film prepared by oxide molecular beam epitaxy, Appl. Phys. Lett. 103 (2013) 131914. https://doi.org/10.1063/1.4823511.
[102] H. Paik, J.A. Moyer, T. Spila, J.W. Tashman, J.A. Mundy, E. Freeman, N. Shukla, J.M. Lapano, R. Engel-Herbert, W. Zander, J. Schubert, D.A. Muller, S. Datta, P. Schiffer, D.G. Schlom, Transport properties of ultra-thin VO2 films on (001) TiO2 grown by reactive molecular-beam epitaxy, Appl. Phys. Lett. 107 (2015) 163101. https://doi.org/10.1063/1.4932123.
[103] V.P. Prasadam, B. Dey, S. Bulou, T. Schenk, N. Bahlawane, Study of VO2 thin film synthesis by atomic layer deposition, Mater. Today Chem. 12 (2019) 332–342. https://doi.org/10.1016/j.mtchem.2019.03.005.
[104] G. Hamaoui, N. Horny, C.L. Gomez-Heredia, J.A. Ramirez-Rincon, J. Ordonez-Miranda, C. Champeaux, F. Dumas-Bouchiat, J.J. Alvarado-Gil, Y. Ezzahri, K. Joulain, M. Chirtoc, Thermophysical characterisation of VO2 thin films hysteresis and its application in thermal rectification, Sci. Rep. 9 (2019) 1–10. https://doi.org/10.1038/s41598-019-45436-0.
[105] F. Dumas-Bouchiat, C. Champeaux, A. Catherinot, A. Crunteanu, P. Blondy, rf-microwave switches based on reversible semiconductor-metal transition of VO2 thin films synthesized by pulsed-laser deposition, Appl. Phys. Lett. 91 (2007) 223505. https://doi.org/10.1063/1.2815927.
[106] A. Rougier, A. Blyr, A. Quédé, Electrochromism of Mixed Tungsten-Vanadium Oxide Thin Films Grown by Pulsed Laser Deposition, J. Electrochem. Soc. 148 (2001) H7. https://doi.org/10.1149/1.1339861.
[107] J. Yoon, C. Park, S. Park, B.S. Mun, H. Ju, Correlation between surface morphology and electrical properties of VO2 films grown by direct thermal oxidation method, Appl. Surf. Sci. 353 (2015) 1082–1086. https://doi.org/10.1016/j.apsusc.2015.07.036.
[108] H. Yuce, H. Alaboz, Y. Demirhan, M. Ozdemir, L. Ozyuzer, G. Aygun, Investigation of electron beam lithography effects on metal–insulator transition behavior of vanadium dioxide, Phys. Scr. 92 (2017) 114007. https://doi.org/10.1088/1402-4896/aa90a3.
[109] D.H. Kim, H.S. Kwok, Pulsed laser deposition of VO2 thin films, Appl. Phys. Lett. 65 (1994) 3188–3190. https://doi.org/10.1063/1.112476.

[110] Y. Zhao, C. Chen, X. Pan, Y. Zhu, M. Holtz, A. Bernussi, Z. Fan, Tuning the properties of VO2 thin films through growth temperature for infrared and terahertz modulation applications, J. Appl. Phys. 114 (2013) 113509. https://doi.org/10.1063/1.4821846.
[111] D. Brassard, S. Fourmaux, M. Jean-Jacques, J.C. Kieffer, M.A. El Khakani, Grain size effect on the semiconductor-metal phase transition characteristics of magnetron-sputtered VO2 thin films, Appl. Phys. Lett. 87 (2005) 051910. https://doi.org/10.1063/1.2001139.
[112] J. Vlček, D. Kolenatý, J. Houška, T. Kozák, R. Čerstvý, Controlled reactive HiPIMS—effective technique for low-temperature (300°C) synthesis of VO2 films with semiconductor-to-metal transition, J. Phys. Appl. Phys. 50 (2017) 38LT01. https://doi.org/10.1088/1361-6463/aa8356.
[113] J. Vlček, D. Kolenatý, T. Kozák, J. Houška, J. Čapek, Š. Kos, Ion-flux characteristics during low-temperature (300°C) deposition of thermochromic VO2 films using controlled reactive HiPIMS, J. Phys. Appl. Phys. 52 (2018) 025205. https://doi.org/10.1088/1361-6463/aae9c6.
[114] J.-P. Fortier, B. Baloukas, O. Zabeida, J.E. Klemberg-Sapieha, L. Martinu, Thermochromic VO2 thin films deposited by HiPIMS, Sol. Energy Mater. Sol. Cells. 125 (2014) 291–296. https://doi.org/10.1016/j.solmat.2014.03.007.
[115] S. Loquai, B. Baloukas, J.E. Klemberg-Sapieha, L. Martinu, HiPIMS-deposited thermochromic VO2 films with high environmental stability, Sol. Energy Mater. Sol. Cells. 160 (2017) 217–224. https://doi.org/10.1016/j.solmat.2016.10.038.
[116] V. Melnik, I. Khatsevych, V. Kladko, A. Kuchuk, V. Nikirin, B. Romanyuk, Low-temperature method for thermochromic high ordered VO2 phase formation, Mater. Lett. 68 (2012) 215–217. https://doi.org/10.1016/j.matlet.2011.10.075.
[117] Q. Yu, W. Li, J. Liang, Z. Duan, Z. Hu, J. Liu, H. Chen, J. Chu, Oxygen pressure manipulations on the metal–insulator transition characteristics of highly (0 1 1)-oriented vanadium dioxide films grown by magnetron sputtering, J. Phys. Appl. Phys. 46 (2013) 055310. https://doi.org/10.1088/0022-3727/46/5/055310.
[118] Y.-K. Dou, J.-B. Li, M.-S. Cao, D.-Z. Su, F. Rehman, J.-S. Zhang, H.-B. Jin, Oxidizing annealing effects on VO2 films with different microstructures, Appl. Surf. Sci. 345 (2015) 232–237. https://doi.org/10.1016/j.apsusc.2015.03.044.
[119] J. Qi, G. Ning, Y. Lin, Synthesis, characterization, and thermodynamic parameters of vanadium dioxide, Mater. Res. Bull. 43 (2008) 2300–2307. https://doi.org/10.1016/j.materresbull.2007.08.016.
[120] Y. Ningyi, L. Jinhua, L. Chenglu, Valence reduction process from sol–gel V2O5 to VO2 thin films, Appl. Surf. Sci. 191 (2002) 176–180. https://doi.org/10.1016/S0169-4332(02)00180-0.
[121] Y. Sun, X. Xiao, G. Xu, G. Dong, G. Chai, H. Zhang, P. Liu, H. Zhu, Y. Zhan, Anisotropic vanadium dioxide sculptured thin films with superior thermochromic properties, Sci. Rep. 3 (2013) 1–10. https://doi.org/10.1038/srep02756.
[122] S. Guan, M. Gaudon, M. Souquet-Basiège, O. Viraphong, N. Penin, A. Rougier, Carbon-reduction as an easy route for the synthesis of VO2(M1) and further Al, Ti doping, Dalton Trans. 48 (2019) 3080–3089. https://doi.org/10.1039/C8DT04914A.
[123] Y.-X. Ji, G.A. Niklasson, C.G. Granqvist, M. Boman, Thermochromic VO2 films by thermal oxidation of vanadium in SO2, Sol. Energy Mater. Sol. Cells. 144 (2016) 713–716. https://doi.org/10.1016/j.solmat.2015.10.012.
[124] S.-J. Jiang, C.-B. Ye, M.S.R. Khan, C.-G. Granqvist, Evolution of thermochromism during oxidation of evaporated vanadium films, Appl. Opt. 30 (1991) 847–851. https://doi.org/10.1364/AO.30.000847.

[125] X. Xu, A. Yin, X. Du, J. Wang, J. Liu, X. He, X. Liu, Y. Huan, A novel sputtering oxidation coupling (SOC) method to fabricate VO2 thin film, Appl. Surf. Sci. 256 (2010) 2750–2753. https://doi.org/10.1016/j.apsusc.2009.11.022.
[126] X. Xu, X. He, G. Wang, X. Yuan, X. Liu, H. Huang, S. Yao, H. Xing, X. Chen, J. Chu, The study of optimal oxidation time and different temperatures for high quality VO2 thin film based on the sputtering oxidation coupling method, Appl. Surf. Sci. 257 (2011) 8824–8827. https://doi.org/10.1016/j.apsusc.2011.04.068.
[127] C. Marwitz, B. Stegemann, M. Breitkreitz, D. Spaltmann, H. Kloss, M. Woydt, H. Sturm, Correlation of adhesion force and electrical conductivity in Magnéli-type vanadium oxides and highly oriented pyrolytic graphite, Surf. Sci. 605 (2011) 1271–1274. https://doi.org/10.1016/j.susc.2011.04.014.
[128] U. Schwingenschlögl, V. Eyert, The vanadium Magnéli phases VnO2n-1, Ann. Phys. 13 (2004) 475–510. https://doi.org/10.1002/andp.200410099.
[129] N. Bahlawane, D. Lenoble, Vanadium Oxide Compounds: Structure, Properties, and Growth from the Gas Phase, Chem. Vap. Depos. 20 (2014) 299–311. https://doi.org/10.1002/cvde.201400057.
[130] W. Zeng, X. Fu, L. Yu, T. Shi, P. Liu, J. Xu, J. Chen, C. Qiulan, X. Wang, W. Xie, Growth dynamics and photoresponse of the Wadsley phase V6O13 crystals, J. Mater. Chem. C. 8 (2020) 6470–6477. https://doi.org/10.1039/C9TC06761B.
[131] S. Yamazaki, C. Li, K. Ohoyama, M. Nishi, M. Ichihara, H. Ueda, Y. Ueda, Synthesis, structure and magnetic properties of V4O9—A missing link in binary vanadium oxides, J. Solid State Chem. 183 (2010) 1496–1503. https://doi.org/10.1016/j.jssc.2010.04.007.
[132] S. Choi, J. Kang, S. Ryu, H. Jeen, J. Son, S. Lee, High infrared transparency up to 8-μm-wavelength in correlated vanadium Wadsley conductors, APL Mater. 8 (2020) 041111. https://doi.org/10.1063/1.5136059.
[133] P. Sigmund, Theory of Sputtering. I. Sputtering Yield of Amorphous and Polycrystalline Targets, Phys. Rev. 184 (1969) 383–416. https://doi.org/10.1103/PhysRev.184.383.
[134] D. Depla, Magnetrons, reactive gases and sputtering, Diederik Depla, 2013. http://hdl.handle.net/1854/LU-4239033.
[135] R.D. Arnell, P.J. Kelly, Recent advances in magnetron sputtering, Surf. Coat. Technol. 112 (1999) 170–176. https://doi.org/10.1016/S0257-8972(98)00749-X.
[136] P.J. Kelly, R.D. Arnell, Magnetron sputtering: a review of recent developments and applications, Vacuum. 56 (2000) 159–172. https://doi.org/10.1016/S0042-207X(99)00189-X.
[137] T. Minami, H. Nanto, S. Takata, Highly Conductive and Transparent Aluminum Doped Zinc Oxide Thin Films Prepared by RF Magnetron Sputtering, Jpn. J. Appl. Phys. 23 (1984) L280. https://doi.org/10.1143/JJAP.23.L280.
[138] H. Yabuta, M. Sano, K. Abe, T. Aiba, T. Den, H. Kumomi, K. Nomura, T. Kamiya, H. Hosono, High-mobility thin-film transistor with amorphous InGaZnO4 channel fabricated by room temperature rf-magnetron sputtering, Appl. Phys. Lett. 89 (2006) 112123. https://doi.org/10.1063/1.2353811.
[139] A.V. Singh, S. Chandra, A.K. Srivastava, B.R. Chakroborty, G. Sehgal, M.K. Dalai, G. Bose, Structural and optical properties of RF magnetron sputtered aluminum nitride films without external substrate heating, Appl. Surf. Sci. 257 (2011) 9568–9573. https://doi.org/10.1016/j.apsusc.2011.06.065.
[140] Y. Shigesato, M. Enomoto, H. Odaka, Thermochromic VO2 Films Deposited by RF Magnetron Sputtering Using V2O3 or V2O5 Targets, Jpn. J. Appl. Phys. 39 (2000) 6016. https://doi.org/10.1143/JJAP.39.6016.
[141] H.-C. Ho, Y.-C. Lai, K. Chen, T.D. Dao, C.-H. Hsueh, T. Nagao, High quality thermochromic VO2 films prepared by magnetron sputtering using V2O5 target with in

situ annealing, Appl. Surf. Sci. 495 (2019) 143436. https://doi.org/10.1016/j.apsusc.2019.07.178.
[142] I. Safi, Recent aspects concerning DC reactive magnetron sputtering of thin films: a review, Surf. Coat. Technol. 127 (2000) 203–218. https://doi.org/10.1016/S0257-8972(00)00566-1.
[143] S. Berg, H. Blom, T. Larsson, C. Nender, Modeling of reactive sputtering of compound materials, J. Vac. Sci. Technol. A. 5 (1987) 202–207. https://doi.org/10.1116/1.574104.
[144] J. Schulte, G. Sobe, Magnetron sputtering of aluminium using oxygen or nitrogen as reactive gas, Thin Solid Films. 324 (1998) 19–24. https://doi.org/10.1016/S0040-6090(97)01197-8.
[145] S. Kadlec, J. Musil, J. Vyskocil, Influence of the pumping speed on the hysteresis effect in the reactive sputtering of thin films, Vacuum. 37 (1987) 729–738. https://doi.org/10.1016/0042-207X(87)90262-4.
[146] S. Kadlec, J. Musil, H. Vyskocil, Hysteresis effect in reactive sputtering: a problem of system stability, J. Phys. Appl. Phys. 19 (1986) L187–L190. https://doi.org/10.1088/0022-3727/19/9/004.
[147] A. Le Febvrier, J. Jensen, P. Eklund, Wet-cleaning of MgO(001): Modification of surface chemistry and effects on thin film growth investigated by x-ray photoelectron spectroscopy and time-of-flight secondary ion mass spectroscopy, J. Vac. Sci. Technol. A. 35 (2017) 021407. https://doi.org/10.1116/1.4975595.
[148] A.B. Mei, R.B. Wilson, D. Li, D.G. Cahill, A. Rockett, J. Birch, L. Hultman, J.E. Greene, I. Petrov, Elastic constants, Poisson ratios, and the elastic anisotropy of VN(001), (011), and (111) epitaxial layers grown by reactive magnetron sputter deposition, J. Appl. Phys. 115 (2014) 214908. https://doi.org/10.1063/1.4881817.
[149] A.B. Mei, M. Tuteja, D.G. Sangiovanni, R.T. Haasch, A. Rockett, L. Hultman, I. Petrov, J.E. Greene, Growth, nanostructure, and optical properties of epitaxial VNx/MgO(001) ($0.80 \leq x \leq 1.00$) layers deposited by reactive magnetron sputtering, J. Mater. Chem. C. 4 (2016) 7924–7938. https://doi.org/10.1039/C6TC02289H.
[150] K.M. Calamba, J.F. Pierson, S. Bruyère, A.L. Febvrier, P. Eklund, J. Barrirero, F. Mücklich, R. Boyd, M.P. Johansson Jõesaar, M. Odén, Dislocation structure and microstrain evolution during spinodal decomposition of reactive magnetron sputtered heteroepixatial c-(Ti0.37,Al0.63)N/c-TiN films grown on MgO(001) and (111) substrates, J. Appl. Phys. 125 (2019) 105301. https://doi.org/10.1063/1.5051609.
[151] K. Meyer, I.K. Schuller, C.M. Falco, Thermalization of sputtered atoms, J. Appl. Phys. 52 (1981) 5803–5805. https://doi.org/10.1063/1.329473.
[152] A. Gras-Marti, J.A. Valles-Abarca, Slowing down and thermalization of sputtered particle fluxes: Energy distributions, J. Appl. Phys. 54 (1983) 1071–1075. https://doi.org/10.1063/1.332113.
[153] A. Takeuchi, A. Inoue, Classification of Bulk Metallic Glasses by Atomic Size Difference, Heat of Mixing and Period of Constituent Elements and Its Application to Characterization of the Main Alloying Element, Mater. Trans. 46 (2005) 2817–2829. https://doi.org/10.2320/matertrans.46.2817.
[154] M.W. Thompson, II. The energy spectrum of ejected atoms during the high energy sputtering of gold, Philos. Mag. J. Theor. Exp. Appl. Phys. 18 (1968) 377–414. https://doi.org/10.1080/14786436808227358.
[155] Y. Yamamura, H. Tawara, Energy dependence of ion-induced sputtering yields from monatomic solids at normal incidence, At. Data Nucl. Data Tables. 62 (1996) 149–253. https://doi.org/10.1006/adnd.1996.0005.

[156] D. Gall, S. Kodambaka, M.A. Wall, I. Petrov, J.E. Greene, Pathways of atomistic processes on TiN(001) and (111) surfaces during film growth: an ab initio study, J. Appl. Phys. 93 (2003) 9086–9094. https://doi.org/10.1063/1.1567797.
[157] E. Wirth, F. Guitteny, C. Mathonat, Thermogravimétrie (Technique de l'ingénieur), Réf. : P1260 V3, (2014).
[158] Bragg William Henry, Bragg William Lawrence, The reflection of X-rays by crystals, Proc. R. Soc. Lond. Ser. Contain. Pap. Math. Phys. Character. 88 (1913) 428–438. https://doi.org/10.1098/rspa.1913.0040.
[159] J.I. Langford, A.J.C. Wilson, Scherrer after sixty years: A survey and some new results in the determination of crystallite size, J. Appl. Crystallogr. 11 (1978) 102–113. https://doi.org/10.1107/S0021889878012844.
[160] S. Andrieu, P. Müller, Les Surfaces solides : concepts et méthodes, EDP Sciences, 2005.
[161] N. Colthup, L.H. Daly, S.E. Wiberley, Introduction to Infrared and Raman Spectroscopy, 3rd ed., Academic Press, Inc., 2012.
[162] P. van der Heide, Secondary Ion Mass Spectrometry: An Introduction to Principles and Practices, John Wiley & Sons, Inc., 2014.
[163] D.B. Williams, C.B. Carter, Transmission Electron Microscopy: A Textbook for Materials Science, 2nd ed., Springer US, 2009. https://doi.org/10.1007/978-0-387-76501-3.
[164] C. Ji, Z. Wu, X. Wu, J. Wang, J. Gou, Z. Huang, H. Zhou, W. Yao, Y. Jiang, Al-doped VO2 films as smart window coatings: Reduced phase transition temperature and improved thermochromic performance, Sol. Energy Mater. Sol. Cells. 176 (2018) 174–180. https://doi.org/10.1016/j.solmat.2017.11.026.
[165] S.-Y. Li, G.A. Niklasson, C.G. Granqvist, Thermochromic undoped and Mg-doped VO2 thin films and nanoparticles: Optical properties and performance limits for energy efficient windows, J. Appl. Phys. 115 (2014) 053513. https://doi.org/10.1063/1.4862930.
[166] X. Liang, M. Chen, Q. Wang, S. Guo, L. Zhang, H. Yang, Active and passive modulation of solar light transmittance in a hybrid thermochromic soft-matter system for energy-saving smart window applications, J. Mater. Chem. C. 6 (2018) 7054–7062. https://doi.org/10.1039/C8TC01274A.
[167] C. Ji, Z. Wu, L. Lu, X. Wu, J. Wang, X. Liu, H. Zhou, Z. Huang, J. Gou, Y. Jiang, High thermochromic performance of Fe/Mg co-doped VO2 thin films for smart window applications, J. Mater. Chem. C. 6 (2018) 6502–6509. https://doi.org/10.1039/C8TC01111G.
[168] H. Ji, D. Liu, H. Cheng, C. Zhang, Inkjet printing of vanadium dioxide nanoparticles for smart windows, J. Mater. Chem. C. 6 (2018) 2424–2429. https://doi.org/10.1039/C8TC00286J.
[169] Y. Kim, S. Yu, J. Park, D. Yoon, A.M. Dayaghi, K.J. Kim, J.S. Ahn, J. Son, High-throughput roll-to-roll fabrication of flexible thermochromic coatings for smart windows with VO2 nanoparticles, J. Mater. Chem. C. 6 (2018) 3451–3458. https://doi.org/10.1039/C7TC05876D.
[170] T.D. Vu, Z. Chen, X. Zeng, M. Jiang, S. Liu, Y. Gao, Y. Long, Physical vapour deposition of vanadium dioxide for thermochromic smart window applications, J. Mater. Chem. C. 7 (2019) 2121–2145. https://doi.org/10.1039/C8TC05014G.
[171] A. Paone, M. Geiger, R. Sanjines, A. Schüler, Thermal solar collector with VO2 absorber coating and V1-xWxO2 thermochromic glazing – Temperature matching and triggering, Sol. Energy. 110 (2014) 151–159. https://doi.org/10.1016/j.solener.2014.08.033.
[172] A.L. Pergament, G.B. Stefanovich, A.A. Velichko, Oxide Electronics and Vanadium Dioxide Perspective: A Review, J. Sel. Top. NANO Electron. Comput. 1 (2013) 24–43. https://doi.org/10.15393/j8.art.2013.3002.

[173] D.-H. Qiu, Q.-Y. Wen, Q.-H. Yang, Z. Chen, Y.-L. Jing, H.-W. Zhang, Electrically-driven metal–insulator transition of vanadium dioxide thin films in a metal–oxide-insulator–metal device structure, Mater. Sci. Semicond. Process. 27 (2014) 140–144. https://doi.org/10.1016/j.mssp.2014.06.030.
[174] Y.-B. Kang, Critical evaluation and thermodynamic optimization of the VO–VO2.5 system, J. Eur. Ceram. Soc. 32 (2012) 3187–3198. https://doi.org/10.1016/j.jeurceramsoc.2012.04.045.
[175] M. Zhu, H. Qi, B. Wang, H. Wang, T. Guan, D. Zhang, Thermochromism of vanadium dioxide films controlled by the thickness of ZnO buffer layer under low substrate temperature, J. Alloys Compd. 740 (2018) 844–851. https://doi.org/10.1016/j.jallcom.2018.01.066.
[176] J.B.K. Kana, J.M. Ndjaka, P.O. Ateba, B.D. Ngom, N. Manyala, O. Nemraoui, A.C. Beye, M. Maaza, Thermochromic VO2 thin films synthesized by rf-inverted cylindrical magnetron sputtering, Appl. Surf. Sci. 254 (2008) 3959–3963. https://doi.org/10.1016/j.apsusc.2007.12.021.
[177] F. Kubel, W. Lengauer, K. Yvon, K. Knorr, A. Junod, Structural phase transition at 205 K in stoichiometric vanadium nitride, Phys. Rev. B. 38 (1988) 12908–12912. https://doi.org/10.1103/PhysRevB.38.12908.
[178] A.B. Mei, O. Hellman, N. Wireklint, C.M. Schlepütz, D.G. Sangiovanni, B. Alling, A. Rockett, L. Hultman, I. Petrov, J.E. Greene, Dynamic and structural stability of cubic vanadium nitride, Phys. Rev. B. 91 (2015) 054101. https://doi.org/10.1103/PhysRevB.91.054101.
[179] H. Guo, C. Lu, Z. Zhang, B. Liang, J. Jia, Comparison of microstructures and properties of VN and VN/Ag nanocomposite films fabricated by pulsed laser deposition, Appl. Phys. A. 124 (2018) 694. https://doi.org/10.1007/s00339-018-2055-x.
[180] N. Fateh, G.A. Fontalvo, G. Gassner, C. Mitterer, The Beneficial Effect of High-Temperature Oxidation on the Tribological Behaviour of V and VN Coatings, Tribol. Lett. 28 (2007) 1–7. https://doi.org/10.1007/s11249-007-9241-x.
[181] G. Rampelberg, B.D. Schutter, W. Devulder, K. Martens, I. Radu, C. Detavernier, In situ X-ray diffraction study of the controlled oxidation and reduction in the V–O system for the synthesis of VO2 and V2O3 thin films, J. Mater. Chem. C. 3 (2015) 11357–11365. https://doi.org/10.1039/C5TC02553B.
[182] C. Zhang, Q. Yang, C. Koughia, F. Ye, M. Sanayei, S.-J. Wen, S. Kasap, Characterization of vanadium oxide thin films with different stoichiometry using Raman spectroscopy, Thin Solid Films. 620 (2016) 64–69. https://doi.org/10.1016/j.tsf.2016.07.082.
[183] F. Ureña-Begara, A. Crunteanu, J.-P. Raskin, Raman and XPS characterization of vanadium oxide thin films with temperature, Appl. Surf. Sci. 403 (2017) 717–727. https://doi.org/10.1016/j.apsusc.2017.01.160.
[184] J.C. Parker, Raman scattering from VO2 single crystals: A study of the effects of surface oxidation, Phys. Rev. B. 42 (1990) 3164–3166. https://doi.org/10.1103/PhysRevB.42.3164.
[185] P. Schilbe, Raman scattering in VO2, Phys. B Condens. Matter. 316–317 (2002) 600–602. https://doi.org/10.1016/S0921-4526(02)00584-7.
[186] R. Baddour-Hadjean, J.P. Pereira-Ramos, C. Navone, M. Smirnov, Raman Microspectrometry Study of Electrochemical Lithium Intercalation into Sputtered Crystalline V2O5 Thin Films, Chem. Mater. 20 (2008) 1916–1923. https://doi.org/10.1021/cm702979k.

[187] N.R. Mlyuka, G.A. Niklasson, C.G. Granqvist, Thermochromic VO2-based multilayer films with enhanced luminous transmittance and solar modulation, Phys. Status Solidi A. 206 (2009) 2155–2160. https://doi.org/10.1002/pssa.200881798.
[188] R.L. Voti, M.C. Larciprete, G. Leahu, C. Sibilia, M. Bertolotti, Optimization of thermochromic VO2 based structures with tunable thermal emissivity, J. Appl. Phys. 112 (2012) 034305. https://doi.org/10.1063/1.4739489.
[189] P. Jin, G. Xu, M. Tazawa, K. Yoshimura, Design, formation and characterization of a novel multifunctional window with VO2 and TiO2 coatings, Appl. Phys. A. 77 (2003) 455–459. https://doi.org/10.1007/s00339-002-1460-2.
[190] J. Zheng, S. Bao, P. Jin, TiO2(R)/VO2(M)/TiO2(A) multilayer film as smart window: Combination of energy-saving, antifogging and self-cleaning functions, Nano Energy. 11 (2015) 136–145. https://doi.org/10.1016/j.nanoen.2014.09.023.
[191] J.-H. Yu, S.-H. Nam, J.W. Lee, J.-H. Boo, Enhanced Visible Transmittance of Thermochromic VO2 Thin Films by SiO2 Passivation Layer and Their Optical Characterization, Materials. 9 (2016) 556. https://doi.org/10.3390/ma9070556.
[192] L. Kang, Y. Gao, H. Luo, J. Wang, B. Zhu, Z. Zhang, J. Du, M. Kanehira, Y. Zhang, Thermochromic properties and low emissivity of ZnO:Al/VO2 double-layered films with a lowered phase transition temperature, Sol. Energy Mater. Sol. Cells. 95 (2011) 3189–3194. https://doi.org/10.1016/j.solmat.2011.06.047.
[193] S. Long, X. Cao, N. Li, Y. Xin, G. Sun, T. Chang, S. Bao, P. Jin, Application-oriented VO2 thermochromic coatings with composite structures: Optimized optical performance and robust fatigue properties, Sol. Energy Mater. Sol. Cells. 189 (2019) 138–148. https://doi.org/10.1016/j.solmat.2018.09.023.
[194] A.C. García-Wong, D. Pilloud, S. Bruyère, S. Mathieu, S. Migot, J.F. Pierson, F. Capon, Oxidation of sputter-deposited vanadium nitride as a new precursor to achieve thermochromic VO2 thin films, Sol. Energy Mater. Sol. Cells. 210 (2020) 110474. https://doi.org/10.1016/j.solmat.2020.110474.
[195] K. Sun, C.A. Riedel, A. Urbani, M. Simeoni, S. Mengali, M. Zalkovskij, B. Bilenberg, C.H. de Groot, O.L. Muskens, VO2 Thermochromic Metamaterial-Based Smart Optical Solar Reflector, ACS Photonics. 5 (2018) 2280–2286. https://doi.org/10.1021/acsphotonics.8b00119.
[196] I.G. Madiba, N. Émond, M. Chaker, F.T. Thema, S.I. Tadadjeu, U. Muller, P. Zolliker, A. Braun, L. Kotsedi, M. Maaza, Effects of gamma irradiations on reactive pulsed laser deposited vanadium dioxide thin films, Appl. Surf. Sci. 411 (2017) 271–278. https://doi.org/10.1016/j.apsusc.2017.03.131.
[197] M. Gurvitch, S. Luryi, A. Polyakov, A. Shabalov, Nonhysteretic behavior inside the hysteresis loop of VO2 and its possible application in infrared imaging, J. Appl. Phys. 106 (2009) 104504. https://doi.org/10.1063/1.3243286.
[198] L.N. Son, T. Tachiki, T. Uchida, Characteristics of Vanadium Oxide Thin Films Prepared by Metal–Organic Decomposition for Bolometer Detectors, Jpn. J. Appl. Phys. 50 (2011) 025803. https://doi.org/10.1143/JJAP.50.025803.
[199] L. Xiao, H. Ma, J. Liu, W. Zhao, Y. Jia, Q. Zhao, K. Liu, Y. Wu, Y. Wei, S. Fan, K. Jiang, Fast Adaptive Thermal Camouflage Based on Flexible VO2/Graphene/CNT Thin Films, Nano Lett. 15 (2015) 8365–8370. https://doi.org/10.1021/acs.nanolett.5b04090.
[200] M.A. Kats, R. Blanchard, S. Zhang, P. Genevet, C. Ko, S. Ramanathan, F. Capasso, Vanadium Dioxide as a Natural Disordered Metamaterial: Perfect Thermal Emission and Large Broadband Negative Differential Thermal Emittance, Phys. Rev. X. 3 (2013) 041004. https://doi.org/10.1103/PhysRevX.3.041004.
[201] H. Ji, D. Liu, H. Cheng, C. Zhang, L. Yang, Vanadium dioxide nanopowders with tunable emissivity for adaptive infrared camouflage in both thermal atmospheric windows, Sol.

Energy Mater. Sol. Cells. 175 (2018) 96–101. https://doi.org/10.1016/j.solmat.2017.10.013.
[202] H. Ji, D. Liu, C. Zhang, H. Cheng, VO2/ZnS core-shell nanoparticle for the adaptive infrared camouflage application with modified color and enhanced oxidation resistance, Sol. Energy Mater. Sol. Cells. 176 (2018) 1–8. https://doi.org/10.1016/j.solmat.2017.11.037.
[203] J. Sakai, M. Zaghrioui, M. Matsushima, H. Funakubo, K. Okimura, Impact of thermal expansion of substrates on phase transition temperature of VO2 films, J. Appl. Phys. 116 (2014) 123510. https://doi.org/10.1063/1.4896500.
[204] E. Radue, L. Wang, S. Kittiwatanakul, J. Lu, S.A. Wolf, E. Rossi, R.A. Lukaszew, I. Novikova, Substrate-induced microstructure effects on the dynamics of the photo-induced metal–insulator transition in VO2 thin films, J. Opt. 17 (2015) 025503. https://doi.org/10.1088/2040-8978/17/2/025503.
[205] X. Wang, Y. Cao, Y. Zhang, L. Yan, Y. Li, Fabrication of VO2-based multilayer structure with variable emittance, Appl. Surf. Sci. 344 (2015) 230–235. https://doi.org/10.1016/j.apsusc.2015.03.116.
[206] A. Paone, R. Sanjines, P. Jeanneret, H.J. Whitlow, E. Guibert, G. Guibert, F. Bussy, J.-L. Scartezzini, A. Schüler, Influence of doping in thermochromic V1−xWxO2 and V1−xAlxO2 thin films: Twice improved doping efficiency in V1−xWxO2, J. Alloys Compd. 621 (2015) 206–211. https://doi.org/10.1016/j.jallcom.2014.08.264.
[207] A. Krammer, A. Magrez, W.A. Vitale, P. Mocny, P. Jeanneret, E. Guibert, H.J. Whitlow, A.M. Ionescu, A. Schüler, Elevated transition temperature in Ge doped VO2 thin films, J. Appl. Phys. 122 (2017) 045304. https://doi.org/10.1063/1.4995965.
[208] N.R. Mlyuka, G.A. Niklasson, C.G. Granqvist, Mg doping of thermochromic VO2 films enhances the optical transmittance and decreases the metal-insulator transition temperature, Appl. Phys. Lett. 95 (2009) 171909. https://doi.org/10.1063/1.3229949.
[209] Z. Zhao, Y. Liu, D. Wang, C. Ling, Q. Chang, J. Li, Y. Zhao, H. Jin, Sn dopants improve the visible transmittance of VO2 films achieving excellent thermochromic performance for smart window, Sol. Energy Mater. Sol. Cells. 209 (2020) 110443. https://doi.org/10.1016/j.solmat.2020.110443.
[210] M.K. Dietrich, B.G. Kramm, M. Becker, B.K. Meyer, A. Polity, P.J. Klar, Influence of doping with alkaline earth metals on the optical properties of thermochromic VO2, J. Appl. Phys. 117 (2015) 185301. https://doi.org/10.1063/1.4919433.
[211] G. Xu, P. Jin, M. Tazawa, K. Yoshimura, Optimization of antireflection coating for VO2-based energy efficient window, Sol. Energy Mater. Sol. Cells. 83 (2004) 29–37. https://doi.org/10.1016/j.solmat.2004.02.014.
[212] C.L. Gomez-Heredia, J.A. Ramirez-Rincon, J. Ordonez-Miranda, O. Ares, J.J. Alvarado-Gil, C. Champeaux, F. Dumas-Bouchiat, Y. Ezzahri, K. Joulain, Thermal hysteresis measurement of the VO2 emissivity and its application in thermal rectification, Sci. Rep. 8 (2018) 1–11. https://doi.org/10.1038/s41598-018-26687-9.
[213] A.C. García-Wong, D. Pilloud, S. Bruyère, D. Mangin, S. Migot, J.F. Pierson, F. Capon, Surface morphology-optical properties relationship in thermochromic VO2 thin films obtained by air oxidation of vanadium nitride, J. Materiomics. (2020). https://doi.org/10.1016/j.jmat.2020.12.005.
[214] H. Ju, P. Jia, J. Xu, L. Yu, Y. Geng, Y. chen, M. Liu, T. Wei, The effects of adding aluminum on crystal structure, mechanical, oxidation resistance, friction and wear properties of nanocomposite vanadium nitride hard films by reactive magnetron sputtering, Mater. Chem. Phys. 215 (2018) 368–375. https://doi.org/10.1016/j.matchemphys.2018.05.061.

[215] B.L. Brown, M. Lee, P.G. Clem, C.D. Nordquist, T.S. Jordan, S.L. Wolfley, D. Leonhardt, C. Edney, J.A. Custer, Electrical and optical characterization of the metal-insulator transition temperature in Cr-doped VO2 thin films, J. Appl. Phys. 113 (2013) 173704. https://doi.org/10.1063/1.4803551.
[216] Z. Zou, Z. Zhang, J. Xu, Z. Yu, M. Cheng, R. Xiong, Z. Lu, Y. Liu, J. Shi, Thermochromic, threshold switching, and optical properties of Cr-doped VO2 thin films, J. Alloys Compd. 806 (2019) 310–315. https://doi.org/10.1016/j.jallcom.2019.07.264.
[217] X. Chu, S.A. Barnett, M.S. Wong, W.D. Sproul, Reactive magnetron sputter deposition of polycrystalline vanadium nitride films, J. Vac. Sci. Technol. A. 14 (1996) 3124–3129. https://doi.org/10.1116/1.580180.
[218] C.-K. Wu, J.-H. Huang, G.-P. Yu, Optimization of deposition processing of VN thin films using design of experiment and single-variable (nitrogen flow rate) methods, Mater. Chem. Phys. 224 (2019) 246–256. https://doi.org/10.1016/j.matchemphys.2018.12.038.
[219] H. Luo, H. Wang, G. Zou, E. Bauer, T. Mccleskey, A. Burrell, Q. Jia, A Review of Epitaxial Metal-Nitride Films by Polymer-Assisted Deposition, (2010). https://doi.org/10.4313/TEEM.2010.11.2.054.
[220] X. Liu, H. Lu, M. He, K. Jin, G. Yang, H. Ni, K. Zhao, Epitaxial growth of vanadium nitride thin films by laser molecule beam epitaxy, Mater. Lett. 123 (2014) 38–40. https://doi.org/10.1016/j.matlet.2014.02.079.
[221] A. Glaser, S. Surnev, M.G. Ramsey, P. Lazar, J. Redinger, R. Podloucky, F.P. Netzer, The growth of epitaxial VN(111) nanolayer surfaces, Surf. Sci. 601 (2007) 4817–4823. https://doi.org/10.1016/j.susc.2007.07.032.
[222] Q. Zheng, A.B. Mei, M. Tuteja, D.G. Sangiovanni, L. Hultman, I. Petrov, J.E. Greene, D.G. Cahill, Phonon and electron contributions to the thermal conductivity of VNx epitaxial layers, Phys. Rev. Mater. 1 (2017) 065002. https://doi.org/10.1103/PhysRevMaterials.1.065002.
[223] Z. Zhang, B. Rashkova, G. Dehm, P. Lazar, J. Redinger, R. Podloucky, Unveiling the atomic and electronic structure of the VN/MgO interface, Phys. Rev. B. 82 (2010) 060103. https://doi.org/10.1103/PhysRevB.82.060103.
[224] P. Lazar, B. Rashkova, J. Redinger, R. Podloucky, C. Mitterer, C. Scheu, G. Dehm, Interface structure of epitaxial (111) VN films on (111) MgO substrates, Thin Solid Films. 517 (2008) 1177–1181. https://doi.org/10.1016/j.tsf.2008.06.006.
[225] H. Holleck, Material selection for hard coatings, J. Vac. Sci. Technol. Vac. Surf. Films. 4 (1986) 2661–2669. https://doi.org/10.1116/1.573700.
[226] W. Lengauer, P. Ettmayer, Lattice parameters and thermal expansion of δ-VN1−x from 298–1000 K, Monatshefte Für Chem. Chem. Mon. 117 (1986) 713–719. https://doi.org/10.1007/BF00810062.
[227] J.-H. Huang, C.-H. Lin, G.-P. Yu, Texture evolution of vanadium nitride thin films, Thin Solid Films. 688 (2019) 137415. https://doi.org/10.1016/j.tsf.2019.137415.
[228] X.J. Wang, H.D. Li, Y.J. Fei, X. Wang, Y.Y. Xiong, Y.X. Nie, K.A. Feng, XRD and Raman study of vanadium oxide thin films deposited on fused silica substrates by RF magnetron sputtering, Appl. Surf. Sci. 177 (2001) 8–14. https://doi.org/10.1016/S0169-4332(00)00918-1.
[229] C. Julien, G.A. Nazri, O. Bergström, Raman Scattering Studies of Microcrystalline V6O13, Phys. Status Solidi B. 201 (1997) 319–326. https://doi.org/10.1002/1521-3951(199705)201:1<319::AID-PSSB319>3.0.CO;2-T.
[230] S. Lee, I.N. Ivanov, J.K. Keum, H.N. Lee, Epitaxial stabilization and phase instability of VO2 polymorphs, Sci. Rep. 6 (2016) 19621. https://doi.org/10.1038/srep19621.

[231] P. Miao, J. Wu, Y. Du, Y. Sun, P. Xu, Phase transition induced Raman enhancement on vanadium dioxide (VO2) nanosheets, J. Mater. Chem. C. 6 (2018) 10855–10860. https://doi.org/10.1039/C8TC04269A.
[232] P. Shvets, O. Dikaya, K. Maksimova, A. Goikhman, A review of Raman spectroscopy of vanadium oxides, J. Raman Spectrosc. 50 (2019) 1226–1244. https://doi.org/10.1002/jrs.5616.
[233] R. Sanjinés, P. Hones, F. Lévy, Hexagonal nitride coatings: electronic and mechanical properties of V2N, Cr2N and δ-MoN, Thin Solid Films. 332 (1998) 225–229. https://doi.org/10.1016/S0040-6090(98)00991-2.
[234] O. Lavigne, C. Alemany-Dumont, B. Normand, M.H. Berger, C. Duhamel, P. Delichére, The effect of nitrogen on the passivation mechanisms and electronic properties of chromium oxide layers, Corros. Sci. 53 (2011) 2087–2096. https://doi.org/10.1016/j.corsci.2011.02.026.
[235] P. Hones, R. Sanjines, F. Levy, Characterization of sputter-deposited chromium nitride thin films for hard coatings, Surf. Coat. Technol. 94–95 (1997) 398–402. https://doi.org/10.1016/S0257-8972(97)00443-X.
[236] M.D. Aguas, A.M. Nartowski, I.P. Parkin, M. MacKenzie, A.J. Craven, Chromium nitrides (CrN, Cr2N) from solid state metathesis reactions: effects of dilution and nitriding reagent, J. Mater. Chem. 8 (1998) 1875–1880. https://doi.org/10.1039/A802149J.
[237] C. Mitterbauer, C. Hébert, G. Kothleitner, F. Hofer, P. Schattschneider, H.W. Zandbergen, Electron energy loss-near edge structure as a fingerprint for identifying chromium nitrides, Solid State Commun. 130 (2004) 209–213. https://doi.org/10.1016/j.ssc.2004.01.045.
[238] G. Kothleitner, M. Rogers, A. Berendes, W. Bock, B.O. Kolbesen, A combined SNMS and EFTEM/EELS study on focused ion beam prepared vanadium nitride thin films, Appl. Surf. Sci. 252 (2005) 66–76. https://doi.org/10.1016/j.apsusc.2005.02.013.
[239] F. Hofer, P. Warbichler, A. Scott, R. Brydson, I. Galesic, B. Kolbesen, Electron energy loss near edge structure on the nitrogen K-edge in vanadium nitrides, J. Microsc. 204 (2001) 166–171. https://doi.org/10.1046/j.1365-2818.2001.00946.x.
[240] G. Farges, E. Beauprez, D. Degout, Preparation and characterization of V—N films deposited by reactive triode magnetron sputtering, Surf. Coat. Technol. 54–55 (1992) 115–120. https://doi.org/10.1016/S0257-8972(09)90037-8.
[241] P. Patsalas, N. Kalfagiannis, S. Kassavetis, G. Abadias, D.V. Bellas, Ch. Lekka, E. Lidorikis, Conductive nitrides: Growth principles, optical and electronic properties, and their perspectives in photonics and plasmonics, Mater. Sci. Eng. R Rep. 123 (2018) 1–55. https://doi.org/10.1016/j.mser.2017.11.001.
[242] T.T. Hu, J.H. Hsu, J.C. Huang, S.Y. Kuan, C.J. Lee, T.G. Nieh, Correlation between reflectivity and resistivity in multi-component metallic systems, Appl. Phys. Lett. 101 (2012) 011902. https://doi.org/10.1063/1.4732143.
[243] S. Canulescu, C.N. Borca, K. Rechendorff, S. Daviðsdóttir, K. Pagh Almtoft, L.P. Nielsen, J. Schou, Optical and electrical properties of polycrystalline and amorphous Al-Ti thin films, Appl. Phys. Lett. 108 (2016) 141909. https://doi.org/10.1063/1.4945769.
[244] C. Zhang, O. Gunes, C. Koughia, J. Peng, S.-J. Wen, R. Wong, Q. Yang, S.O. Kasap, Structural mapping of single-crystal VO2 microrods through metal-to-insulator phase transition, J. Mater. Sci. 56 (2021) 260–268. https://doi.org/10.1007/s10853-020-05297-9.
[245] C. Zhang, C. Koughia, O. Güneş, J. Luo, N. Hossain, Y. Li, X. Cui, S.-J. Wen, R. Wong, Q. Yang, S. Kasap, Synthesis, structure and optical properties of high-quality VO2 thin films grown on silicon, quartz and sapphire substrates by high temperature magnetron

sputtering: Properties through the transition temperature, J. Alloys Compd. 848 (2020) 156323. https://doi.org/10.1016/j.jallcom.2020.156323.
[246] F.D. Hardcastle, I.E. Wachs, Determination of vanadium-oxygen bond distances and bond orders by Raman spectroscopy, J. Phys. Chem. 95 (1991) 5031–5041. https://doi.org/10.1021/j100166a025.
[247] T. Kacsich, K.-P. Lieb, Oxidation of thin CrN and Cr2N films analyzed via nuclear reaction analysis and Rutherford backscattering spectrometry, Thin Solid Films. 245 (1994) 4–6. https://doi.org/10.1016/0040-6090(94)90868-0.
[248] Z.B. Qi, B. Liu, Z.T. Wu, F.P. Zhu, Z.C. Wang, C.H. Wu, A comparative study of the oxidation behavior of Cr2N and CrN coatings, Thin Solid Films. 544 (2013) 515–520. https://doi.org/10.1016/j.tsf.2013.01.031.